DOKUZ EYLÜL UNIVERSITY
GRADUATE SCHOOL OF NATURAL AND APPLIED SCIENCES

INCREASING LIQUEFACTION RESISTANCE OF SATURATED COHESIONLESS SOILS ALONG MAJOR COASTAL HIGHWAY ARTERIES OF IZMIR BAY AREA

by

Pınar ATEŞ

February, 2025

İZMİR

INCREASING LIQUEFACTION RESISTANCE OF SATURATED COHESIONLESS SOILS ALONG MAJOR COASTAL HIGHWAY ARTERIES OF IZMIR BAY AREA

A Thesis Submitted to the
Graduate School of Natural and Applied Sciences of Dokuz Eylül University
In Partial Fulfillment of the Requirements for Master of Science in
Department of Civil Engineering, Geotechnical Engineering Program

by

Pınar ATEŞ

February, 2025

İZMİR

M.Sc THESIS EXAMINATION RESULT FORM

We have read the thesis entitled **"INCREASING LIQUEFACTION RESISTANCE OF SATURATED COHESIONLESS SOILS ALONG MAJOR COASTAL HIGHWAY ARTERIES OF IZMIR BAY AREA"** completed by **PINAR ATEŞ** under supervision of **PROF.DR. GÜRKAN ÖZDEN** and we certify that in our opinion it is fully adequate, in scope and in quality, as a thesis for the degree of.Master of Science.

Prof.Dr. Gürkan ÖZDEN

Supervisor

Prof. Dr. Okan ÖNAL

Jury Member

Doç. Dr. Hasan Fırat PULAT

Jury Member

Prof. Dr. Abdullah Seçgin

Director

Graduate School of Natural and Applied Sciences

ACKNOWLEDGMENT

I am grateful to my advisor, Prof. Dr. Gürkan Özden, for their invaluable guidance, encouragement, and insightful feedback throughout my master's studies. Their knowledge and assistance have been invaluable in shaping our research.

I am deeply grateful to my friends, who have always supported me and believed in my accomplishments.

Finally, and most importantly, I want to thank my family, my mother Nevin Ateş, my father Alpaslan Ateş, my sister Tuğçe Ateş, and most importantly my grandmother Nevriye Temel, for their continuous support and understanding throughout this difficult road. Their encouragement has given me strength and motivation.

I would like to dedicate this work to everyone committed to advancing knowledge in geotechnical engineering.

Pınar ATEŞ

INCREASING LIQUEFACTION RESISTANCE OF SATURATED COHESIONLESS SOILS ALONG MAJOR COASTAL HIGHWAY ARTERIES OF IZMIR BAY AREA

ABSTRACT

Liquefaction, a critical geotechnical hazard, occurs when saturated sandy soils lose their strength during seismic events, causing the soil to behave like a liquid. This phenomenon, along with the resultant damage, is a fundamental problem in cities such as İzmir, which are located near active tectonic boundaries and are characterized by saturated sandy soil compositions.

This thesis examines the impact of earthquakes on major coastal highway arteries along the İzmir Bay area, with a specific focus on liquefaction and post-earthquake settlement analysis. A comprehensive geotechnical database was devoleped using Geographic Information System (GIS) technology, incorporating borehole data from 82 drilling sites along the İzmir coastline. GIS-based maps were created to evaluate the factor of safety against liquefaction and induced settlement along the Konak-Üçkuyular and Altınyol highways under different seismic scenarios (DD-2 and DD-3, corresponding to magnitudes Mw=6.5 and M_w=5.5 respectively). The analyses revealed that the safety factor in all regions, Alsancak-Konak, Konak-Üçkuyular, and Bayraklı, declined to extremely low levels during the DD-2 earthquake event. It was observed that both at DD-2 and DD-3 levels, post-liquefaction settlements could reach significantly high values.

Therefore, a dynamic compaction procedure has been proposed to enhance liquefaction resistance in these areas, accompanied by an exemplary study. Additionally, colloidal silica, a novel soil improvement technique, has been introduced. The results of the study aim to provide valuable insights for geotechnical engineers and decision-makers in assessing the vulnerability of main coastal arteries.

Keywords: Liquefaction, earthquake, geographical information system (GIS), post-earthquake settlement, liquefaction-resistance, colloidal silica

İZMİR KÖRFEZ BÖLGESİ SAHİL BOYU ANA KARAYOLLARI BOYUNCA SUYA DOYGUN KOHEZYONSUZ ZEMİNLERİN SIVILAŞMA DİRENCİNİN ARTTIRILMASI

ÖZ

Sıvılaşma, doymuş kumlu zeminlerin sismik olaylar sırasında dayanımını kaybetmesi ile sonuçlanan en önemli geoteknik tehlikelerden biridir. Sıvılaşma ve sonucunda meydana gelen deformasyonlar, aktif tektonik faylara yakın olan ve suya doygun kumlu zeminleri yapısında bulunduran İzmir gibi şehirlerde temel bir sorun teşkil etmektedir. Bu tez kapsamında, İzmir körfezi boyunca ana otoyol arterlerinde sıvılaşma ve sıvılaşma sonrası oturma analizi gerçekleştirilmiştir. İzmir kıyı kesimindeki 82 adet sondaj kuyusuna ait veriler kullanılarak Coğrafi Bilgi Sistemi (CBS) ortamında geoteknik veri tabanı oluşturulmuştur.

Alsancak-Konak, Konak-Üçkuyular ve Bayraklı otoyolları boyunca sıvılaşmaya karşı güvenlik faktörleri ve bu tabakalarda oturma analizleri yapılarak farklı deprem büyüklükleri (M_w=6.5 ve M_w=5.5 büyüklüğüne karşılık gelen DD-2 ve D-3) için hesaplanmış CBS tabanlı enterpolasyon haritaları elde edilmiştir. Analizler, Alsancak-Konak, Konak-Üçkuyular ve Bayraklı bölgelerinde güvenlik faktörünün DD-2 deprem seviyesinde son derece düşük değerlere düştüğünü ortaya koymuştur. DD-2 ve DD-3 seviyelerinde ise sıvılaşma sonrası oturmaların oldukça yüksek değerlere ulaşabileceği gözlemlenmiştir.

Bu sonuçlara göre, bu bölgede dinamik kompaksiyon ile iyileştirme yapılması tavsiye edilmiş ve örnek bir çalışma gerçekleştirilmiştir. Bunun yanı sıra, yeni bir teknik olan kolloidal silika ile iyileştirme yöntemi de tanıtılmıştır. Çalışmanın sonuçlarının, bölgenin sismik risklere karşı hassasiyetini değerlendirmek ve bu tür tehlikelere karşı dayanıklılığı artırmak adına, geoteknik mühendisleri ve karar vericilere değerli bilgiler sağlaması amaçlanmaktadır.

Anahtar kelimeler: Sıvılaşma, deprem, coğrafi bilgi sistemleri (CBS), deprem sonrası oturma, sıvılaşma direnci, kolloidal silika

CONTENTS

Page

M.Sc THESIS EXAMINATION RESULT FORM ii
ACKNOWLEDGMENT iii
ABSTRACT iv
ÖZ v
CONTENTS vi
LIST OF FIGURES ix
LIST OF TABLES xv
LIST OF SYMBOL xvi
ABBREVIATIONS xix

CHAPTER ONE - INTRODUCTION 1

1.1 Study Area 1
1.2 Motivation of the Thesis 2
1.3 Scope of Thesis 3

CHAPTER TWO - STATEMENT OF THE PROBLEM 5

2.1 Introduction 5
2.2 Liquefaction 8
2.2.1 Liquefaction Mechanism 9
2.2.2 Liquefaction Types 10
2.2.3 Liquefaction Susceptibility 13
2.2.4 Assessment of Liquefaction Resistance 18
2.3 Post-Earthquake Settlement 32
2.3.1 Introduction 32
2.3.2 Mechanism of Post-earthquake Settlement 33
2.3.3 Studies on Post-Earthquake Settlement Characteristics 36
2.3.4 Prediction of Post-Earthquake Settlement Approaches 40
2.4 GIS in Lifeline Performance Assessment 45

CHAPTER THREE - ESTABLISHMENT OF THE DATABASE 47

3.1 Data Sources 47
3.1.1 Borehole Data 47
3.1.2 Standart Penetration Test (SPT) Data 48
3.1.3 Laboratory Test Data 48
3.1.4 Geotechnical Database Creation 49
3.1.5 Historical Seismic Data 49
3.1.6 Geographical Information Systems (GIS) Data 49
3.2 Soil Profiles 50
3.2.1 Konak-Üçkuyular Area 51
3.2.2 Alsancak-Konak Area 53
3.2.3 Bayraklı Area (Altınyol) 56
3.3 Data Layers 58

CHAPTER FOUR - LIQUEFACTION ANALYSIS 61

4.1 Liquefaction Maps for the Konak-Üçkuyular Area 63
4.2 Liquefaction Maps for the Alsancak-Konak Area 66
4.3 Liquefaction Maps for the Bayraklı (Altınyol) Area 69

CHAPTER FIVE - POST-EARTHQUAKE SETTLEMENT ANALYSIS 72

CHAPTER SIX - DISCUSSION OF THE RESULTS 76

CHAPTER SEVEN - INCREASING LIQUEFACTION RESISTANCE OF SOIL IN THE STUDY AREA USING CONTEMPORARY TECHNIQUES ... 80

7.1 Dynamic Compaction 80
7.1.1 Process and Mechanism 83
7.1.2 Advantages and Limitations 83
7.1.3 Design Guideline of Dynamic Compaction Method 84
7.2 Proposal for Improvement through Dynamic Compaction in the Konak Coastal Area 87
7.3 A Novel Technique Against Liquefaction with Colloidal Silica 91

7.3.1 Physical Properties of Colloidal Silica 93
7.3.2 Mechanism 94
7.3.3 Literature Review 96
7.3.4 Applicability of the CSM in Konak-Üçkuyular Area 107

CHAPTER EIGHT - CONCLUSIONS AND RECOMMENDATIONS 109

REFERENCES 112

APPENDICES 120

Appendix-1: Borehole Data Information 120
Appendix-2: Data Layers 122
Appendix-3: Liquefaction Analysis Results 158
Appendix-4: Post-Earthquake Settlement Analysis Results 205
Appendix-5: ArcGIS Database 210
Appendix-6: Python Codes 211

LIST OF FIGURES

Page

Figure 1.1 Location map of the study area..... 1

Figure 1.2 The change of İzmir's coastline throughout time due to earthfills (a) Coastline with the inner harbor in the 18th century, (b) In the 2000s earthfilling works along the kordon (Ozbey & Gunes Golbey, 2021)..... 3

Figure 2.1 Simplified geological map showing the neogene–quaternary basins in western Anatolia with main tectonic lines and distribution of the neogene−quaternary deposits (modified from MTA 2002, Geological Map of Türkiye, Scale 1:500.000; Bozkurt 2000, 2001, Uzel et al. 2012) 6

Figure 2.2 Simplified geological map of the region around the Gulf of İzmir. UFZ: Uzunada Fault Zone, IF: Izmir Fault Zone, ICG: Izmir Central Graben, FSF: FocaSuzbeyli Fault, OFZ: Orhanli (Tuzla) Fault Zone, GFZ: Gulbahce Fault Zone, GB: Gulbahce Bay, MEFZ: Menemen Fault Zone, SFZ: Seferihisar Fault Zone, KFZ: Karsiyaka Fault Zone, UI: Uzun Island, HI: Hekim Island, CA: Cicek Archipelago (modified from Uzel et al.,2012 and Coşkun et al., 2017)..... 6

Figure 2.3 Transfer of state of deposition via liquefaction (Ishiara, 1985)..... 10

Figure 2.4 Flow-liquefaction example of a highway embankment during the 1957 Daly City, California, earthquake (Youd, 2003)..... 11

Figure 2.5 Piles sheared by lateral spreading during the 1964 Niigata, Japan, earthquake (Youd, 2003)..... 11

Figure 2.6 (a) Sand boiling caused by liquefaction of underlying sediments during the 1978 Miyagi-ken-oki, Japan, earthquake (source unknown), (b) Sand boil after liquefaction-induced boiling from the 1989 Loma Prieta, California, earthquake has ceased (Idriss and Boulanger, 2008) 12

Figure 2.7 Schematic illustration of flow failure, lateral spread, and ground oscillation: (a) flow failure: liquefaction develops beneath the ground surface, causing the soil to lose strength and flow, (b) lateral spread: the surface layer moves laterally and breaks up from the fissures, (c) ground oscillation: liquefaction decouples the surface layer from the stable ground beneath, causing the surface to vibrate differently, leading to fissures and impacts between oscillating blocks and the firm ground (National Research Council, 1985 and Youd 1984b) 12

Figure 2.8 Data presented by Wang on plasticity chart 14

Figure 2.9 Liquefiable soils on plasticity chart (Seed et al., 2003) 16

Figure 2.10 (a) Data from a cyclic triaxial test from Bray and Sancio (2006); (b) Data from Bray et al. (2004a) 18

Figure 2.11 Method of evaluating liquefaction potential (Seed & Idriss, 1971) 20

Figure 2.12 Determination of maximum shear stress (Seed & Idriss, 1971) 21

Figure 2.13 Stress reduction factor recommendations (Seed & Idriss, 1971) 22

Figure 2.14 Stress reduction factor recommendations by Seed & Idriss (1971) with added average lines from the above equations by National Center for Earthquake Engineering Research (2001) 23

Figure 2.15 Simplified base curve modified from Seed et al., 1985 (Seed et al.,2003) 26

Figure 2.16 Relationship between CRR and $(N1)60f$ for clean sand curve (Idriss & Boulanger, 2010) 27

Figure 2.17 Schematic illustration of liquefaction-induced ground vertical displacement mechanisms (Seed et al., 2001) 34

Figure 2.18 Stress-strain and pore pressure curves from undrained triaxial compression tests on saturated Ottawa sand (data from Castro, 1969; curves modified from Youd, 1975; Youd, 2003). 36

Figure 2.19 Relationship between post-liquefaction volumetric strain and maximum shear strain (Tkusumoto et al., 2004) 37

Figure 2.20 Relationship between the factor of safety and post-liquefaction volumetric strain (Tkusumoto et al., 2004) 38

Figure 2.21 Connection between vertical strain and cumulative shear strain at different strain levels (Matsuda et al., 2011) 39

Figure 2.22 The variation of vertical strain with the number of cycles for multi-directional and single-directional shear (Matsuda et al., 2004) 40

Figure 2.23 Proposed chart for volumetric strain based on CSR and SPT-N from field performance (Tokimatsu and Seed, 1987) 42

Figure 2.24 Relationship between the factor of safety and post-liquefaction volumetric strain 43

Figure 2.25 Relationship between the factor of safety and post-liquefaction volumetric strain 44

Figure 2.26 Relationship between CSR and volumetric strain as a function of $(N1)60f$ (Wu et al., 2003) 45

Figure 3.1 Borehole locations along the study area 48

Figure 3.2 Borehole data incorporated into ArcGIS map 50

Figure 3.3 Konak-Üçkuyular borehole locations 52

Figure 3.4 Soil classification distribution for boreholes in the Konak-Üçkuyular area 52

Figure 3.5 Schematic illustration and N_{30} values for boreholes 1_SK-1, 1_SK-2, and 1_SK-3 53

Figure 3.6 Alsancak-Konak borehole locations 54

Figure 3.7 Soil classification distribution for boreholes in the Alsancak-Konak area 54

Figure 3.8 Schematic illustration for boreholes 4_SK-1, 4_SK-2, and 4_SK-3 55

Figure 3.9 Bayraklı borehole locations 57

Figure 3.10 Soil classification distribution for boreholes in the Bayraklı area..... 57

Figure 3.11 Schematic illustration and N_{30} values for boreholes 6_SK-1, 6_SK-2, and 6_SK-3 58

Figure 3.12 Measured SPT ($N30$) distribution at 3m, 5m, 10m depths in the Konak-Üçkuyular and Alsancak Konak Area 59

Figure 3.13 Measured SPT ($N30$) distribution at 3m, 5m, 10m depths in the Bayraklı Area 60

Figure 4.1 The workflow of data processing and liquefaction analysis..... 63

Figure 4.2 Factor of safety distribution for DD-2 (M_w=6.5) and DD-3 (M_w=5.5) earthquake levels at 3m, 5m, 10m depths in the Alsancak-Konak area.. 64

Figure 4.3 Factor of safety distribution for scenarios; minimum, maximum, and average for DD-2 (M_w=6.5) and DD-3 (M_w=5.5) earthquake level in the Konak-Üçkuyular area 65

Figure 4.4 Factor of safety distribution for DD-2 (M_w=6.5) earthquake level at 3m, 5m, 10m depths in the Alsancak-Konak area..... 66

Figure 4.5 Factor of safety distribution for DD-3 (M_w=5.5) earthquake level at 3m, 5m, and 10m depths in the Alsancak-Konak area..... 67

Figure 4.6 Factor of safety distribution for scenarios; minimum, maximum, and average for DD-2 (M_w=6.5) and DD-3 (M_w=5.5) earthquake level in the Alsancak-Konak area 68

Figure 4.7 Factor of safety distribution for DD-2 (M_w=6.5) earthquake level at 3m, 5m, 10m depths in the Bayraklı (Altınyol) area..... 69

Figure 4.8 Factor of safety distribution for DD-3 (M_w=5.5) earthquake level at 3m, 5m, and 10m depths in the Bayraklı (Altınyol) area..... 70

Figure 4.9 Factor of safety distribution for scenarios; minimum, maximum, and average for DD-2 (M_w=6.5) and DD-3 (M_w=5.5) earthquake level in the Bayraklı (Altınyol) area 71

Figure 5.1 Volumetric strain determination (Wu et al., 2003)..... 73

Figure 5.2 Post-earthquake settlement distribution for DD-2 (M_w=6.5) and DD-3 (M_w=5.5) earthquake levels in the Konak-Üçkuyular area 74

Figure 5.3 Post-earthquake settlement distribution for DD-2 (M_w=6.5) and DD-3 (M_w=5.5) earthquake levels in the Alsancak-Konak area 75

Figure 7.1 Schematic illustration of dynamic compaction method (Nicholson,2014) 81

Figure 7.2 Soil types for dynamic compaction (Lukas, 1995)..... 82

Figure 7.3 Square layout of drop points (Shaban, 2018) 83

Figure 7.4 Location of improvement area..... 88

Figure 7.5 Soil profile of improvement area..... 89

Figure 7.6 30m x 150m Improvement area pattern..... 91

Figure 7.7 Passive site stabilization concept (Gallagher et al., 2002) 93

Figure 7.8 Colloidal silica particle illustration (Silco International, 2005) 94

Figure 7.9 Surface charge of silica particles for the cases of different pH values; (a) pH> 8, O^- on the particle surface and repulsive forces, (b) 5≤pH≤8, some particles still have negative charges, (c) pH<5, H_2O^+ ions attach to the particle surfaces (Zhao et al., 2019)..... 95

Figure 7.10 Gelling mechanism (a) before gelling, (b) during gelling (c) after gelling (Wong et al., 2018)..... 95

Figure 7.11 Variation of peak static strength with silica content (Rosenharb & Hackman, 1981) 97

Figure 7.12 Static stress-strain response: confined and unconfined (Rosenharb & Hackman, 1981) 97

Figure 7.13 Colloidal silica versus strain during cyclic loading (Gallagher & Mitchell, 2002)..... 98

Figure 7.14 Untreated Monterey sand (CSR:0.27) and treated sand (CSR:0.24) axial strain vs cycles (Gallagher & Mitchell, 2002) 99

Figure 7.15 Strain during cyclic loading for 10% CS Samples with different curing time (Gallagher & Mitchell, 2002)..... 99

Figure 7.16 Strain during cyclic loading for 10% CS samples with different curing time (Liao et al., 2003) 100

Figure 7.17 Comparison of liquefaction resistance between untreated sand and treated sand at various curing durations (Liao et al., 2003) 101

Figure 7.18 Observed settlements in treated and untreated zones (Gallagher et al., 2007)..... 102

Figure 7.19 Dynamic properties comparison: shear modulus and damping ratio of treated and untreated samples (Spencer et al., 2007) 102

Figure 7.20 Change in shear modulus of 5% CS sample over a 28-day aging period (Spencer et al., 2007)..... 103

Figure 7.21 Unconfined compression test (a) before and (b) after cyclic loading (Mahmutoğlu & Yılmaz, 2010)..... 104

Figure 7.22 Impact of colloidal silica content on axial strain at different confining pressures (relative density: 30%, 40%, 60%) (Krishnan et al., 2020). 106

Figure 7.23 Hysteresis response during cyclic loading (a) untread sand, (b) treated sand (Krishnan et al., 2020)..... 106

Figure 7.24 Excess pore water pressure vs. axial strain during cyclic loading (a) untread sand, (b) treated sand (Krishnan et al., 2020)..... 107

LIST OF TABLES

Page

Table 2.1 Liquefactions susceptibility of silty soils (Andrews & Martin, 2000)..... 15

Table 2.2 Comparison of field test accounting liquefaction resistance (Youd & Idriss, 1997) 24

Table 2.3 Corrections to SPT (modified from Skempton, 1986) as listed by Robertson and Wride (1998) 30

Table 2.4 Representative number of cyclic and corresponding factors (Seed and Idriss, 1982) 32

Table 3.1 Borehole data information 47

Table 4.1 Local soil classes (TBDY, 2018) 62

Table 4.2 Peak ground acceleration (PGA) values 62

Table 7.1 Suitability of dynamic compaction method 82

Table 7.2 Recommended n_c value for different soil types (Lukas, 1995) 85

Table 7.3 Required unit applied energy from standard proctor test (Lukas, 1995) ... 86

Table 7.4 Approximate induced settlement relation with improvement depth (Shaban, 2015) 87

Table 7.5 Input values for dynamic compaction energy 89

Table 7.6 Dynamic compaction energy calculations 90

LIST OF SYMBOL

M_w : Moment magnitude

N_{30} : Measured SPT blow count

No200 : The percentage of soil particles that pass through a 200-mesh sieve

w_n : Water content

τ_{max} : Maximum shear stress

γ : Unit weight of soil

h : Depth

a_{max} : Peak horizontal acceleration

g : The acceleration of gravity

r_d : Stress reduction coefficient

τ'_{av} : Avarage effective shear stress

σ_{vo} : Overburden pressure

σ'_{vo} : Effective overburden pressure

V_S : Shear wave velocity

$(N_1)_{60}$: Corrected SPT blow count

$CRR_{7.5}$: Cyclic resistance ratio for a magnitude 7.5 earthquake

$(N_1)_{60f}$: Corrected SPT blow count for clean sand

K_s : Fines correction factor

C_{FINES} : Fines correction factor

p_a : Reference pressure

C_N : Overburden pressure correction

C_E : Energy ratio correction

C_B : Borehole diameter correction

C_R : Rod length correction

C_S : Sampling method correction

τ_r : Liquefaction resistance of soil

$\tau_{earthquake}$: Average cyclic shear stress in the ground caused by an earthquake

ε_v : Vertical strain/ Post-liquefaction volumetric strain

D_r : Relative density

c_u : Undrained shear resistance

γ_{max} : Maximum shear strain

γ_{cum} : Cumulative shear strain

Δz_i : Thickness of the layer

N_a : Adjusted SPT blow count in Japanese Standart

N_{60} : Corrected SPT blow count without overburden correction

D_i : Depth of improvement

n_c : Coefficient according to soil type

W_t : Weight of temper

H_d : Drop height

AE_{total} : Total applied energy

AE_{HEP} : Applied energy during high energy pass

AE_{IP} : Applied energy during ironing pass

N_D : Number of drops

N_P : Number of passess

A_e : Effective area

d_{cd} : Crater depth

r_u : Pore Water Pressure Ratio

H_2O^+ : Water Molecule

ABBREVIATIONS

GIS	: Geographical Information System
SPT	: Standart penetration test
USCS	: Unified Soil Classification System
FS	: Safety factor
LL	: Liquid limit
IP, PI	: Plasticity index
CRR	: Cyclic resistance ratio
CSR	: Cyclic stress ratio
CPT	: Cone penetration test
BPT	: Becker penetration test
FC	: Fine content
MSF	: Magnitude scaling factor
S	: Settlement
NCEER	: National Center for Earthquake Engineering Research
SPT-N	: Measured SPT resistance
UU	: Unconfined compression test
PGA	: Peak ground accelaration
EBK	: Emprical bayesian kriging
DC	: Dynamic Compaction
UAE	: Unit Applied Energy

HEP : High Energy Pass

CS : Colloidal silica

CSM : Colloidal Silica Method

CHAPTER ONE
INTRODUCTION

1.1 Study Area

İzmir is the third-largest city in Türkiye and is located in the Aegean Region. Its geographical coordinates are 38° 25′ 19″ N and 27° 07′ 44″ E (Figure 1.1). The coastal regions of Izmir serve as the focal point of the thesis. The study investigates two major transportation arteries the Konak-Üçkuyular and Altınyol coastal highways, to characterize earthquake hazards associated with liquefiable soils that underlain the highways.

Figure 1.1 Location map of the study area

İzmir is highly susceptible to seismic events due to its proximity to the active tectonic boundaries. Earthquakes in the region can lead to severe consequences such as liquefaction, post-earthquake settlement or even ground failure. Understanding the

area's earthquake potential and its implications is crucial for assessing the region's resilience. Moreover, this area hosts critical transportation links for relief efforts in the event of a major earthquake and is adjacent to densely populated districts.

1.2 Motivation of the Thesis

The phenomenon of liquefaction, which will be discussed in more detail in the following section, occurs when repeated earthquake shaking causes the soil to lose strength and stiffness. This leads to a condition where the soil behaves like a liquid. Liquefied soil can no longer support the structures above it, potentially causing buildings to sink and tilt. Additionally, liquefaction can rupture underground utilities and destabilize embankments and levees. In most severe cases, it can result in the total collapse of the structures and infrastructure.

Liquefaction is more pronounced in cities like İzmir, where loose soils and shallow groundwater levels create favourable conditions for its occurence. The interest area of this thesis is the coastline of İzmir. During the early 20th century, earthfill projects were conducted to expand the land area available for urban development. Extensive earthfill activities were carried out in areas such as Alsancak and Kordon area over time. In the early 2000s, the coastal area was further modified, with the see along the coastline being filled to facilitate the construction of a highway, shaping the coastline into its present form (Figure 1.2).

This thesis seeks to investigate the effects of earthquakes on İzmir's coastal lifeline roads, focusing on post-earthquake settlement, liquefaction, and the influence of potential tectonic plate movements. The study aims to provide insight into liquefaction hazards in this area by gathering geotechnical data and spatial information powered by a geographic information system (GIS). GIS technology enables spatial analysis, visualization, and meaningful evaluation of subsurface data. This information is vital for geotechnical engineers in assessing the area and for policymakers in developing strategies to enhance the region's resilience.

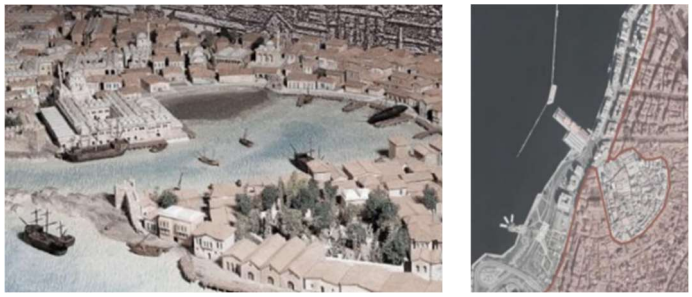

(a)

(b)

Figure 1.2 The change of İzmir's coastline throughout time due to earthfills (a) Coastline with the inner harbor in the 18th century, (b) In the 2000s earthfilling works along the kordon (Ozbey & Gunes Golbey, 2021)

1.3 Scope of Thesis

This thesis explores the state of the lifelines of the İzmir coastal area, with a particular emphasis on liquefaction and post-earthquake settlement under different seismic scenarios, including DD-2, and DD-3, corresponding to magnitudes M_w=6.5 and M_w=5.5. The primary objectives of this research are to analyze the effects of liquefaction and settlement risks along the İzmir coastline following seismic events and to visualize these properties for future reference through mapping. In addressing this topic, the research seeks to answer several essential questions. These include identifying the soil layers in the region, evaluating liquefaction risks along the primary transportation routes on the İzmir coastline and estimating the expected post-earthquake settlement in the area following seismic activity.

The study focuses explicitly on İzmir's coastal regions, particularly two major transportation arteries: the Konak-Üçkuyular Coastal Highway and Altınyol. The data for this analysis are from boreholes drilled in the area between 1990 and 2010,

covering approximately 82 locations during various projects along İzmir's coastline. A geotechnical database was created in ArcGIS utilizing these data.

Liquefaction analyses were based on the Standard Penetration Test (SPT) and laboratory data. The factor of safety against liquefaction was calculated using the Standard Penetration Resistance (N_{30}), fines content (No200) and according to the Unified Soil Classification System (USCS). The safety factors, denoted as FS (2) and FS (3) for DD-2 and DD-3 respectively, were visualized at various depths to create maps. These safety values were also visualized by computing each borehole's minimum, maximum, and average values.

Liquefaction-induced settlement was assessed for the layers expected to undergo liquefaction, employing established methodologies from the literature. Interpolation maps, such as safety factor analysis, were generated at depths (3m, 5m, 10m). These three specific depths were chosen because modal structural failure will likely be affected by liquefaction without occurrence at these depths. Assessing these soil layers will provide engineers with critical insights to enhance risk assessment and devise effective mitigation strategies. Furthermore, this study presents a dynamic improvement project proposal covering 30x150 meters as a liquefaction mitigation measure between the Konak-Üçkuyular section. A novel liquefaction mitigation technique utilizing colloidal silica has been proposed.

The focus on lifelines along the coastal areas, rather than the entire İzmir region, is attributed to their role as critical transportation routes essential for regional connectivity and mobility. These routes are vital for maintaining resilience and ensuring the efficient movement of goods and services during emergencies, constituting the study's key emphasis. The thesis concentrates on this area due to its importance in supporting essential services, infrastructure functioning and continuity.

CHAPTER TWO
STATEMENT OF THE PROBLEM

2.1 Introduction

İzmir coastal region, a critical area for social and economic activity in Türkiye, is exceptionally vulnerable to seismic events since it is located near the active tectonic boundaries of the Aegean Sea.

Izmir Bay is located within a tectonically active region, shaped by N-S extension and the reactivation of ancient tectonic structures (Figure 2.1 and Figure 2.2). The Bornova flysch zone underlies the basin, forming the basement, with a distinct metamorphic core complex to the west. The area is intersected by E-W and NE-SW trending normal faults, while NE-SW trending strike-slip faults have played a very significant role in the region's structural evolution (Bozkurt, 2001; Sözbilir, 2002; Uzel et al., 2012).

Two faults that continue the Gediz Graben to the north and south surround the inner Gulf Area: The southern shore of the Gulf is home to the Izmir Fault Zone (IF). It can be followed up east of Balçova, beginning in the neighbors of İzmir (Coşkun et al., 2017). IF constitutes the northern boundary of the Seferihisar Heights (Emre & Barka, 2000). On the other hand, its offshore continuation westward from Balçova-Narlıdere has not been investigated. IF was accepted as an active normal fault zone in the past (Sözbilir et al., 2004; Emre et al., 2005). By the geomorphologic indicators such as drainage nets and alluvial fans, IF was accepted as an active normal fault zone in the past (Sözbilir et al., 2004; Emre et al., 2005; Coskun et. Al, 2017). The Karşıyaka Fault Zone (KFZ), which stretches from Karşıyaka in the west to the E-W direction, influences the northern shoreline of the Inner Gulf. This is a normal fault, with the northern block acting as the footwall, while the majority of the hanging wall block to the south is submerged beneath the waters of the Gulf of Izmir (Sözbilir et al., 2008).

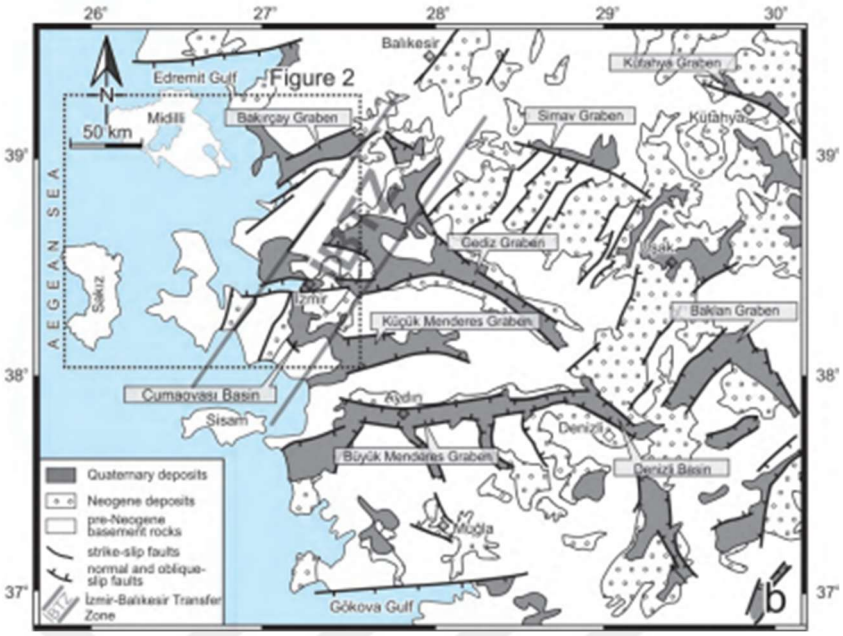

Figure 2.1 Simplified geological map showing the neogene–quaternary basins in western Anatolia with main tectonic lines and distribution of the neogene−quaternary deposits (modified from MTA 2002, Geological Map of Türkiye, Scale 1:500.000; Bozkurt 2000, 2001, Uzel et al. 2012)

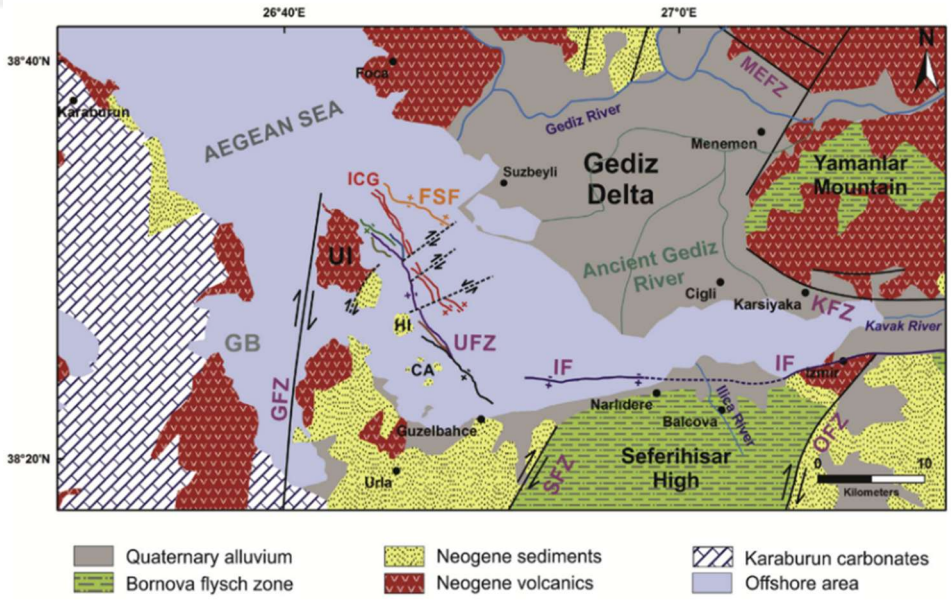

Figure 2.2 Simplified geological map of the region around the Gulf of İzmir. UFZ: Uzunada Fault Zone, IF: Izmir Fault Zone, ICG: Izmir Central Graben, FSF: FocaSuzbeyli Fault, OFZ: Orhanli (Tuzla) Fault Zone, GFZ: Gulbahce Fault Zone, GB: Gulbahce Bay, MEFZ: Menemen Fault Zone, SFZ: Seferihisar Fault Zone, KFZ: Karsiyaka Fault Zone, UI: Uzun Island, HI: Hekim Island, CA: Cicek Archipelago (modified from Uzel et al.,2012 and Coşkun et al., 2017)

There are also two well-known Seferihisar (SFZ) and Orhanlı fault zone (OFZ) bounds the Seferihisar massif between the western and eastern sides (Uzel et al., 2012)

The Seferihisar Fault Zone (SFZ) is a NE-trending dextral fault zone located between Sığacık Bay and the Güzelbahçe district. (İnci et al. 2003; Ocakoğlu et al. 2004, 2005; Emre et al. 2005; Sözbilir et al. 2008). This fault zone begins with Yelki town, striking N20°E and then in the north fault changes to N40–50°E and it connects with the İzmir Fault Zone (IFZ) (Uzel et al., 2012).

The Orhanlı Fault Zone (OFZ) is mainly aligned NE–SW fault zone. It reaches out to İzmir Bay from Kuşadası Bay about 45 km. The main motion along the slip surfaces is dextral strike-slip, however, there is some geomorphological and structural evidence for an earlier sinistral strike-slip motion (Uzel & Sözbilir, 2008)).

The northern part of İzmir Bay is surrounded by E-W trending normal and oblique faults, while the southern part has NE-SW trending strike-slip faults (Figure 2.1 and Figure 2.2). Normal faults normally result in vertical displacements, while strike-slip ones result in horizontal displacements. The simultaneous rupture of both fault types can lead to complex ground movements, severely threatening the stability of buildings and infrastructure. Simultaneously normal and strike-slip fault ruptures could create an extensive fault rupture zone on the surface, especially the inner part of the L-shaped basin area which is the main focus of this work, bringing about widespread structural damage affecting roads, buildings, and energy lines. Additionally, the movement of the water in the bay could increase the risk of tsunamis.

Furthermore, the reclaimed lands and artificial fills along İzmir's coastline make it one of the city's most earthquake-vulnerable places. This study investigates the geotechnical and infrastructural impacts on the lifeline performance of the İzmir coastal area in the event of an earthquake. Liquefaction is a major concern in this context, as it often occurs in loose, saturated soils during large-scale earthquakes.

Historical information also promotes the area's susceptibility and underlines the need for detailed geotechnical investigations and precautions.

Geographic Information Systems (GIS) are a widely used for managing complex and dense databases, integrating diverse data and to creating a meaningful framework. GIS offers numerous applications in geotechnical engineering, including consolidating various geotechnical data sources with spatial information, hazard mapping and modeling potential scenarios. By leveraging these capabilities, we can estimate and propose mitigatiton solutions for potential seismic hazards affecting the İzmir coast's vital infrastructure.

2.2 Liquefaction

Liquefaction, one of the most important geotechnical hazards, was first coined by Terzaghi and Peck (1948). Initially, it was described as the spontaneous liquefaction of sand and causing become liquid. Subsequently, Mogami and Kubo (1953) highlighted the term "liquefaction" as an engineering term that occurs during an earthquake (Ishiara, 1993). The Niigata Earthquake is considered a milestone in recognizing this phenomenon in the modern age. Similarly, The Great Alaskan Earthquake of 1964 raised significant awareness within the geotechnical community. Early contributions to the field was made by Yoshimi et al. (1977), Seed (1979) and Finn et al. (1981).

Liquefaction occurs when seismic events cause saturated, loose sandy soils and non-plastic silts to lose strength and behave like a liquid. The change of state occurs most readily in loose to moderately dense granular soils with poor drainages, such as silty sands or sands and gravels capped by or containing seams of impermeable sediments (Youd et al., 2001)

When cyclic stress is applied during an earthquake event, loose sands tend to contract and decrease in volume. Due to the rapid nature of the event, pore water pressure increases in a short time if the soil is saturated and unable to drain in such a short time. This increase in pore water pressure reduces the effective stress between the soil particles, thereby decreasing the overall strength of the soil and causing it to behave like a viscous fluid. This behavior allows for significant ground deformations, which can range from several feet to several thousand feet depending on the severity of the earthquake and soil conditions (Seed and Idriss, 1971). This can lead to significant ground deformations such as settlements, slope failures, lateral spreadings, and structural failures.

2.2.1 Liquefaction Mechanism

Liquefaction, as previously mentioned, describes the behavior of loose and saturated sands exhibiting a liquid-like response during strong ground shaking. This phenomenon is triggered by cyclic shear stresses induced by seismic waves propagating from the underlying bedrock.

Ishihara's 1985 study provided a clear schematic of liquefaction, illustrating how water and soil grains interact in such cases and offering straightforward approach to understanding the core mechanics of liquefaction. Under normal circumstances, soil is only affected by confining pressure (a). Soil particles tend to compress during an earthquake and strive to occupy a densely packed position, thereby increasing the water pressure inside the pores (b). Thus, decreasing confining pressure may reach zero if the sand is loose enough and shear stresses are high. At this stage, there is no intergranular stress, causing sand particles to become suspended in the water. It is the primary characteristics of liquefaction phenomena. When the earthquake ceased, sand particles settled in a denser way (c). Grain size, drainage conditions, and the duration and magnitude of the shaking influence the length of the liquefied state (Figure 2.3).

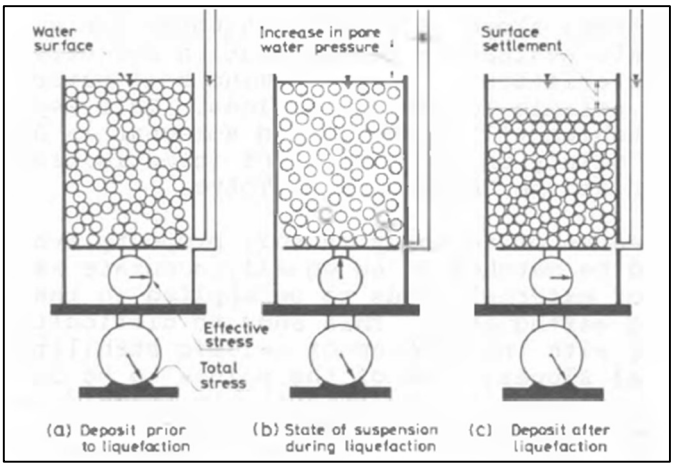

Figure 2.3 Transfer of state of deposition via liquefaction (Ishiara, 1985)

2.2.2 Liquefaction Types

According to Kramer (1996), liquefaction-related processes can be divided into two main groups: flow liquefaction and cyclic mobility. The static shear stresses drive flow liquefaction. Under cyclic loading, soil strength decreases, leading to an unstable state, and this instability combined with the static stresses already present in the field, can result in flow failure. Briefly, it can be described as static shear stresses in a liquefied state exceeding the undrained shear strength. It leads to flow-like movement, happens abruptly and causes large deformations (Figure 2.4).

On the other hand, cyclic mobility differs in that it progresses gradually under repeated loading and unloading conditions. The accumulation of shear strain can cause significant damage, such as tilting or settling, even when developing slowly. According to Kramer, cyclic mobility is influenced by both static and cyclic shear stresses and is often associated with lateral spreading (Figure 2.5). In cyclic mobility, the soil's behavior depends on density, confining pressure and amplitude, and loading duration.

Level-ground liquefaction, a specific instance of cyclic mobility, results in ground oscillation. It is often described by observers as slow-moving ground waves, reaching up to one meter in height, accompanied by the opening and closing of fissures (Youd, 2003). The built-up pore water pressure, induced by seismic loading gradually dissipates upward, manifesting as excessive settlement, flooding, and the formation of sand boils (Figure 2.6). Flow failure, lateral spread, and ground oscillation are schematically illustrated in Figure 2.7.

Figure 2.4 Flow-liquefaction example of a highway embankment during the 1957 Daly City, California, earthquake (Youd, 2003)

Figure 2.5 Piles sheared by lateral spreading during the 1964 Niigata, Japan, earthquake (Youd, 2003)

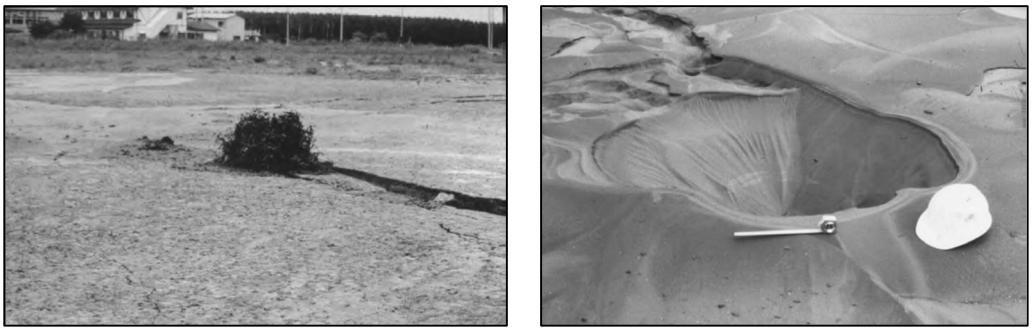

(a) (b)

Figure 2.6 (a) Sand boiling caused by liquefaction of underlying sediments during the 1978 Miyagi-ken-oki, Japan, earthquake (source unknown), (b) Sand boil after liquefaction-induced boiling from the 1989 Loma Prieta, California, earthquake has ceased (Idriss and Boulanger, 2008)

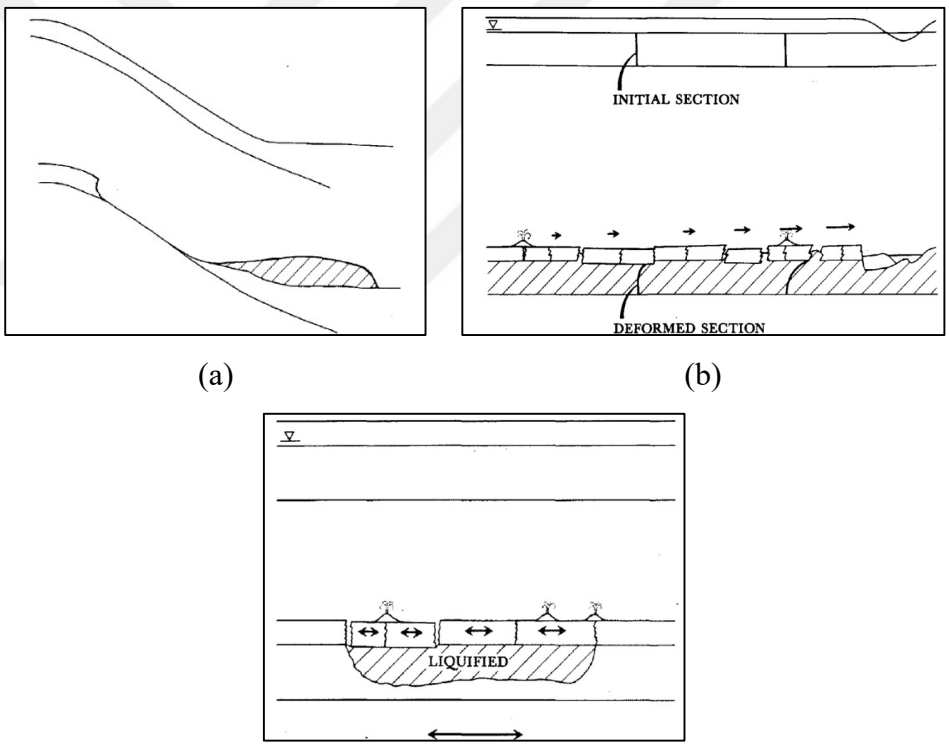

(a) (b)

(c)

Figure 2.7 Schematic illustration of flow failure, lateral spread, and ground oscillation: (a) flow failure: liquefaction develops beneath the ground surface, causing the soil to lose strength and flow, (b) lateral spread: the surface layer moves laterally and breaks up from the fissures, (c) ground oscillation: liquefaction decouples the surface layer from the stable ground beneath, causing the surface to vibrate differently, leading to fissures and impacts between oscillating blocks and the firm ground (National Research Council, 1985 and Youd 1984b)

2.2.3 Liquefaction Susceptibility

Liquefaction susceptibility refers to the likelihood of soil undergoing liquefaction when subjected to seismic loading or other dynamic stresses. It is a critical concept for evaluating the potential for liquefaction in specific soil types under given conditions. Key factors influencing liquefaction susceptibility include soil types, grain size distribution, density of soil, soil plasticity and the depth of the groundwater table.

2.2.3.1 Liquefiable Soil Types

Identifying soil types susceptible to liquefaction is essential before investigating the triggers and onset of soil liquefaction. Early liquefaction studies primarily focused on clean sand with low fines contents. However, research has since demonstrated that soils with high fines content can also liquefy during significant seismic events. Laboratory findings have colloborated field observations (Kishida, 1969; Tohno & Yasuda, 1981). Numerous studies (Chu et al., 2004; Bray et al., 2004a; Martin et al., 2004) have shown that sandy soils as well as saturated silty and clayey soils undergo substantial strength reduction and large deformations under earthquake loading. Post-earthquake investigations, including those following the 1994 Northridge, 1999 Kocaeli, and 1999 Chi-Chi earthquakes, revealed ground failures and structural damage in areas with soils containing more than 15% silt and clay fractions.

The ‘Chinese Criteria’ were widely adopted in the United States as a practical method for designating clayey soils as non-liquefiable. This criterion, established by Wang (1979) based on various sites where liquefaction was observed during strong earthquakes in China, was later summarized by Seed and Idriss (1982). It indicates that soils with over 15%-20% of particles smaller than 0.005, a liquid limit to water content ratio greater than 0.9 and a liquid limit below 35, are prone to liquefaction. However, according to Figure 2.8, no evidence suggests that silty (ML) soils would undergo liquefaction.

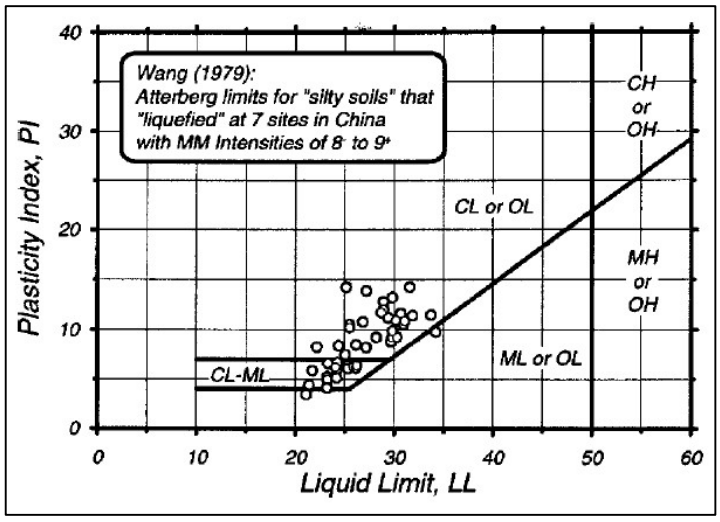

Figure 2.8 Data presented by Wang on plasticity chart

Andrews and Martin (2000) clarified the misconceptions about silty soils and refined the criteria outlined by Seed et al. (1983), summarized below Table 2.1. They indicated that silt grains are, in fact, regarded as very fine sand. Both sand grains and silt grains are rock-forming minerals and they share the same grain form. As a result, attraction forces such as hydrogen and van der Waals bonds are negligible for silt grains, just as they are between sand grains (Mitchell, 1976). On the other hand, clay minerals exhibit plasticity. The susceptibility characteristics of the silts are very similar to those of sands. Consequently, they arrived at the following conclusions:

- Silty soils can be susceptible to liquefaction
- Clay content can be a key parameter for distinguishing liquefiable and non-liquefiable silty soils.
- Liquid limit can be a key parameter for distinguishing liquefiable and non-liquefiable silty soils.
- Using a liquid limit criterion and a clay content criterion helps address cases where clay-sized grains are non-plastic and non-clay-sized grains are plastic.

Table 2.1 Liquefactions susceptibility of silty soils (Andrews & Martin, 2000)

	Liquid Limit < 32	**Liquid Limit ≥ 32**
Clay Content < 10%	Susceptible	Further Studies Required (Considering plastic non-clay sized grains – such as Mica)
Clay Content ≥ 10%	Further Studies Required (Considering non-plastic clay sized grains – such as mine and quarry tailings	Not susceptible

From 1994 to 1999, a group of experts collaborated and published a summary article in the ASCE Journal of Geotechnical and Geoenvironmental Engineering (Youd et al., 2001). The article emphasized re-examination of Chinese Criteria defining fines regarding cohesive soil. However, no concensus was reached on this matter.

In 1999, Chi Chi and Kocaeli led to changes in the liquefaction susceptibility criteria for fines. It was discovered that, contrary to the Modified Chinese Criteria, significant liquefaction-induced ground deformations occurred in cohesive soils. Based on field performance observations, many researchers concluded the following:

- Soils with higher plasticity might be prone to remarkable cyclic pore pressure increase and subsequently loss of strength contrasting with Modified Chinese Criteria
- Soils with even higher plasticity may have also been exposed to cyclic pore pressure generation in a gradual rather than prompt form.

Seed et.al. (2003) examined the advancements in soil liquefaction within a comprehensive framework. Sandy soils and low-plasticity silty soils tend to develop cyclically induced liquefaction at relatively low shear strains of 3% to 6%, primarily accompanied by a substantial loss in strength. In higher-plasticity soils, strength loss accompanied by a rise in pore pressures can occur, but these effects are observed at larger shear strains with less severe pore pressure buildup. As soil plasticity increases, the behavior becomes more ductile and the transition between soils prone to classic

liquefaction and those that are not, is more gradual than distinct. To categorize this behavior, the liquefaction susceptibility of soils with a high fine content has been examined by dividing them into three distinct zones on the plasticity chart. In Figure 2.9 soils containing sufficient fines to influence their behavior and that fall within Zone A are considered potentially susceptible to classic, cyclic-induced liquefaction. Soils in Zone B represent a transitional range; they may liquefy, particularly if their in-situ water content exceeds 85% of their liquid limit. However, these soils tend to behave more ductilely and may not fully lose strength under low cyclic shear strains. While conventional penetration-based liquefaction evaluations are less reliable for these soils, they can be effectively tested in the laboratory using undisturbed samples and sensitivity should also be assessed in these cohesive soils. Soils located within Zone C (the area except Zone-A and Zone-B), on the other hand, rarely experience classic liquefaction. Nevertheless, they may experience significant strength loss due to remolding or large shear movements. Cohesive soils, such as clays and plastic silts, are particularly sensitive and prone to substantial strength loss if sheared or remolded and they may fall into Zones B and C depending on their specific composition and behavior.

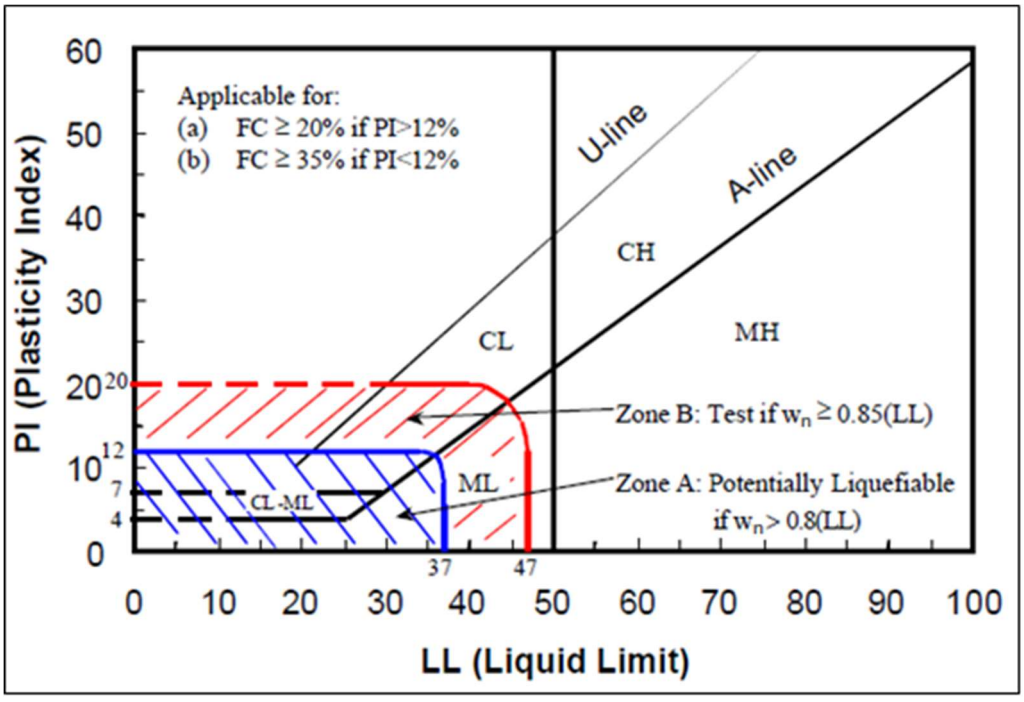

Figure 2.9 Liquefiable soils on plasticity chart (Seed et al., 2003)

Bray and his colleagues (2004) revealed that low-plasticity silts in Adapazarı were typically responsible of severe structural damage. Low liquid limits (LL<35) and high water contents (w_n>0.9 LL) were identified as reliable markers of liquefaction or notable strength loss from shaking in the Adapazari silts. Fine-grained soils were more frequently softened by cyclic mobility and the working of buildings into the softer soils beneath these structures. Bray et al. (2004a) also highlighted that contrary to the Chinese method, fine-grained soils with clay contents greater than 15% liquefied and led to significant ground failure. They concluded that loose soils with PI> 12 and w_n/LL> 0.85 were liquefaction-prone. Conversely, the loose soils for which 12<PI<20 and w_n/LL>0.8 were always more resistant to liquefaction but still less resistant to cyclic mobility, and the soils with PI>20 were not liquefiable.

Bray and Sancio (2006) performed the cyclic triaxial and cyclic simple shear tests (Figure 2.10). They concluded that the plasticity index (PI) plays a significant role for clay-sized particles. Loose soils with a PI of less than 12 and w_n/LL>0.85 were shown to be susceptible to liquefaction. In contrast, soils with 12<PI<18 and w_n/LL>0.8 consistently demonstrated higher resistance to liquefaction. Additionally, when w_n/LL>0.8, a relatively constant liquefaction resistance level was observed. For soils with low plasticity index (PI) values, resistance to liquefaction and the associated seismic demand were generally considered negligible when PI exceeded 18.

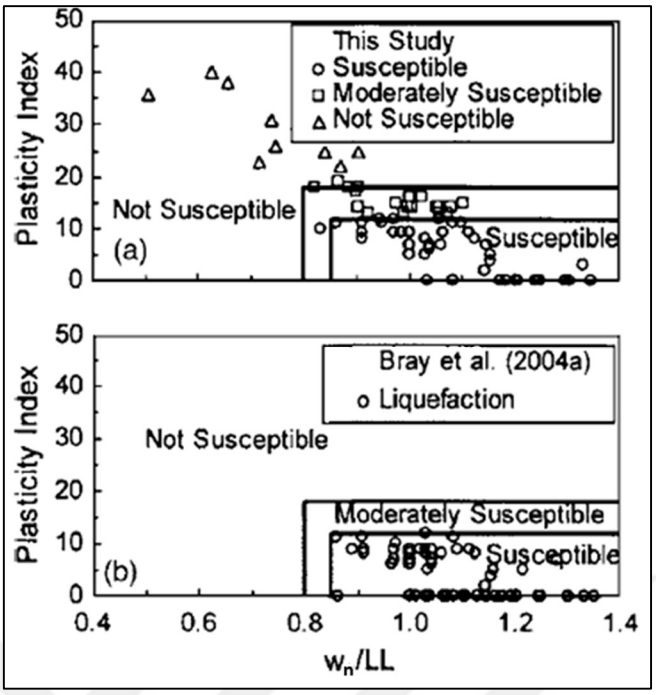

Figure 2.10 (a) Data from a cyclic triaxial test from Bray and Sancio (2006); (b) Data from Bray et al. (2004a)

2.2.4 Assessment of Liquefaction Resistance

In geotechnical engineering, evaluating liquefaction resistance is a critical process, as it addresses the fundamental question of soil stability during seismic events. Accurately predicting liquefaction resistance is essential for assessing the safety of existing structures and guiding the design of future developments.

Liquefaction resistance is generally described as a soil's ability to endure seismic activity without losing its strength. Two key factors influence soil behaviour during seismic shaking: liquefaction resistance (Cyclic Resistance Ratio; CRR) and the seismic demand imposed on the soil. (Cyclic Stress Ratio; CSR).

The most popular approach for evaluating liquefaction resistance is still the "simplified procedure" established by Seed and Idriss in 1971. This method uses the depth of the soil layer, the maximum ground acceleration, and the earthquake

magnitude to determine CSR. It is normalized by vertical consolidation effective stress. On the other hand, while cyclic resistance ratios are estimated through practical testing methods like standard penetration tests (SPT), cone penetration tests (CPT), or analyzing shear wave velocity, the insight into soil behavior and the crucial role played by on-site evaluations in the assessment process cannot be overstated. Since they offer insight into soil behavior, the in-situ tests are particularly helpful and play a vital role in the assessment process.

Liquefaction is anticipated when the CSR value exceeds CRR for a given depth. Therefore, accurately identifying these parameters and assessing their interaction with the relevant soil layers is essential for evaluating liquefaction potential. This process has evolved over the years, incorporating advancements in understanding soil behaivor, earthquake dynamics and spatial variability. Numerous researchers have contributed new perspectives, proposing modifications and innovative techniques to refine the assessment process.

2.2.4.1 Cyclic Stress Ratio, CSR

Seed and Idriss (1971) introduced a comprehensive method for evaluating liquefaction potential, involving the following steps:

1. **Determination of shear stress:** During an earthquake, the shear stress history at various soil depths is analyzed and converted into an equivalent number of uniform stress cycles.

2. **Calculation of Cyclic Stress Ratio (CSR):** The equivalent cycles are used to develop a CSR curve as a depth function, which represent the cyclic shear stress induced by the earthquake (Figure 2.11).

3. **Estimation of Cylic Resistance Ratio (CRR):** Laboratory tests, such as cyclic triaxial compression or cyclic simple shear tests, are conducted to determine the cyclic shear stress required to induce liquefaction. These values are plotted against depth,

forming the CRR curve, which reflects the soil's shear strength under cyclic loading conditions.

The comparison of these results led to the conclusion that liquefaction occurs only in areas where the shear stresses induced by the earthquake exceed the soil's critical resistance. At other depths, the shear stresses generated by the earthquake are insufficient to trigger liquefaction.

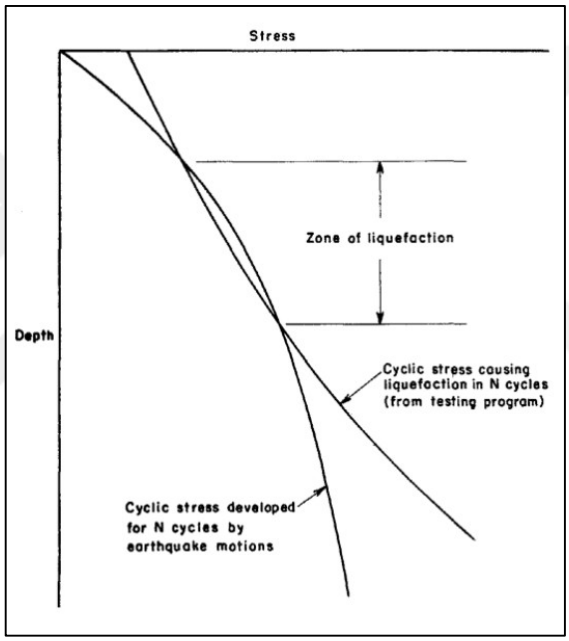

Figure 2.11 Method of evaluating liquefaction potential (Seed & Idriss, 1971)

As previously indicated, a simplified approach for assessing liquefaction resistance has been suggested. The upward propagation of shear waves during an earthquake is the primary cause of the shear stresses in a soil deposit. The maximum shear stress would be if the soil column above a soil element at depth h behaved as a rigid body (Figure 2.12a).

During an earthquake, the shear stresses in a soil deposit can be illustrated as a soil block and the loads acting on it at depth h to calculate CSR. The maximum shear stress would be:

$$(\tau_{max})_r = \gamma h \frac{a_{max}}{g} \tag{2.1}$$

Since the soil column is a deformable body, the actual shear stress at depth h, is reduced by the stress reduction coefficient (r_d) (Figure 2.12c). It starts with 1 near the ground surface and drops significantly with depth. Actual shear stress can be expressed by Equation 2.2:

$$(\tau_{max})_r = r_d (\tau_{max})_r \tag{2.2}$$

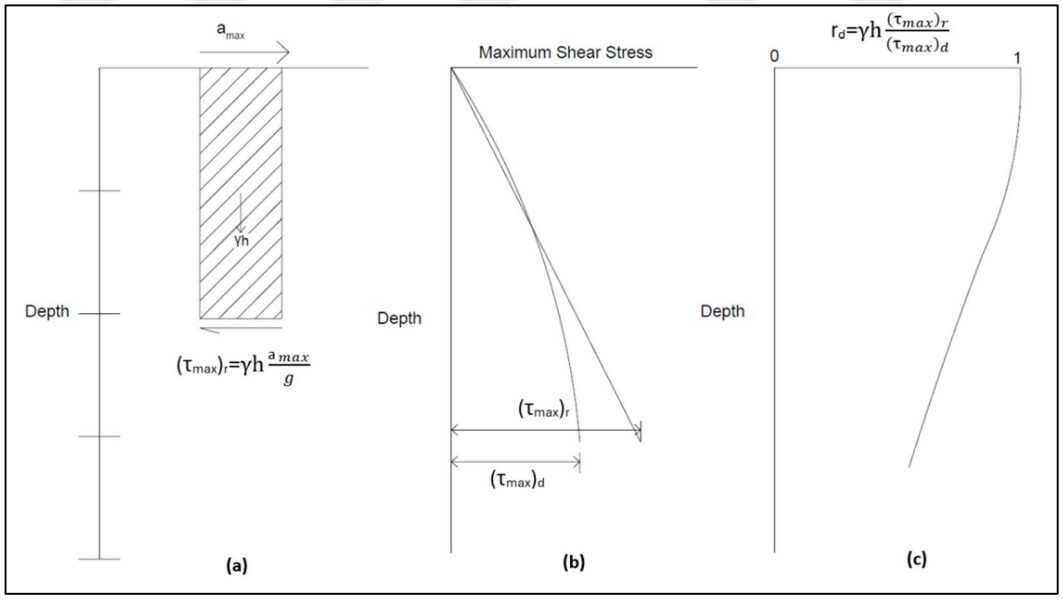

Figure 2.12 Determination of maximum shear stress (Seed & Idriss, 1971)

Laboratory and field data have shown that the average shear stress (τ'_{av}) is approximately 65% of the maximum shear stress. The CSR value is then calculated using Equation 2.3. The cyclic stress ratio (CSR), τ'_{av}/σ'_{vo}, in a soil layer can be described as (Seed and Idriss, 1971);

$$CSR = (\frac{\tau'_{av}}{\sigma'_{vo}})=0.65\ (\frac{a_{max}}{g})\left(\frac{\sigma_{v0}}{\sigma'_{vo}}\right) r_d \tag{2.3}$$

where

a_{max}: Peak horizontal Acceleration

g: The acceleration of gravity

σ_{v0}: Overburden pressure

σ'_{v0}: Effective overburden pressure

r_d: Stress reduction coefficient

Therefore, CSR is a crucial parameter for predicting liquefaction resistance.

Seed and Idriss (1971) introduced the stress reduction coefficient (r_d), shown in Figure 2.13.

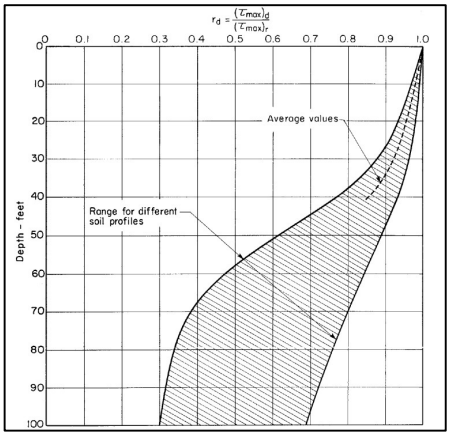

Figure 2.13 Stress reduction factor recommendations (Seed & Idriss, 1971)

Liao and Whitman (1986b) offered the 2.4a and 2.4b equations below. Robertson and Wride (1997) presented the 2.4c, and William F. Marcuson (US Army Engineers, oral commun) added the last equations for the stress reduction factor (Youd & Idriss, 1997). The average line proposed by Seed and Idriss (1971) for the stress reduction coefficient was revised by the National Center for Earthquake Engineering Research in the session organized in 2001, by adding an approximate average line, as in Figure 2.14.

$$r_d = 1.0 - 0.00765\,z \quad \text{for } z \leq 9.15 \text{ m} \tag{2.4a}$$

$$r_d = 1.174 - 0.0267\,z \quad \text{for } 9.15 \text{ m} \leq z \leq 23.0 \text{ m} \tag{2.4b}$$

$$r_d = 0.744 - 0.008\,z \quad \text{for } 23.0 \text{ m} \leq z \leq 30.0 \text{ m} \tag{2.4c}$$

$$r_d = 0.5 \quad \text{for } z > 30.0 \text{ m} \tag{2.4d}$$

T.F. Blake (1996) approximated the mean curve and stated the r_d as the equation below.

$$r_d = \frac{(1.000 - .4113z^{0.5} + 0.04052z + 0.001753z^{1.5})}{(1.000 - 0.4177^{\ 0.5} + 0.05729z - 0.00620^{\ 1.5} + 0.001210z^2}} \tag{2.5}$$

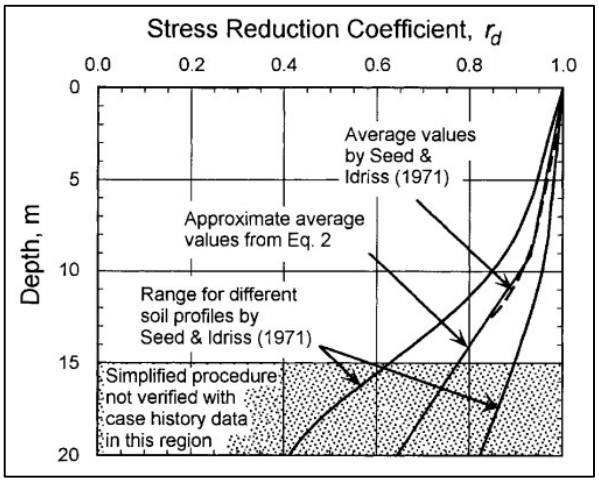

Figure 2.14 Stress reduction factor recommendations by Seed & Idriss (1971) with added average lines from the above equations by National Center for Earthquake Engineering Research (2001)

2.2.4.2 Cyclic Resistance Ratio, CRR

Cyclic resistance ratio (CRR) must be determined to estimate the potential of liquefaction. The only feasible method for this might be retrieving the undisturbed soil and testing it under cyclic loading. However, removing the granular soil is inherently disruptive and it is challenging to imitate site conditions in the laboratory. As a result, a field test would be a better fit for the liquefaction evaluation procedure. Standard penetration tests, cone penetration tests, shear wave velocity tests, and Becker penetration tests (BPT) are frequently applied in the field. SPTs and CPTs are commonly used due to their extensive database and performance records, but other tests may apply to sites underlain by gravelly sediments, such as BPT. Field tests other than the SPT (Standard Penetration Test), such as the BPT (Becker Penetration Test), CPT (Cone Penetration Test), and other similar in-situ tests, are excluded from the scope of this thesis. Youd and Idriss, in the National Center for Earthquake Engineering Research Workshop, summarized the advantages and disadvantages of field tests (Table 2.2).

Table 2.2 Comparison of field test accounting liquefaction resistance (Youd & Idriss, 1997)

Feature	Test Type			
	SPT	**CPT**	**V_s**	**BPT**
Past Measurements at liquefaction sites	Abundant	Abundant	Limited	Sparse
Type of stress-strain behavior influencing test	Partially drained, considerable strain	Drained, large strain	Small Strain	Partially drained, considerable strain
Quality control and repeatability	Poor to good	Very Good	Good	Poor
Detection of variability of soil deposits	Good for closely spaced test	Very Good	Fair	Fair
Soil types in which the test is recommended	Nongravel	Nongravel	All	Primarily Gravel
Soil sample retrieved	Yes	No	No	No
Test measures index or engineering property	Index	Index	Engineering	Index

2.2.4.2.1 Standard Penetration Test, SPT

The evaluation of liquefaction resistance using Standard Penetration Test (SPT) blow counts has been a standard method in geotechnical engineering for many years. However, it's important to consider the quality issues that often arise in SPT testing in Türkiye. The reliability of SPT results can be influenced by various real-world challenges. Essentially, the Standart Penetration Test (SPT) is used to assess liquefaction, settlement and soil behavior. However, the results obtained can vary for various reasons, such as failure to follow proper test procedures, the use of low-quality drilling equipment, insufficiently trained operators or site-specific conditions. Common issues include deformed drilling rods, improper sample collection and test durations that are too short. These problems can lead to inaccurate soil parameter estimates and flawed conclusions regarding critical factors, like liquefaction potential.

A major challenge in Türkiye is the absence of water in the borehole during drilling in sandy soils. In these cases, water can flow into the borehole and create a boiling effect at the bottom of the well in sandy soils. This causes SPT resistance values to be lower than expected. As a result, the estimated soil properties, based on standard SPT correlations, appear weaker than they are. Regretfully, neglecting this problem degrades the quality of SPT results in Türkiye. However, these problems are ignored, which produces great uncertainties of SPT results for Türkiye. SPT resistances as low as 0-1 were observed in this study of the analyzed boreholes, even at depths of 15 to 20 meters which is not a common condition. This highlights the urgent need for accurate and reliable geotechnical assessment results. Without adressing the issue, the foundation for engineering solutions remains uncertain and risky.

The Cyclic Stress Ratio (CSR) versus corrected blow count $(N_1)_{60}$ plot is widely used for assessment, as it effectively differentiates between liquified and non-liquified zones. The figure below presents Critical Resistance Ratio (CRR) curves for various fine contents, incorporating data from multiple field experiments, where liquefaction was either observed or not. A commonly used criterion for assessing liquefaction resistance is the simplified base curve for fine contents of 5%, 15% and 35%. This

CRR curve is specifically calibrated for earthquakes of magnitude 7.5, while adjustments required for other magnitudes.

In Figure 2.15, several instances of liquefaction that would not have occurred above the fines content lines are observed, as represented by the criteria established by Seed et al. (1984). However, Liao et al. (1985) confirmed the significant impact of fines on liquefaction susceptibility. (National Research Council, 1985).

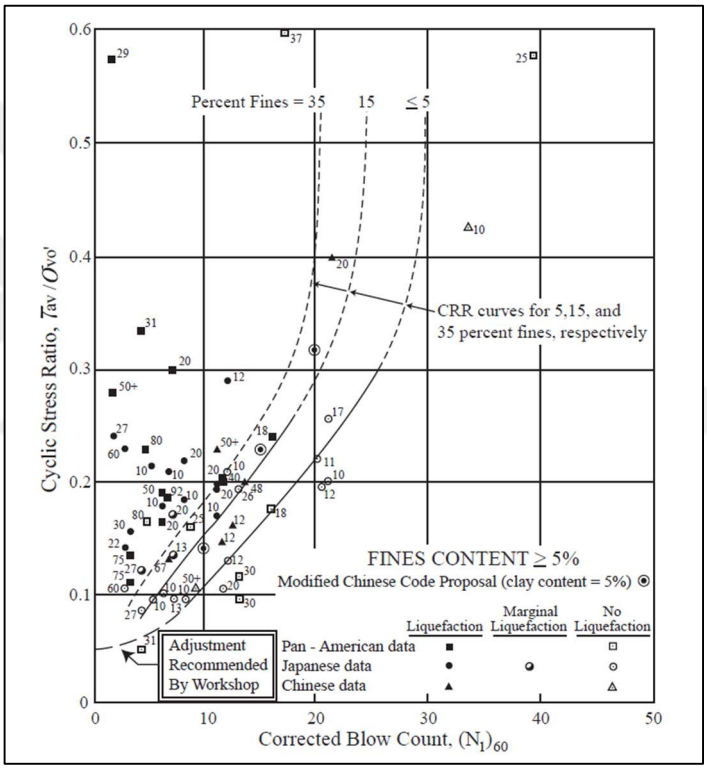

Figure 2.15 Simplified base curve modified from Seed et al., 1985 (Seed et al.,2003)

Thomas F. Blake (Fugro-West, Inc., Ventura, Calif., written commun.), expressed the base curve by below equation.

$$CRR_{7.5}=\frac{a+cx+ex^2+gx^3}{1+bx+d\ \ ^2+fx^3+hx^4} \tag{2.6}$$

where $CRR_{7.5}$ is the cyclic resistance ratio for earthquake magnitude 7.5; x: $(N_1)_{60}$; a=0.048; b=-0.1248; c=-0.004721; d=0.009578; e=0.0006136; f=-0.0003285; g=-1.673E-05; h=3.714E-06

A.F. Rauch (personal communication, 1998) also suggested the base curve equation as below (Youd and Idriss, 2001).

$$CRR_{7.5}=\frac{1}{34-(N_1)_{60}}\left(\frac{(N_1)_{60}}{135}\right)+\frac{50}{(10(N_1)_{60}+45)^2}-\frac{1}{200} \quad (2.7)$$

Both equations valid for $(N_1)_{60}$ less than 30.

Idriss and Boulanger (2004) and Cetin et.al. (2004) also recommended CRR-$(N_1)_{60}$ curves for clean sand (Figure 2.16).

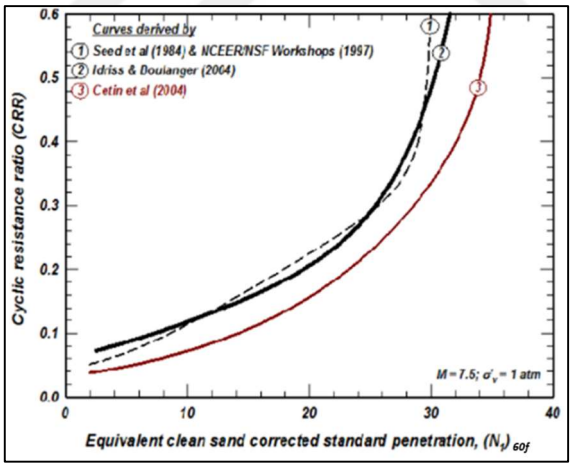

Figure 2.16 Relationship between CRR and $(N_1)_{60f}$ for clean sand curve (Idriss & Boulanger, 2010)

2.2.4.2.2 Influence of Fine Content

Assessing liquefaction potential in sandy soils often requires fine content correction to Standard Penetration Test (SPT) values, as the presence of fines (FC) significantly affects the soil's resistance to liquefaction. Fines can fill the voids between sand particles, increasing soil density and reducing its permeability, which in turn affects the buildup of pore water pressure during seismic activity.

For soils with a fine content of less than 5%, no correction is needed, as this amount of fines does not significantly affect the behavior of the sand. However, for fines content between 5% and 35%, corrections are applied using specific correlations. Since liquefaction-triggering correlations are primarily based on clean sands, the presence of fines reduces the SPT resistance of sandy soils. These corrections account for that effect, ensuring more accurate assessments. When the fine content exceeds 35%, studies in the literature indicate that the behavior of the soil governed by the fine particles, and liquefaction is no longer the primary concern. Instead, other failure mechanisms or behaviors are expected, and liquefaction analysis is therefore not performed for such soils.

SPT-based CRR curves were initially developed by Seed and Idriss in 1971 for clean sands (FC≤5%). In 1985, Seed et al. suggested that the fines content in sand influences the CRR value for the given $(N_1)_{60}$. The equations developed by I.M. Idriss with support from R.B. Seed are used to adjust the standard penetration resistance values in silty sands to represent clean sands.

$$(N_1)_{60f}=\alpha+\beta(N_1)_{60} \tag{2.8}$$

$$\alpha=0;\ \beta=1.0 \text{ for } FC\leq 5 \tag{2.9a}$$

$$\alpha=e^{1.76-(\frac{190}{FC^2})};\ \beta=[0.99+((\frac{FC^2}{1000})] \text{ for } 5\%<FC<35\% \tag{2.9b}$$

$$\alpha=5.0;\ \beta=1.2 \text{ for } FC\geq 35\% \tag{2.9c}$$

Idriss and Boulanger (2004) developed the curve mentioned above and recommended fines content correction for standard penetration.

$$(N_1)_{60f}=(N_1)_{60}+\Delta(N_1)_{60} \tag{2.10}$$

$$\Delta(\mathrm{N_1})_{60}=e^{(1.63+\frac{9.7}{\mathrm{FC}}-(\frac{15.7}{FC})^2} \tag{2.11}$$

The fines content discussed here applies to silty soil. While plasticity is a significant factor influencing CRR, data on its effects are currently unavailable.

In the National Center for Earthquake Engineering Research Workshop 1997, Robertson and Wride reviewed fines content data and proposed a correction factor K_s to adjust standard penetration value.

$$(N_1)_{60f}=K_s(N_1)_{60} \tag{2.12}$$

$$K_s=1+[\left(\frac{0.75}{30}\right)*(FC-5) \tag{2.13}$$

Seed et al. (2001) proposed a new fines content correction using the 'regression method' as part of the Bayesian update analyses. This correction addresses and minimizes the overestimation of the 35% fines content present in the correction proposed by Seed et al. (1984).

$$(N_1)_{60f}=C_{FINES}(N_1)_{60} \tag{2.14}$$

$$C_{FINES}=(1+0.004*FC)+0.05*(\frac{FC}{(N_1)_{60}}) \tag{2.15}$$

for FC≥5% and FC≤%35

2.2.4.2.3 Other SPT Corrections

Additional corrections must be applied to calibrate the SPT results in Equation 2.16, alongside fine content adjustments. A list of correction factors is provided in Table 2.3.

$$(N_1)_{60} = N_{30} C_N C_E C_B \, C_R \, C_S \tag{2.16}$$

where N_{30}=measured standard penetration resistance

Table 2.3 Corrections to SPT (modified from Skempton, 1986) as listed by Robertson and Wride (1998)

Factor	Equipment Variable	Term	Correction
Overburden Pressure	-	C_N	$(\frac{p_a}{\sigma'_{VO}})^{9.5}$ $C_N \leq 1.7$
Energy Ratio	Donut Hammer Safety Hammer Automatic-trip Donut-type Hammer	C_E	0.5-1.0 0.7-1.2 0.8-1.3
Borehole Diameter	65-115mm 150mm 200mm	C_B	1.0 1.05 1.15
Rod Length	<3 m 3-4 m 4-6 m 6-10 m 10-30 m	C_R	0.75 0.8 0.85 0.95 1.0
Sampling Method	Standard sampler Sampler without liners	C_S	1.0 1.1-1.3

Liao and Whitman (1986a) proposed the following equation to account for overburden correction.

$$C_N = (\frac{p_a}{\sigma'_{vo}})^{0.5} \tag{2.17}$$

where p_a≈100 kPa (1 atm)

Youd and Idriss, National Center for Earthquake Engineering Research workshops held in 1996 and 1998, stated that the following equation better fits the original curve proposed by Seed and Idriss (1982).

$$C_N=(\frac{2.2}{1.2+\frac{\sigma'_{vo}}{p_a}}) \tag{2.18}$$

2.2.4.2.4 The Factor of Safety

The factor of safety (FS) is a critical concept in liquefaction analysis, as it helps to assess whether the soil is prone to liquefaction during an earthquake. In simple terms, the FS compares the soil's resistance liquefaction, known as the cyclic resistance ratio (CRR), with the stresses induced by seismic activity, referred to as the cyclic stress ratio (CSR). The Turkish Building Earthquake Code states that soil with a FS> 1.1 may withstand seismic pressures, whereas soil with a FS < 1.1 may have higher liquefaction potential. This simple method offers a clear method for evaluating liquefaction potential and serves as a guide to risk-reduction strategies.

A commonly accepted expression for the factor of safety for liquefaction resistance introduced as follows:

$$FS = \frac{CRR_{7.5}}{CSR} * MSF \tag{2.19a}$$

$$FS = \frac{CRR}{CSR} \tag{2.19b}$$

Equation 2.20 defines the factor of safety, which is more than or equal to 1.1 by the Turkish Building Earthquake Code (2018).

$$FS = \frac{\tau_r}{\tau_{earthquake}} = \frac{CRR}{CSR} \geq 1.1 \quad (2.20)$$

Table 2.4 Representative number of cyclic and corresponding factors (Seed and Idriss, 1982)

Earthquake Magnitude	Number of Representatives at 0.65 τ_{max}	Factor to Correct
8.5	26	0.89
7.5	15	1.0
6.75	10	1.13
6	5-6	1.32
5.25	2-3	1.5

The CRR curves are calculated for earthquakes with a magnitude of 7.5, regardless of the method used. Therefore, the MSF (magnitude scaling factor) can account for the selected earthquake magnitude when calculating the safety factor. There are many methods for calculating MSF in literature. Seed and Idriss (1982) suggested MSF factors corresponding magnitudes in Table 2.4. The following equation, which was agreed upon by researchers at the 1998 National Center for Earthquake Engineering Research workshop (Youd and Idriss, 2001), is recommended.

$$MSF = \frac{10^{2.24}}{M_W^{2.56}} \quad (2.21)$$

2.3 Post-Earthquake Settlement

2.3.1 Introduction

In recent years, understanding and mitigating the effects of liquefaction on the seismic performance of vital infrastructure has become increasingly important. This growing recognition has underscored the need for reliable methodologies to predict ground deformations, particularly minor to moderate ones. Liquefaction-induced ground settlements and lateral displacement have become major contributors to earthquake-related structural damage. Despite decades of research focusing on

determining liquefaction susceptibility, little attention has been paid to post-earthquake settlement caused by liquefaction.

When an earthquake shakes saturated sandy soil, pore pressure rises significantly causing strength reduction or complete liquefaction. Granular soils are compacted by cyclic shear forces induced by earthquake-induced shaking. Immediate volume decrease is impeded by temporary pore water pressures that arise from inadequate drainage. However, as these pore pressures gradually dissipate, the soil layer consolidates, resulting in ground settlement and volumetric strain. Post-earthquake settlement is one of the major geotechnical risks caused by soil liquefaction during earthquakes.

2.3.2 Mechanism of Post-earthquake Settlement

It has been possible to divide the two main types of liquefaction-induced settlement: large displacement and small to moderate displacement. In the former, there is usually a movement of ground greater than 1 meter, normally occasioned by gravity-induced slumping after seismic shaking. This occurs when the strength of the soil after liquefaction is not adequate to resist the static shear stresses that develop substantial deformations. A notable example of history is the 1964 Niigata earthquake, during which triggered massive flow failures, resulting in the displacement of embankments and structures. On the other hand, small to moderate displacements are less severe and more confined. These deformations occur when liquefaction leads to a temporary loss of strength without causing extensive failures. This kind of settlement is relatively more common in regions with dense soils or where shear stresses are insufficient to cause significant movement. Figure 2.17 illustrates different ways settlement and displacement as an example of small to moderate type. In Figure 2.17(a) and (b), the focus is on settlement caused by the densification of soils and the escape of pore water during drainage, as well as secondary ground loss from the soil being eroded through cracks, often seen as “sand boils.” Figure 2.17(c) and (d) show how rotational movements and shear deformations can lead to settlements around slopes and embankments. Issues such as localized soil movement, which can result in areas of

both uplift and settlement, and lateral spreading, which produces pull-apart zones, are highlighted in Figure 2.17(e) and (f). Finally, structural settlements, such as those brought on by whole or partial bearing failures and restricted "punching" settlements where soil softening and re-stiffening take place, are examined in Figure 2.17(g) through (i). Since predicting these behaviors is challenging and currrent instruments are sufficient, engineers often rely on cautious and conservative methods to mitigate hazards.

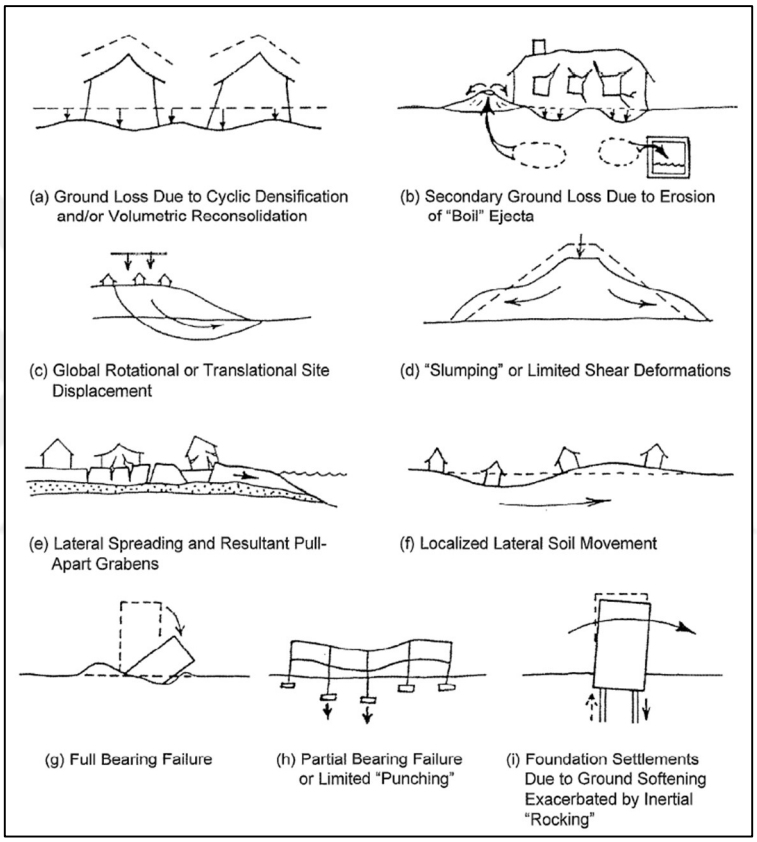

Figure 2.17 Schematic illustration of liquefaction-induced ground vertical displacement mechanisms (Seed et al., 2001)

Liquefaction-induced ground deformations depend strongly on cyclic stresses produced by strong shaking and the engineering properties of the liquefiable soil layer (Dashti et al., 2010). Granular soils exhibit different behaviors under cyclic loading depending on their density, such as loose, moderately dense, and dense conditions. For instance, triaxial compression tests were conducted on Ottawa sand with three different densities. The stress-strain behavior and pore water pressure development were

analyzed to understand the soil's response under cyclic loading. The response curves from specimens 4-4, 4-7, and 4-8 show how various granular soils behave under loading in Figure 2.18. The loose granular material in specimen 4-4 liquefies readily under stress, and the pore pressures increase to almost equal the lateral confining pressure. This triggers significant flow deformation, with about 20% shear strain occurring in just one second. Such soils are termed "contractive" because their loose structure allows shear deformation at constant volume while pore pressures either stabilize or rise slightly. In this case, the pore pressure increases as the soil attempts to transition from a loose to a dense state. The soil's density decreases as a result. Even if the pore pressure remains constant, the continued increase in axial deformation indicates that the soil is undergoing plastic deformation. This leads to a loss of bearing capacity and causes the expected settlement to be much higher than anticipated.

On the other hand, specimen 4-7, in a moderately dense state, behaves differently. The increased density prevents uncontrollable flow deformation even when it liquefies under load. At 1% shear strain, pore pressures reach a critical level, triggering liquefaction. However, shortly after, dilatation occurs, which increases shear resistance, decreases pore pressures, and halts the flow. This phenomenon, known as "dilative arrest," restores the soil to its cemented state. Since the soil is moderately dense, there is an initial rise in pore pressure and axial strain. After that, the soil reaches a point where it starts to expand, which causes the pore pressure to decrease. Even though this happens, some settlement is still likely to take place.

In conclusion, specimen 4-8, which depict a dense granular soil, does not liquefy despite an increase in pore pressure. Finally, even when pressure increases in the gaps between the particles, specimen 4-8, composed of closely spaced tiny particles, do not become a liquid. Rather, it dilates, which makes the particles more widely spaced. Because of this expansion, the earth becomes more resilient to sliding forces and the pressure is reduced. Although some settlement may still occur in densely packed soils like samples 4–8, which expand significantly under stress, it is typically limited. The soil is less likely to undergo significant shape change because of its ability to expand,

which widens the interval between particles and reduces pressure in those spaces. However, a slight settlement may occur due to repetitive stress, particularly if the shaking is severe or prolonged. Even though there is little risk of significant settlement due to liquefaction, depending on the intensity and duration of the loading, some settlement, either mild or moderate, may still happen.

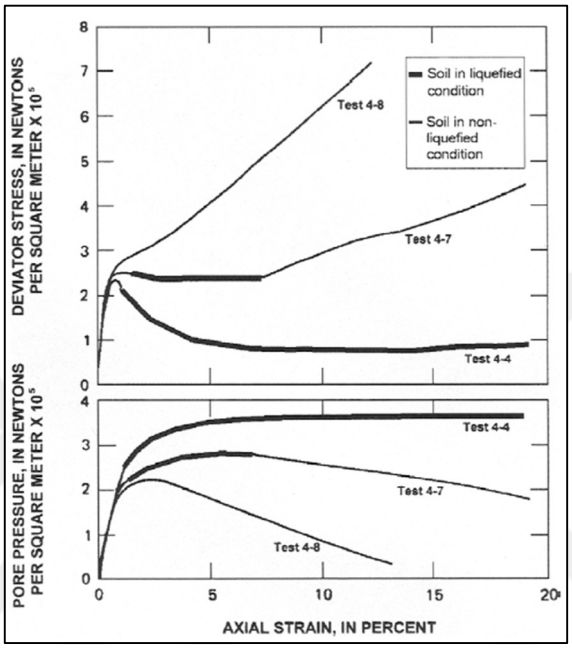

Figure 2.18 Stress-strain and pore pressure curves from undrained triaxial compression tests on saturated Ottawa sand (data from Castro, 1969; curves modified from Youd, 1975; Youd, 2003).

2.3.3 Studies on Post-Earthquake Settlement Characteristics

Lee and Albasia (1974), Yoshimi et al. (1975), and Tatsuoka et al. (1984) were the first to examine the characteristics of settlements caused by earthquakes. They conducted undrained cyclic loading tests and drained consolidation tests to investigate the volumetric changes in sandy soils following earthquakes. Post-liquefaction settlement refers to the vertical strain ε_v, representing the deformation the soil undergoes during the reconsolidation stage. It is defined as the ratio of the settlement to the initial height of the specimen in the tests. Identifying the parameters that influence post-liquefaction volumetric strain is crucial for a better understanding of its effects. Key factors influencing post-earthquake settlement include shear strain, cumulative shear strain during cyclic loading, soil relative density, number of cycles,

and the direction of cyclic loading. These factors have been examined through laboratory tests conducted by researchers, and some of their findings will be presented below.

Tsukamoto et al. (2004) demonstrated the relationship between the maximum shear strain experienced by the soil and post-liquefaction volumetric strain through undrained triaxial tests conducted on silty sands (Figure 2.19). The results of studies conducted on Toyoura sand indicated that as the maximum shear strain applied during undrained triaxial tests increased, the reconsolidation volumetric strain also increased. Beyond a certain point, however, it began to stabilize. Additionally, experiments conducted at varying relative densities showed that the volumetric strain increased with decreasing relative density. From this point, it can be understood that the shear strain experienced by the soil and relative density are significant contributors to volumetric strain. Similar research was done in the study of by Tatsuoka et al. (1984) and they found that during cyclic loading, volumetric strain increased with maximum shear strain. However, their findings did not show a stabilization of volumetric strain beyond a certain point.

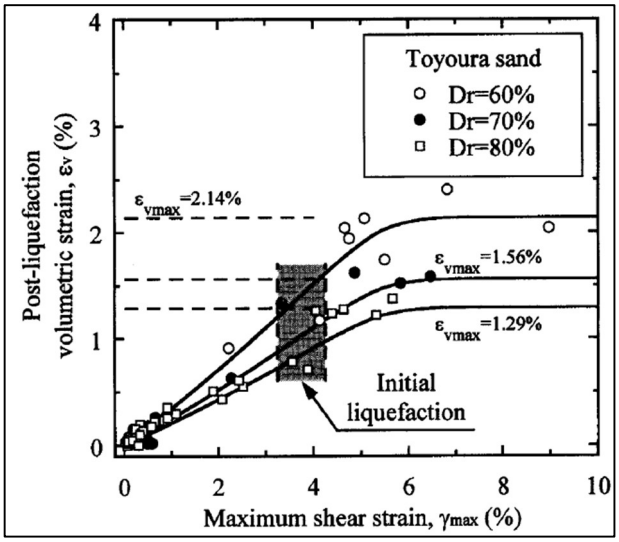

Figure 2.19 Relationship between post-liquefaction volumetric strain and maximum shear strain (Tkusumoto et al., 2004)

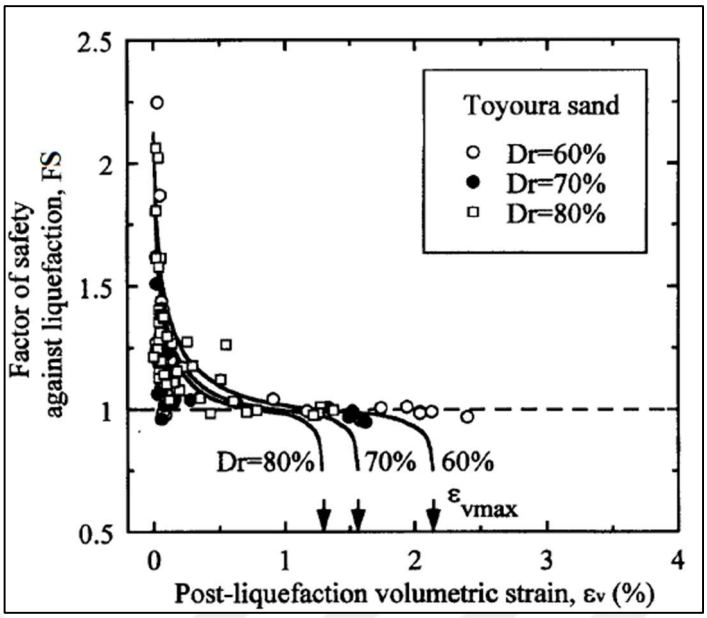

Figure 2.20 Relationship between the factor of safety and post-liquefaction volumetric strain (Tkusumoto et al., 2004)

Additionally, to determine the volumetric strain at the point where liquefaction begins, a graph showing the relationship between volumetric strain and the safety factor (FS) has been presented. In the study, the point where the factor of safety reaches 1, marking the onset of liquefaction, is clearly indicated. As shown in Figure 2.24, as the factor of safety decreases, the volumetric deformations increase. Even after liquefaction starts, some additional deformation occurs before it stabilizes. Therefore, at the point of initial liquefaction (FS = 1), the volumetric deformation in the soil is approximately 60% of the total post-liquefaction volumetric deformation.

Another important factor influencing post-liquefaction volumetric strain is cumulative shear strain (γ_{cum}). It represents the total deformation accumulated during cyclic loading and is critical for interpreting the post-liquefaction settlement. Experimental results demonstrate a clear relationship between higher (γ_{cum}) values and greater settlement magnitudes. Matsuda et al. (2011) carried out a series of multidirectional simple shear tests on Toyoura sand at various shear strain levels. They found that increasing the total shear strain accumulated during cyclic loading also

increases the vertical strain but with different patterns (Figure 2.21). The observed increase in settlement at higher shear strain levels aligns with the results of Tsukamoto et al. (2004) and Tatsuoka et al. (1984).

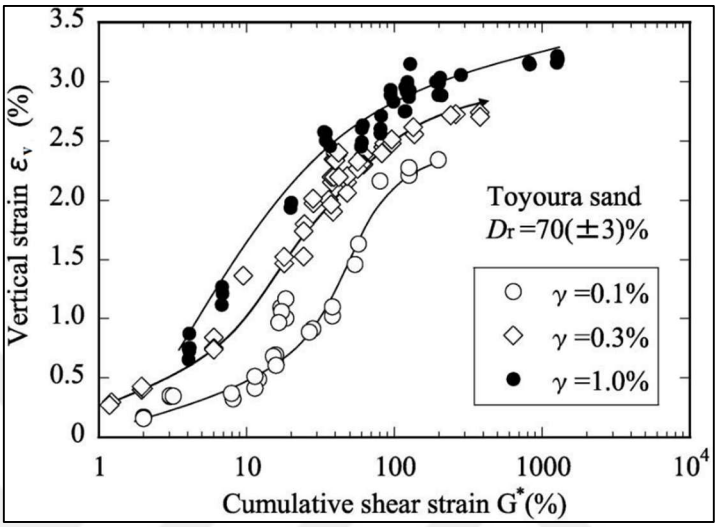

Figure 2.21 Connection between vertical strain and cumulative shear strain at different strain levels (Matsuda et al., 2011)

Matsuda et al. (2004) examined the effects of the effects of number of loading cycles and earthquake direction on vertical strain (ε_v). They concluded that vertical strain increased significantly at low strain levels as the number of cycles increased. Furthermore, samples subjected to multidirectional loading exhibited vertical strains 1.5 to 2 times higher than those under unidirectional loading. This findings highlights the importance of considering the multidirectional nature of earthquakes to ensure accurate evaluations.

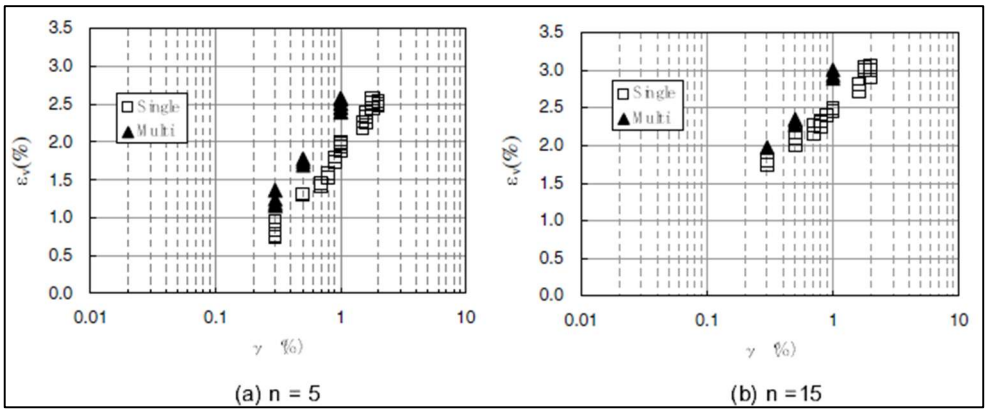

Figure 2.22 The variation of vertical strain with the number of cycles for multi-directional and single-directional shear (Matsuda et al., 2004)

2.3.4 Prediction of Post-Earthquake Settlement Approaches

Understanding post-earthquake settlement is important in assessing the potential impacts of liquefaction on structures and infrastructure. Several investigators have developed simplified methods to estimate how much settlement might occur, relying on data from laboratory tests and real-world case studies of earthquake-induced ground deformations over the last decades. Among others, contributions to such methods come from Lee and Albasia (1974), Yoshimi et al. (1975), Tokimatsu and Seed (1987), Shamoto (1998), and Wu et al. (2003), who have helped establish a practical method for settlement prediction in liquefied soils. These approaches are based on a combination of laboratory results and field observations and aim to provide a quick and reliable way to estimate settlement when soil liquefies during an earthquake. The ground surface settlement for one-dimensional reconsolidation can be computed by equating the vertical strains to the volumetric strains and then integrating the vertical strains over the depth interval of concern. This relationship is expressed in the following equation:

$$S = \sum_{i=1}^{n} \varepsilon_{vi} \, \Delta z_i \tag{2.22}$$

This equation expresses the settlement as the sum of the vertical strains (ε_{vi}) in each layer multiplied by the thickness of the layers. Simplified procedures for this purpose are widely used in engineering practice to provide a rapid estimate of probable settlement in liquefiable ground. These provide useful guidelines for the design and planning of earthquake-resistant infrastructure. While these methods provide an approach to estimating settlement, it remains a useful tool in early-stage assessments and help engineers make informed decisions within earthquake-prone regions.

2.3.4.1 Tokimatsu and Seed (1987) Approach

This method provides a basic approximation for estimating earthquake-induced settlements in sandy soils. It uses primary factors cyclic stress ratio, maximum shear strain, SPT-N and earthquake magnitude in both dry and partially saturated sands.

This predictive approach has been derived based on the strains developed past earthquakes. Considering the works of Lee and Albasia (1974) and Yoshimi et al. (1975), Tatsuoka et al. (1984) established the relationships between relative density and volumetric deformation following liquefaction. Seed et al. (1984a) also demonstrated the potential for shear deformation during the earthquake based on a combination of in-situ shear deformation, cyclic stress ratio (CSR), and normalized SPT-N values. These two works combined with the aid of the relationship between SPT-N and relative density and obtained the relation of CSR, $(N_1)_{60}$ and volumetric strain (Figure 2.23). This basic approach involves determining the CSR (Cyclic Stress Ratio) of an earthquake and the $(N_1)_{60}$ value of the soil layer. Once these parameters are identified, the corresponding volumetric strain line can be specified, which represents the deformation in the soil layer. From here, the settlement value can be calculated.

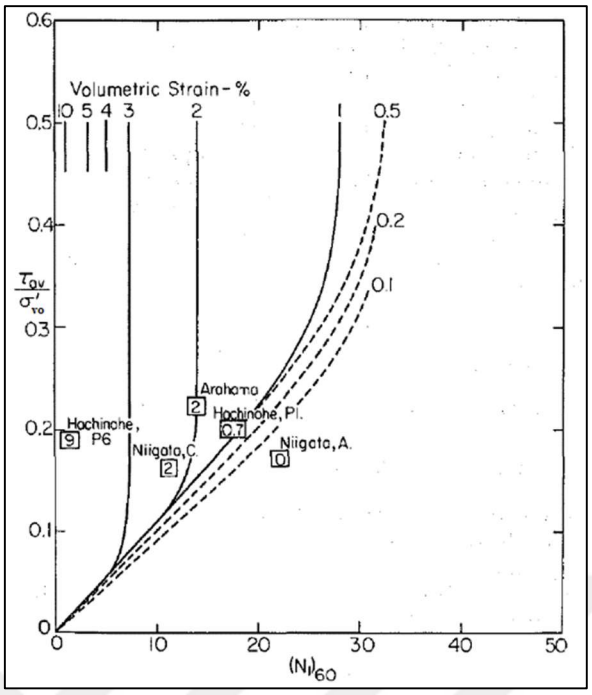

Figure 2.23 Proposed chart for volumetric strain based on CSR and SPT-N from field performance (Tokimatsu and Seed, 1987)

2.3.4.2 Ishiara and Yoshimine (1992) Approach

This study examined laboratory test data on sands using a simple shear device. A series of curves were developed relating the volumetric stain resulting from the dissipation of pore water pressures to the sand's density and the safety factor against liquefaction. The proposed method has been applied to soil samples at several sites affected by liquefaction during the recent major earthquake. The relationship between the safety factor and shear stress amplitude is established based on the laboratory test data. This method was developed based on clean sands with little fines. When the settlement values calculated using this method are compared with the observed settlements from the 1964 Niigata earthquake in Japan, highly consistent results are obtained. Once the safety factor is known, the post-liquefaction volumetric strain (ε_v) can be determined according to relative density (Figure 2.24). The factor of safety should be evaluated procedures according to Seed et al. (1983) and Ishiara (1985). Relative density (D_r) correlations with SPT and CPT exist in the literature.

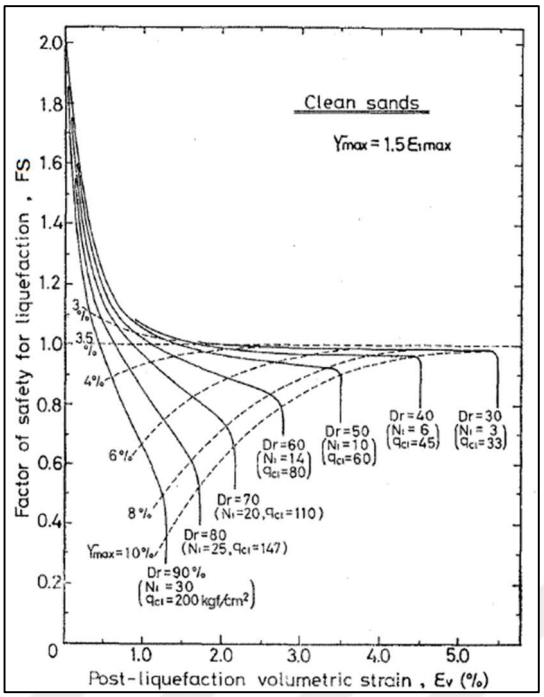

Figure 2.24 Relationship between the factor of safety and post-liquefaction volumetric strain

2.3.4.3 Shamoto et al. (1992) Approach

Shamoto and colleagues investigated the lateral and vertical deformations during the Hyogoken-Nambu earthquake and developed empirical correlations for shear strain and volumetric strain. A relationship between γ_{max}, N_a and $(\gamma_{max})_{seis}$ was established by Tokimatsu and Osaka (1998). It is important to note that N_a values are based on typical Japanese SPT practice and can be adjusted by multiplying 1.1 to obtain $(N_1)_{60}$ values. The relationship and correlations developed in this study were used to generate graphs for determining residual volumetric deformation based on CSR and SPT-N for FC=0%, 10% and 20%. The results are presented in Figure 2.25.

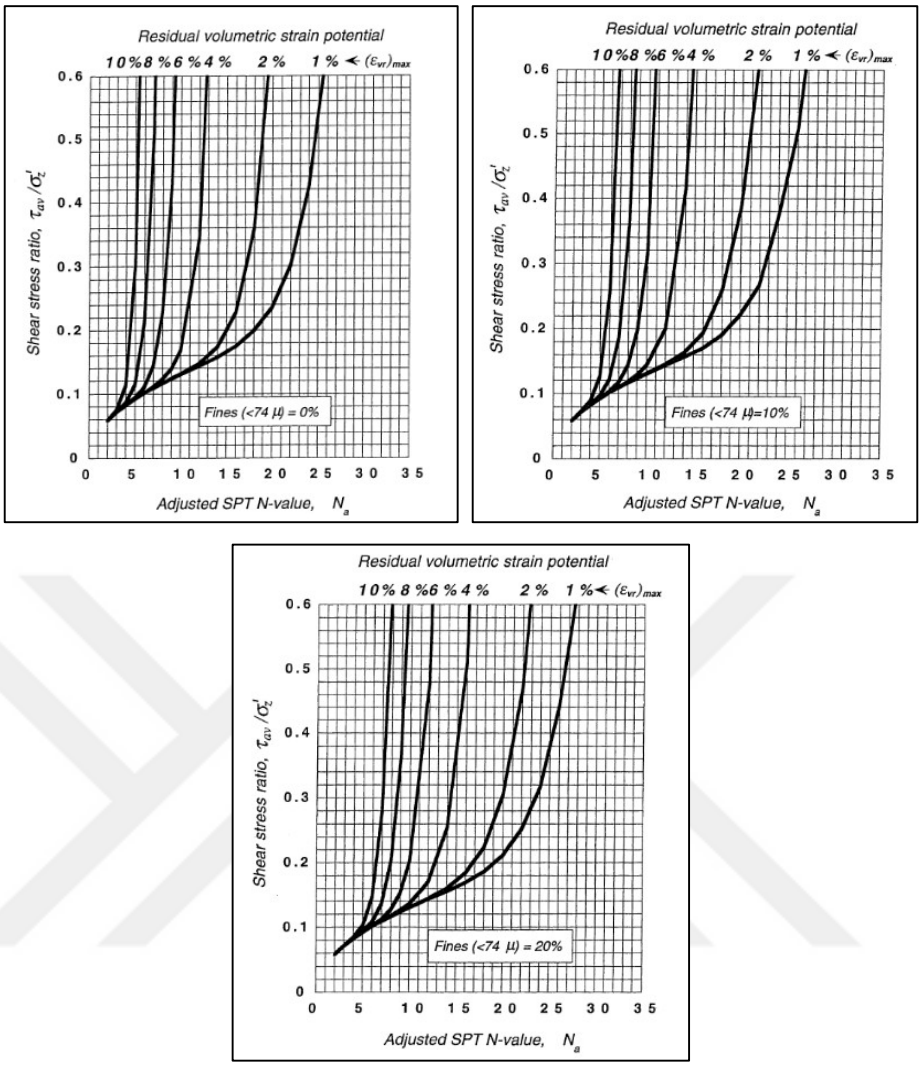

Figure 2.25 Relationship between the factor of safety and post-liquefaction volumetric strain

2.3.4.4 Wu and Seed (2004) Approach

A recent comprehensive laboratory study at U.C. Berkeley (Kammerer et al., 2002; Wu et al., 2003) focused on liquefaction-related difficulties using cyclic simple shear tests on fully saturated Monterey 0/30 sand samples. By using the reconsolidation of volumetric strain, they enlarged the chart developed by Wu. et al. (2003). Key steps in assessing liquefaction susceptibility for this procedure are as follows.

-Assess the liquefaction susceptibility of each saturated soil layer or sub-layer using the $(N_1)_{60}$ and CSR, M=7.5 values from Seed et al. (2001).

- Use the hypothesized correlations between CSR and $(N_1)_{60f}$ (Figure 2.26) to estimate reconsolidation volumetric strain for each layer.

-To calculate overall settlement, sum the volumetric changes across all levels.

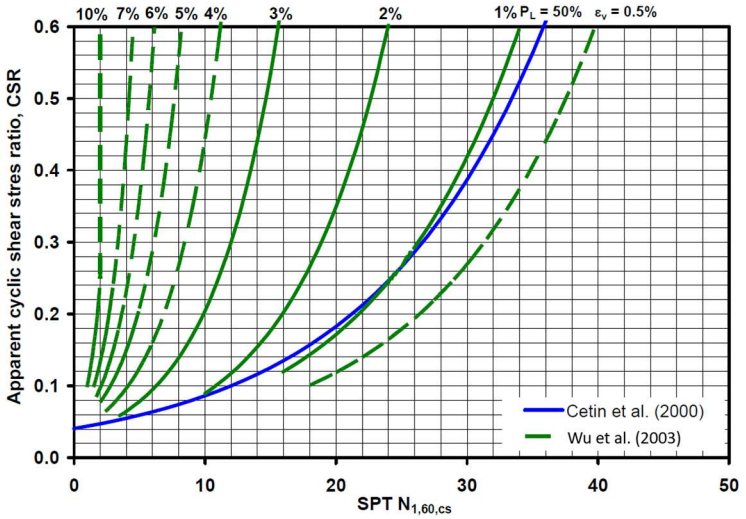

Figure 2.26 Relationship between CSR and volumetric strain as a function of $(N_1)_{60f}$ (Wu et al., 2003)

2.4 GIS in Lifeline Performance Assessment

Major arteries or "lifeline" infrastructure are crucial to the functioning of cities. Basic assessments for the liquefaction potential of lifelines are required to further inform disaster planning and building resilience during future events in seismically active regions, as recently experienced in İzmir, Türkiye.

The Geographical Information System (GIS) provides powerful tools for mapping and analyzing the vulnerabilities of these essential arteries to liquefaction, which can severely disrupt transportation networks and emergency response systems. This thesis

concentrates on liquefaction risk assessment of İzmir vitals arterial roads: Altınyol, Alsancak, Konak and extending to Üçkuyular.

The city of İzmir is a geotechnically significant due to its location within an active tectonic setting and the presence of several major fault lines. The İzmir fault zone, along with the Seferihisar and Karaburun faults, are among the area's that are most active and potentially hazardous faults. The combination of loose cohesionless, saturated soil in the Bay Area and the seismic activity potential of nearby faults increases the risk of liquefaction. This poses a particular threat to vital infrastructure including the Üçkuyular, Konak, Alsancak and Altınyol arteries, where liquefaction-induced ground failure could severely disrupt emergency response and transportation.

By leveraging GIS capabilities, these vulnerabilities along the lifeline arteries can be spatially analyzed and detailed visualization created. The integration of geological data, borehole information and soil properties enables the identification of zones with the highest potential of liquefaction. This study focuses on developing liquefaction susceptibility maps based on geographical and geotechnical data.

İzmir’s primary routes, the Altınyol and Konak-Üçkuyular highways, serve as critical lifeline arteries, facilitating the movement of goods, services and emergency response in and out of the city. Any disruption to these routes caused by liquefaction or liquefaction-induced settlement could severely hinder immediate relief efforts and long-term recovery. Mapping these risks allows urban planners and engineers to prioritize the mitigation measures, such as soil improvement, ensuring this vital routes remain accessible during seismic emergencies. Utilizing GIS capabilities to pinpoint and display regions highly vulnerable to seismic hazards enables authorities to take proactive steps in protecting İzmir’s critical lifeline infrastructure.

CHAPTER THREE
ESTABLISHMENT OF THE DATABASE

3.1 Data Sources

The study incorporated approximately 82 boreholes from previous projects along İzmir's coastline. The study area is divided into 3 parts: Bayraklı, which covers Altınyol, Alsancak-Konak, and Konak-Üçkuyular. These sections encompass İzmir's vital lifeline arteries, making them primary focus of thesis.

3.1.1 Borehole Data

This study utilized the data from boreholes drilled in the İzmir coastal region. It consists of 82 borehole data collected from different companies (Figure 3.1). The boreholes were drilled over a period from 1990 to 2010. Depending on site-specific conditions, information was gathered through standard drilling techniques, including rotary and auger drilling. Borehole information is given in Table 3.1, and it will be presented in detail in Appendix 1.

Table 3.1 Borehole data information

Location #	Name	Company	Borehole #
1	Gümrük Üçkuyular Sahil Yolu	Ege Üniversitesi	33
2	SGK Ek Hizmet Binası	Alanyalı Sondajcılık	1
3	İzmir Büyükşehir Belediyesi	Radon Mühendislik	7
4	Konak-İkiztepe Yolu	Temelson Jeoteknik	22
5	Konak Akişhanı	Ege Temel Sondajcılık	2
6	Bayraklı Sahil Güvenlik	Yüksel Proje	7
7	Yeni Kent Merkezi	Gedik/Geokon/Radon	8
8	Ahmet Adnan Saygun Kültür Merkezi	Toker Sondajcılık	2
		Total	82

3.1.2 Standart Penetration Test (SPT) Data

SPT data plays a crucial role in assessing soil resistance, which is particularly important for evaluating liquefaction susceptibility and post-earthquake settlement. As one of the most widely used field tests, the SPT is supported by numerous empirical correlations in the literature. When integrated with these correlations, it offers valuable insights into the soil's mechanical properties.

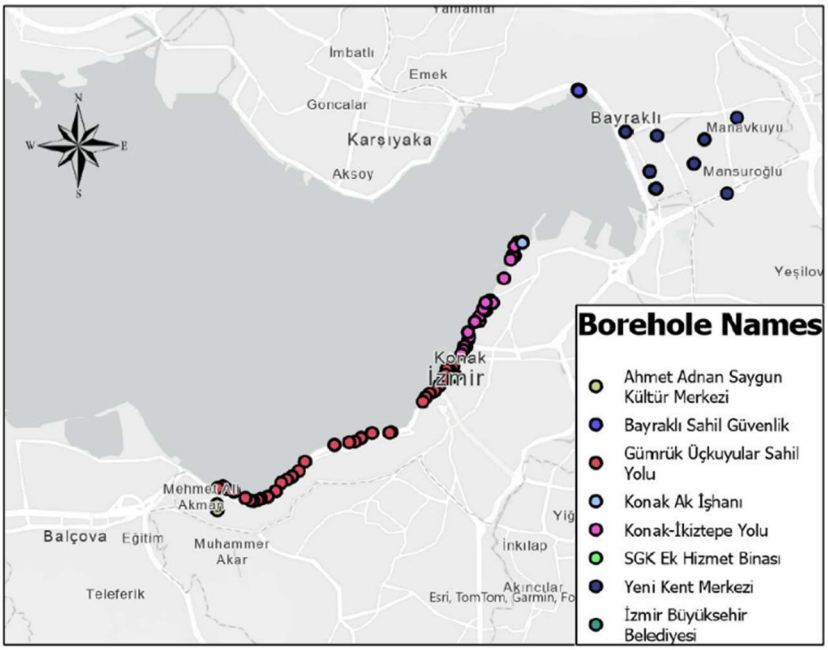

Figure 3.1 Borehole locations along the study area

3.1.3 Laboratory Test Data

Multiple laboratory tests were performed to determine soil characteristics, including:

- Sieve Analysis and Hydrometry Test to assess the particle distribution
- Specific Gravity Test
- Unconfined Compression Test or Triaxial Test (UU)
- Consolidation Test

These tests help classify soils and understand their behavior.

3.1.4 Geotechnical Database Creation

The ArcGIS program created a geotechnical database that integrates all collected data. The database includes spatial data representation, allowing for the visualization of geotechnical properties across the İzmir coastline. This database combined SPT field data, laboratory test information, and geographical information. This information includes depth, soil type, groundwater level, SPT-N values, soil properties obtained from laboratory tests, soil classification and borehole coordinates.

3.1.5 Historical Seismic Data

This thesis investigates the condition of the lifelines within the İzmir coastal region, emphasizing liquefaction and post-earthquake settlement under varying seismic scenarios, specifically DD-2 and DD-3, corresponding to magnitudes M_w=6.5 and M_w=5.5, respectively. Using AFAD's seismic hazard maps application, the peak ground acceleration (PGA) values will be later used in the calculation of CSR. Furthermore, the active fault map of Türkiye, available in the ArcGIS library, has been added to the study area to facilitate interpretation during a seismic event.

3.1.6 Geographical Information Systems (GIS) Data

The role of geographical Information Systems (GIS) in organizing, analyzing and visualizing geotechnical data is crucial for the İzmir coastal region. By integrating borehole data with soil profiles into the GIS environment, an effective spatial database has been developed. This database enables efficient management and analysis of geotechnical information, supporting better decision-making regarding liquefaction potential, settlement risks and other soil-related factors. This, in turn, the mapping of liquefaction risks and induced settlement predictions at various depths. Moreover, GIS allows the intersection of critical infrastructure, like transportation arteries and active faults data, to clearly understand vulnerabilities and where risk would be spatially concentrated. The incorporation of GIS enhances decision-making by visually presenting further steps in planning, risk assessment and mitigation.

3.2 Soil Profiles

The profile identification and characterization of the soils along the major coastal highway arteries of the İzmir Bay area are crucial for understanding the behavior of these soils under seismic loading. All the borehole data from different geotechnical projects between 1990 and 2010 provide extensive information on the subsurface, including soil type, layer thickness, classification, and strength properties.

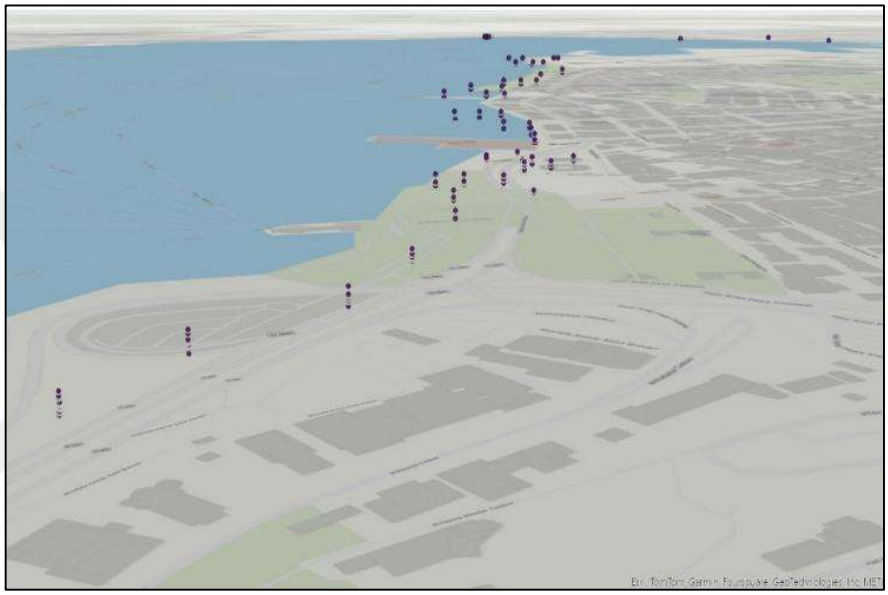

Figure 3.2 Borehole data incorporated into ArcGIS map

Each depth at which the Standard Penetration Test (SPT) is conducted provides unique information about the soil at that level. In this way, the soil stratification is determined along the borehole depth. At certain depths, the SPT-N values and the results of laboratory tests performed on samples taken from those depths allow for the determination of soil properties such as grain size distribution, Atterberg limits, specific gravity, water content and strength parameters. The results classified each soil layer according to the Unified Soil Classification System (USCS). Combined with the borehole coordinates, these data are merged into ArcGIS, enabling the 3D visualization of the soil properties at various depths within the mapping system (Figure 3.2).

The study area has been divided into 3 regions based on relevant boreholes: the Bayraklı boreholes representing the Altınyol section, the area between Alsancak-Konak and the region extending from Konak to Üçkuyular. These divisions were made to enhance the interpretation of the interpolation and visualization processes. Region numbers 1,2,3,8 belong to the Konak-Üçkuyular section. The Alsancak-Konak region is represented by boreholes 4 and 5, while the Bayraklı region is represented by boreholes 6,7.

3.2.1 Konak-Üçkuyular Area

In the region between Konak and Üçkuyular (Borehole Region #1, 2, 3 and 8), 45 boreholes were considered. The locations of these boreholes are illustrated on the map in Figure 3.3. Borehole depths in this area vary between 6 and 30 meters, with groundwater levels ranging from 10 to 1 meter (near ground level). The soil stratigraphy encountered throughout the borehole depths is often composed of sand, silt sand, clayey sand, or gravelly sand with occasional layers of inorganic clay. To better visualize the soil classification distribution, it is presented as a pie chart in Figure 3.4). The SPT-N values around 3 meters depth range from 1 to 25, occasionally reaching 50. At 5 meters, these values range between 5-25 and 50 at some locations, whereas at 10-meter depths, the values range between 22-50, occasionally reaching 6-8. Refusal values were found where the borehole encountered weathered rock (sandstone or claystone). In other depths, gravel within the layer is believed to be an affecting factor. Figure 3.5 illustrates the soil stratification and corresponding SPT-N values for boreholes 1_SK-1, 1_SK-2 and 1_SK-3.

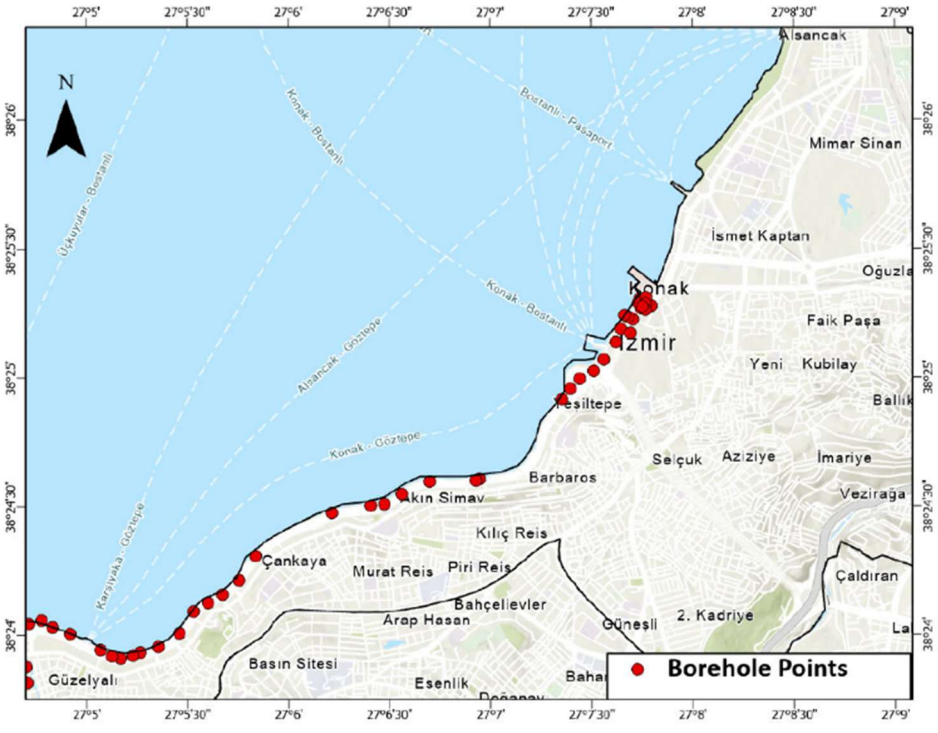

Figure 3.3 Konak-Üçkuyular borehole locations

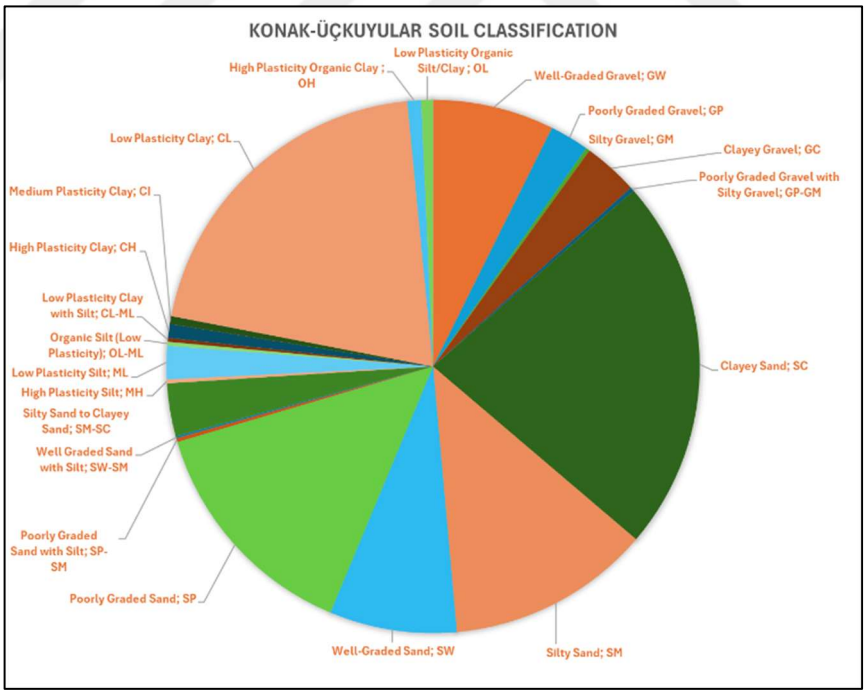

Figure 3.4 Soil classification distribution for boreholes in the Konak-Üçkuyular area

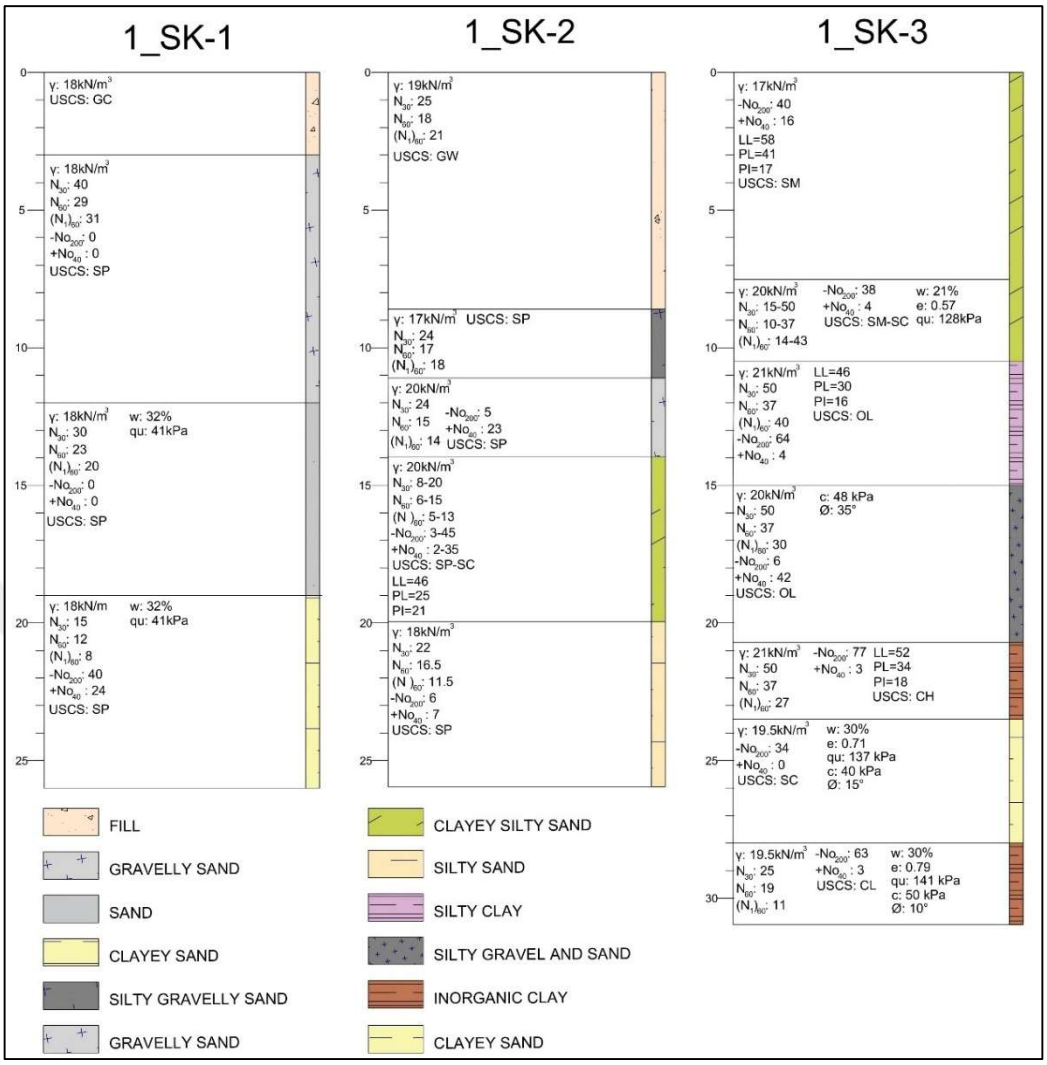

Figure 3.5 Schematic illustration and N_{30} values for boreholes 1_SK-1, 1_SK-2, and 1_SK-3

3.2.2 Alsancak-Konak Area

There are 24 borehole records in the Alsancak-Konak area (Borehole Region #4 and 5). This area extends between Konak Pier and Alsancak Harbor (Figure 3.6). The depths of boreholes range between 20 and 50 meters, while the groundwater level varies between 3-10m. The general profile of the boreholes in this area consists of silty clay and clayey silt layers. The distribution of soil classes is illustrated in the pie chart below (Figure 3.7). Clayey and gravelly sand layers with thicknesses varying from 2 to 6 meters can be found between these layers.

In the first 3 meters, SPT-N values range from 30 to 50 in gravelly sandy layers, while clay layers show much lower values, like 0 to 1. At 5 meters depth, the SPT-N values are around 50 in gravelly sections, 20 to 30 in sandy layers, and as low as 1 in clays. At 10 meters, SPT-N values fluctuate between 0 and 12 in sandy layers and 0 to 13 in clayey ones. The schematic illustration of the soil layering and corresponding SPT-N values for boreholes 4_SK-1, 4_SK-2 and 4_SK-3 is provided in Figure 3.8.

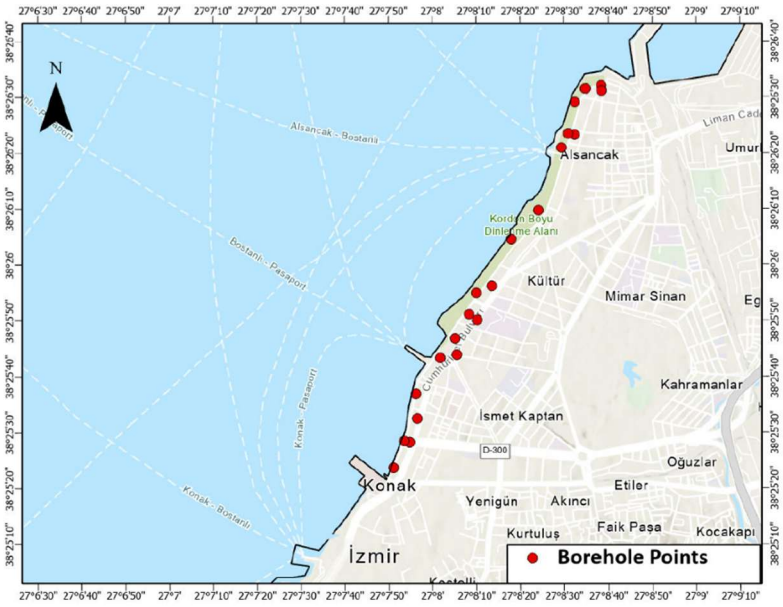

Figure 3.6 Alsancak-Konak borehole locations

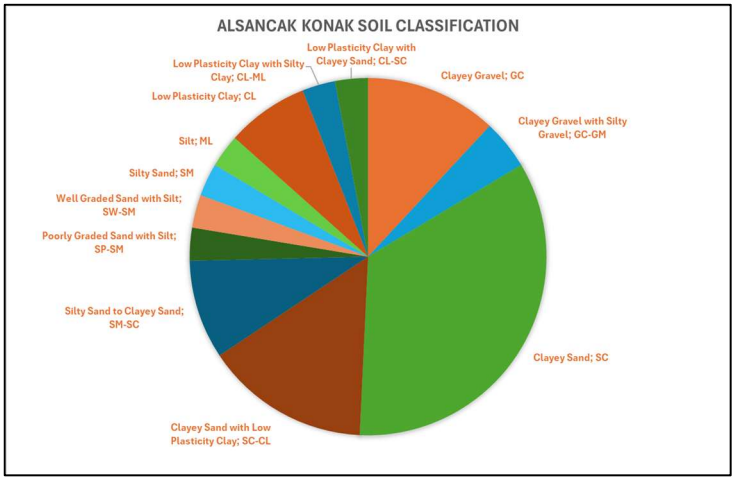

Figure 3.7 Soil classification distribution for boreholes in the Alsancak-Konak area

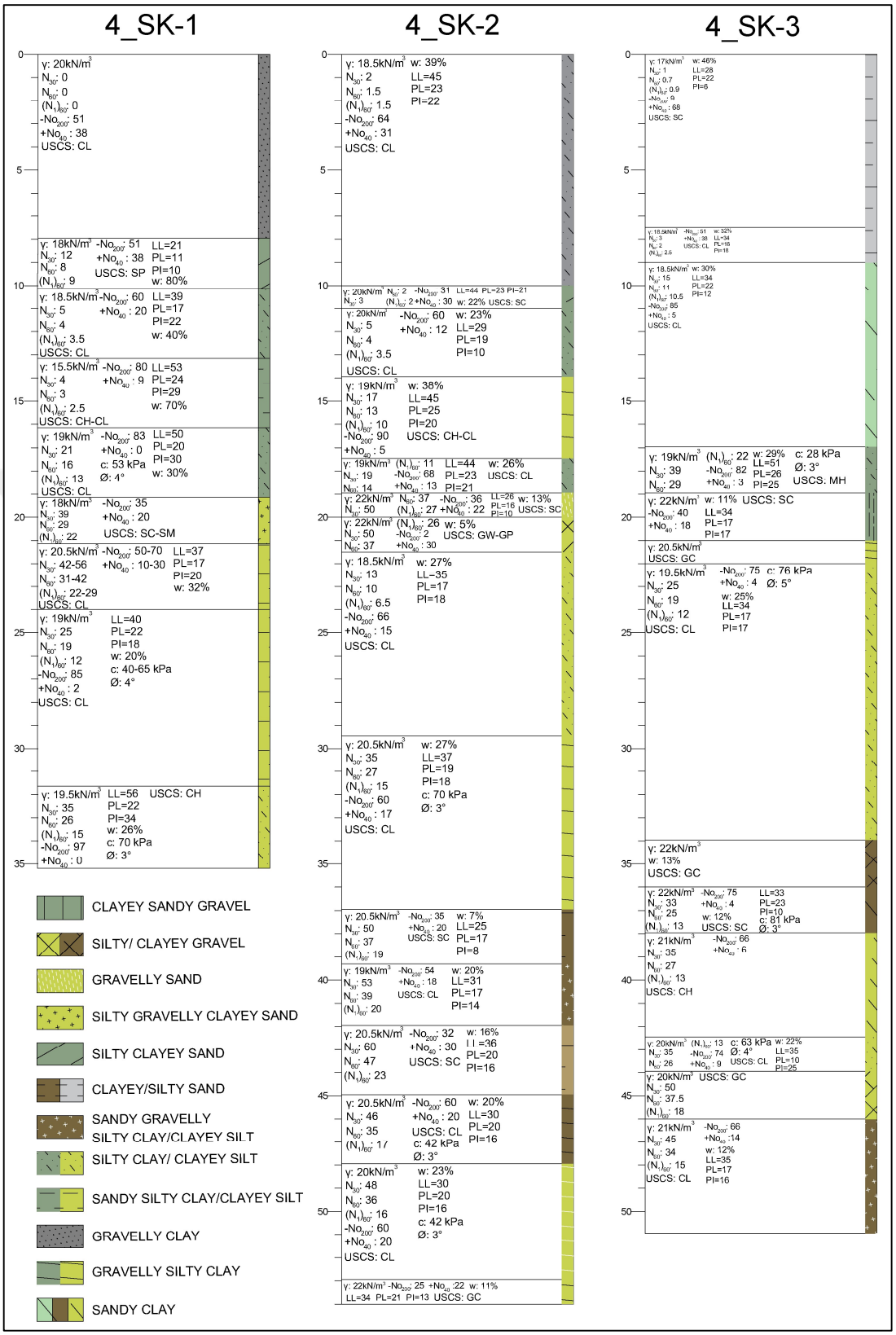

Figure 3.8 Schematic illustration for boreholes 4_SK-1, 4_SK-2, and 4_SK-3

3.2.3 Bayraklı Area (Altınyol)

Altınyol has been included in this study due to its significance as one of İzmir's primary transportation arteries. Although abundant borehole data exist along the Konak-Üçkuyular road's coastal section, there is a notable deficiency in data around Altınyol. Consequently, 15 borehole logs (Borehole Region #6 and 7), located on or near the road have been incorporated into the analysis. It is assumed that these data adequately represent the geotechnical conditions of the area. Borehole locations is shown on the map in Figure 3.9.

The borehole depths vary from 30 meters to 80 meters. In the boreholes from Bayraklı Sahil Güvenlik (Borehole Region #7), the groundwater is nearly at the surface (GWL≈0.75m), whereas in other boreholes, it is encountered at approximately 5 meters. The general soil stratification consists of silty clay and clayey silt layers. Interspersed within these layers are sandy gravel deposits and clayey sand/silty sand layers that reach up to 10 meters thick. In the Bayraklı Sahil Güvenlik area boreholes, clayey silty sand layers are present within the first 10 meters of depth, and the andesite layer has been encountered at 30 meters. The soil classification distribution is presented as a pie chart in Figure 3.10.

At a depth of 3 meters, SPT-N values were recorded as 35 in the gravel layer, 3-8 in the clayey and silty layer, and 0-5 in the sand layer. At 5 meters, the values were 36 in the gravel layer and 0-18 in the sand and clay layers. At 10 meters, in areas where the andesite layer was encountered, the values ranged from 40 to 50. In the gravel layer, the SPT-N value remained at 36, while in the clayey silt layers, it ranged from 1 to 10, and in the sand layer, from 18 to 39. A depiction of the soil layer, along with the corresponding SPT-N values for boreholes 6_SK-1, 6_SK-2, and 6_SK-3, can be found in Figure 3.11.

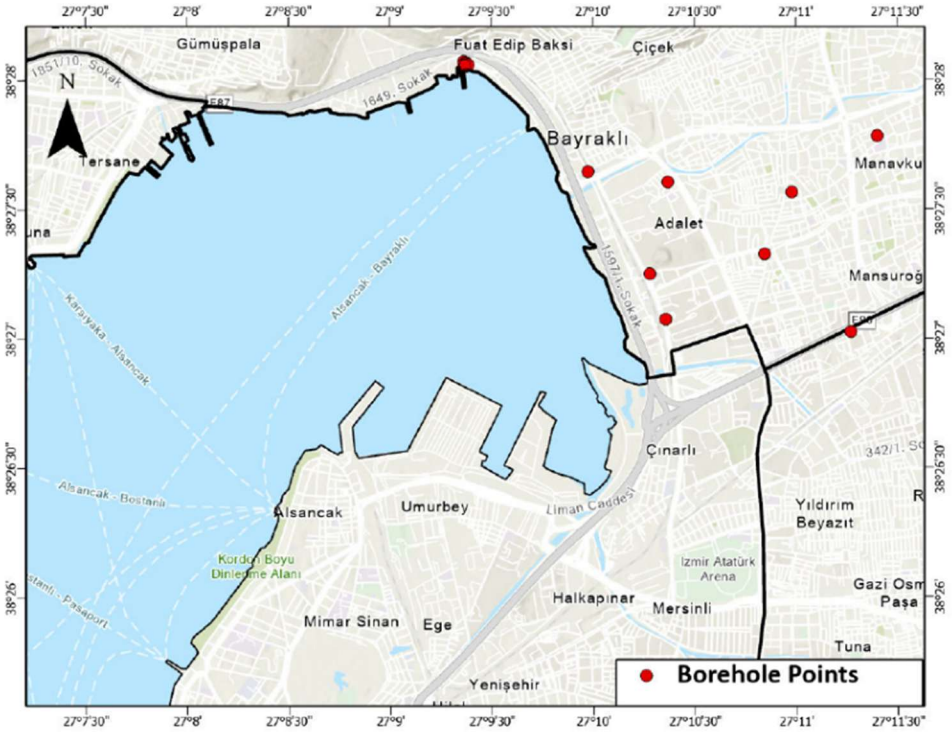

Figure 3.9 Bayraklı borehole locations

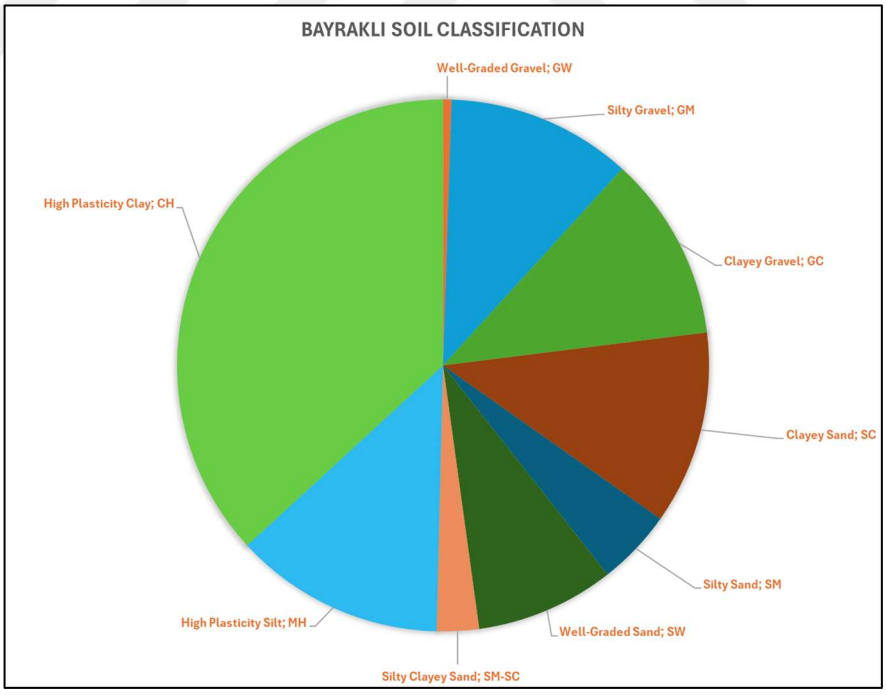

Figure 3.10 Soil classification distribution for boreholes in the Bayraklı area

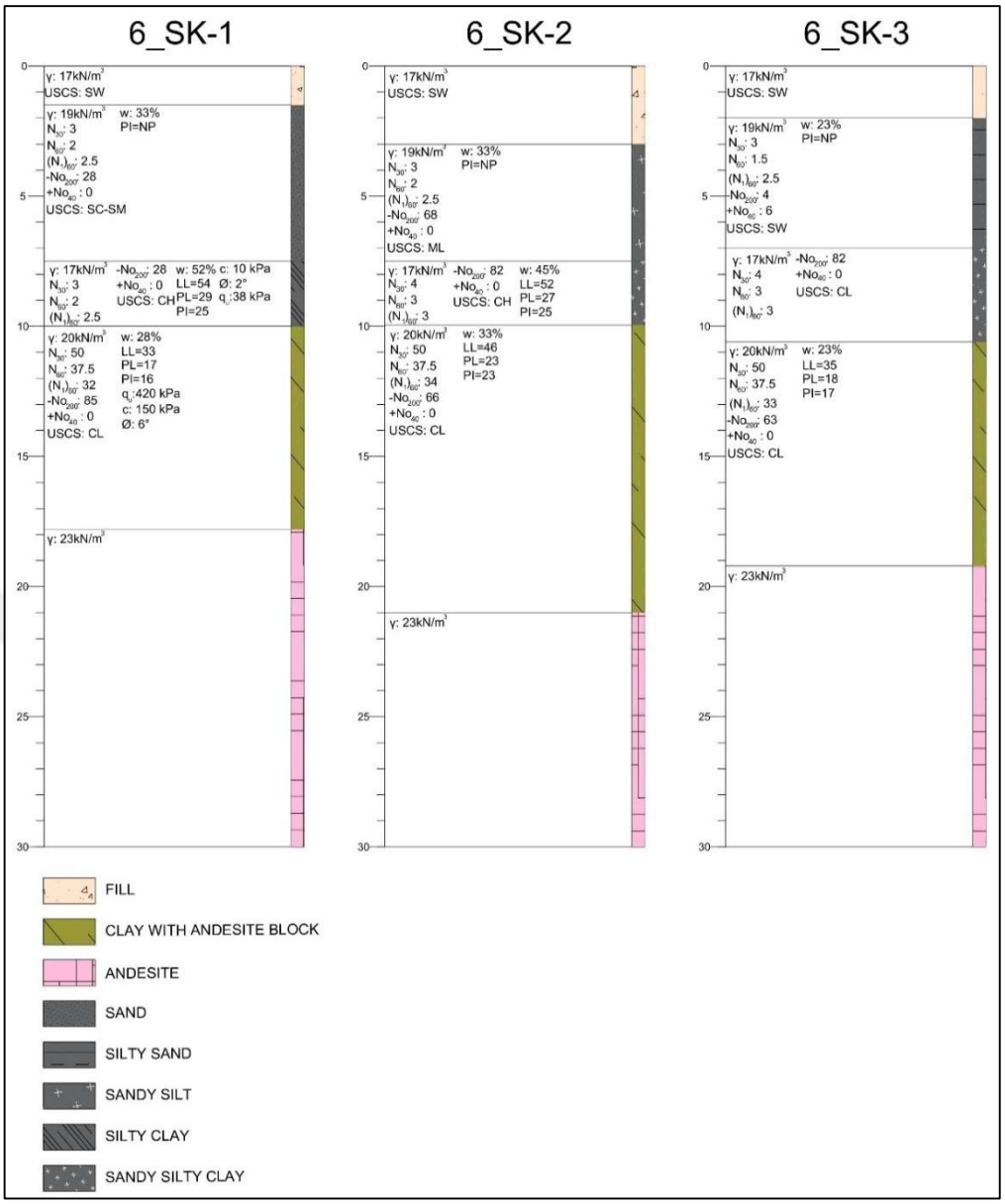

Figure 3.11 Schematic illustration and N_{30} values for boreholes 6_SK-1, 6_SK-2, and 6_SK-3

3.3 Data Layers

This section presents maps of the geotechnical parameters integrated into the GIS environment by using an exported table. This database will be presented in Appendix-3. Parameters such as N_{30}, N_{60}, $(N_1)_{60}$ and also other relevant information were derived from field and laboratory data, then processed and visualized using ArcGIS. These maps illustrate the spatial variation within the study area and provide essential

information for interpreting results, which is usually required in further geotechnical analysis. The following figures represent the N_{30} distribution maps. The SPT-N values for the Konak-Üçkuyular, Alsancak-Konak, and Bayraklı regions at depths of 3 m, 5 m, and 10 m are presented in Figure 3.12 and Figure 3.13, respectively. Other maps will be presented in the Appendices.

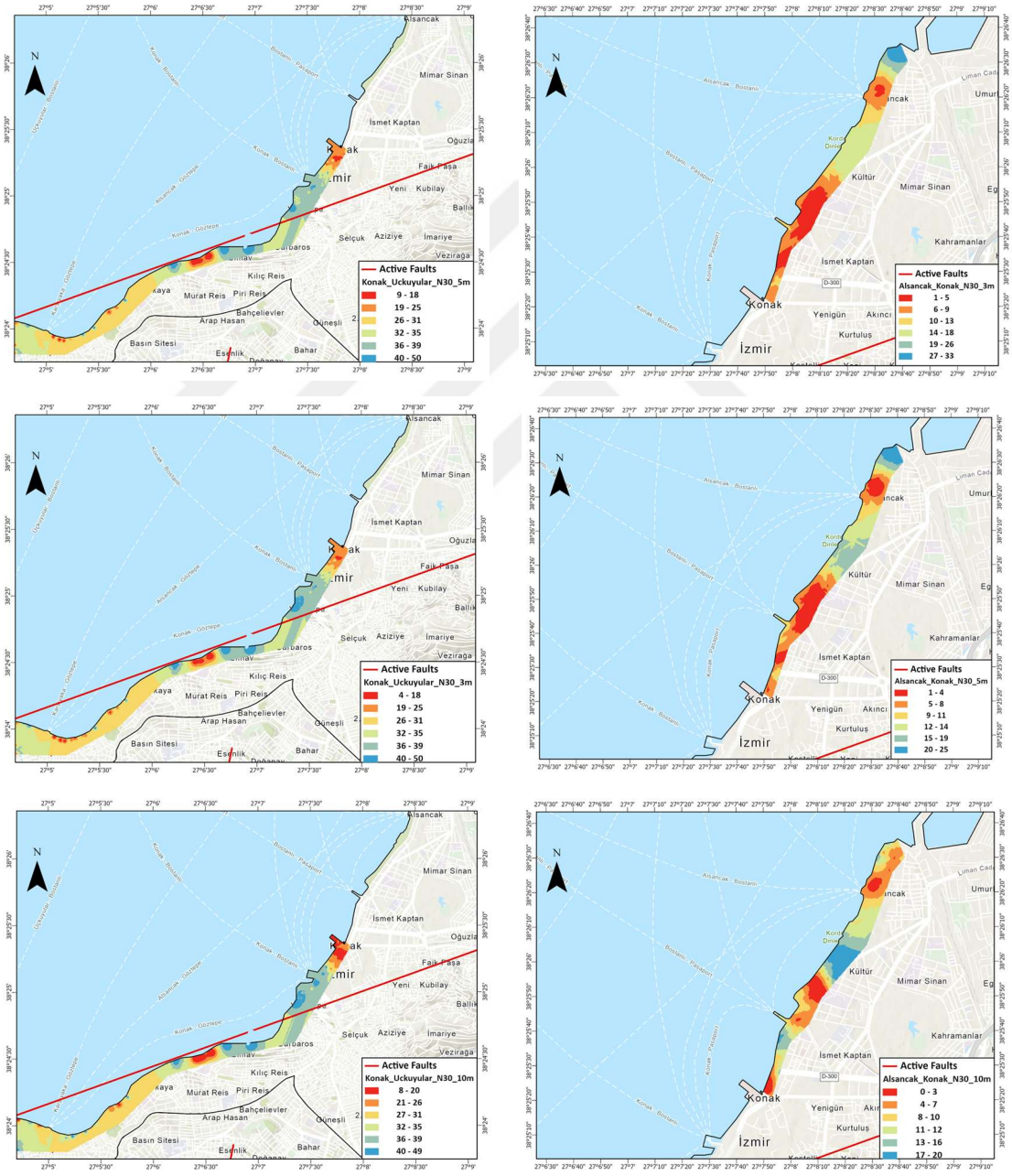

Figure 3.12 Measured SPT (N_{30}) distribution at 3m, 5m, 10m depths in the Konak-Üçkuyular and Alsancak Konak Area

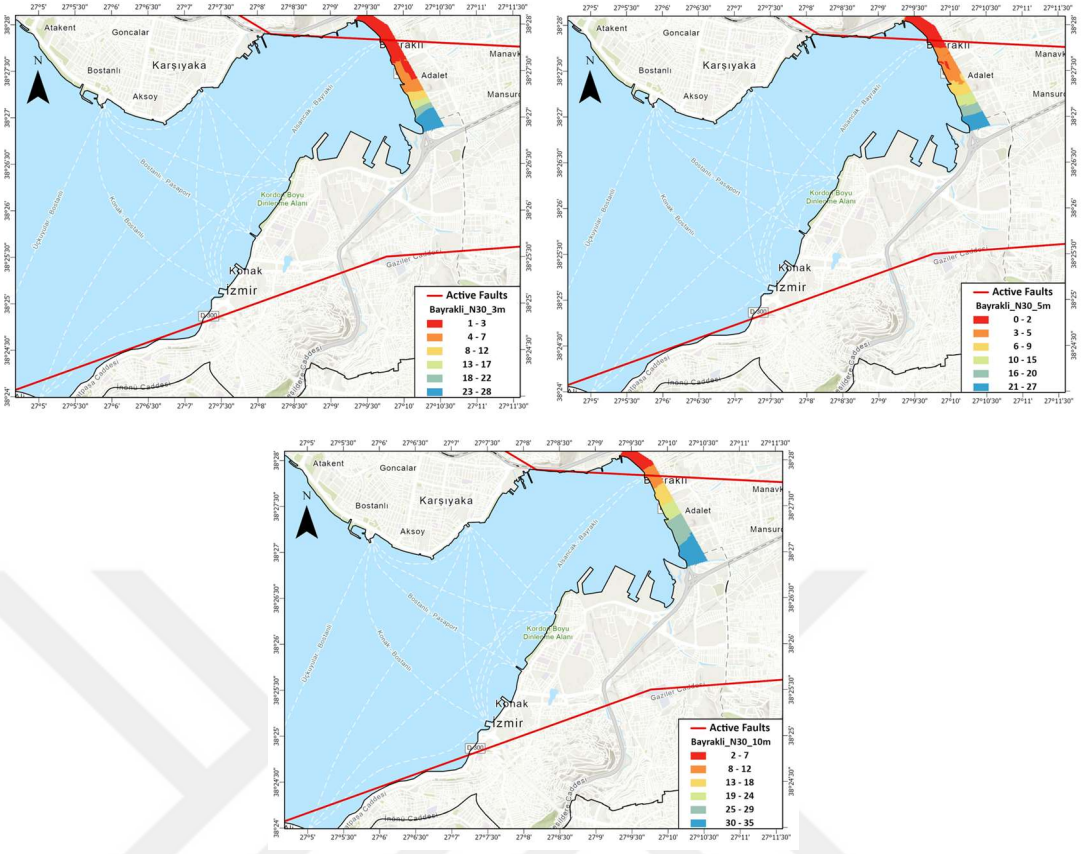

Figure 3.13 Measured SPT (N_{30}) distribution at 3m, 5m, 10m depths in the Bayraklı Area

CHAPTER FOUR
LIQUEFACTION ANALYSIS

In the scope of the study, a total of borehole data points from different projects have been collected from Üçkuyular-Konak, Konak-Alsancak and Bayraklı regions, which encompass the main arterial roads along the İzmir coastal area. Utilizing the borehole data, liquefaction analyses were conducted according to the SPT-based calculations in TBDY-2018. The safety factors against liquefaction have been visualized in the ArcGIS Pro application for the critical depths of 3m, 5m, and 10m.

This thesis considers the liquefiable soil layers at varying depths from boreholes in the three regions described in the previous section. Liquefaction analyses were conducted at these borehole locations, specifically on saturated, sandy soils. The plasticity of fines was not considered in the scope of this study. The liquefaction analysis was performed using a simplified SPT-based method described in Appendix 16-B of the Turkish Seismic Design Code (TBDY). The calculations were conducted for earthquake levels DD-2 and DD-3, with corresponding earthquake magnitudes of 6.5 and 5.5, respectively. It is essential to know the peak ground acceleration values corresponding to these seismic levels to calculate the shear stress induced by an earthquake. The maximum ground accelerations for the İzmir coastal region were determined by inputting the local soil class and earthquake level on the AFAD TDTH platform (https://tdth.afad.gov.tr). Considering the general soil conditions, including SPT resistance values ranging from 0 to 10, and gravel layers with resistances reaching 20-30 or even refusal values, the local soil class was deemed appropriate as ZE, according to Table 4.1. Accordingly, the PGA values considered are shown in Table 4.2.

Table 4.1 Local soil classes (TBDY, 2018)

Local Soil Class	Soil Type	First 30 m		
		$(V_s)_{30}$ [m/sn]	$(N_{60})_{30}$ (blows/30 cm)	$(c_u)_{30}$
ZA	Strong, hard rocks	>1500	-	-
ZB	Slightly weathered, moderately strong rocks	760-1500	-	-
ZC	Very dense sand, gravel and stiff clay layers	360-760	>50	>250
ZD	Medium-dense to dense sand, gravel, or very stiff clay layers	180-360	15-50	70-250
ZE	Loose sand, gravel, or soft to firm clay layers, or profiles containing a soft clay layer (c_u < 25 kPa) thicker than 3 meters in total that meet the conditions of PI > 20 and w > 40%.	<180	<15	<70
ZF	Soils requiring site-specific investigation and assessment: 1.Soils with settlement and potential collapse risk under seismic impact (liquefiable soils, highly sensitive clays, weakly cemented collapsible soils, etc.), 2.Peat and/or high-organic-content clays with a total thickness greater than 3 meters, 3.High-plasticity clays (PI > 50) with a total thickness exceeding 8 meters, 4.Very thick (> 35 m) soft or medium-firm clays.			

Table 4.2 Peak ground acceleration (PGA) values

Earthquake Level	M_w	a_{max} (g)
DD-2	6.5	0.459
DD-3	5.5	0.175

Using the ArcGIS software, SPT-N values and soil information at the depths where SPT tests were conducted were transferred into the GIS environment. Based on this transferred data, the factor of safety against liquefaction can be calculated through Python scripting and the computational tools available within the software. The Python scripts used for these calculations are provided in Appendix-6. Initially, the SPT-N values were corrected according to Table 2.3 to obtain the $(N)_{60}$ and $(N_1)_{60}$ values. Then, the CSR and CRR values required for the liquefaction analysis were calculated. The CSR values for the corresponding seismic levels were determined using Equation 2.3 based on the ground accelerations specified in Table 4.2. The $\mathrm{CRR}_{7.5}$ values were calculated using Equation 2.7. The $(N_1)_{60}$ value, corrected for fine grains, was adjusted as described in Equation 2.8. Accordingly, the factor of safety was calculated using Equation 2.19. The workflow of the data processing and analysis is presented in Figure 4.1.

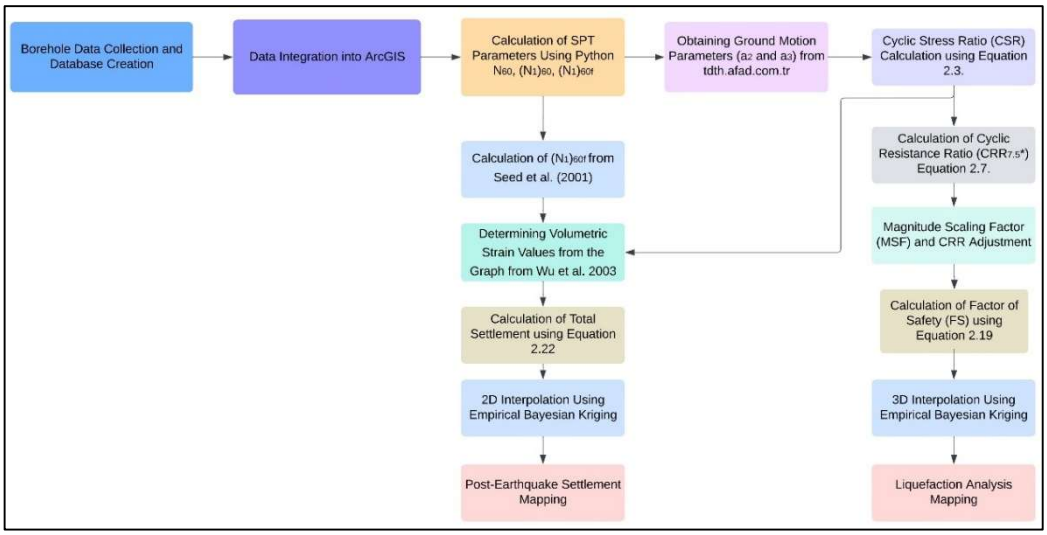

Figure 4.1 The workflow of data processing and liquefaction analysis

Based on the data presented in Appendix 3, the liquefaction safety factor distribution maps have been created using the 3D Empirical Bayesian Kriging (EBK) tool for three regions. These maps were developed through three-dimensional interpolation utilizing the data from the boreholes in the respective areas. The calculations were conducted for the first 30 meters, and the results for the critical depths of 3,5 and 10 meters are presented. Additionally, the minimum, maximum and average factor of safety values calculated for each borehole were determined, and the worst-case scenario, best-case scenario and average situation have been visualized accordingly. The results obtained for the Konak-Üçkuyular, Alsancak-Konak, and Bayraklı regions will be presented respectively.

4.1 Liquefaction Maps for the Konak-Üçkuyular Area

Figure 4.2 illustrates the liquefaction safety factors at depths of 3m, 5m, and 10m in the Konak-Üçkuyular area for two different earthquake levels. Moreover, Figure 4.3 presents the worst-case, best-case, and average scenarios for these two earthquake magnitudes. The minimum, maximum, and average values were calculated using a 2D Empirical Bayesian Kriging (EBK) interpolation method based on the lowest, highest, and average values recorded for each borehole.

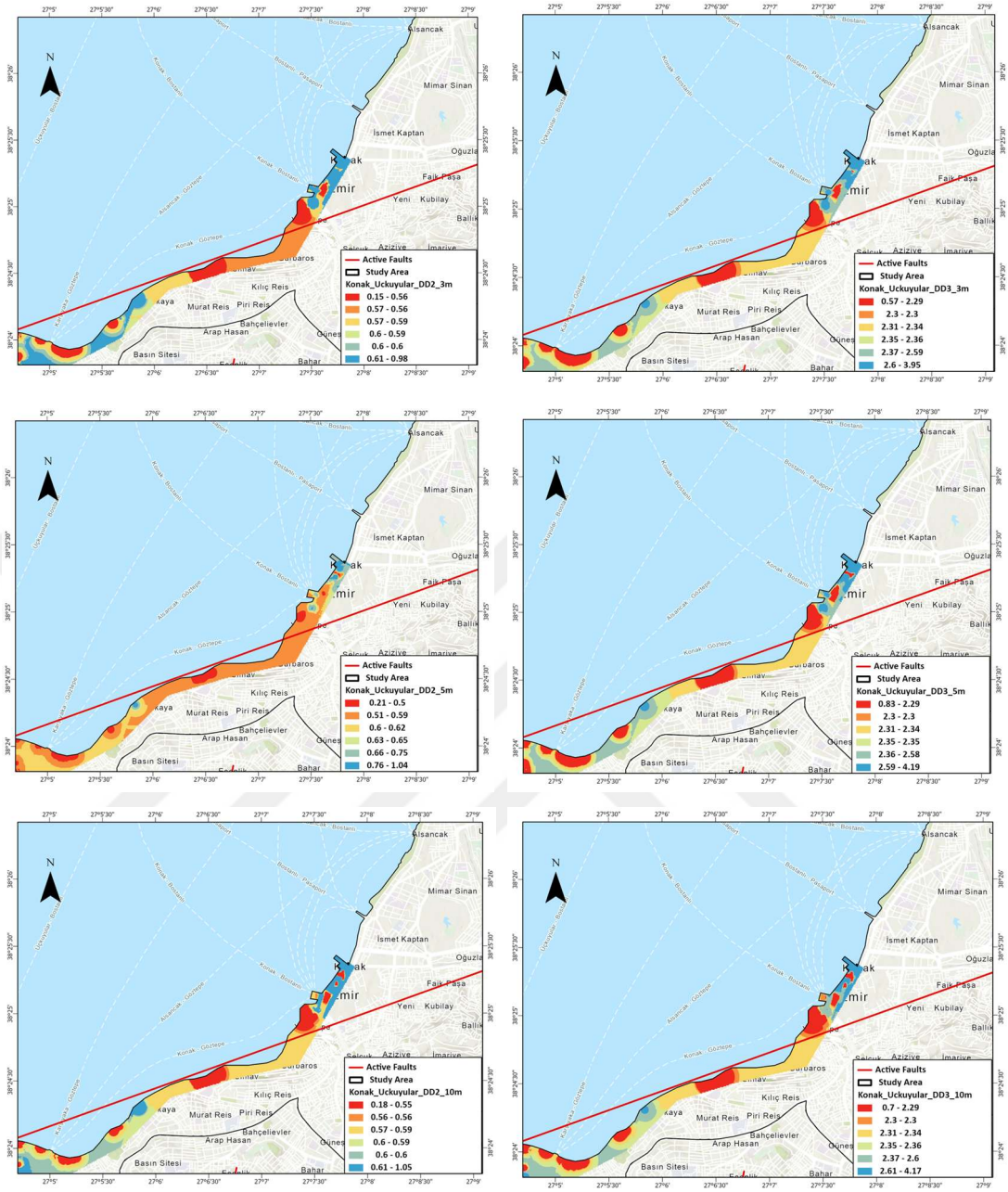

Figure 4.2 Factor of safety distribution for DD-2 (M_w=6.5) and DD-3 (M_w=5.5) earthquake levels at 3m, 5m, 10m depths in the Alsancak-Konak area

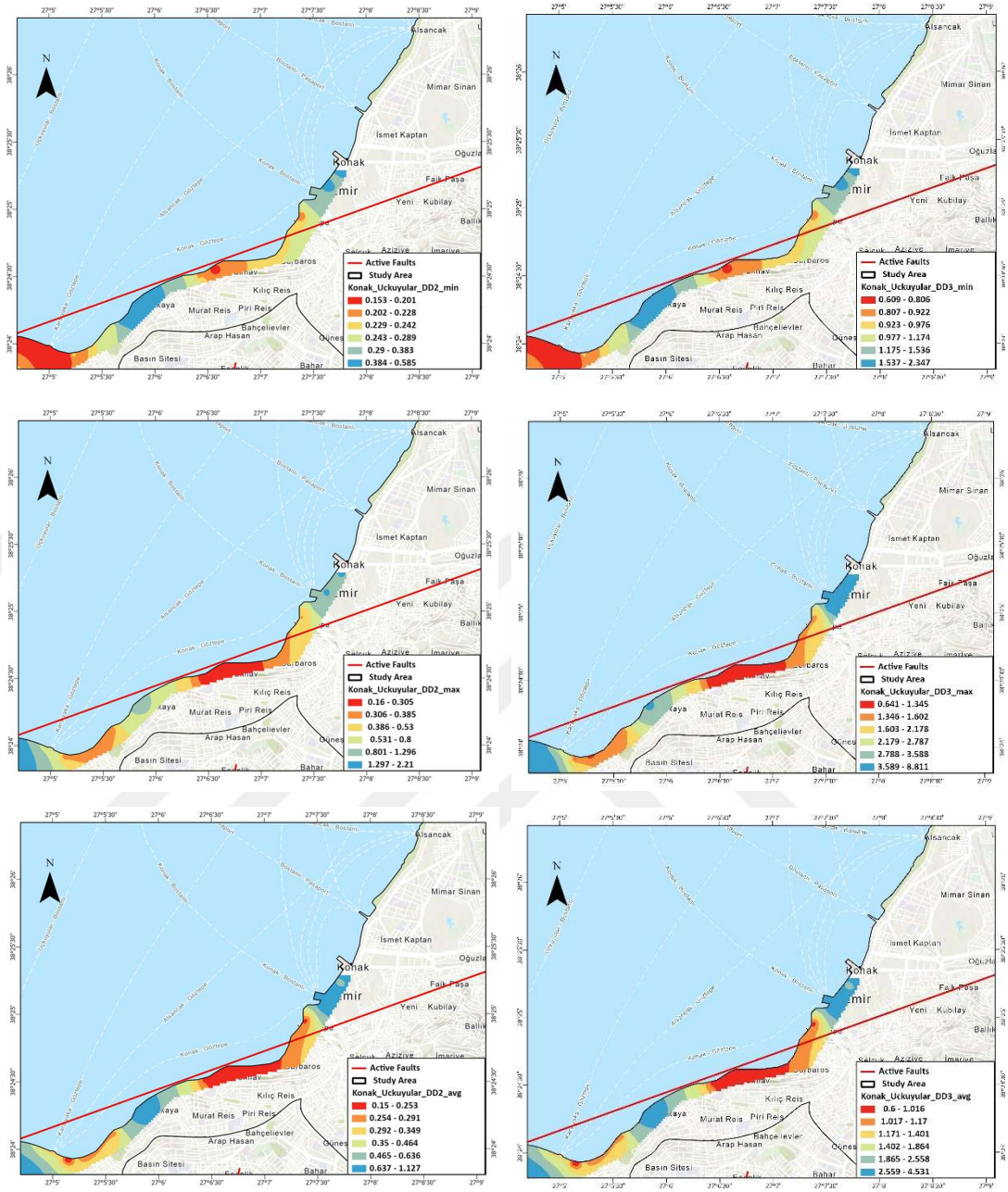

Figure 4.3 Factor of safety distribution for scenarios; minimum, maximum, and average for DD-2 (M_w=6.5) and DD-3 (M_w=5.5) earthquake level in the Konak-Üçkuyular area

4.2 Liquefaction Maps for the Alsancak-Konak Area

Figure 4.4 and Figure 4.5 illustrate the liquefaction safety factors at depths of 3m, 5m, and 10m in the Konak-Üçkuyular area for two different earthquake levels. Moreover, Figure 4.6 presents the worst-case, best-case, and average scenarios for these two earthquake magnitudes. The minimum, maximum, and average values were calculated using a 2D Empirical Bayesian Kriging (EBK) interpolation method, based on the lowest, highest, and average values recorded for each borehole.

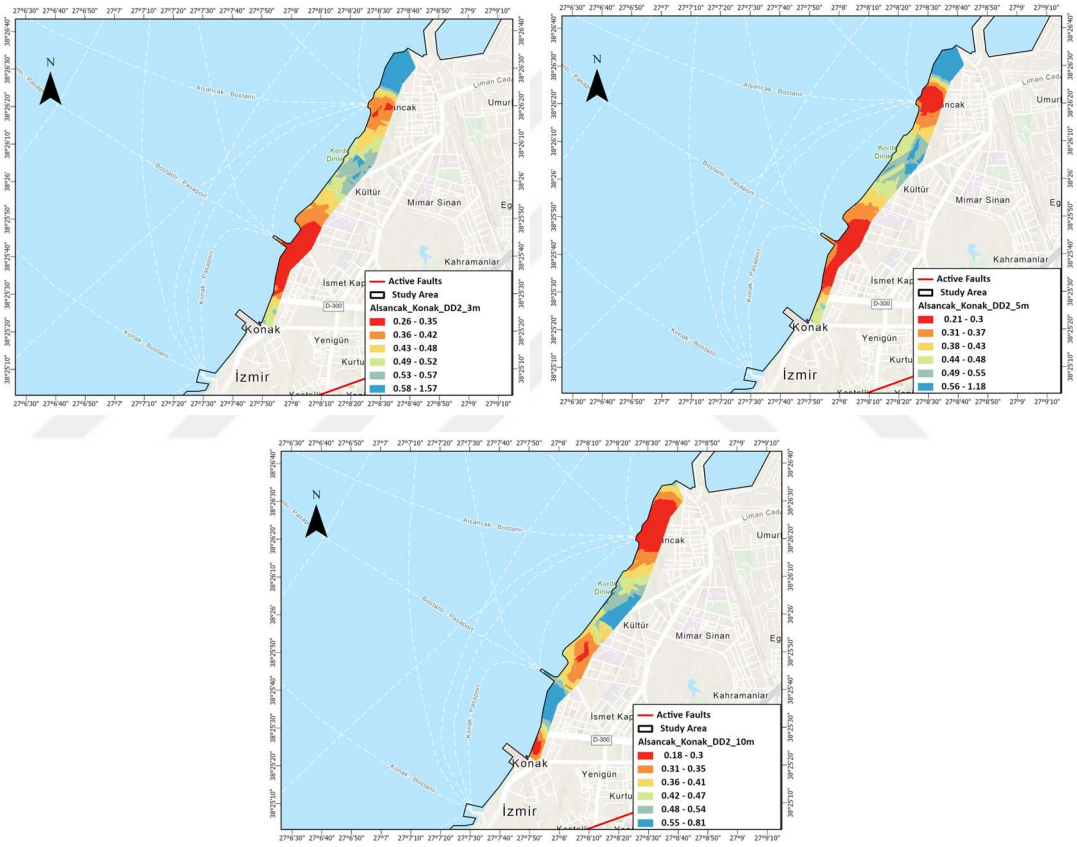

Figure 4.4 Factor of safety distribution for DD-2 (M_w=6.5) earthquake level at 3m, 5m, 10m depths in the Alsancak-Konak area

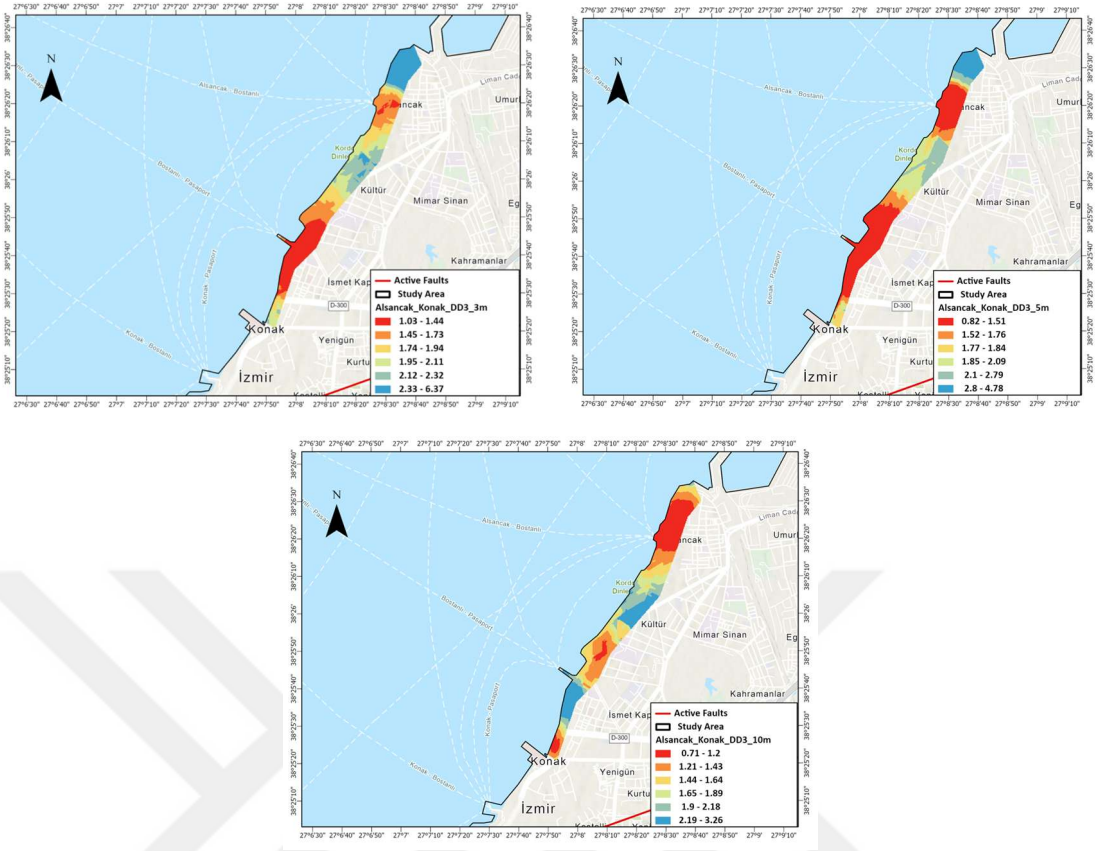

Figure 4.5 Factor of safety distribution for DD-3 (M_w=5.5) earthquake level at 3m, 5m, and 10m depths in the Alsancak-Konak area

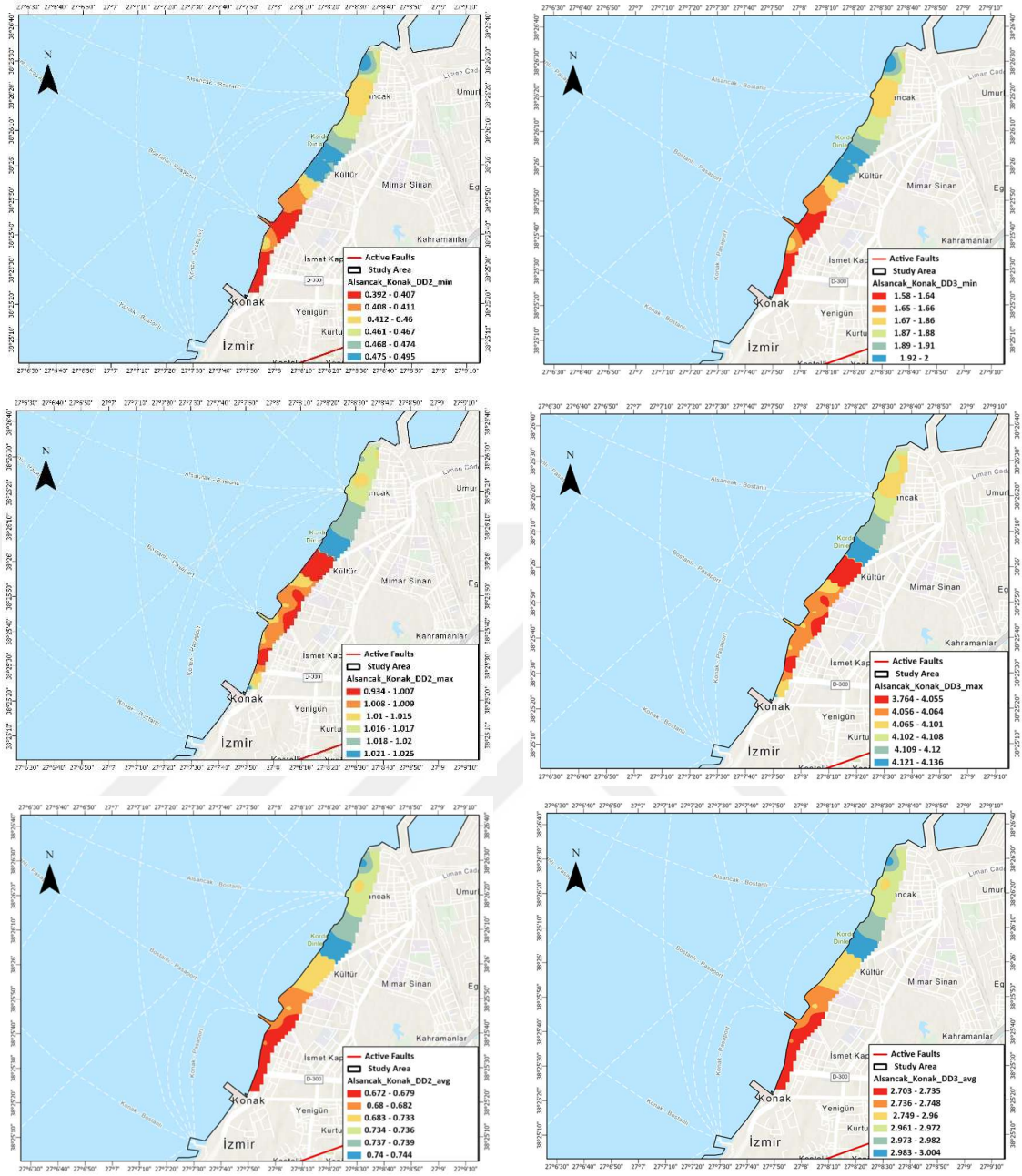

Figure 4.6 Factor of safety distribution for scenarios; minimum, maximum, and average for DD-2 (M_w=6.5) and DD-3 (M_w=5.5) earthquake level in the Alsancak-Konak area

4.3 Liquefaction Maps for the Bayraklı (Altınyol) Area

Figure 4.7 and Figure 4.8 illustrate the liquefaction safety factors at depths of 3m, 5m, and 10m in the Konak-Üçkuyular area for two different earthquake levels. Moreover, Figure 4.9 presents the worst-case, best-case, and average scenarios for these two earthquake magnitudes. The minimum, maximum, and average values were calculated using a 2D Empirical Bayesian Kriging (EBK) interpolation method, based on the lowest, highest, and average values recorded for each borehole.

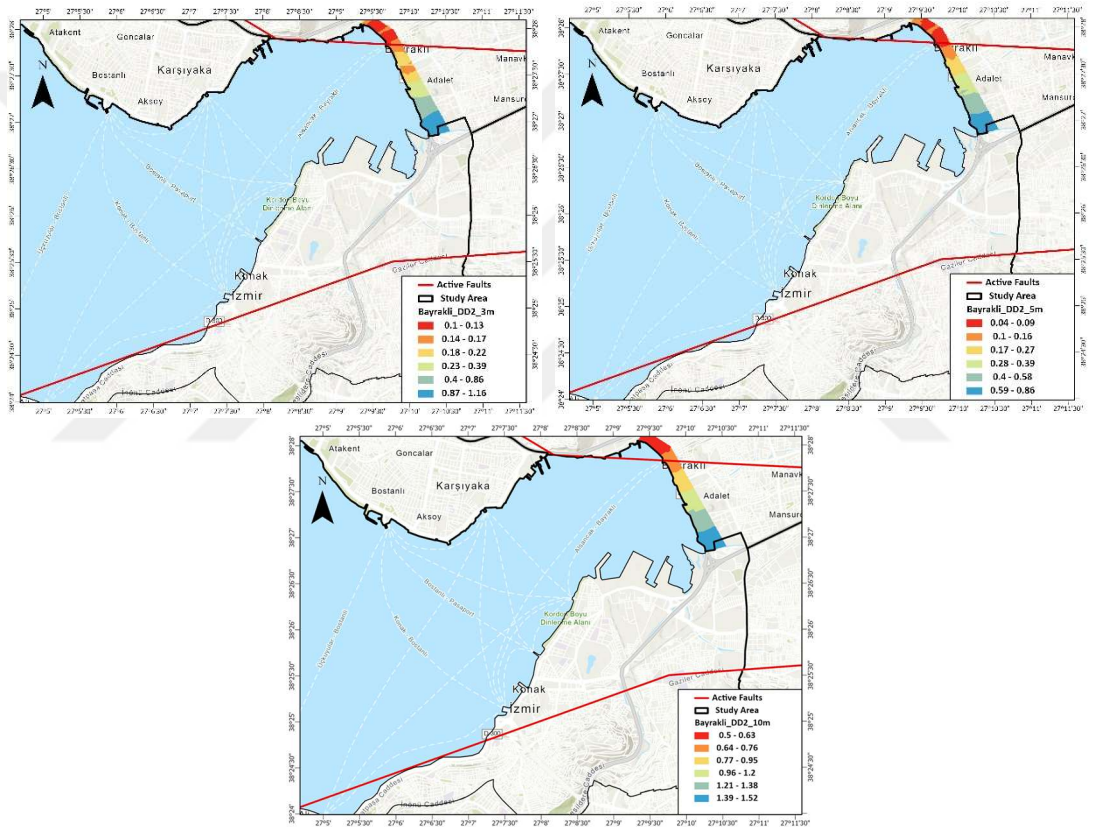

Figure 4.7 Factor of safety distribution for DD-2 (M_w=6.5) earthquake level at 3m, 5m, 10m depths in the Bayraklı (Altınyol) area

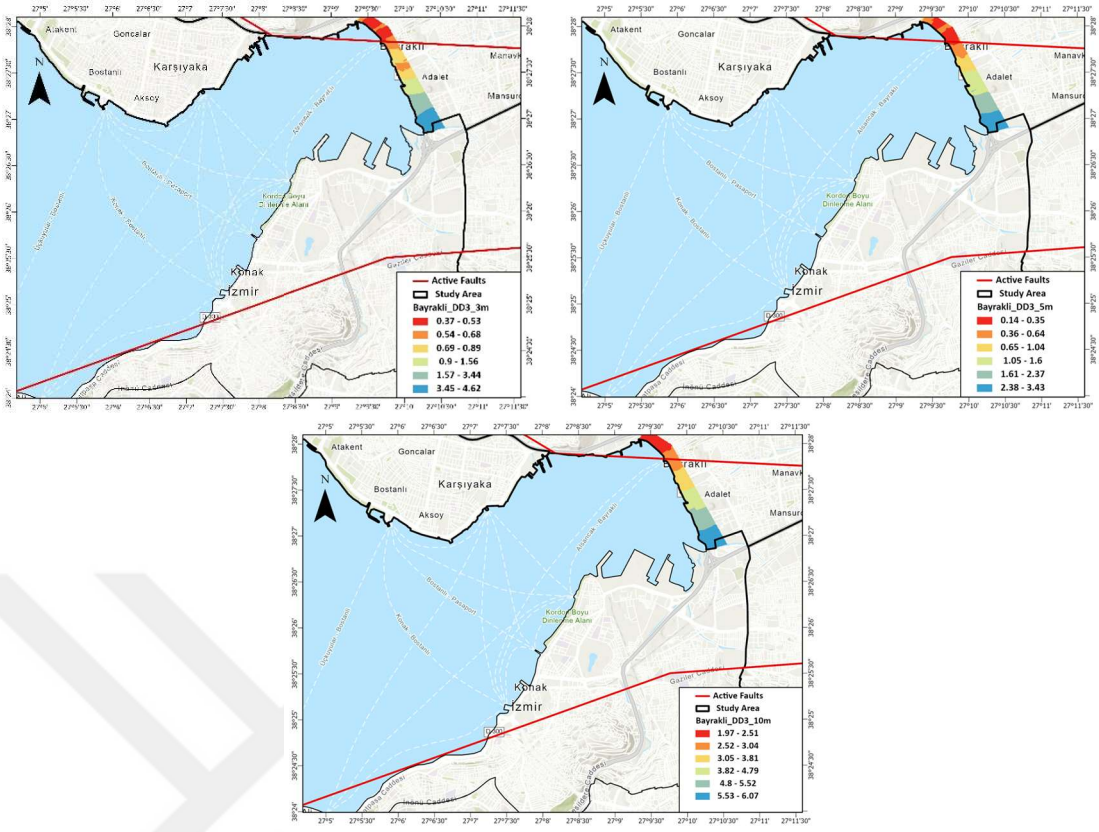

Figure 4.8 Factor of safety distribution for DD-3 (M_w=5.5) earthquake level at 3m, 5m, and 10m depths in the Bayraklı (Altınyol) area

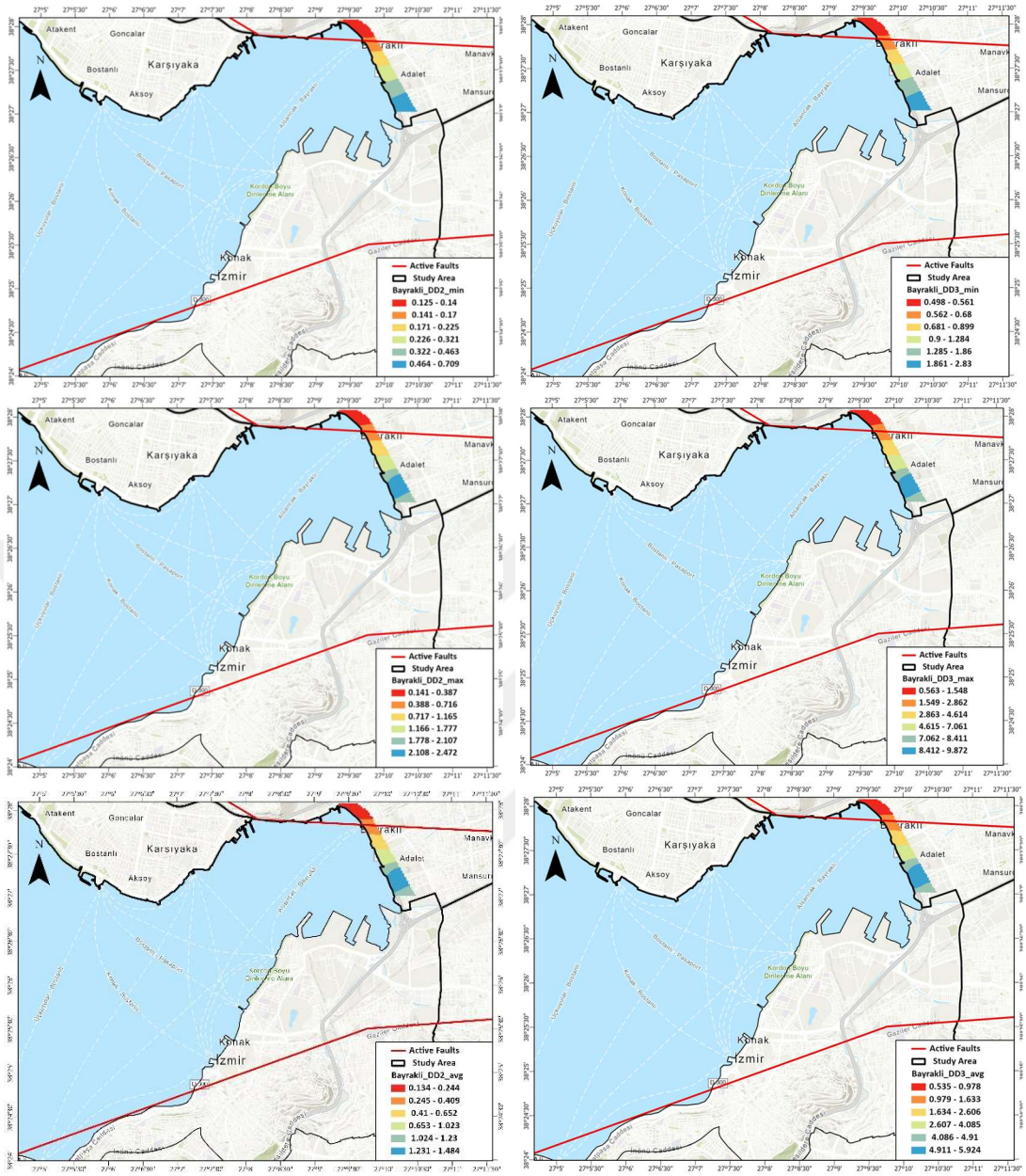

Figure 4.9 Factor of safety distribution for scenarios; minimum, maximum, and average for DD-2 (M_w=6.5) and DD-3 (M_w=5.5) earthquake level in the Bayraklı (Altınyol) area

CHAPTER FİVE
POST-EARTHQUAKE SETTLEMENT ANALYSIS

A post-earthquake settlement study is conducted to better understand ground settlement resulting from seismic loads during an earthquake. This analysis is essential for ensuring the safety of buildings and infrastructure. Settlement calculations were performed at 36 borehole locations in the Üçkuyular-Konak area, 31 in the Alsancak-Konak area, and 15 in Bayraklı area. Settlement values were calculated for each layer to determine the liquefaction safety factor. The total settlement values at each borehole location was then obtained by summing the settlement values of all layers. These settlement estimates were then utilized to build interpolation maps in ArcGIS using the 2D Empirical Bayesian Kriging tool, which enabled spatial display of settlement distribution across the region.

Post-earthquake settlement calculations for liquefaction are performed by obtaining volumetric deformation values using the relationship between Cyclic Stress Ratio (CSR) and $(N_1)_{60f}$ data, as applied in Wu and Seed (2004) approach which has shown to to be well correlated with other common methods. Since the Ishihara Yoshmine (1992) and Tokimatsu and Seed (1984) approaches do not consider fine content, Wu and Seed (2004) have been selected for this study.

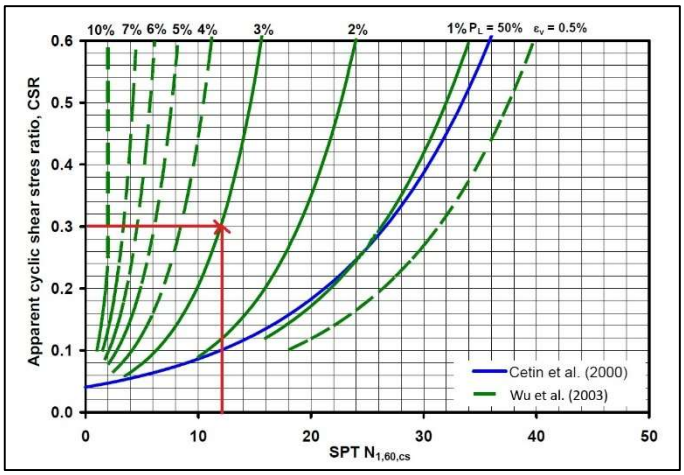

Figure 5.1 Volumetric strain determination (Wu et al., 2003)

The $(N_1)_{60f}$ values must be computed using the method of Seed et al. (2001) in order to utilize the Wu and Seed (2004) graph. Equation 2.15 is used to get the C_{FINES} values, and Equation 2.14 is used to estimate the $(N_1)_{60f}$ values for each layer. For example, for a $(N_1)_{60f}$=11 and CSR = 0.25, the volumetric strain is determined as shown in Figure 5.1. For each layer, the volumetric strains are calculated in this manner, and the total settlement is obtained using Equation 2.22.

In Figure 5.1, the CSR value is limited to 0.6. Since the CSR value indicates soil stability and liquefaction potential, a critical threshold of 0.6 is commonly accepted for assessing liquefaction risk. When CSR exceeds 0.6, it suggests that liquefaction should be addressed in more complex methods, as standard approaches may no longer be insufficient. In such cases, instead of post-earthquake settlement, the main issue would be the total strength loss. This indicates a potential for severe consequences if an earthquake of this magnitude occurs in these areas.

The calculations resulted in the maps for the DD-2 and DD-3 earthquake levels, which are presented in Figure 5.2 and Figure 5.3. However, due to the insufficient distribution of boreholes in the Bayraklı area, the liquefaction distribution map could not be generated for this region.

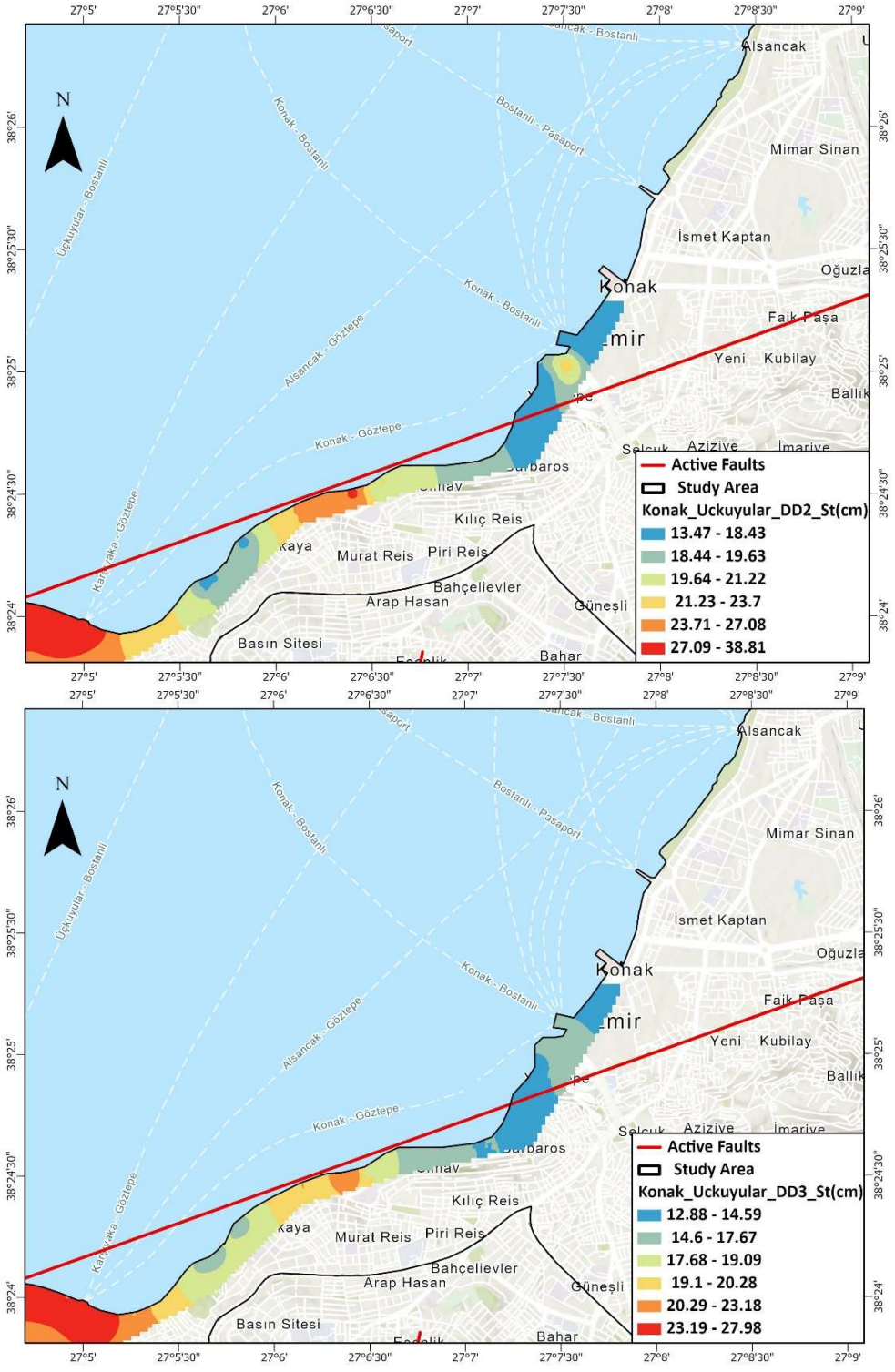

Figure 5.2 Post-earthquake settlement distribution for DD-2 (M_w=6.5) and DD-3 (M_w=5.5) earthquake levels in the Konak-Üçkuyular area

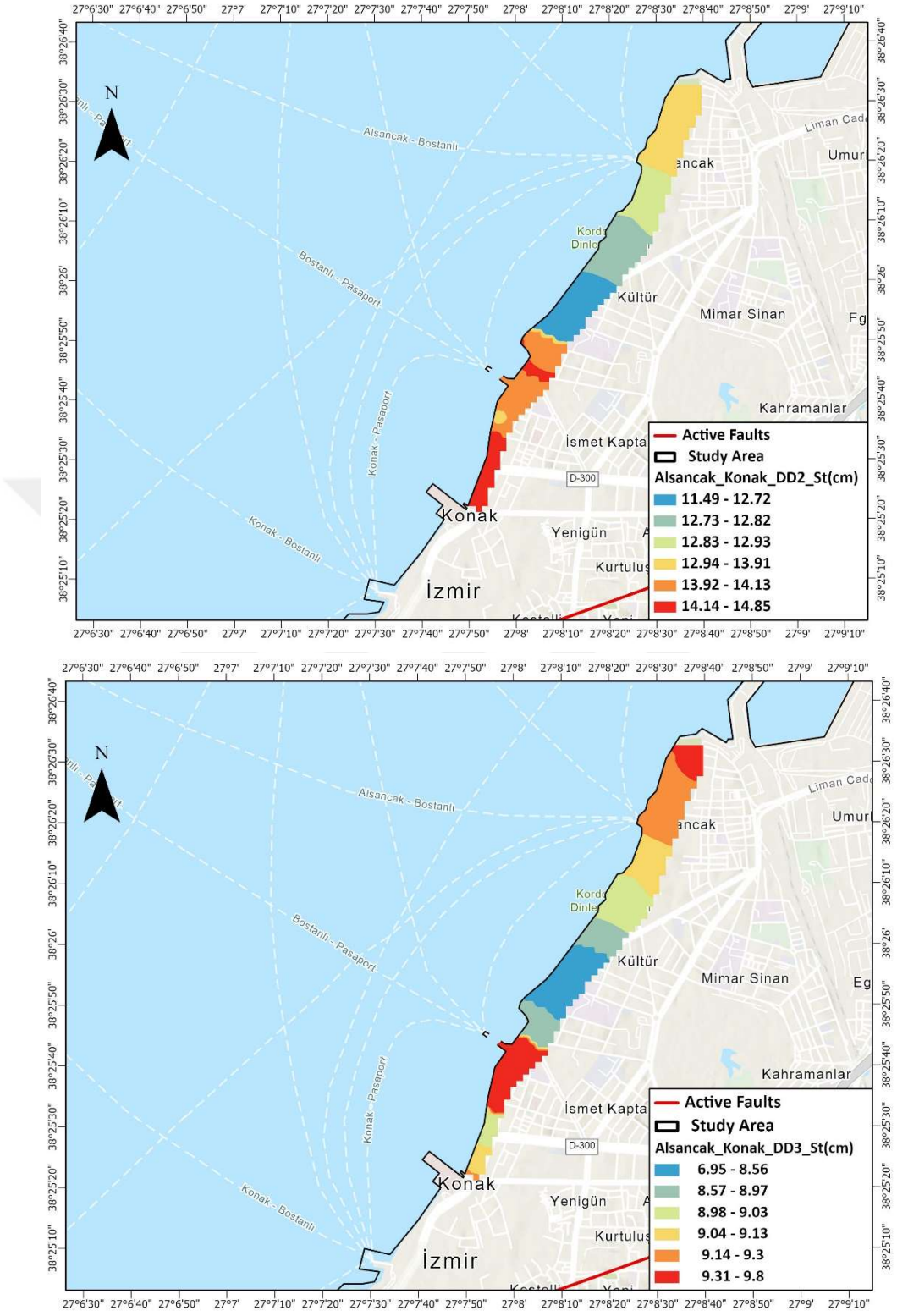

Figure 5.3 Post-earthquake settlement distribution for DD-2 (M_w=6.5) and DD-3 (M_w=5.5) earthquake levels in the Alsancak-Konak area

CHAPTER SİX
DISCUSSION OF THE RESULTS

The findings of this chapter provide a detailed analysis of the liquefaction potential and post-earthquake settlement along the major coastal highways of the İzmir Bay area. The results highlight the varying levels of safety factors (FS) under different seismic scenarios (DD-2 and DD-3), offering valuable insights into the vulnerabilities across various regions. The calculation of the liquefaction safety factor was performed exclusively for sandy soils. The plasticity of fine-grained soils was not considered in this study.

In the Konak-Üçkuyular region, at the DD-2 earthquake level, the safety factor reaches a maximum of 1 in some areas but generally remains around 0.5. Specific values for this seismic level include a minimum of 0.2, a maximum of 0.4, and an average of 0.3, indicating significant vulnerability to liquefaction. Under the DD-3 earthquake level, the safety factor generally exceeds the threshold value of 1.1, with distributions ranging between 2 and 4. However, a small portion of the region exhibits safety factors as low as 0.6–1.1. Overall, most areas in this region appear to be safe against liquefaction at this level. This region predominantly consists of sandy layers with very low fine-grained content, and the groundwater table is approximately 1 meter below the surface. The presence of significantly low SPT values, ranging between 1 and 20, indicates a high likelihood of liquefaction occurrence in this area.

In the Alsancak-Konak region, although the results in this area are pretty similar to those obtained in the Konak-Üçkuyular region, the soil profile is predominantly composed of sandy and clayey soils. The groundwater level ranges between 5 and 10 meters, while the SPT-N values vary from 0 to 30. At the DD-2 seismic level, the safety factor decreases to as low as 0.3 in some regions, with a maximum value of 1. Even at depths of 10m, the average safety factor is approximately 0.4, exposing a high risk of liquefaction. Specific borehole analyses yielded minimum, maximum, and

average FS values of 0.45, 1.0, and 0.75, respectively. Safety factors for the DD-3 earthquake level drop to around 0.7, especially at depths of 5m and 10m but typically exceed the 1.1 threshold as depth increases. These results are also reflected in the minimum, maximum, and average distribution maps.

In the Bayraklı region, the safety factor exhibits a homogeneous and similar distribution across DD-2, and DD-3 earthquake levels. At the DD-2 earthquake level, except for a small portion, the values range between 0.1 and 1, indicating a very high likelihood of liquefaction in the Bayraklı coastal area at this seismic level. In the minimum factor of safety distribution map, the values range between 0.125 and 0.7, while in the maximum distribution map, they vary between 0.13 and 1.50. The average values obtained in this region are approximately 0.5. At the DD-3 earthquake level, most of the region shows values lower than 1 at depths of 3m and 5m, with only a tiny portion ranging between 1 and 3. At a depth of 10m, the values range between 2 and 6. Although the minimum values range between 0.5 and 2.8, the overall distribution appears to be around 0.75. In the map of the average result, the general distribution is observed to be around 2.1.The borehole depths in this area range from 30 to 80 meters, predominantly of clayey silt layers. Among these layers, there are notably thick sandy strata where the SPT-N values generally range from 0 to 18, occasionally reaching up to 39 in certain sections. The Bayraklı region is identified as the most vulnerable area to liquefaction, as evidenced by the devastating effects it experienced during the 2020 Samos earthquake.

Post-earthquake settlement calculations were performed using well-established correlations in the literature. Volumetric stresses in sandy soil were calculated using the association between cyclic shear strength (CSR) and corrected $N_{1,60}$ values provided by Wu and Seed (2004). Settlement values for each layer were then calculated, and the total settlements at each borehole were obtained by summing the layer-specific settlements. These settlement values were mapped in ArcGIS, and a 2D Empirical Bayesian Kriging (EBK) interpolation map was created to visualize the spatial distribution of settlements. According to the results, settlements in the Konak-

Üçkuyular region ranged between 10 cm and 80 cm for the DD-2 earthquake level and between 4 cm and 60 cm for the DD-3 earthquake level. However, the interpolation map reflects the distribution weighted, avoiding extreme values to provide a more representative settlement distribution. As a result, the EBK interpolation map shows settlement values predominantly in the range of 10-40 cm (DD-2) and 10-30 cm (DD-3).

Similarly, in the Alsancak-Konak region, settlements ranged between 3 cm and 40 cm for the DD-2 earthquake level and between 4 cm and 30 cm for the DD-3 earthquake level. However, the weighted distribution reflects settlements predominantly in the 11-15 cm range for DD-2 and 7-10 cm for DD-3. Although the safety factor for DD-3 exceeds 1.1 in this region, the settlements still reach critical levels, highlighting potential concerns for post-earthquake performance.

The calculation results for the Bayraklı region indicate that, at the DD-2 earthquake level, settlements range from 7 cm to 50 cm, with an average of 30 cm. At the DD-3 earthquake level, settlements vary between 5 cm and 35 cm, with an average of 20 cm. Considering the abundance of sandy layers in this region, with SPT-N values ranging from 1 to 15 in these layers, significant settlements are expected for both seismic levels. Due to insufficient data distribution in the Bayraklı region, mapping through 2D interpolation could not be achieved.

The results indicate that a significant liquefaction risk is expected in all three regions at the DD-2 level. Although the situation is critical in the first 3 meters of depth, similar conditions are also observed in the analyses at 10 meters. For a general evaluation on a borehole basis, minimum, maximum, and average graphs can be examined. Upon reviewing the average interpolation maps, liquefaction is expected across all sections of the coastal areas, including the major highway arteries, in all three regions. At the DD-3 level, although the safety factor generally exceeds 1.1, certain areas in the Konak-Üçkuyular and Bayraklı regions remain below this

threshold. The findings indicate that liquefaction-induced settlements are a significant concern for the study area, particularly for earthquakes with magnitudes greater than 6.5. The study's findings reveal that safety and post-earthquake settlement values are overly crucial along major coastal highway arteries.

CHAPTER SEVEN
INCREASING LIQUEFACTION RESISTANCE OF SOIL IN THE STUDY AREA USING CONTEMPORARY TECHNIQUES

Dynamic compaction will be applied along the major coastal highway arteries in the İzmir Bay area to mitigate the risk of liquefaction and improve the stability of the region's soil. This method has been chosen for its ability to quickly and cost-effectively enhance the soil's load-bearing capacity, which is vital in areas with time and budget constraints. The presence of large rock formations in the region further justifies the use of dynamic compaction, as it can be effectively implemented in locations with underlying hard layers without causing significant disruption to the surrounding environment.

In densely built areas where rapid results are required, dynamic compaction is a flexible and practical option. By delivering a heavyweight multiple times to compact loose soil, this technique can significantly improve the stability of areas susceptible to liquefaction or with loose soil, especially along transportation routes. It ensures that the infrastructure, such as highways, remains stable and secure in the long term. As a result, dynamic compaction is the ideal method for improving the stability and safety of major urban roads, providing a balance of speed, cost, and environmental considerations for long-term performance.

7.1 Dynamic Compaction

Dynamic compaction is one of the in-situ ground improvement methods widely adapted to densify loose, granular soils and engineered fills by dropping heavy weights from significant heights onto the ground surface. In this way, the energy of impact is imported profoundly into the soil to increase its density and strength while reducing settlement and liquefaction potential. Initially developed by Louis Menard, the process has been in application for many years in stabilizing loose soils for significant projects such as roads, airports, and industrial areas. Generally, the dynamic compaction

process involves dropping a heavy steel or concrete tamper weighing 5 to 40 tons from heights between 10 to 40 meters.

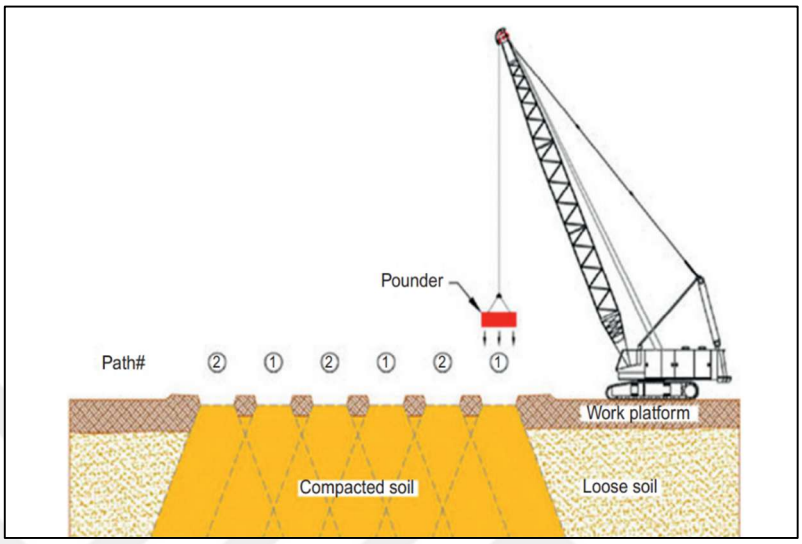

Figure 7.1 Schematic illustration of dynamic compaction method (Nicholson,2014)

The dynamic compaction method applies to sandy soils and is not recommended for clayey soils of the nature of the soil type. However, it can be applied by giving time to dissipate porewater pressure due to applied dynamic load. Dynamic compaction can be used for many kinds of soils and purposes. These can be loose, natural soils like alluvial, floodplain, new or old landfills, mine spoils, collapsible soils, loose sand and silt, etc. Lukas (1995) presented the soil types into three categories to which dynamic compaction can be applied. Dynamic compaction is most effective in soils with high permeability.

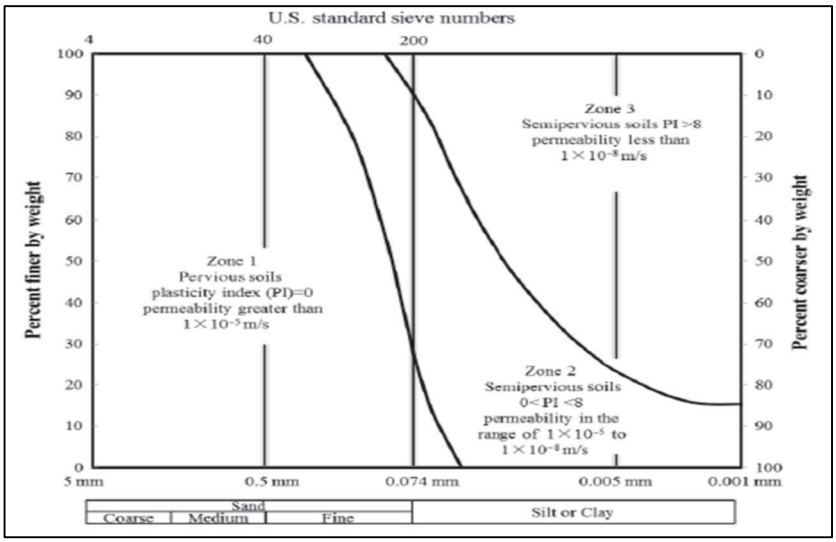

Figure 7.2 Soil types for dynamic compaction (Lukas, 1995)

In the table below, some recommendations were made by Fletcher Construction Private Ltd. according to soil type and saturation degree.

Table 7.1 Suitability of dynamic compaction method

General Soil Type	Degree of Saturation	Suitability of DC
Granular Deposits in the grain size range of boulders to sand with 0% passing the 0.074mm sieve	High/Low	Excellent
Granular deposits containing not more than 35% silts	High	Good
	Low	Excellent
Semi-permeable soil deposits are generally silty soils containing some sand but less than 25% clay with PI<8	High	Fair
	Low	Good
Impermeable soil deposits generally clayey soils where PI>8	High	**Not Recommended**
	Low	Fair minor improvements w(%)<PI
Miscellaneous fill, including paper, organic deposits, metal and wood	Low	Fair-long term settlement anticipated due to decomposition. Limit use the of embankments
Highly organic deposits of peat-organic silts	High	**Not recommended** unless sufficient energy is applied to mix granular with organic soils

7.1.1 Process and Mechanism

Dynamic compaction involves several passes over the treatment area, each consisting of crossing over the area at least once. Thereafter, the tamper is dropped at pre-determined grid positions a specified number of times per pass. These grid patterns can be square or triangular. Figure 7.3 shows a square pattern; phase 1 consists of two phases, Phases 1-1 and 1-2. In phase 1, compaction is applied with larger spacing to reach deeper depths. Phase 2 is applied over smaller spacing to densify shallow depths and use lower energy. This phase is also called ironing compaction.

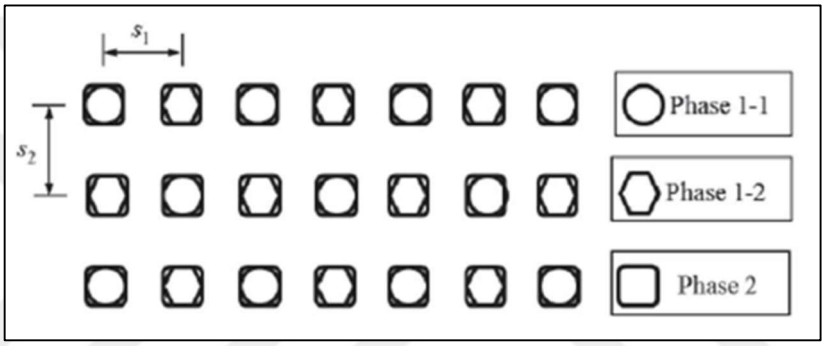

Figure 7.3 Square layout of drop points (Shaban, 2018)

Key factors are the weight of the tamper, the height of the fall, grid spacing, and the number of passes. The weight of the tamper generally falls between 5-27 tons, and the drop height ranges from 12-30 m. The grain size distribution and saturation are the most influential factors in the amount of energy required to achieve the proper depth of compaction and efficiency. Indeed, adequate densification may require two or three processes, especially in deep or highly variable soils.

7.1.2 Advantages and Limitations

The major advantage of dynamic compaction is that large areas of poor-quality soil can be treated with minimum excavation and disturbances. This method can also reach moderately significant depths, eliminating the need for costly deep foundation systems

such as piles and caissons. Moreover, it is quite cheaper than other improvement techniques such as stone columns and vibro compaction. It provides improved bearing capacity, reduced differential settlement and enhanced liquefaction susceptibility.

However, it does have some limitations. While it is a highly effective method on granular soils such as sand, in clayey soil, since it absorbs the energy, it reduces the effect of compaction. The compaction weight may sink or embed itself into the soil if the clay soil is highly plastic and water saturated. For compaction in such soils, a granular layer should be added to aid in effective compaction. Additionally, to prevent sinking, the depth of the craters formed after each impact should be monitored and should not exceed the value of the tamper height+0.3 meters.

This process generates some noises, vibrations, and lateral movement, which could affect the area in which the treatment is located. If compaction is close to a residential area, vibrations become a significant concern and it should be monitored and prevention has been taken. According to the U.S. Bureau of Mines, particle velocities around 13–19 mm/s are unlikely to cause cracking in modern buildings, and structural damage is unlikely if particle velocities are kept below 50 mm/s. To prevent Rayleigh waves generated by impacts from reaching nearby structures and residential areas, a trench approximately 3 meters wide can be excavated. If positioned carefully to avoid impacting other nearby structures, this method can effectively mitigate vibration effects.

7.1.3 Design Guideline of Dynamic Compaction Method

An empirical formula developed by Menard (1975) as follows.

$$D_i = n_c\sqrt{W_t H_d} \tag{7.1}$$

where D_i (m) is depth of improvement, W_t (ton) is weight of tamper and H_d (m) is drop height. Depth of improvement is determined approximately and constant n_c is determined below table. $\sqrt{W_t H_d}$ can be calculated using Equation 7.1.

Table 7.2 Recommended n_c value for different soil types (Lukas, 1995)

Soil Type	Degree of Saturation	Recommended n_c value
Pervious soil deposits	High	0.5
Granular soils	Low	0.5-0.6
Semipervious deposits	High	0.35-0.4
Primary silts with PI<8	Low	0.4-0.5
Impervious soil deposits	High	Not Recommended
Primarily clayey soils	Low	0.35-0.4 (w<P_L)
[a]PI =Plasticity index, w=water content, P_L=plastic limit		

Mayne et al. (1984) provided a relationship based on field data;

$$H_d = (W_t H_d)^{0.54} \tag{7.2}$$

Then, drop height can be calculated as in Equation 7.2.

Total applied energy (AE_{total}) during compaction represents the unit applied energy (UAE) multiplied by the thickness of the layer (D_i) to be improved. It is also a sum of the Phase 1 (Deep Compaction Stage) and Phase 2 (Ironing Phase). Deep compaction stage energy at one phase (AE_{HEP}) can be calculated as Equation 7.4 where A_e denotes the effective area according to applied pattern (square or triangular). The total applied energy is the sum of the energy applied during the high-energy pass phases (AE_{HEP}) and ironing pass (AE_{IP}).

$$AE_{total} = UAE\ D_i \tag{7.3}$$

$$AE_{HEP} = \frac{N_D N_P W_t H_d}{A_e} \tag{7.4}$$

$$A_e = s^2 \text{ for square pattern} \quad (7.5a)$$

$$A_e = 0.867s^2 \text{ for triangular pattern} \quad (7.5b)$$

where N_D is number of drops, N_P is number of passess and s is grid spacing.

This process is used in a triangular or square design with uniform spacing. Drop spacing (s) is generally taken by multiplying the tamper diameter or width by 1.5-2.5. Energy applied during high-energy passes assumes for one pass. If the number of drops differs from 7-15, grid spacing should be adjusted.

Table 7.3 allows you to select the required unit applied energy (UAE) for the compacted and ironing layers according to the zones in Figure 7.2.

Table 7.3 Required unit applied energy from standard proctor test (Lukas, 1995)

Soil Type	Unit Applied Energy (kj/m^3)	Standard Proctor Energy (%)
Pervious coarse-grained soil-Zone-1	200-250	33-41
Semipervious fine-grained soil-Zone-2 Clay fills above water table -Zone 3	250-350	41-60
Landfills	600-1100	100-180

The loosened upper section of the layer will be compacted using low-level energy, known as ironing layer energy (AE_{IP}), applied across the entire surface. During the ironing pass, energy should be at least 400 kj/m^2 (Lukas, 1995). This energy requirement can be estimated based on the expected crater depth, assumed to be approximately 1.0–1.5 meters.

$$AE_{IP} = UAE * d_{cd} \quad (7.6)$$

Where d_{cd} is crater depth in m.

Allowable crater depth $(d_{cd})_{al}$ calculated as follows:

$$(d_{cd})\text{al} = 0.075(d_{cd}) + 0.3 \quad (7.7)$$

The depth of the crater formed should not exceed this depth. Then, number of passes can be calculated from Equation 7.3.

After several drops and passes were completed, the bulldozers leveled the surface. The ground settlement is measured by comparing the current elevation of the ground from the initial level. In unsaturated soils, it happens abruptly after compaction, whereas in saturated soils, it develops with time after every compaction phase. Most of the settlement arises from filling large craters created by the tampers. The approximate percentage of induced settlement is provided below.

Table 7.4 Approximate induced settlement relation with improvement depth (Shaban, 2015)

Soil Type	Percent of Depth
Natural Clays	1-3
Clay Fills	3-5
Natural Sands	3-10
Granular Fills	5-15
Uncontrolled Fills	5-20

7.2 Proposal for Improvement through Dynamic Compaction in the Konak Coastal Area

As observed from the calculated safety factors against liquefaction along the İzmir coastal region, liquefaction is anticipated in these areas. This section proposes an improvement approach using dynamic compaction over a 30x150 m area. The improvement will be applied in a designated area on the map, as shown in Figure 7.4, encompassing a section of the coastal road within the Konak-Üçkuyular region, where the general soil profile consists of sandy layers. The calculations will follow the "Dynamic Compaction" methods outlined by the "U.S. Department of Transportation, Federal Highway Administration" (Lukas,1995).

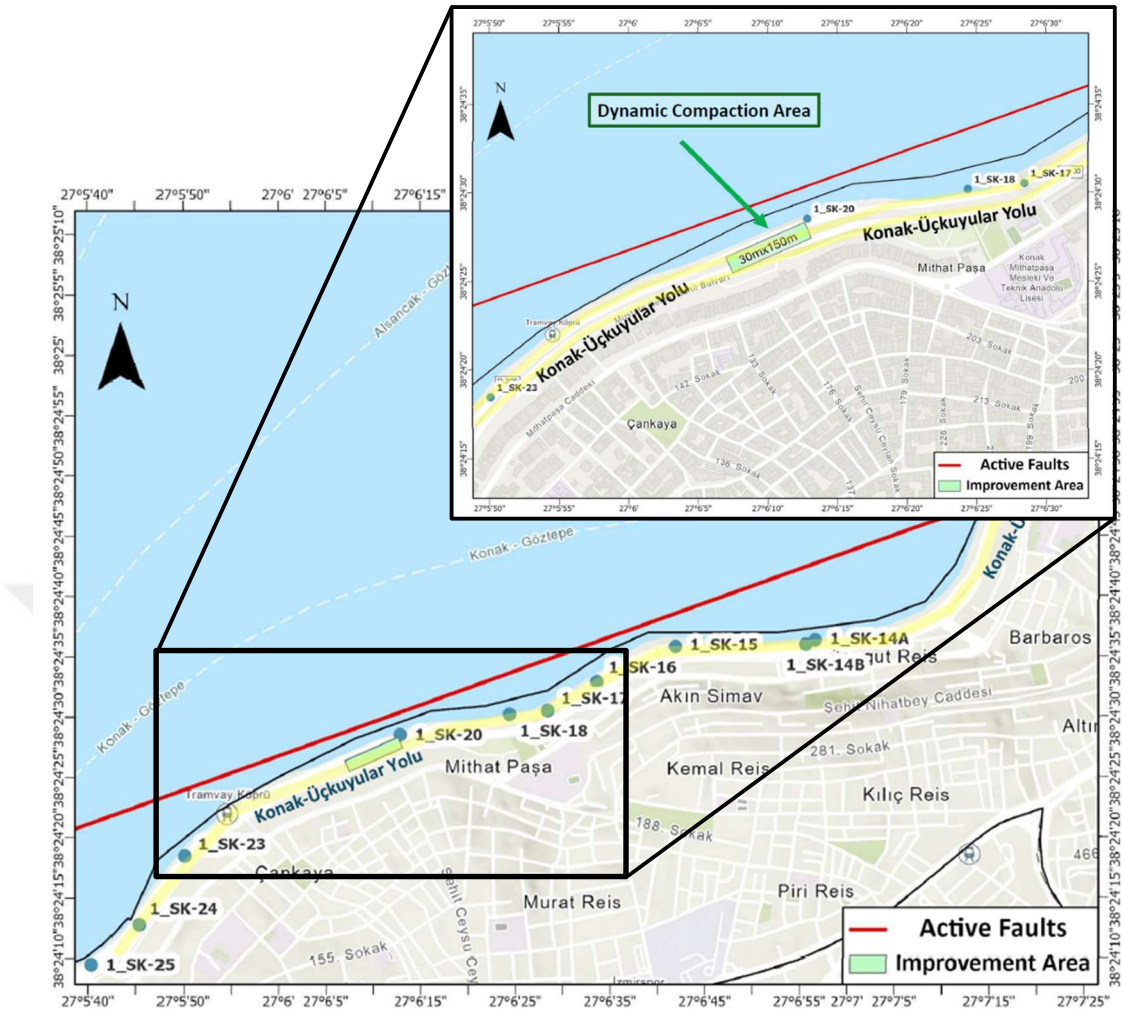

Figure 7.4 Location of improvement area

The soil profile within the selected improvement area between Konak and Üçkuyular consists of silty-clayey sandy layers. The required compaction energy for soil improvement has been determined based on the specified depth and area pattern. The improvement target depth is set to an average of 7 meters. This calculation estimates the energy needed for adequate deep compaction across the improvement zone. Borehole 1_SK-18 was chosen to representative example of the area where ground improvement was implemented, and the soil layers in this borehole are illustrated in Figure 7.5.

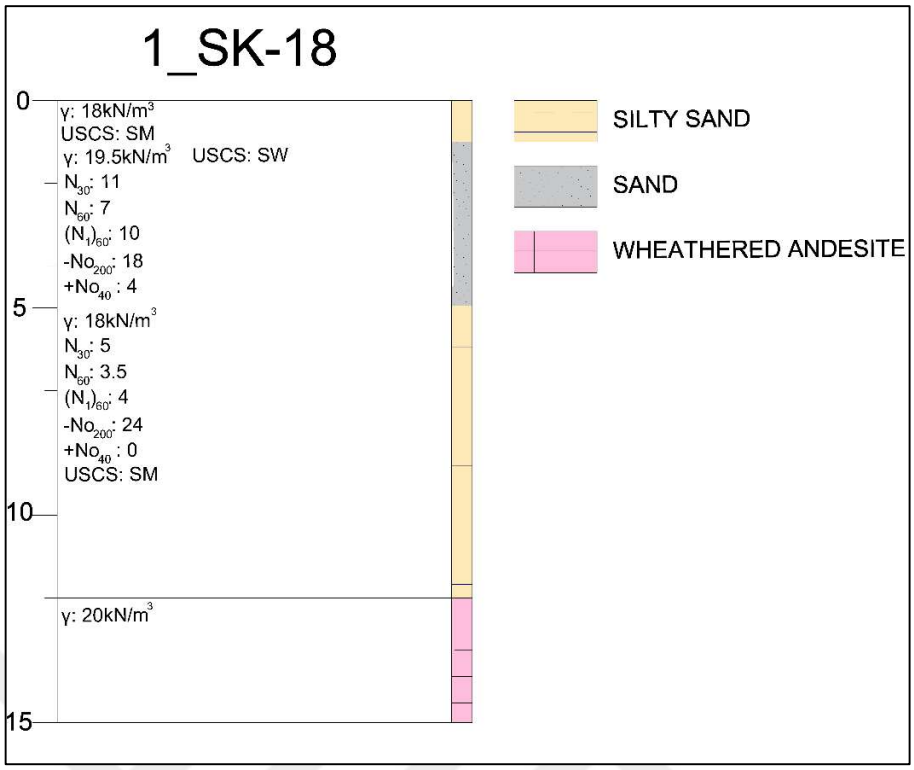

Figure 7.5 Soil profile of improvement area

The selected area is categorized as Zone-1, which is the most suitable area for compaction, according to Figure 7.2. Specific input parameters must be chosen to perform the dynamic compaction analysis, and calculations should be carried out accordingly. The input values for compaction calculations are provided in Table 7.5. The tamper weight and drop height are obtained using the n_c coefficient based on the improvement depth, according to Equation 7.2. Although the selected area consists primarily of sand, the n_c coefficient is chosen as 0.4 due to the presence of silt and clay in specific locations (Table 7.2).

Table 7.5 Input values for dynamic compaction energy

Depth of improvement, D_i	7 m
Coefficient, n_c	0.4
UAE -Compacted Layer-	300 kJ/m^3
Tamper Diameter	1.5 m
UAE -Upper Layer-	350 kJ/m^3

Using the improvement depth (D_i) and a coefficient, the tamper weight was determined to be 15 tons, and the drop height was selected as 21 meters based on Equation 7.2. According to Table 7.3, the required unit energy for the compaction layer will be determined. The sandy layer, classified as coarse-grained permeable soil, was assigned an average value of 300 kJ/m³ in the selected area due to the presence of clay and silt. Tamper diameter is taken as 1.5m. Due to the presence of layers falling into Zone-2 in specific boreholes, the required unit energy for the ironing phase has been determined as 350 kJ/m³.

Table 7.6 Dynamic compaction energy calculations

Depth of improvement, D_i	**Coefficient, n_c**	$\sqrt{W_t H_d}$	**Height of Drop, H_d**	**Weight of Tamper, W_t**	**Tamper Diameter**
m	**-**	**tonm**	**m**	**ton**	**m**
7	0.4	17.5	21	15	1.5
Drop Spacing, s	**Effective Area, A_e**	**Number of Drops, N_D**	**Number of Passes, N_P**	**Total Applied Energy, AE_{total}**	**Total Applied Energy, AE_{total}**
m	**m²**	**-**	**-**	**kJ/m²**	**MJ/m²**
3	9	3	2	2060.1	2.06
Unit Applied Energy, UAE [Upper Layer]	**Applied Energy for Ironing Pass, AE_{IP}**	AE_{IP}+AE_{total}	**Unit Applied Energy, UAE**	**Total Applied Energy, AE_{total}**	**Total Applied Energy, AE_{total}**
kJ/m³	**kJ/m²**	**kJ/m²**	**kJ/m³**	**kJ/m²**	**MJ/m²**
350	525	2585	300	2100	2.1

Equation 7.3 calculates the total energy required for the compaction layer as 2100 kJ/m². The applied energy will be calculated based on the parameters selected, and the required energy will be obtained. This energy is often supplied in many phases for clayey soils, enabling excess pore water pressures to dissipate between phases. However, because the soil in this case is sand, the energy will be delivered in a single phase.

Equation 7.4 calculates the High Energy Pass (HEP), representing the energy applied to the compaction layer. To make this computation, first decide the application pattern and then select the drop spacing (s) value. Typically, s is 1.5 to 2 times the

diameter of the tamper, which can be computed as s = 1.5 × 2 = 3 meters. The application pattern is square (Figure 7.5). To achieve the required 2100 kJ/m² energy using Equation 7.4, the number of drops and passes are determined which are N_d=3 and N_P=2. If the number of drops is too high, the parameters or application spacing should be adjusted. After selecting the number of drops and number of passes, the applied energy is calculated as 2060 kJ/m² based on these values. For the ironing phase, the unit applied energy for the surface layer is obtained as 350 kJ/m³ using Equation 7.6, and with a d_{cd} of 1.5 m, the value becomes 525 kJ/m³. The total applied energy is, therefore, 2060 + 525 = 2585 kJ/m² (Table 7.6).

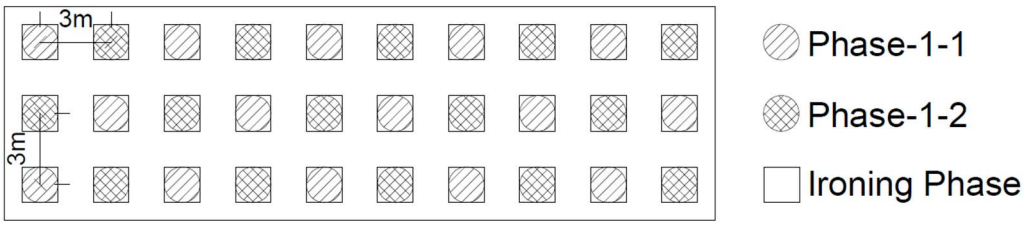

Figure 7.6 30m x 150m Improvement area pattern

The selected points will be executed with a drop spacing of 3 meters, , following an alternating pattern of one active and one inactive point as shown in Figure 7.5. Each point will be impacted three times per pass, with two passes conducted in total. Finally, each point will be subjected to a single impact during the ironing phase to complete the process. Since the application area is close to buildings, excavating a trench to mitigate the impact may be beneficial.

7.3 A Novel Technique Against Liquefaction with Colloidal Silica

The primary strategies for improving liquefaction resistance and minimizing ground deformations mainly focus on densification techniques. Approaches such as dynamic compaction, vibro-compaction, and explosive compaction have been widely utilized to compact soil and lower the likelihood of liquefaction (Zhao et al., 2019). Nonetheless, these methods can challenge nearby structures due to the vibrations and

dynamic forces they generate, which restricts their use mainly to undeveloped or open areas. As a result, geotechnical engineers are investigating alternative solutions that reduce disruption.

Colloidal silica (CS) has emerged as a promising material in nanotechnology for addressing liquefaction issues (Zhao et al., 2019). The method involves gradually injecting colloidal silica at the upgradient edge of a site, allowing groundwater flow to transport the stabilizer to the intended location (Gallagher et al., 2007b) (Figure 7.7). Applying improvement materials to the desired area is a critical consideration in terrains without natural slopes. Therefore, CS, which has a viscosity very close to that of water and excellent permeability, is a highly suitable material for this process.

Sodium silicate (commonly known as waterglass) grout, despite its chemical similarity to colloidal silica (CS), exhibits a distinct behavior known as syneresis, where the gel undergoes shrinkage accompanied by the expulsion of water (Yonekura & Kaga, 1992). In contrast, colloidal silica does not display this property. Sodium silicate is typically used at 38% solids with a viscosity of 200 centipoise and requires dilution to achieve sufficient flowability for grouting. In contrast, colloidal silica can be used at up to 50% solids by weight while maintaining a much lower viscosity of around 5 centipoises, allowing for easier application and making it more stable. It is a reliable option for long-term soil stabilization.

The application of colloidal silica grout significantly enhances the deformation resistance of loose sand under cyclic loading conditions (Gallagher et al., 2002). This method provides innovative stabilization by preventing pore water pressure buildup during seismic events. CS is economically viable, minimally intrusive, and environmentally friendly, with numerous advantages in soil treatment. It is particularly effective in "passive site stabilization," a relatively novel approach introduced by Gallagher in 2002, characterized by in situ reinforcement with minimal disturbance. Colloidal silica strengthens soil by infiltrating pore spaces and forming a stabilizing

gel that helps reduce ground displacement during seismic activities. Thus, it is an essential resource in geotechnical engineering for enhancing liquefaction resistance.

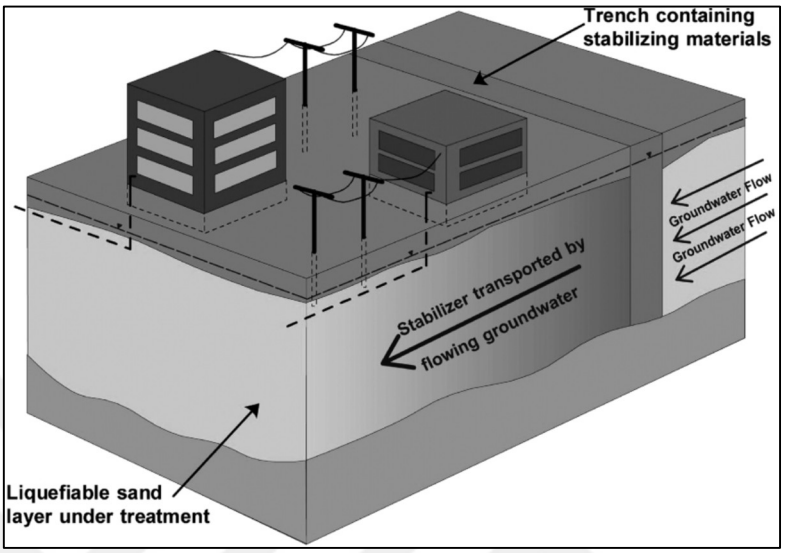

Figure 7.7 Passive site stabilization concept (Gallagher et al., 2002)

7.3.1 Physical Properties of Colloidal Silica

Colloidal silica consists of an aqueous suspension of silica nanoparticles (Iler, 1979), with particle sizes ranging from 7 to 22 nanometers derived from silicic acid solutions. Its low viscosity resembles that of water. Strong interparticle interactions lead to elevated ionic strengths that influence the gelation process; factors such as particle size, ionic strength, pH levels, and silica concentration can affect the duration of gelation (Persoff et al., 1998; Gallagher & Mitchell, 2002; Gallagher et al., 2007; Zhao et al., 2019). The silica molecules possess a polymeric spherical structure with negatively charged surfaces (Spencer et al., 2008) (Figure 7.8).

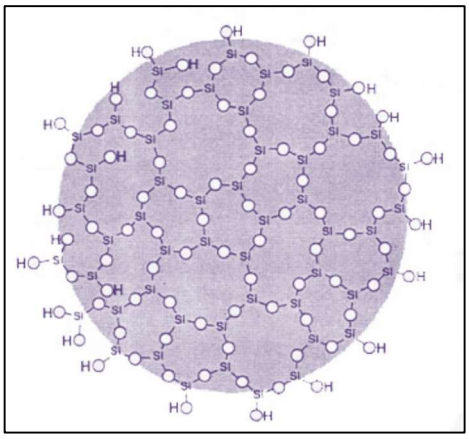

Figure 7.8 Colloidal silica particle illustration (Silco International, 2005)

7.3.2 Mechanism

Colloidal silica functions by uniformly dispersing nanoscale silica particles within water while remaining stable under specific conditions; otherwise, the particles remain fluid. Alkaline solutions like sodium hydroxide stabilize colloidal silica solutions and control premature gelation. These solutions interact with particle surfaces, imparting negative charges that enhance repulsion between particles and effectively inhibit gel formation (Figure 7.9a). Although hydroxyl ions from alkaline solutions can encourage gel formation, maintaining high pH levels ensures stability due to strong particle charges inhibiting rapid reactions at elevated pH levels; however, when pH falls below five, diminishing hydroxyl ion presence, the particles lose their charge, leading toward siloxane bond formation (Figure 7.9b). The fastest gel times occur when pH is maintained between 5 and 6; if it drops below this threshold due to loss of hydroxyl ions, as illustrated in Figure 7.9c, positive charges are created when H_2O^+ ions adhere to the particle surfaces. The particles lose their charge, which slows down siloxane bond formation and extends the gelation time.

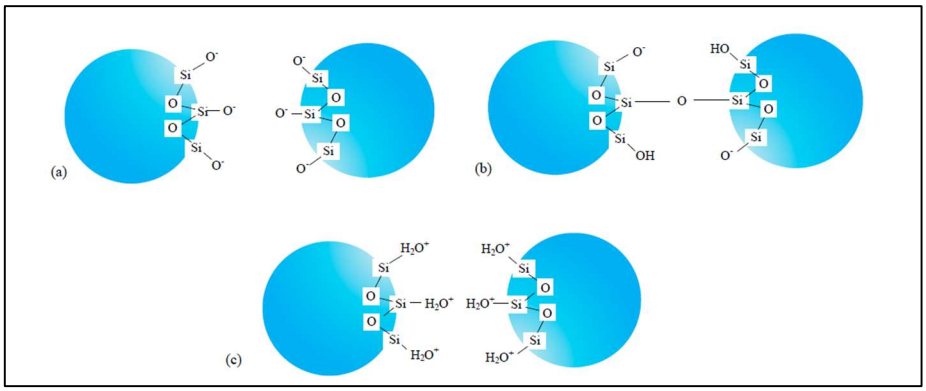

Figure 7.9 Surface charge of silica particles for the cases of different pH values; (a) pH> 8, O^- on the particle surface and repulsive forces, (b) 5≤pH≤8, some particles still have negative charges, (c) pH<5, H_2O^+ ions attach to the particle surfaces (Zhao et al., 2019)

In their study, Wong et al. prepared a colloidal silica (CS) sample using Meyco MP320, which has a silica concentration of 40% by weight. Colloidal silica grouting consists of a colloidal silica suspension and an electrolyte. As shown in Figure 7.10a, the mixture's viscosity initially remains low. However, the viscosity increases rapidly after about one hour, triggering the gelling process, as depicted in Figure 7.10b. Ultimately, a network of nanoparticles is formed, resulting in a solid gel within approximately two hours, as illustrated in Figure 7.10c.

(a) (b) (c)

Figure 7.10 Gelling mechanism (a) before gelling, (b) during gelling (c) after gelling (Wong et al., 2018)

7.3.3 Literature Review

The application of colloidal silica as a ground improvement technique to mitigate liquefaction has grown exponentially as a subject of study in recent decades. This section aims to compile a comprehensive assessment of existing scholarly work examining the effectiveness and usage of colloidal silica for soil stabilization and increasing liquefaction resistance.

Countless experiments have explored the complex interactions by which colloidal silica mingles with particulate matter, enhancing their cohesion and overall integrity. Initial applications of colloidal silica focused primarily on its capacity to reduce fluid transmission by lowering hydraulic conductivity (Durmusoglu & Corapcioglu, 2000) and for immobilizing contaminants (Noll et al., 1993; Persoff et al., 1999). Since then, the technique has evolved considerably, with proliferating research investigating diverse injection methods, required dosages, and soil types.

This review surveys the significant contributions to the field, discussing pivotal methodologies, conclusions, and advancements. It also pinpoints gaps in the literature and proposes potential lines of future inquiry to fully leverage colloidal silica's potential in mitigating risks associated with liquefaction.

7.3.3.1 Rosenfarb and Hackman Study (1981)

In their 1981 study, Rosenfarb and Hackman stabilized the sand with colloidal silica at varying ratios (30% to 45%) and conducted drained static and dynamic triaxial tests. The results from the drained-static triaxial tests illustrate the effect of increasing sodium silicate concentration on static strength. As the silica content in the grout rises, the peak strength also increases. The confinement effect was also investigated and positively influenced static strength (Figure 7.11). Additionally, the confined samples failed at axial strains between 3% and 5%, while the unconfined samples failed at approximately 1.5% axial strain (Figure 7.12). Similar to static loading, under dynamic

loading conditions, specimens showed increasing strength with higher sodium silica percentages. However, dynamic strengths for unconfined stage loading tests are 70-570 kPa and 90-550 kPa in continuous loading tests, which is relatively low when compared to static strength. The corresponding strength values for the confined stage are 380-800 kPa in stage loading and 410-650 kPa in continuous loading.

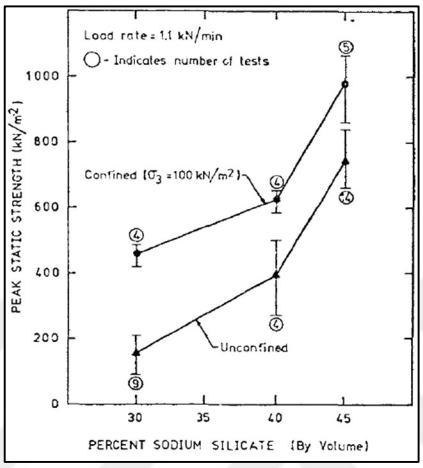

Figure 7.11 Variation of peak static strength with silica content (Rosenharb & Hackman, 1981)

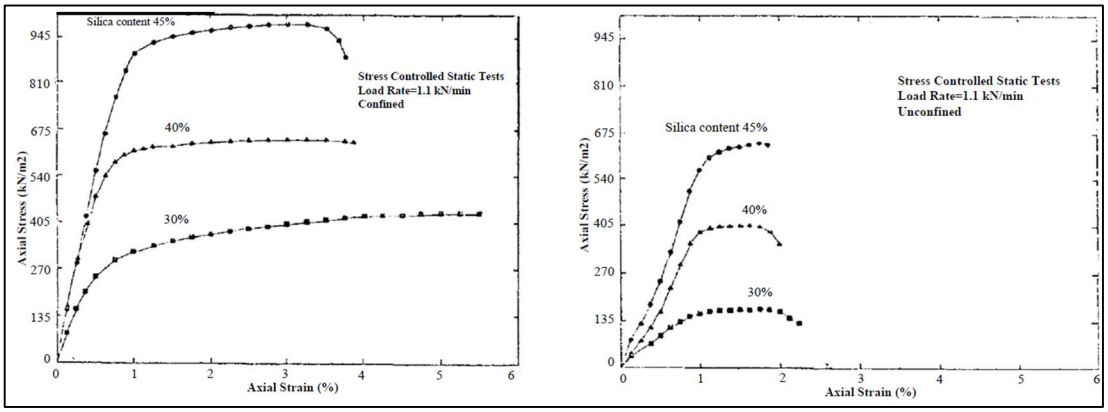

Figure 7.12 Static stress-strain response: confined and unconfined (Rosenharb & Hackman, 1981)

7.3.3.2 Gallagher and Mitchell Study (2002)

In the study conducted by Gallagher and Mitchell (2002), triaxial tests were performed on samples injected with colloidal silica (CS) at concentrations of 5%, 10%,

15%, and 20%. The study used Monterey Sand#0/30 (SP) to analyze the most liquefiable soil class according to grain size distribution. Additionally, unconfined compression tests were conducted on some specimens before and after cyclic triaxial testing to compare baseline and residual strength. Figure 7.13 reveals that specimens containing higher silica concentrations accumulate less axial strain during the dynamic loading. As shown in the Figure, samples with 15%-20% CS show very little strain, whereas samples with 5% CS experience up to 12% strain, but they all remain intact after the test. Figure 7.14 shows untreated and treated samples (with 5% CS) of axial strain development with cycles. As clearly shown in the figure, although the untreated sample exhibits only a negligible amount of strain initially, it suddenly undergoes deformation exceeding 5% once liquefaction begins. Its deformation abruptly increased from 2% to around 7% during the last three cycles, leading to failure in the thirteenth cycle. These findings suggest that about a 5-10% CS rate is performed well to mitigate liquefaction risk. Although it exhibits some deformation, the permanent deformations remain limited, and the sample remains intact. They have stated that increasing the percentage further is not economically feasible.

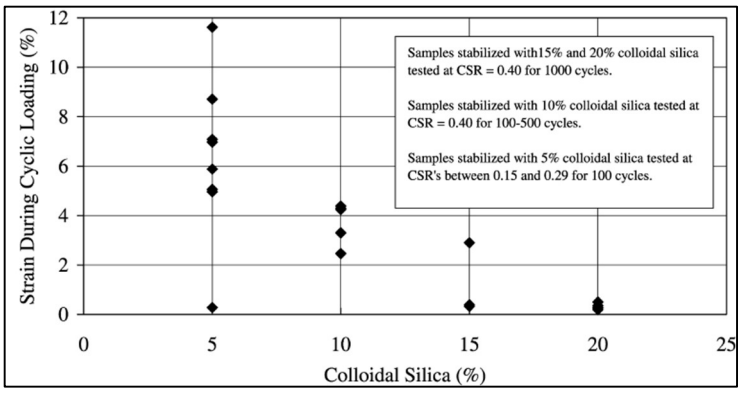

Figure 7.13 Colloidal silica versus strain during cyclic loading (Gallagher & Mitchell, 2002)

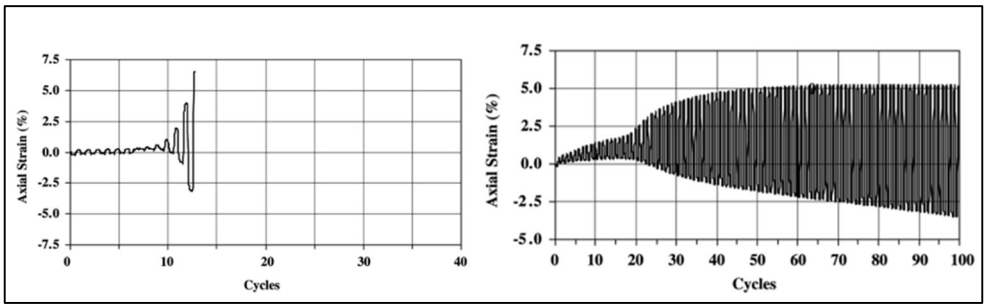

Figure 7.14 Untreated Monterey sand (CSR:0.27) and treated sand (CSR:0.24) axial strain vs cycles (Gallagher & Mitchell, 2002)

Gallagher and Mitchell also investigated the effect of aging on the cyclic loading test. Figure 7.15 highlights that the longer the curing time, the less deformation occurs under dynamic loading.

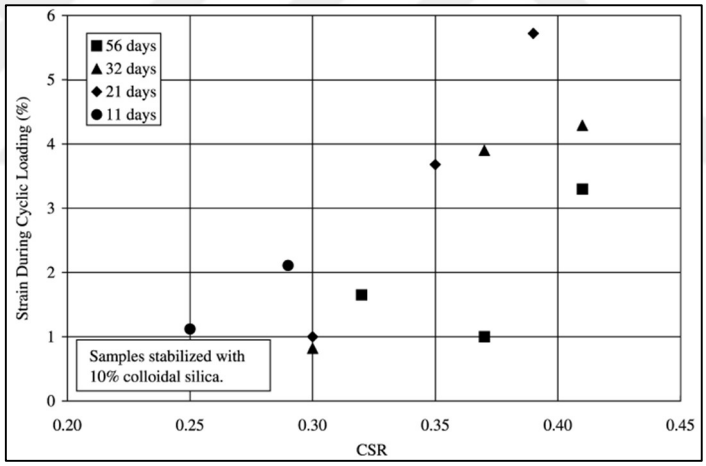

Figure 7.15 Strain during cyclic loading for 10% CS Samples with different curing time (Gallagher & Mitchell, 2002)

7.3.3.3 Liao et al. Study (2003)

In this study, Liao et al. conducted experiments on sand specimens collected from the Taiwanese coastline, which was affected by liquefaction during the Chi-Chi earthquake. The sand used in these experiments had a relative density of 50% and was classified as SP. To stabilize the sand, Perma Rock AT-30 grout, a type of colloidal

silica, was applied. This grout was used to treat the sand samples, and the researchers examined its impact on the soil's properties under different testing conditions. Using unconfined compression tests, they examined the curing effect and observed an increase in strength from 113 kPa on the 7th day to 141 kPa on the 28th day, as shown in Figure 7.16. Furthermore, cyclic triaxial tests on untreated and treated soils showed that the number of cycles and cyclic stress ratio needed to induce liquefaction was 4 to 7 times larger in treated specimens (Figure 7.17). Double amplitude strain reduction from 16% in the untreated samples to 10% in the treated samples cured for 28 days indicated that the liquefaction-induced strain in ungrouted sand was more tremendous by a factor of 1.6 over that in the grouted sample.

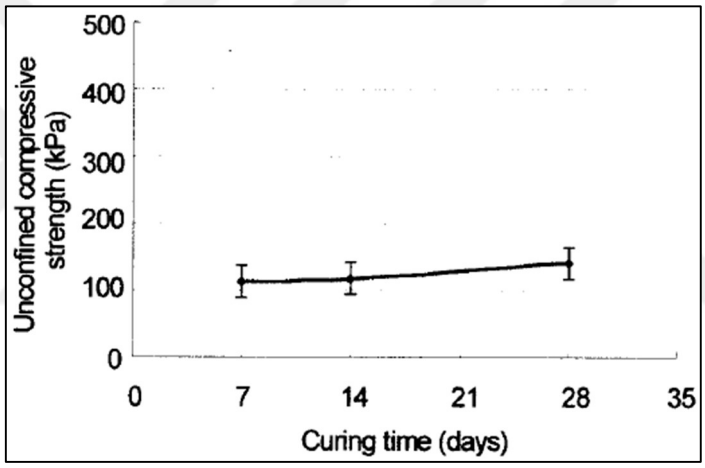

Figure 7.16 Strain during cyclic loading for 10% CS samples with different curing time (Liao et al., 2003)

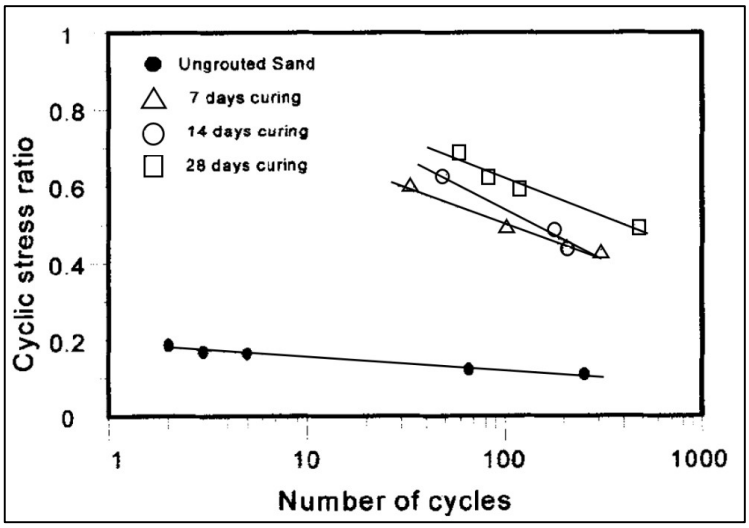

Figure 7.17 Comparison of liquefaction resistance between untreated sand and treated sand at various curing durations (Liao et al., 2003)

7.3.3.4 Gallagher et al. Study (2007)

In their study, Gallagher et al. investigated the effectiveness of colloidal silica in reducing post-liquefaction settlement in the field. The liquefiable layer of sand is classified as SP or SP-SM with 40-45% relative density. Ludox SM-30 colloidal silica was used and a 2-meter-thick sand layer was treated by injecting colloidal silica through circular injection wells, with extraction performed at the center to enhance the improvement effect.

A colloidal silica solution with an 8% concentration was prepared and injected into the target area. Controlled blasting was conducted near the injection wells to induce liquefaction. The results showed that while the untreated area experienced a settlement of 0.5 meters, the treated area exhibited a reduced settlement of 0.3 meters (Figure 7.18), demonstrating the effectiveness of the treatment. Even though liquefaction (r_u = 1) occurred in both, this improvement is believed to be due to the colloidal silica infiltrating the sand particles, forming a bonding agent, and enhancing the strength properties.

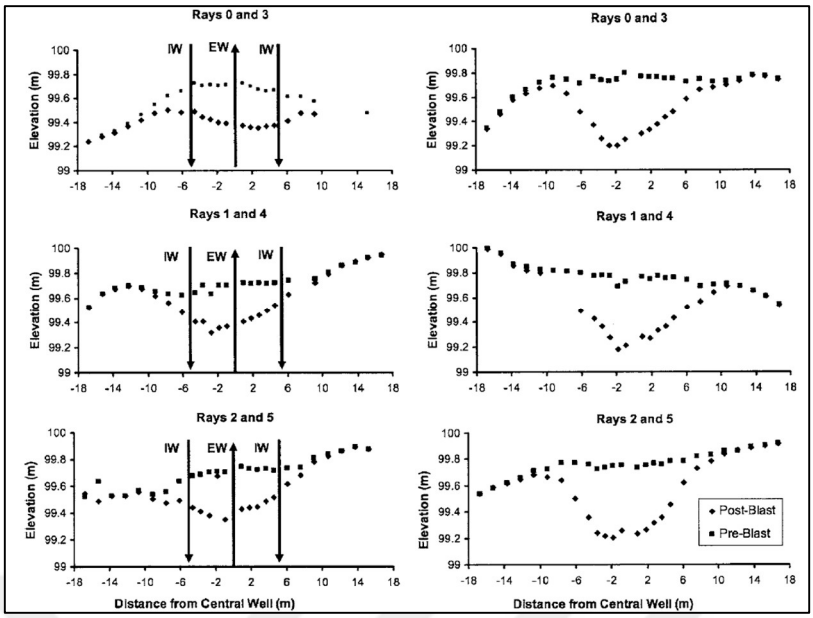

Figure 7.18 Observed settlements in treated and untreated zones (Gallagher et al., 2007)

7.3.3.5 Spencer et al. Study (2008)

This experimental study evaluates the effects of colloidal silica gel on shear modulus and damping ratio, considering cyclic shear strain and aging. No. 120 Nevada Sand (SP) (D_r=50%) was treated with 5% and 9% colloidal silica (Ludox SM-30), and resonant column tests were performed to compare the dynamic parameters of the treated soil with those of untreated soil.

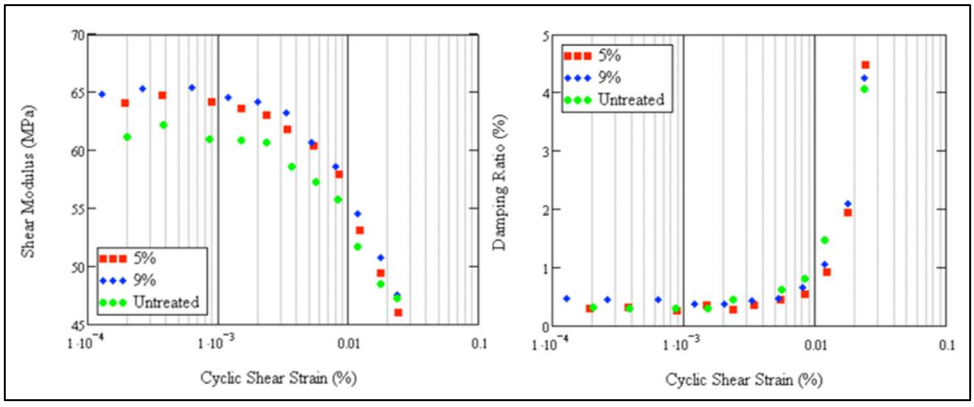

Figure 7.19 Dynamic properties comparison: shear modulus and damping ratio of treated and untreated samples (Spencer et al., 2007)

The shear modulus, in Figure 7.19, is marginally affected by the increasing content of colloidal silica at lower strain levels. However, this effect decreases with increasing strain and plateaus at higher strain values, with no change being observed. The impact of grouting on the damping ratio is minimal, showing minor alteration with changing quantities of colloidal silica in the treatment. This indicates that the colloidal modification of soil potentially increases the stiffness of the soil under low-strain conditions. Still, it does not run groundbreaking changes to the energy dissipation of the soil under constant amplitude cyclic loading.

Moreover, the aging effect on the shear modulus change has been analyzed. Pea-gravel and sand-silica grout samples were monitored at intervals for 28 days. The results of the tests performed during the 28 days of curing indicated that shear strength increased by about 6 MPa.

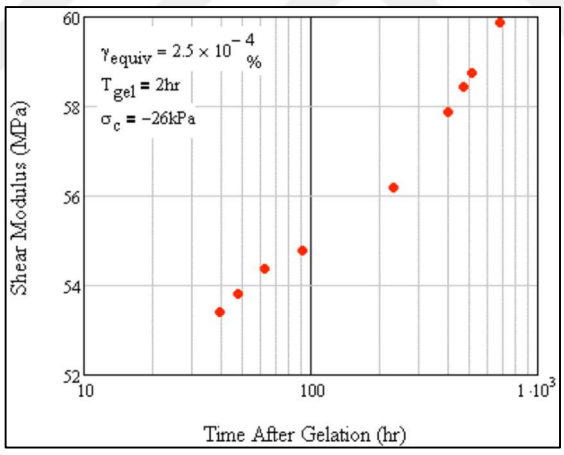

Figure 7.20 Change in shear modulus of 5% CS sample over a 28-day aging period (Spencer et al., 2007)

7.3.3.6 Mahmutoğlu & Yılmaz Study (2010)

In this study, Mahmutoğlu and Yılmaz prepared samples with colloidal silica grout incorporating saline solution at weight ratios ranging from 10% to 25%. The effect of salt concentration in the saline solution on the gelation time was investigated and it

was concluded that the presence of salt shortened the gelation time. The study utilized MEYCO MP 320 silica, and the sand to be improved was classified as SP (Silica Sand). Based on the particle size distribution, it was found that the sand falls into the most liquefiable region.

It can be seen from Figure 7.21 that before dynamic loading, it was observed that the unconfined compression strengths of all samples increased over time with curing. However, no significant increase was observed after one year. In grouts prepared at 20%-25% concentrations, a decrease in unconfined compression strengths was observed after cyclic loading. However, this loss was approximately 10%, which is relatively small, and the strength did not drop to the untreated condition even at a CSR of 0.5.

The grouted specimens were exposed to cyclic loading with CSR values ranging from approximately 0.1 to 0.5 and applied in a sinusoidal pattern for 1000 cycles. The loss of strength in colloidal silica grouted sand after 1000 cycles was minimal, around 10%. These results demonstrate the excellent performance of colloidal silica grouts in resisting cyclic deformation.

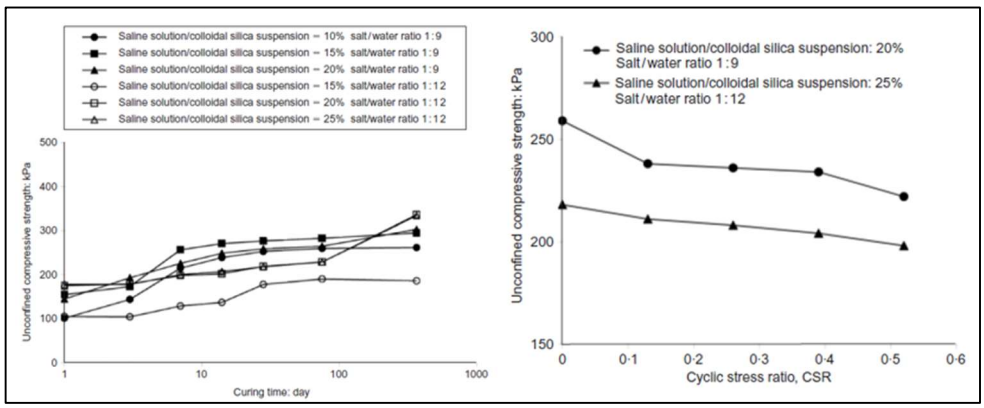

(a) (b)

Figure 7.21 Unconfined compression test (a) before and (b) after cyclic loading (Mahmutoğlu & Yılmaz, 2010)

7.3.3.7 Krishnan et al. Study (2020)

A poorly graded sand was used for the soil in the analysis, and Dupont Ludox SM was selected as grout. Samples containing 7.5%, 10%, 15% and 30% silica were prepared. Samples were treated with three different ratios, and the relative density of the treated samples was observed while the curing time for C5-SM-30, C5-SM-40, and C5-SM-60 was 3 days, 7 days, and 28 days, respectively. Undrained static triaxial tests and undrained consolidated cyclic triaxial tests test were performed. Results of unconsolidated undrained static triaxial tests of sand treated with different colloidal silica % show that the curing time significantly affected the maximum strength, which increased from 3 to 28 days of curing. Increasing the colloidal silica to 15% enhances both cohesion and the internal friction angle. However, beyond this point, higher amounts of colloidal silica reduce these values. Such behavior indicates the ideal concentration of colloidal silica, after which the positive influence on the soil's mechanical properties decreases.

The results of failure axial strains at varying confining pressures and relative densities, as a function of colloidal silica percentages, are presented in Figure 7.22.Up to a certain colloidal silica percentage, axial deformations increased; however, beyond that point, they decreased. This behavior is comparable to that of dense sand, indicating brittle failure. The maximum failure strains were observed at colloidal silica percentages of approximately 10% to 15% for all three relative densities, which corresponding to the point where cohesion values peak. Additionally, it was observed that failure strain increases with the increasing confining pressure.

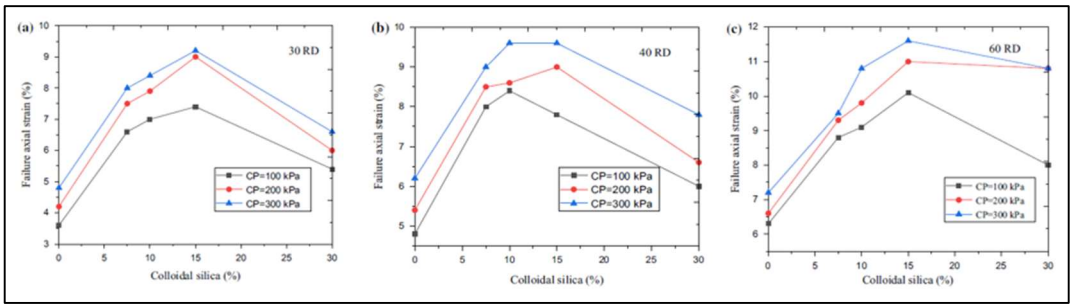

Figure 7.22 Impact of colloidal silica content on axial strain at different confining pressures (relative density: 30%, 40%, 60%) (Krishnan et al., 2020)

Figure 7.23 compares the hysteresis response of untreated sand and sand treated with 11% colloidal silica (CS), both having a relative density of 40%. For the untreated sand, deviatoric stress significantly decreased immediately after the first cycle, indicating strength loss and liquefaction. With each successive cycle, the curve progressively flattened due to increased pore pressure causing a loss of contact between sand grains. In contrast, the treated sand exhibited enhanced stability, demonstrating that the colloidal silica filled the voids between sand grains and developed frictional resistance. While the response resembled elastic behavior, it was asymmetrical, with the treated sand bearing more load during compression.

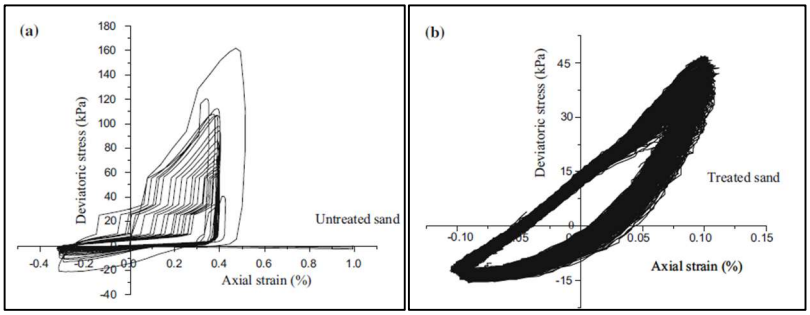

Figure 7.23 Hysteresis response during cyclic loading (a) untread sand, (b) treated sand (Krishnan et al., 2020)

Figure 7.24 illustrates the development of pore pressure and axial strain in untreated and treated sand during cyclic loading. In untreated sand, excess pore water pressure rapidly reaches adequate consolidation pressure within the first few cycles, resulting

in significant strength loss and permanent deformations. In contrast, the treated sand exhibits a steady and controlled development of pore water pressure, demonstrating improved stability under cyclic loading.

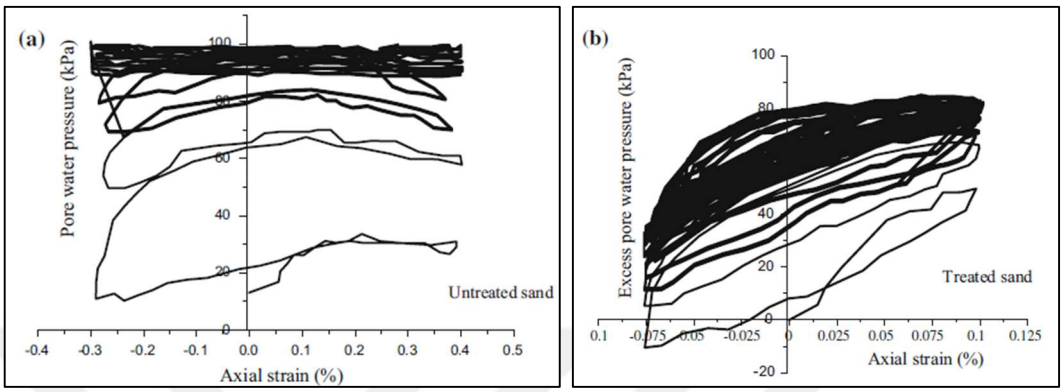

Figure 7.24 Excess pore water pressure vs. axial strain during cyclic loading (a) untread sand, (b) treated sand (Krishnan et al., 2020)

7.3.4 Applicability of the CSM in Konak-Üçkuyular Area

In the region of Konak-Üçkuyular, the soil consists of approximately 25% SP (poorly graded sand) and 55% sandy layers. SP layers contain negligible fine-grained content and thus are highly suitable for CS applications. On the other hand, sandy layers containing 25% fine-grained content may also be considered for this method based on the performance documented in the literature for colloidal silica to improve soil properties. In the previous section, some related studies to assess the method's applicability in the region are summarized.

Considering the regional soil characteristics, colloidal silica seems highly suitable for SP layers because of their negligible fine-grained content. According to the literature, colloidal silica improves the cyclic resistance and stability of sandy soils significantly by the following:

- Axial strain accumulation during dynamic loading is reduced (Gallagher and Mitchell, 2002).

- The number of cycles and CSR required for liquefaction increases (Liao et al., 2003).
- Improvement in soil bonding and settlement reduction under dynamic conditions are reported by Gallagher et al. (2007).

In the case of sandy layers with 25% fines, the application is relevant, as colloidal silica has been shown to be effective even in silty sands (SM) as demonstrated by Krishnan et al. (2020), through the enhancement of pore pressure stability and strain reduction under cyclic loading. Higher concentrations, such as 20-25%, may be required for better performance. These findings align with previous studies regarding applying colloidal silica in the Konak-Üçkuyular region, particularly for SP-dominated layers with an almost negligible fine content. For sandy layers with a moderate fine content, higher concentrations of silica may be needed, but the methodology remains highly effective. Given this liquefaction potential of the area, colloidal silica grouting has proven to be promising in improving seismic performance and reducing the risk of settlement.

In the Konak-Üçkuyular region, applying colloidal silica to sandy layers involves a well-planned injection process aimed at improving liquefaction resistance. The first step is a detailed geotechnical study to understand the soil's permeability and layering. Based on this data, an injection grid is designed to ensure even distribution. The silica is injected at low pressure, allowing it to seep into the soil's pore spaces without disrupting its natural structure. Over time, the silica forms a gel, strengthening the bonds between soil particles, making the ground more resistant to liquefaction. To ensure the process is effective, field monitoring and follow-up tests are carried out, confirming the long-term stability of the treated area.

CHAPTER EİGHT
CONCLUSIONS AND RECOMMENDATIONS

In conclusion, this study examined the liquefaction resistance and post-earthquake settlement along the major coastal highways of the İzmir Bay area, focusing on three segments, Alsancak-Konak, Konak-Üçkuyular and Bayraklı. These highways are critical transportation routes, not only for daily commuting but also for the movement of goods and emergency services, particularly in the aftermath of an earthquake. Their structural integrity is essential for disaster response and maintaining economic stability.

Through GIS-based analysis and geotechnical data, the factors of safety against liquefaction values were interpolated with the 3D Empirical Bayesian Kriging (EBK) tool. These interpolated values were mapped for critical depths of 3m, 5m and 10m. The interpolation maps for safety factors and settlement analysis provide a spatially continuous representation of point-based data, allowing for the identification of high-risk areas prone to liquefaction and associated settlements. The resulting maps help pinpoint high-risk areas susceptible to liquefaction and post-earthquake settlement, offering valuable insights for infrastructure planning and mitigation strategies.

Additionally, post-earthquake settlement values for each borehole were analyzed for earthquakes with magnitudes 6.5 and 5.5 under both scenarios. The findings reveal that areas with FS values below 1.1 are highly susceptible to liquefaction. The results underscore significant vulnerabilities in the region, especially at the DD-2 seismic level, where the risk of liquefaction is widespread across all studied areas. The safety factors (FS) calculated for the sandy soils indicate a higher susceptibility to liquefaction in areas like Bayraklı. Although the safety factor improves at the DD-3 seismic level, some regions still exhibit safety factors below the critical threshold, particularly in the Konak-Üçkuyular and Bayraklı areas.

Post-earthquake settlement analyses revealed critical settlement values in several regions. In particular, the Konak-Üçkuyular and Alsancak-Konak areas show settlement ranges that highlight the potential for significant soil deformation following a major seismic event. The Bayraklı region is identified as the most vulnerable area to liquefaction-induced settlements. The estimated liquefaction values in this major artery indicate that excessive settlement, sliding toward the sea, and loss of bearing capacity are likely. Such hazards could compromise not only road infrastructure but also the overall connectivity of İzmir's transportation network, highlighting the urgent need for intervention. It is strongly recommended that local administrators consider this. The study stresses the need for ground improvement methods to mitigate liquefaction risks and post-earthquake settlements in these regions.

Further mitigation of liquefaction and post-earthquake settlement risks in İzmir Bay requires the enhancement of infrastructure for geotechnical data by increasing the number and quality of borehole logs and records of soil properties. Such a comprehensive database would provide a better basis for accurate modeling and risk assessment.

Key recommendations for reducing liquefaction and post-earthquake settlement risks in İzmir Bay include:

- Enhancing the Geotechnical Database: Expanding borehole data collection and improving soil characterization to refine hazard assessments and infrastructure planning.
- Developing High-Resolution Liquefaction Hazard Maps: These maps would aid urban planning, zoning regulations, and emergency response efforts, ensuring the development of resilient infrastructure.
- Implementing Ground Improvement Techniques: Methods such as dynamic compaction and colloidal silica grouting should be applied in high-risk areas like Bayraklı and Konak-Üçkuyular to reduce liquefaction susceptibility and enhance soil stability.

- Integrating Post-Earthquake Settlement Analysis into Infrastructure Design: Incorporating settlement assessments during the planning and construction phases would help anticipate soil deformations and mitigate their impact on roads, bridges, and other lifeline systems.
- Strengthening Emergency Response and Transportation Planning: Since major highways play a crucial role in disaster relief and supply chain continuity, reinforcing critical road sections against seismic hazards should be a priority. Alternative routes and emergency response plans should also be developed to ensure accessibility after an earthquake.
- Promoting Public Awareness and Professional Training: Educating engineers, policymakers, and local authorities on liquefaction risks and mitigation strategies is essential for fostering a proactive approach to disaster resilience.

In addition, alternative routes should be considered in case these highways become unusable due to liquefaction, or ground improvement techniques can be applied as a preventive measure. The most important step is to establish and expand developing and growing geotechnical databases. This includes updating the borehole data and enriching it by creating a scalable and sustainable database that can evolve over time.

By implementing these measures, İzmir Bay's major highways can be better protected against liquefaction and post-earthquake settlement, ensuring their functionality in both everyday use and emergency situations. Strengthening these transportation corridors is not only an infrastructure priority but also a crucial step in safeguarding public safety, minimizing economic losses, and maintaining the reliability of vital transportation networks in the face of future seismic events.

REFERENCES

Akhtar, S. (2018). *Dynamic compaction*. Springer.

Bolton Seed, H., Tokimatsu, K., Harder, L. F., & Chung, R. M. (1985). Influence of SPT procedures in soil liquefaction resistance evaluations. *Journal of geotechnical engineering*, *111*(12), 1425-1445.

Boulanger, R. W., & Idriss, I. M. (2004). Evaluating the potential for liquefaction or cyclic failure of silts and clays (p. 131). Davis, California: Center for Geotechnical Modeling.

Bozkurt, E. (2001). Neotectonics of Türkiye—a synthesis. *Geodinamica Acta, 14*(1-3), 3-30.

Bray, J. D., et al. (2004a). "Subsurface characterization at ground failure sites in Adapazari, Türkiye." J. Geotech. Geoenviron. Eng., 130(7), 673–685.

Bray, J. D., Sancio, R. B., Riemer, M. F., and Durgunoglu, T. (2004b) ."Liquefaction susceptibility of fine-grained soils." Proc., 11th Int. Conf. On Soil Dynamics and Earthquake Engineering and 3rd Int. Conf. On Earthquake Geotechnical Engineering, Stallion Press, Berkeley, Calif., Vol. 1, 655–662.

Bray, J. D., Sancio, R. B., Durgunoglu, T., Onalp, A., Youd, T. L., Stewart, J. P., Seed, R. B., Cetin, K. O., Bol, E., Baturay, M. B., and Christensen, C. (2004). "Subsurface Characterization at Ground Failure Sites in Adapazari, Türkiye." Journal of Geotechnical and Geoenvironmental Engineering, submitted.

Castro, G. (1969). ''Liquefaction of sands,'' PhD thesis, Division of Engineering and Applied Physics, Harvard University, Cambridge, Mass.

Cetin, K. O., Seed, R. B., Der Kiureghian, A., Tokimatsu, K., Harder, L. F., Kayen, R. E., and Moss, R.E. S. (2004). Standard penetration test-based probabilistic and deterministic assessment of seismic soil liquefaction potential, *J. Geotechnical and Geoenvironmental Eng.*, ASCE 130(12), 1314–340.

Coskun, S., Dondurur, D., Cifci, G., Aydemir, A., Gungor, T., & Drahor, M. G. (2017). Investigation on the tectonic significance of Izmir, Uzunada Fault Zones and other tectonic elements in the Gulf of Izmir, western Türkiye, using high-resolution seismic data. Marine and Petroleum Geology, 83, 73-83.

Dashti, S., Bray, J. D., Pestana, J. M., Riemer, M., & Wilson, D. (2010). Centrifuge testing to evaluate and mitigate liquefaction-induced building settlement mechanisms. Journal of geotechnical and geoenvironmental engineering, 136(7), 918-929.

Durmusoglu, E., & Corapcioglu, M. Y. (2000). Experimental study of horizontal barrier formation by colloidal silica. Journal of Environmental Engineering, 126(9), 833-841.

Finn, W. D. (1981). Liquefaction potential: developments since 1976.

Gallagher, P. M., & Mitchell, J. K. (2002). Influence of colloidal silica grout on liquefaction potential and cyclic undrained behavior of loose sand. Soil Dynamics and Earthquake Engineering, 22(9-12), 1017-1026.

Gallagher, P. M., Pamuk, A., & Abdoun, T. (2007). Stabilization of liquefiable soils using colloidal silica grout. Journal of Materials in Civil Engineering, 19(1), 33-40.

Gallagher, P. M., Conlee, C. T., & Rollins, K. M. (2007). Full-scale field testing of colloidal silica grouting for mitigation of liquefaction risk. Journal of geotechnical and geoenvironmental engineering, 133(2), 186–196.

Görür, N., Monod, O., & Okay, A. I. (1995). Miocene to Pliocene palaeogeographic evolution of Türkiye and its surroundings. *Journal of Human Evolution, 28*(4), 339-361.

Idriss, I. M., & Boulanger, R. W. (2008). Soil liquefaction during earthquakes. Earthquake Engineering Research Institute.

Idriss, I. M., & Boulanger, R. W. (2010). SPT-based liquefaction triggering procedures. *Rep. UCD/CGM-10*, *2*, 4-13.

Iler, R. K. (1979). The chemistry of silica, Solubility, Polymerization. Colloid and Surface Properties, and Biochemistry, 866.

Ishihara K, . (1985). "Stability of natural deposits during earthquakes," Proceedings, 11th International Conference on Soil Mechanics and Foundation Engineering, Vol. 1, pp. 321-376.

Ishihara, K., & Yoshimine, M. (1992). Evaluation of settlements in sand deposits following liquefaction during earthquakes. *Soils and foundations*, *32*(1), 173-188.

Ishihara K,. (1993). Liquefaction and flow failure during earthquakes, Geotechiziq~~Veo, l. 43,No. 3,pp. 351-415.

Jolivet, L. (2001). A comparison of geodetic and finite strain pattern in the Aegean, geodynamic implications. *Earth and Planetary Science Letters, 187*(1-2), 95-104.

Kammerer, A. M. (2002). *Undrained response of Monterey 0/30 sand under multidirectional cyclic simple shear loading conditions*. University of California, Berkeley.

Kishida, H. (1969). Characteristics of liquefied sands during Mino-Owari, Tohnankai and Fukui earthquakes. Soils and Foundations, 9(1), 75-92.

Koçyiğit, A. & Özacar, A.A. 2003. Extensional neotectonic regime through the NE edge of the Outer Isparta Angle, SW Türkiye: new field and seismic data. Turkish Journal of Earth Sciences 12, 67–90.

Krishnan, J., Sharma, P., Shukla, S., Pancholi, V., & Dwivedi, V. K. (2020). Cyclic behaviour and durability analysis of sand grouted with optimum colloidal silica content. Arabian journal for science and engineering, 45, 8129-8144.

Lee, K. L., & Albaisa, A. (1974). Earthquake induced settlements in saturated sands. *Journal of the Geotechnical Engineering Division*, *100*(4), 387-406.

Liao, H. J., Huang, C. C., & Chao, B. S. (2003). Liquefaction resistance of a colloid silica grouted sand. In Grouting and ground treatment (pp. 1305-1313).

Lukas, R. (1995). Geotechnical engineering circular No. 1-dynamic compaction (No. FHWA-SA-95-037). United States. Federal Highway Administration. Office of Technology Applications.

Matsuda, H., Shinozaki, H., Okada, N., Takamiya, K., & Shinyama, K. (2004, August). Effects of multi-directional cyclic shear on the post-earthquake settlement of ground. In 13th world conference on earthquake engineering (Vol. 2890). 13 WCEE Secretariat, Vancouver, Canada.

Matsuda, H., Hendrawan, A. P., Ishikura, R., & Kawahara, S. (2011). Effective stress change and post-earthquake settlement properties of granular materials subjected to multi-directional cyclic simple shear. *Soils and foundations*, *51*(5), 873-884.

Menard, L., & Broise, Y. (1975). Theoretical and practical aspect of dynamic consolidation. Geotechnique, 25(1), 3-18.

Mitchell, J. K. (1976). Fundamentals of Soil Behavior. John Wiley & Sons Inc., p 319.

Mogami, T., and Kubu, K. (1953). The behavior of soil during vibration, Proceedings, 3rd International Conference on Soil Mechanics and Foundation Engineering, Zurich, Vol. l, pp. 152-155.

Mollamahmutoglu, M., & Yilmaz, Y. (2010). Pre- and post-cyclic loading strength of silica-grouted sand. Proceedings of the Institution of Civil Engineers-Geotechnical Engineering, 163(6), 343-348.

Moradi, G., Seyedi, S., Moradi, G., & Seyedi, S. (2015). Effect of sampling method on strength of stabilized silty sands with colloidal nano silica. J Civ Eng Res, 5(6), 129-135.

National Research Council. (1985). Liquefaction of soils during earthquakes. National Academy Press.

Nicholson, P. G. (2014). Soil improvement and ground modification methods. Butterworth-Heinemann.

Noll, M. R., Epps, D. E., Bartlett, C. L., & Chen, P. J. (1993, May). Pilot field application of a colloidal silica gel technology for in situ hot spot stabilization and horizontal grouting. In Proc., 7th National Outdoor Action Conf (pp. 207-219).

Ozbey and Gunes Golbey / Turkish Journal of Forest Science 5(2) 2021: 551-561

Persoff, P., Apps, J., Moridis, G., & Whang, J. M. (1999). Effect of dilution and contaminants on sand grouted with colloidal silica. Journal of geotechnical and geoenvironmental engineering, 125(6), 461-469.

Rosenfarb, J. L., & Hackman, R. E. (1981). The cyclic loading behavior of grouted sand.

Sancio, R. B. (2003). “Ground Failure and Building Performance in Adapazari, Türkiye”, Ph.D. Dissertation (in progress), supervised by Prof. J.D. Bray, University of California, Berkeley.

Seed. H.B. and Idriss, I.M. (1971). "Simplified procedure for evaluating soil liquefaction potential," Journal of the Soil Mechanics and Foundations Division, ASCE, Vol. 107, No. SM9, pp. 1249-1274.

Seed, H. B. (1979) "Soil liquefaction and cyclic mobility evaluation for level ground during earthquakes." Journal of the geotechnical engineering division 105.2: 201-255.

Seed, H. B., and Idriss, I. M. (1982). “Ground motions and soil liquefaction during earthquakes.” EERI Monograph, Berkeley, Calif.

Seed, H. B., Idriss, I. M. and Arango, I. (1983). Evaluation of Liquefaction Potential Using Field Performance Data. Journal of Geotechnical Engineering, Vol. 109, No. GT3, pp 458-482.

Seed, R. B., Cetin, K. O., Moss, R. E. S., Kammerer, A. M., Wu, J., Pestana, J. M., & Reimer, M. F. (2001). Recent advances in soil liquefaction engineering and seismic site response evaluation.

Seed, R. B., Cetin, K. O., Moss, R. E., Kammerer, A. M., Wu, J., Pestana, J. M., ... & Faris, A. (2003). Recent advances in soil liquefaction engineering: a unified and consistent framework. In Proceedings of the 26th Annual ASCE Los Angeles Geotechnical Spring Seminar: Long Beach, CA.

Shamoto, Y., Zhang, J. M., & Tokimatsu, K. (1998). Methods for evaluating residual post-liquefaction ground settlement and horizontal displacement. *Soils and Foundations*, *38*, 69-83.

Silco International. (2005). "Colloidal Silica Technical Information." Silco International, LLC, Portland, OR, http://www.silco-intl.com/technical/index.html.

Sözbilir, H. (2002). Revised stratigraphy and facies of the Upper Cretaceous-Lower Tertiary sequences in the southern part of the Menderes Massif, western Türkiye. *Geodinamica Acta, 15*(1), 1-21.

Spencer, L., Rix, G. J., & Gallagher, P. (2008). Colloidal silica gel and sand mixture dynamic properties. In Geotechnical earthquake engineering and soil dynamics IV (pp. 1-10).

Tatsuoka, F., Sasaki, T. and Yamada, S. (1984): Settlements in saturated sand induced by cyclic undrained simple shear, Proc. 8th.

Tohno, I., & Yasuda, S. (1981). Liquefaction of the ground during the 1978 Miyagiken-Oki earthquake. Soils and Foundations, 21(3), 18-34.

Tokimatsu, K., & Seed, H. B. (1987). Evaluation of settlements in sands due to earthquake shaking. *Journal of geotechnical engineering*, *113*(8), 861-878.

Tokimatsu, K., & Asaka, Y. (1998). Effects of liquefaction-induced ground displacements on pile performance in the 1995 Hyogoken-Nambu earthquake. *Soils and Foundations*, *38*, 163-177.

Tsukamoto, Y., Ishihara, K., & Sawada, S. (2004). Settlement of silty sand deposits following liquefaction during earthquakes. *Soils and Foundations*, *44*(5), 135-148.

Uzel, B., Sözbilir, H., & Özkaymak, Ç. (2012). Neotectonic evolution of an actively growing superimposed basin in western Anatolia: The inner bay of Izmir, Türkiye. *Turkish Journal of Earth Sciences*, *21*(4), 439-471.

Wang, W. (1979). Some findings in soil liquefaction, Water Conservancy and Hydroelectric Power Scientific Research Institute, Beijing, China.

Wong, C., Pedrotti, M., El Mountassir, G., & Lunn, R. J. (2018). A study on the mechanical interaction between soil and colloidal silica gel for ground improvement. Engineering geology, 243, 84-100.

Wu, J. (2002). *Liquefaction triggering and post-liquefaction deformation of Monterey 0/30 sand under unidirectional cyclic simple shear loading*. University of California, Berkeley.

Wu, J., & Seed, R. B. (2004). Estimation of liquefaction-induced ground settlement (case studies).

Yonekura, R., & Kaga, M. (1992). Current chemical grout engineering in Japan. In Grouting, soil improvement and geosynthetics (pp. 725-736). ASCE.

Yoshimi, Y., Kuwabara, F., & Tokimatsu, K. (1975). One-dimensional volume change characteristics of sands under very low confining stresses. *Soils and Foundations*, *15*(3), 51-60.

Youd, T. L., & Craven, T. N. (1975). Lateral stress in sands during cyclic loading. *Journal of the Geotechnical Engineering Division*, *101*(2), 217-221.

Yoshimi, Y., & Tokimatsu, K. (1977). Settlement of buildings on saturated sand during earthquakes. Soils and Foundations, 17(1), 23-38.

Youd, T. L. (1984b). Geologic effects—Liquefaction and associated ground failure. In Proceedings of the Geologic and Hydrologic Hazards Training Program (pp. 210-232). Open-File Report 84-760. U.S. Geological Survey.

Youd, T. L., & Idriss, I. M. 1997,'Summary report.' Proc., NCEER Workshop on Evaluation of Liquefaction Resistance of Soils, Tech. Rep. NCEER-97-0022, National Center for Earthquake Engineering Research, Buffalo,

Youd, T. L., & Idriss, I. M. (2001). Liquefaction resistance of soils: summary report from the 1996 NCEER and 1998 NCEER/NSF workshops on evaluation of liquefaction resistance of soils. *Journal of geotechnical and geoenvironmental engineering*, *127*(4), 297-313.

Youd, T. L. (2003). Liquefaction mechanisms and induced ground failure. In W. H. K. Lee, H. Kanamori, P. C. Jennings, & C. Kisslinger (Eds.), International Geophysics (Vol. 81, Part B, pp. 1159-1173).

Zhao, M., Liu, G., Zhang, C., Guo, W., & Luo, Q. (2019). State-of-the-art of colloidal silica-based soil liquefaction mitigation: An emerging technique for ground improvement. Applied Sciences, 10(1), 15.

Larisch, M. & Pervan, T. (2024, September 15). https://www.slideshare.net/slideshow/menard-uae-dynamic-compaction slidespdf/264743142?from_search=1#46

Earthquake Hazard Map. (2024, July 18). https://tdth.afad.gov.tr/TDTH/main.xhtml

APPENDICES

Appendix-1: Borehole Data Information

Borehole #	Borehole Depth	Groundwater Level	Coordinates	
	(m)	(m)	X	Y
1_SK-1	27.0	-3	511273.5834	4252550.4547
1_SK-2	26.0	0	511211.6605	4252472.6639
1_SK-2A	31.0	0	511176.289	4252490.3835
1_SK-2B	30.0	0	511151.0359	4252502.8322
1_SK-3	31.0	0	511126.9929	4252401.6055
1_SK-4	28.0	0	511089.0795	4252308.3968
1_SK-5	25.0	0	511003.0736	4252184.0272
1_SK-6	28.0	0	510930.2964	4252100.7451
1_SK-7	25.5	0	510827.1519	4252046.0583
1_SK-8	9.5	0	510759.6715	4251973.3341
1_SK-9	12.5	0	510701.6711	4251896.9126
1_SK-14A	13.5	0	510105.6082	4251323.5033
1_SK-15	18.0	0	509747.2164	4251306.0226
1_SK-16	7.0	0	509546.2423	4251216.1098
1_SK-17	7.5	0	509420.8348	4251143.2285
1_SK-18	15.0	0	509322.8564	4251132.5349
1_SK-20	6.5	0	509042.7077	4251081.1291
1_SK-23	6.5	0	508491.8781	4250770.3036
1_SK-24	12.0	0	508375.4803	4250595.5471
1_SK-25	26.5	0	508255.1746	4250493.8666
1_SK-26	7.0	0	508150.7354	4250433.583
1_SK-27	10.0	0	508046.2471	4250371.8476
1_SK-29	8.3	0	507944.0917	4250214.8026
1_SK-30	15.5	0	507791.6213	4250116.90
1_SK-31	16.5	0	507662.8682	4250076.369
1_SK-32	24.0	0	507610.9177	4250054.0353
1_SK-33	23.0	0	507522.878	4250034.1554
1_SK-34	20.5	0	507459.8302	4250048.9233
1_SK-35	29.0	0	507375.9439	4250093.6887
1_SK-36	21.5	0	507155.6167	4250209.1581
1_SK-37	6.5	0	507030.516	4250255.5252
1_SK-38	8.0	0	506949.7832	4250306.4219
1_SK-39	20.0	0	506858.4498	4250282.6701
2_SK-1	40.0	-1.7	511345.92	4252570.62
3_SK-1	20.0	-2.5	511195.2241	4252374.5633
3_SK-2	51.5	-2.5	511259.24	4252616.10
3_SK-3	20.0	-2.6	511247.87	4252592.96
3_SK-4	20.0	-2.6	511305.10	4252630.56
3_SK-5	20.0	-2.7	511300.87	4252585.83

Borehole No	Borehole Depth	Groundwater Level	Coordinates	
	(m)	(m)	X	Y
3_SK-6	51.5	-2.6	511300.87	4252540.92
3_SK-7	20.0	-2.6	511280.09	4252566.53
4_SK-1	35.0	-6.5	511511.8685	4252924.7465
4_SK-2	53.5	-8.5	511481.8346	4252931.7075
4_SK-3	51.0	-6.0	511553.0992	4253055.9002
4_SK-4	53.5	-8.6	511571.3934	4253104.7101
4_SK-5	50.0	-4.5	511771.9011	4253408.1946
4_SK-6	52.5	-7.0	511762.8946	4253497.8863
4_SK-7	49.0	-3.5	512017.8742	4253745.4974
4_SK-8	51.5	-6.5	511965.0993	4253787.3252
4_SK-9	49.0	-5.5	512073.11	4254045.63
4_SK-10	52.0	-5.5	512222.986	4254204.332
4_SK-11	45.5	-4.5	512422.36	4254625.1548
4_SK-12	50.5	-4.5	512387.7731	4254631.1463
4_SK-13	47.5	-1.5	512480.3259	4254876.6258
4_SK-14	48.5	-3.8	512422.9566	4254802.672
4_SK-54	56.0	-10.5	511545.9962	4253192.1989
4_SK-55	54.0	-8.5	511878.5731	4253748.3837
4_SK-56	50.5	-5.5	512350.2852	4254553.0866
4_SK-66	46.0	-9.5	511680.4391	4253390.3728
4_SK-67	41.5	-6.0	511884.5491	4253600.2278
4_SK-68	44.5	-8.0	511839.3662	4253631.8145
4_SK-181	42.0	-7.0	511421.9603	4252784.9517
4_SK-184	43.0	-7.7	511461.826	4252854.1988
5_SK-1	39.5	-2.6	512565.3212	4254893.0513
5_SK-2	21.5	-3.0	505872.2444	4249962.3508
6_SK-1	30.0	-0.75	513614.2069	4257739.5863
6_SK-2	30.0	-0.7	513631.9849	4257730.401
6_SK-3	30.0	-0.75	513615.6884	4257720.3267
6_SK-4	30.0	-0.85	513631.3923	4257706.6969
6_SK-5	30.0	-0.75	513629.0219	4257724.1787
6_SK-6	30.0	-0.6	513646.5036	4257717.0674
6_SK-7	30.0	-0.75	513623.9848	4257713.2155
7_SK-10	36.5	-7.0	516390.1119	4255809.3949
7_SK-11	39.5	-4.2	515077.4163	4256879.4318
7_SK-12	39.5	-6.0	514948.778	4256221.6222
7_SK-14	73.0	-4.6	515965.7537	4256807.5691
7_SK-15	73.0	-11.0	515062.7983	4255897.1028
7_SK-16	40.0	-1.6	516577.2222	4257209.7984
7_SK-17	48.0	0	515770.3091	4256364.8785
7_SK-19	80.0	-3.5	514504.3911	4256952.5217
8_SK-1	30.0	-1.6	506850.2279	4249859.2194
8_SK-2	30.5	-1.4	506841.6556	4249972.0308

Appendix-2: Data Layers

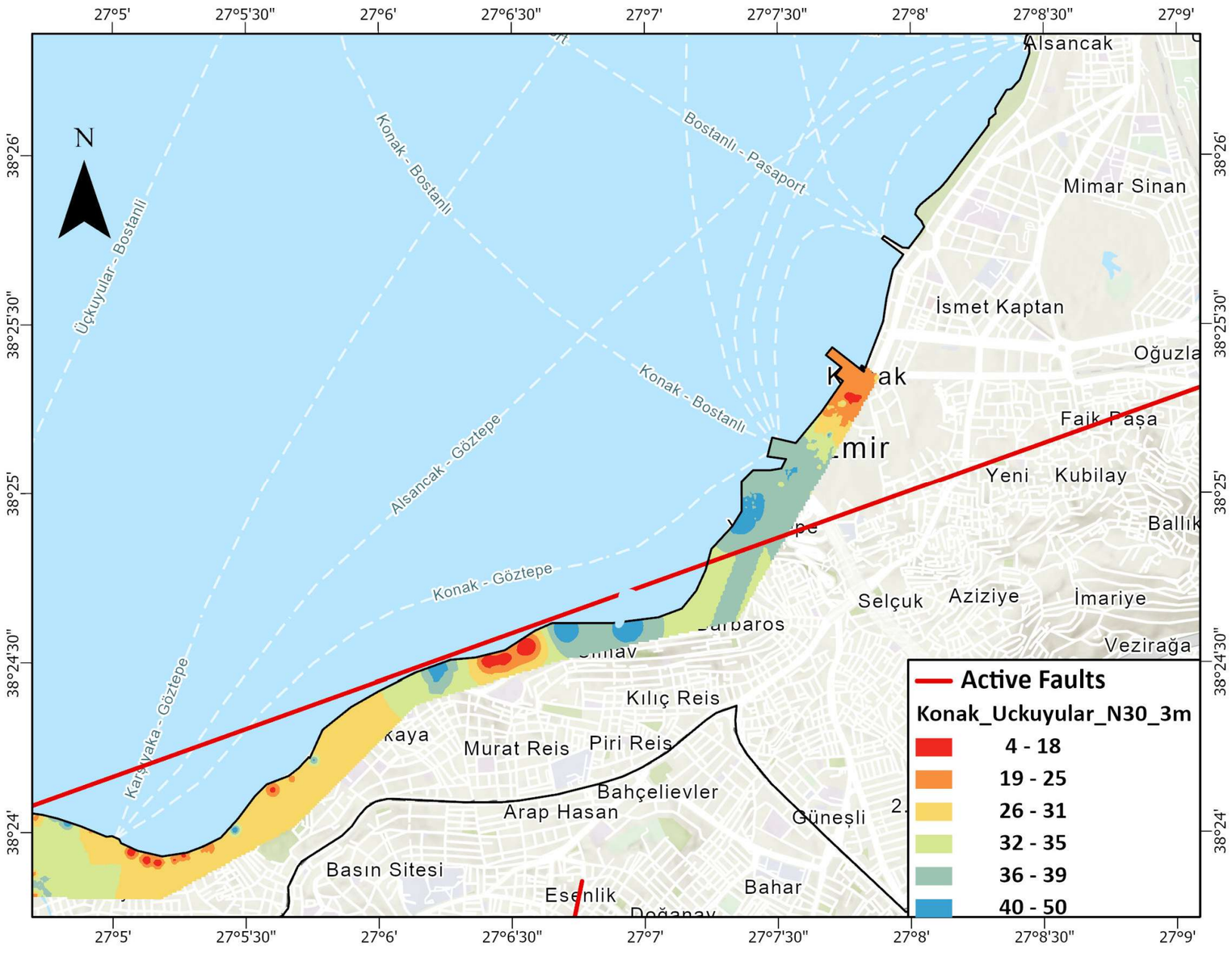

Figure A2.1 N_{30} distribution at 3 m depth in the Konak-Üçkuyular area

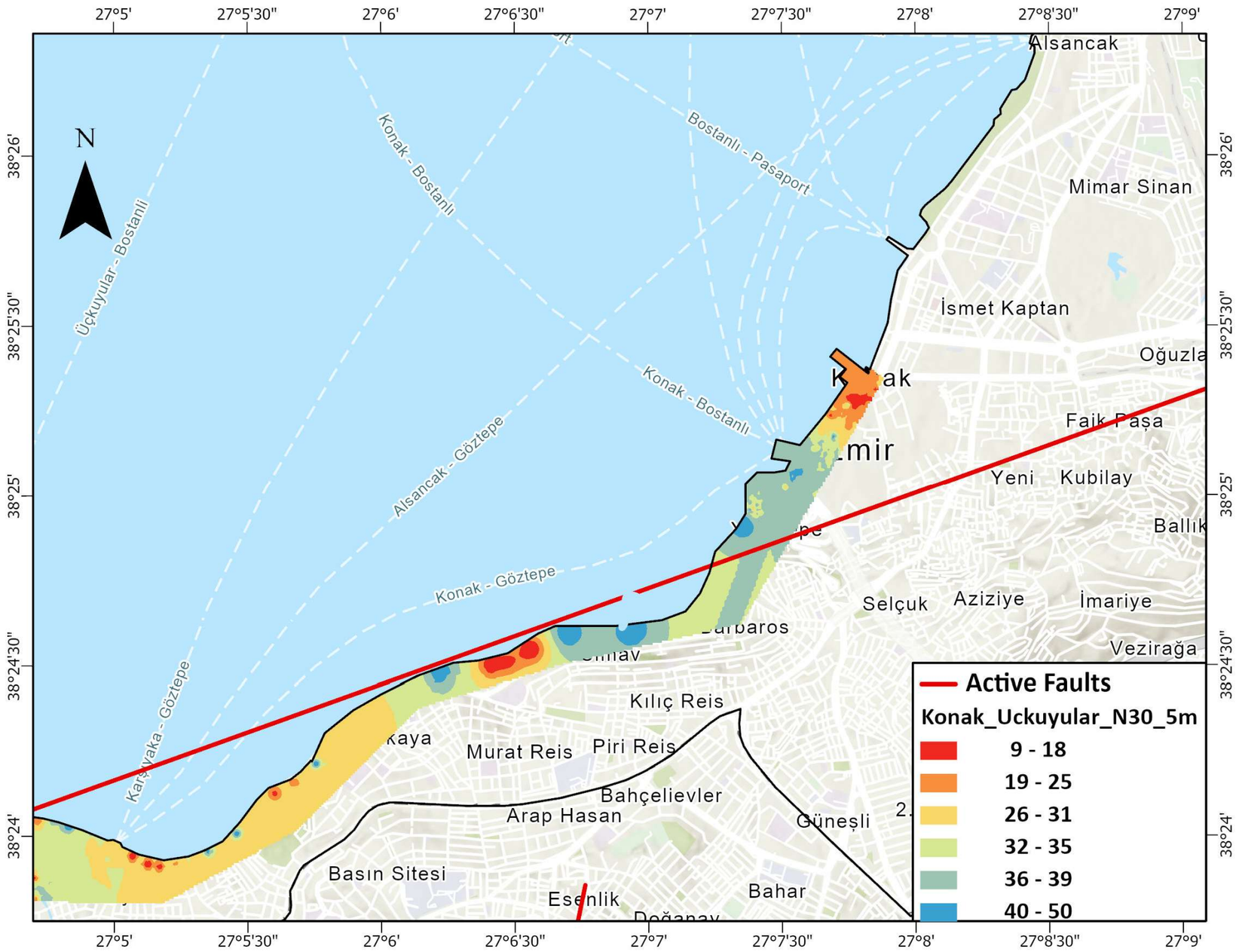

Figure A2.2 N_{30} distribution at 5 m depth in the Konak-Üçkuyular area

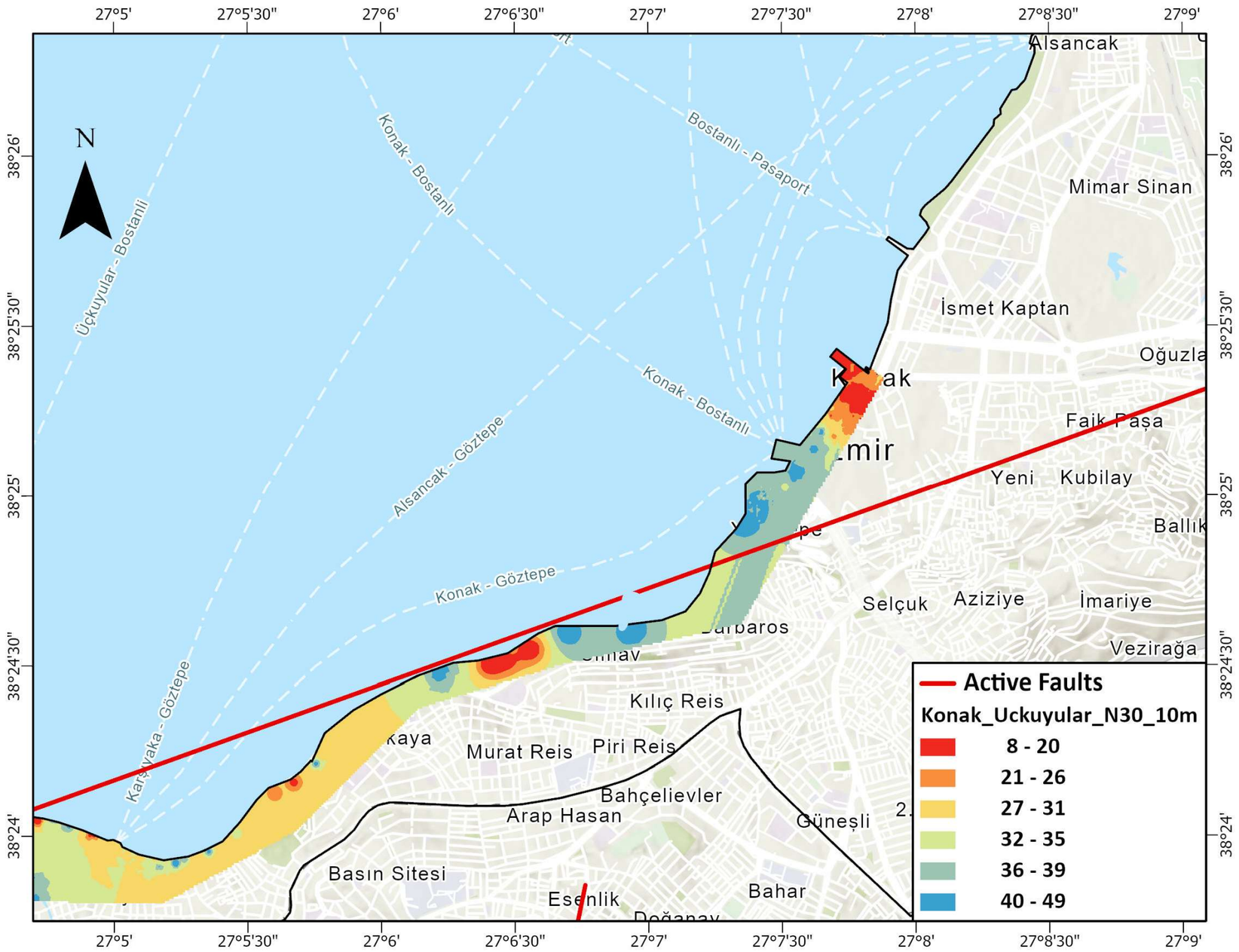

Figure A2.3 N_{30} distribution at 10 m depth in the Konak-Üçkuyular area

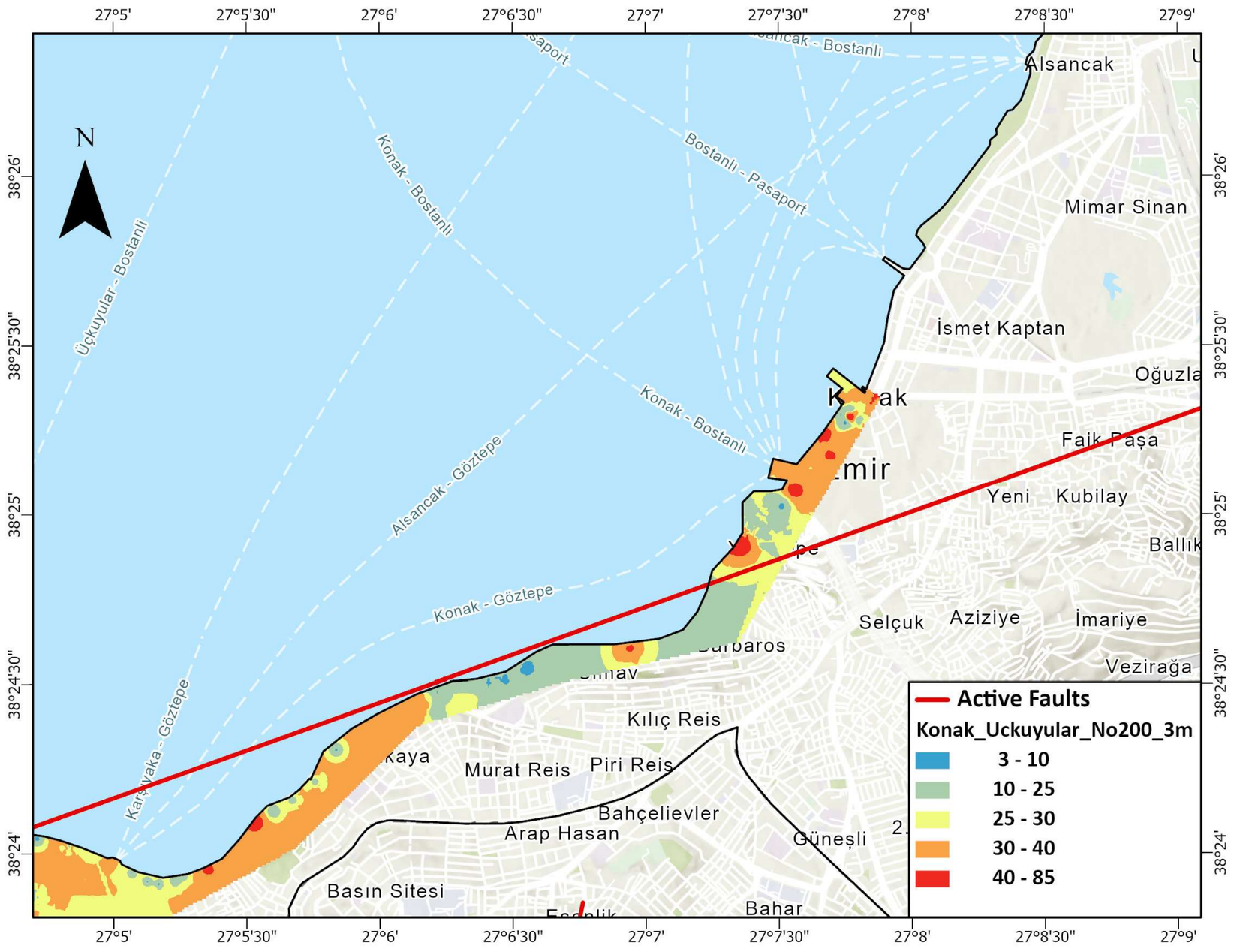

Figure A2.4 No200 distribution at 3 m depth in the Konak-Üçkuyular area

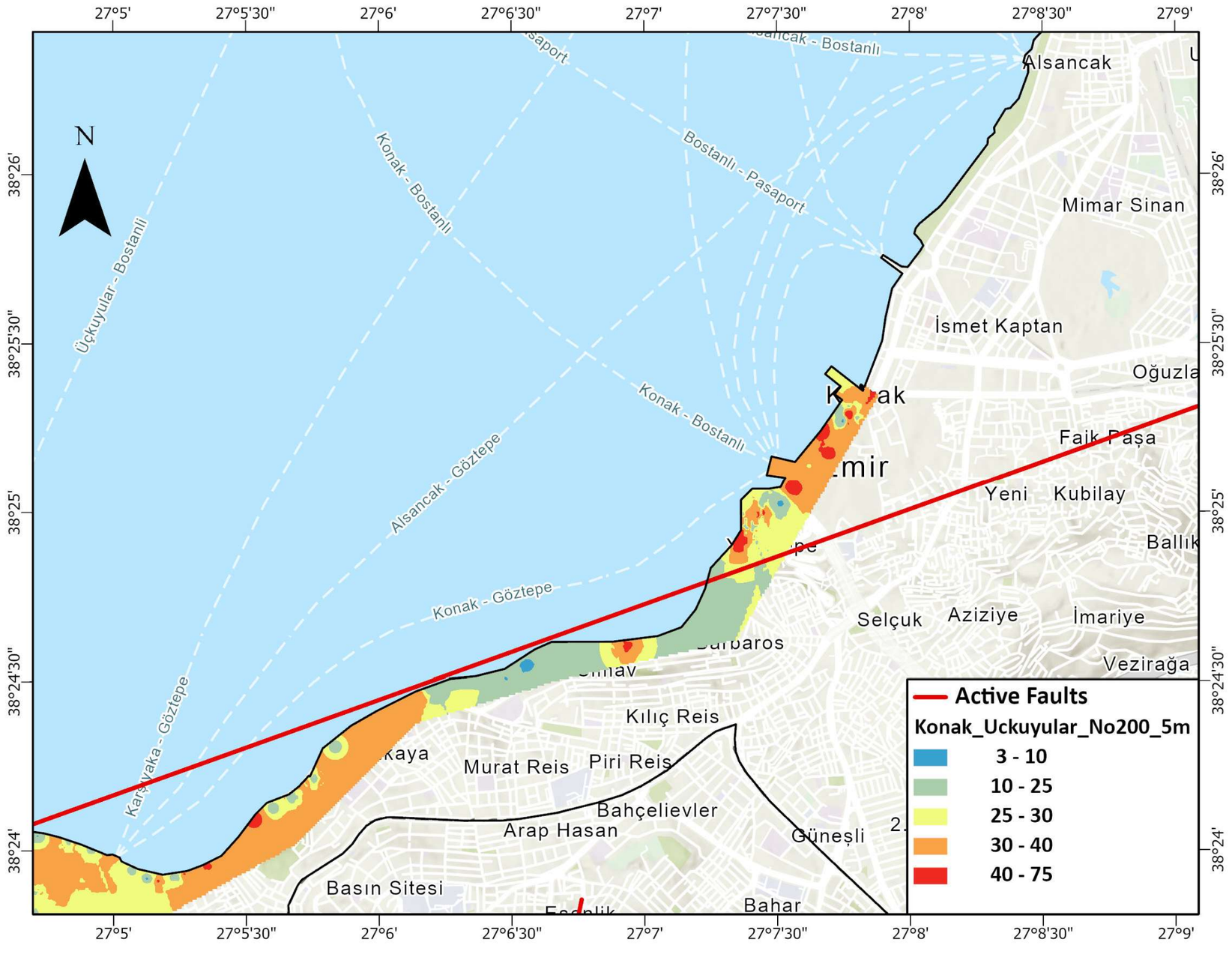

Figure A2.5 No200 distribution at 5 m depth in the Konak-Üçkuyular area

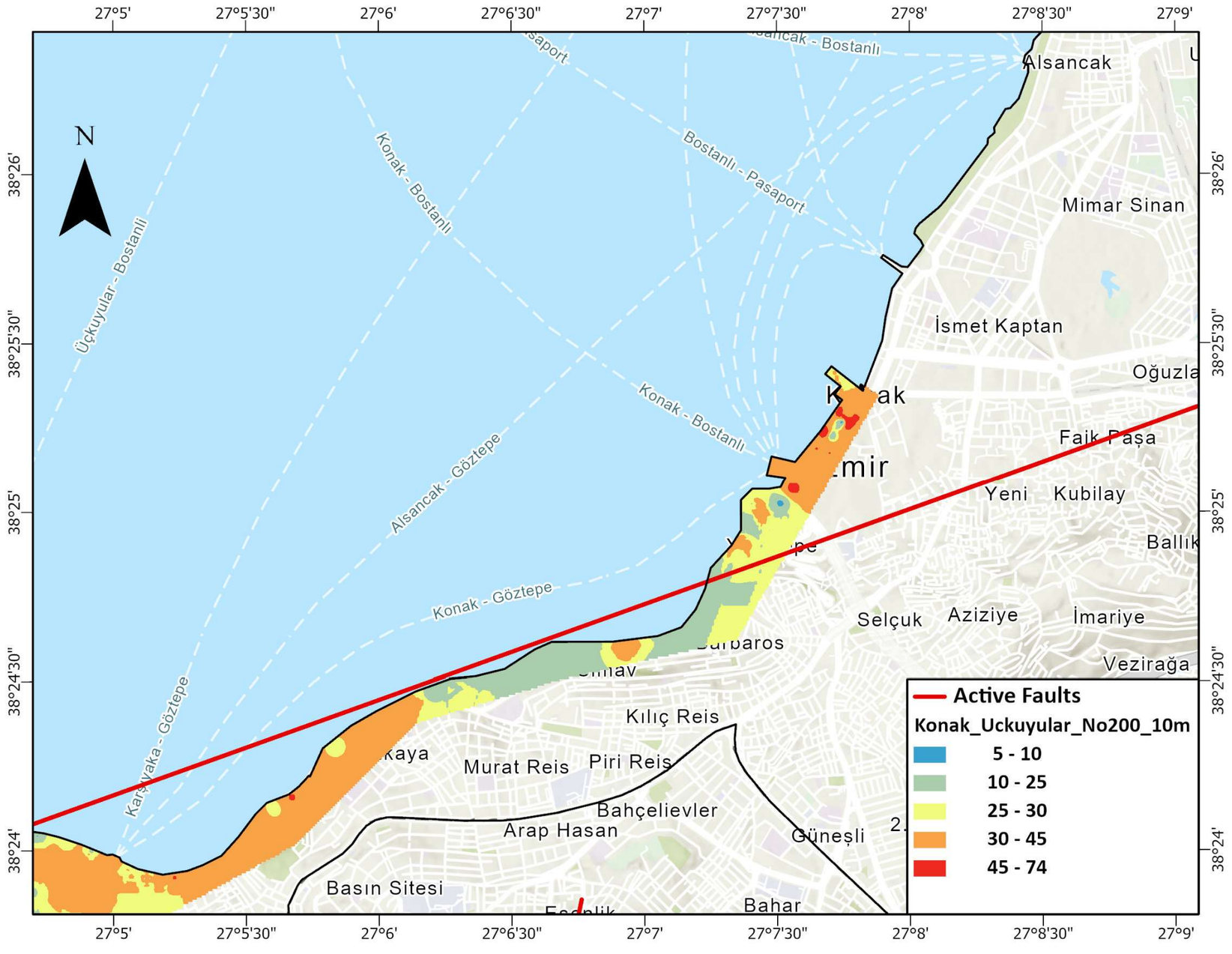

Figure A2.6 No200 distribution at 10 m depth in the Konak-Üçkuyular area

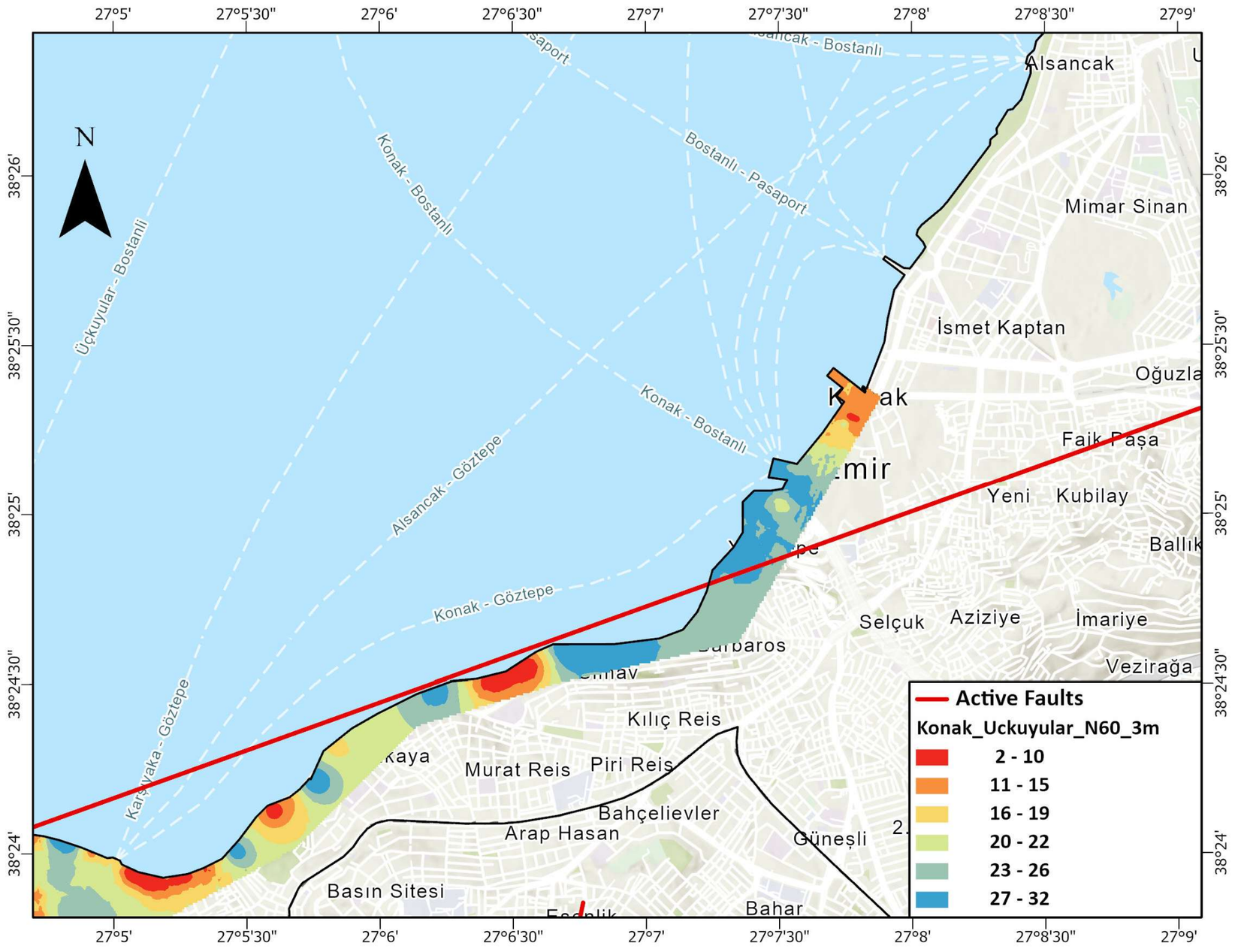

Figure A2.7 N_{60} distribution at 3 m depth in the Konak-Üçkuyular area

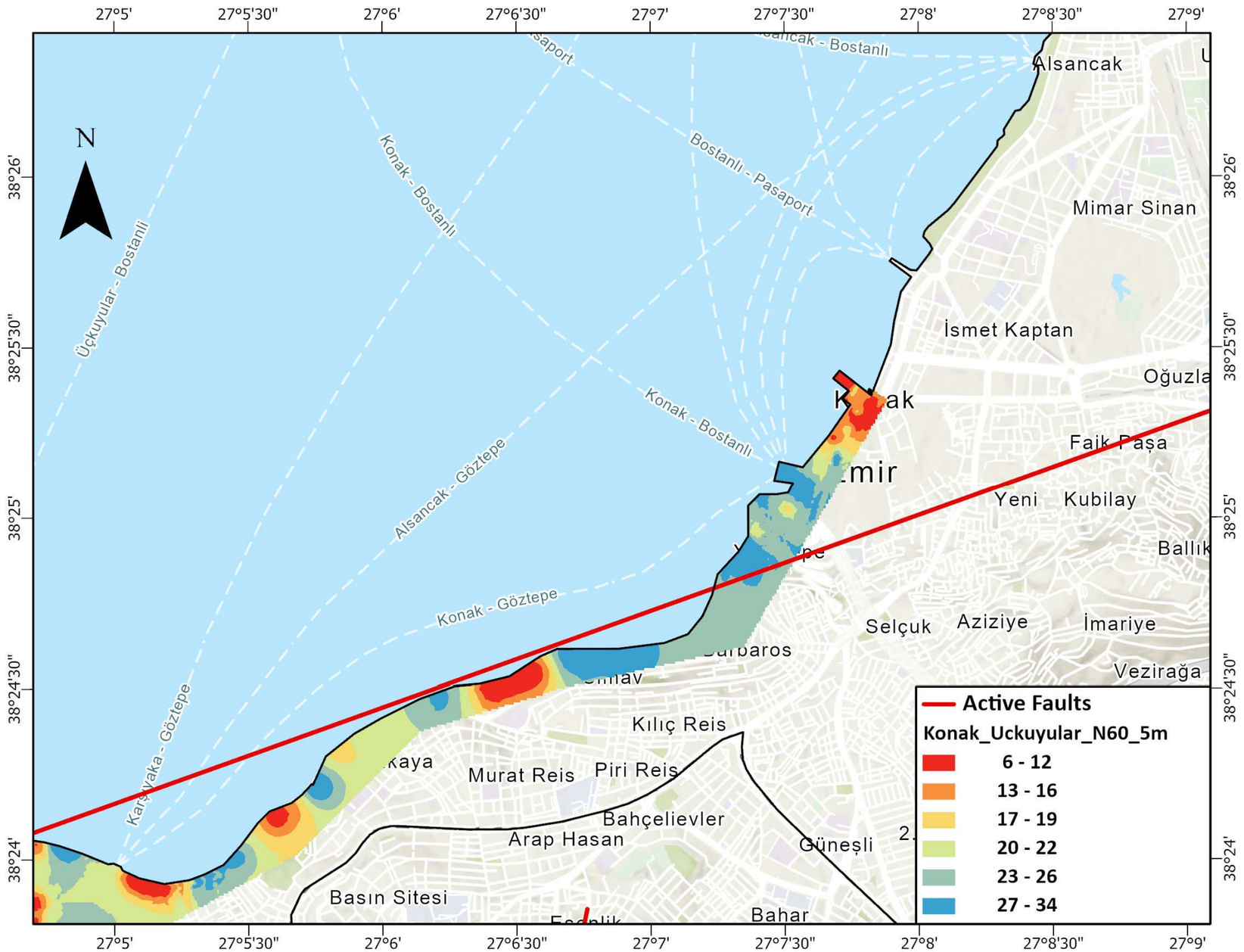

Figure A2.8 N_{60} distribution at 5 m depth in the Konak-Üçkuyular area

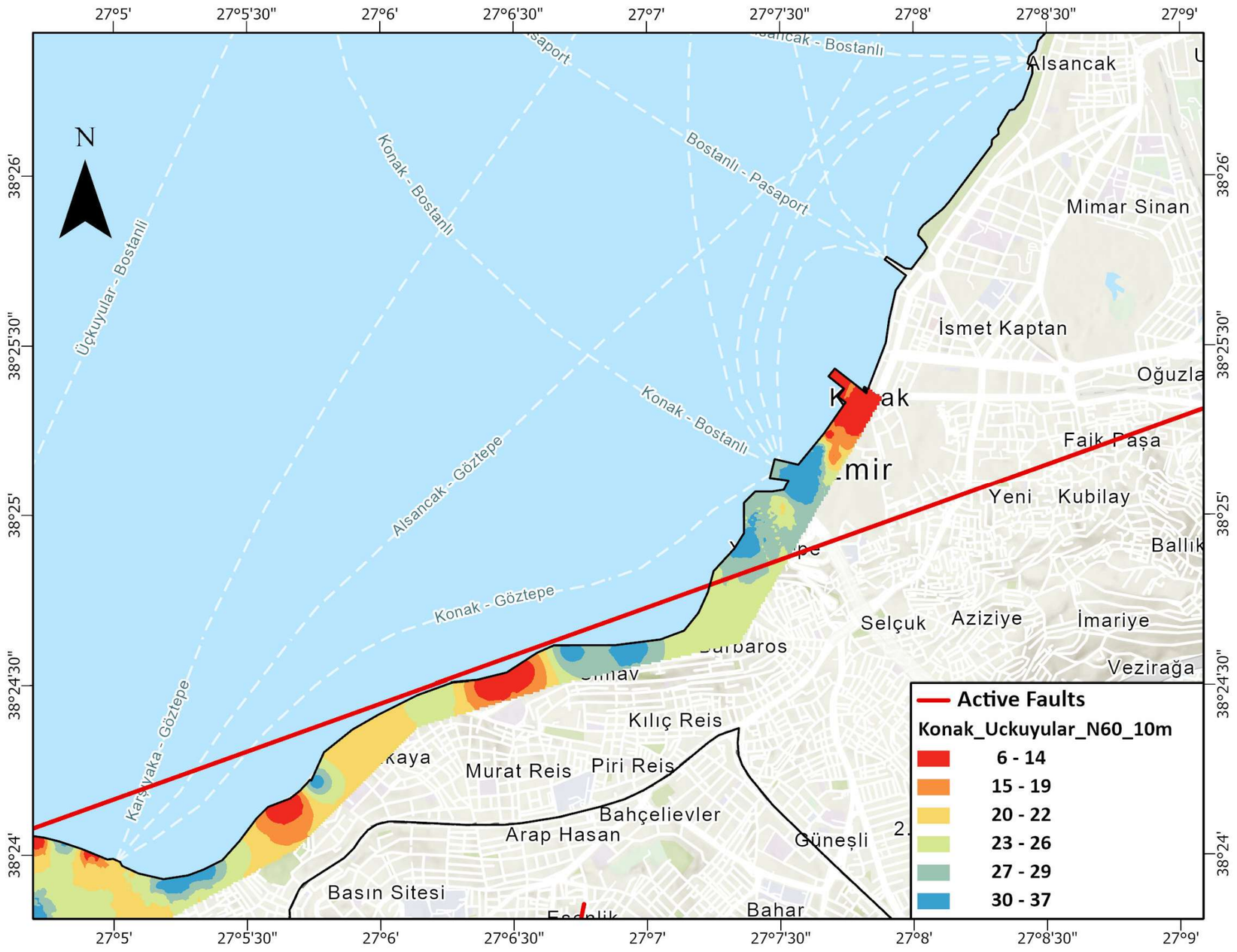

Figure A2.9 N_{60} distribution at 10 m depth in the Konak-Üçkuyular area

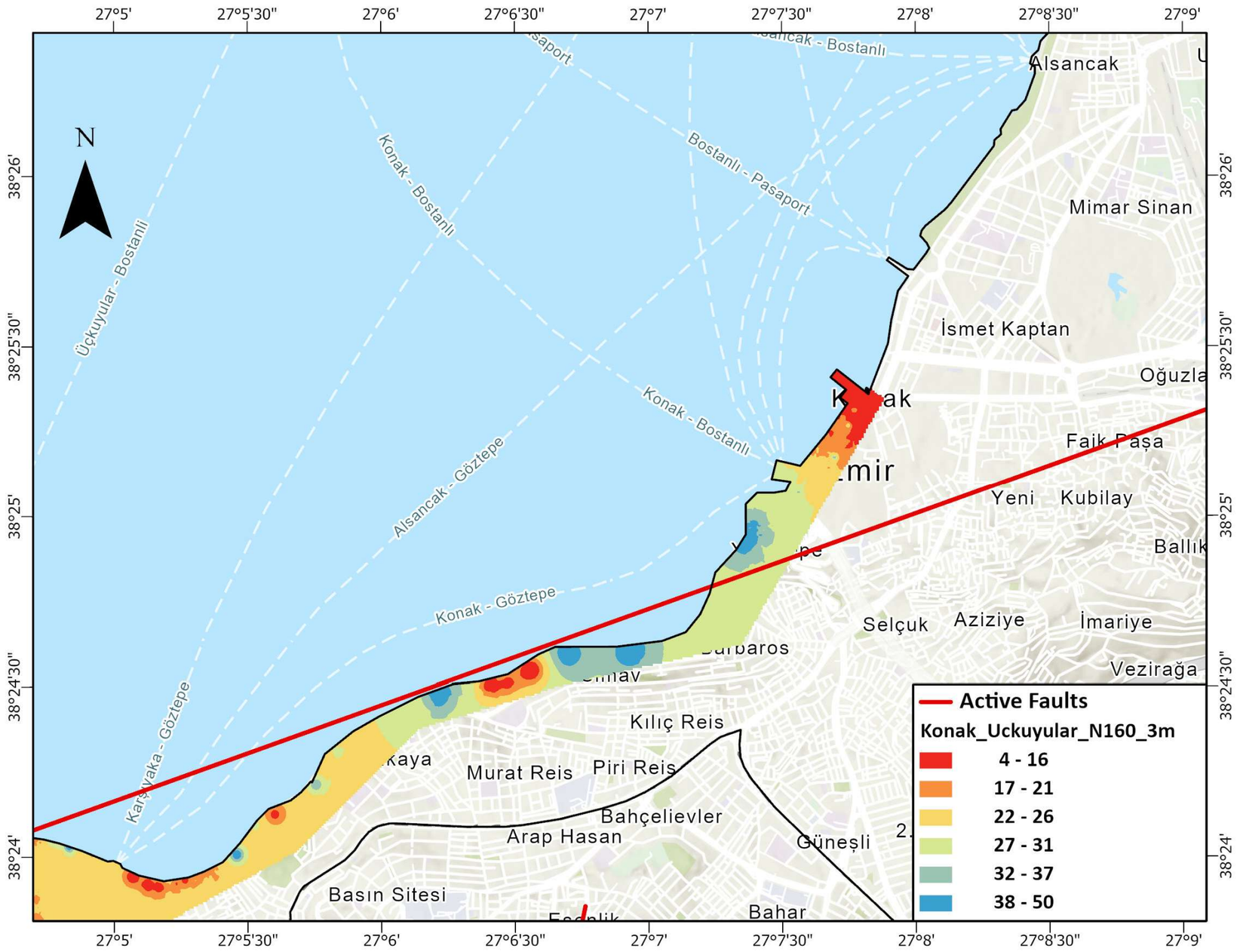

Figure A2.10 $(N_1)_{60}$ distribution at 3 m depth in the Konak-Üçkuyular area

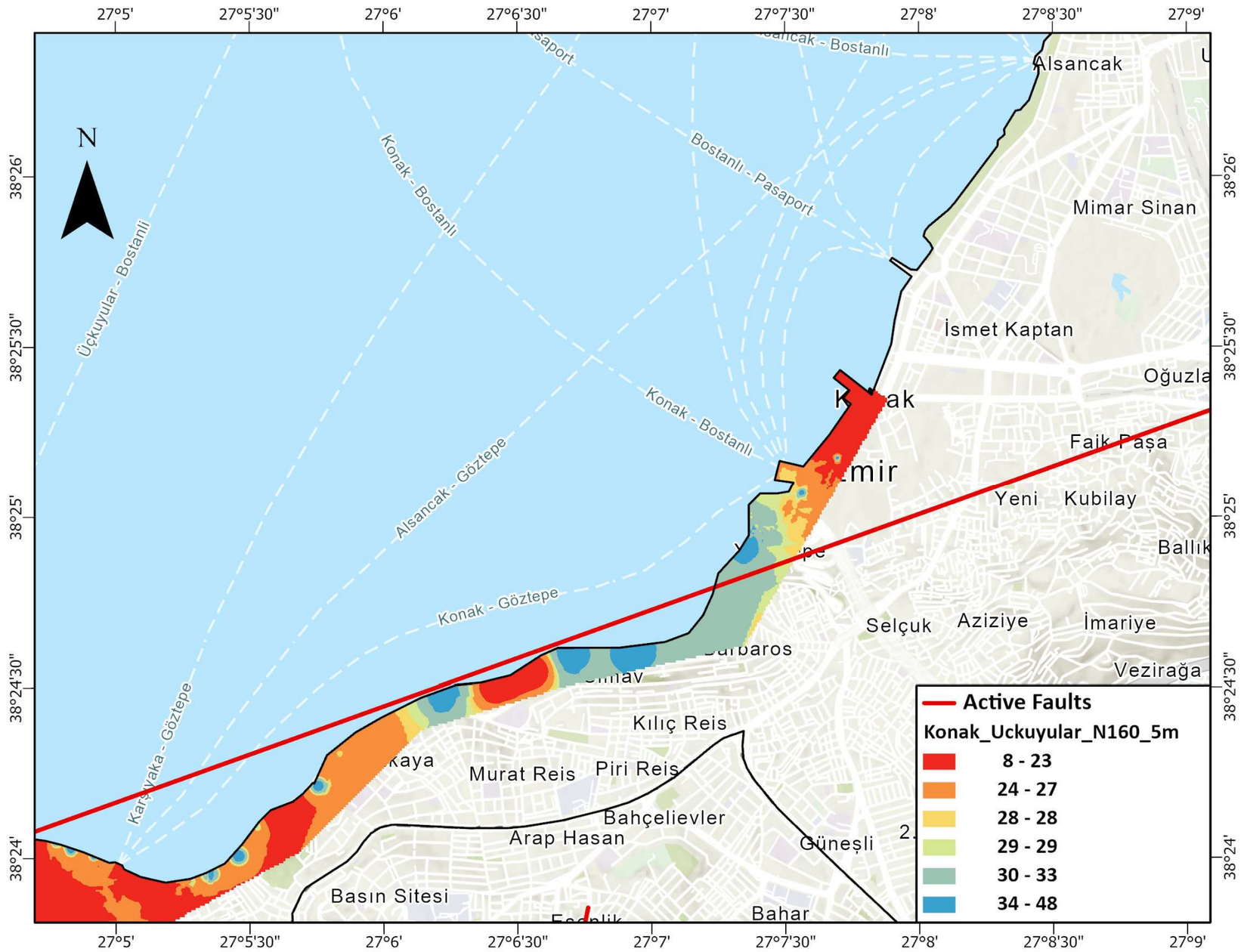

Figure A2.11 $(N_1)_{60}$ distribution at 5 m depth in the Konak-Üçkuyular area

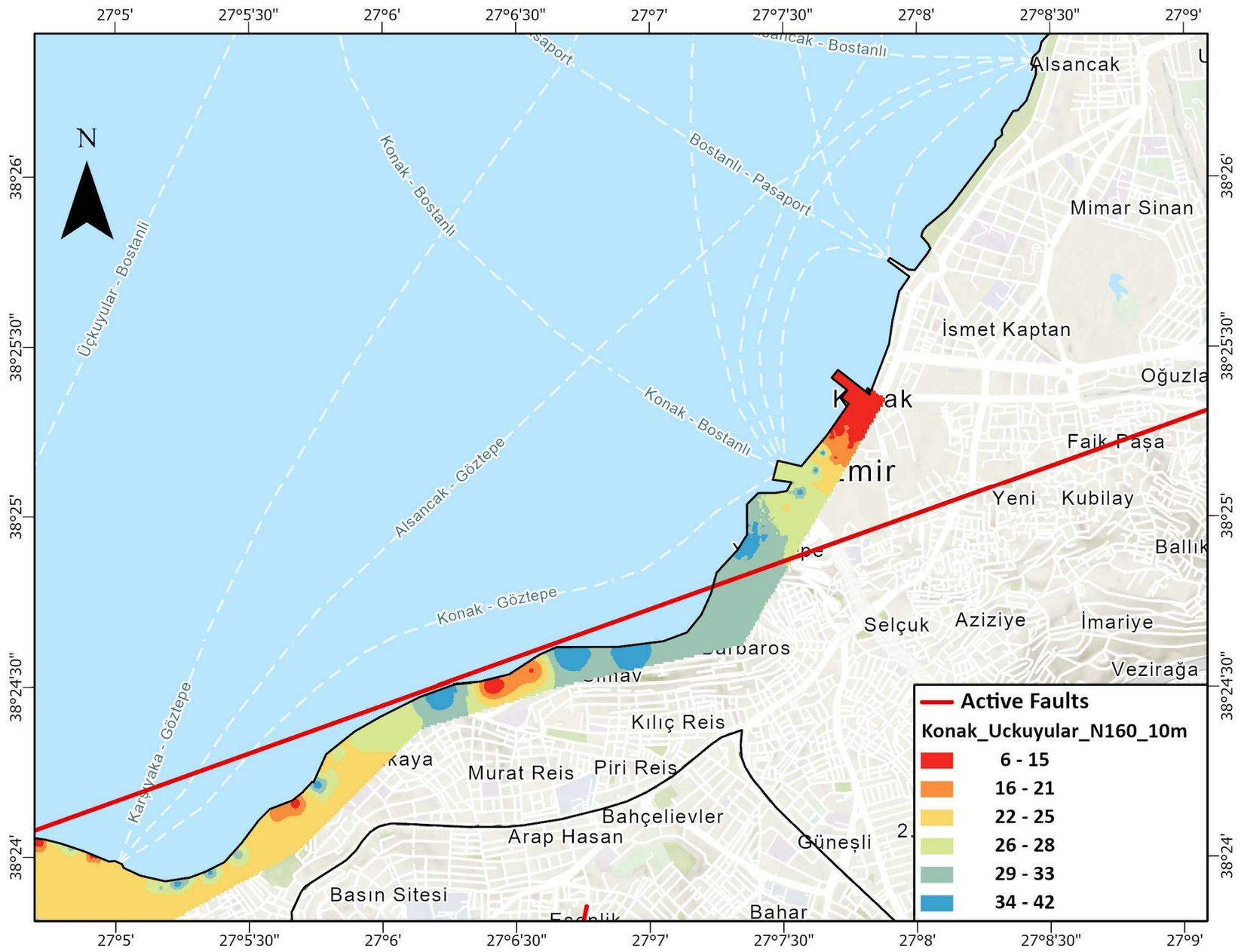

Figure A2.12 $(N_1)_{60}$ distribution at 10 m depth in the Konak-Üçkuyular area

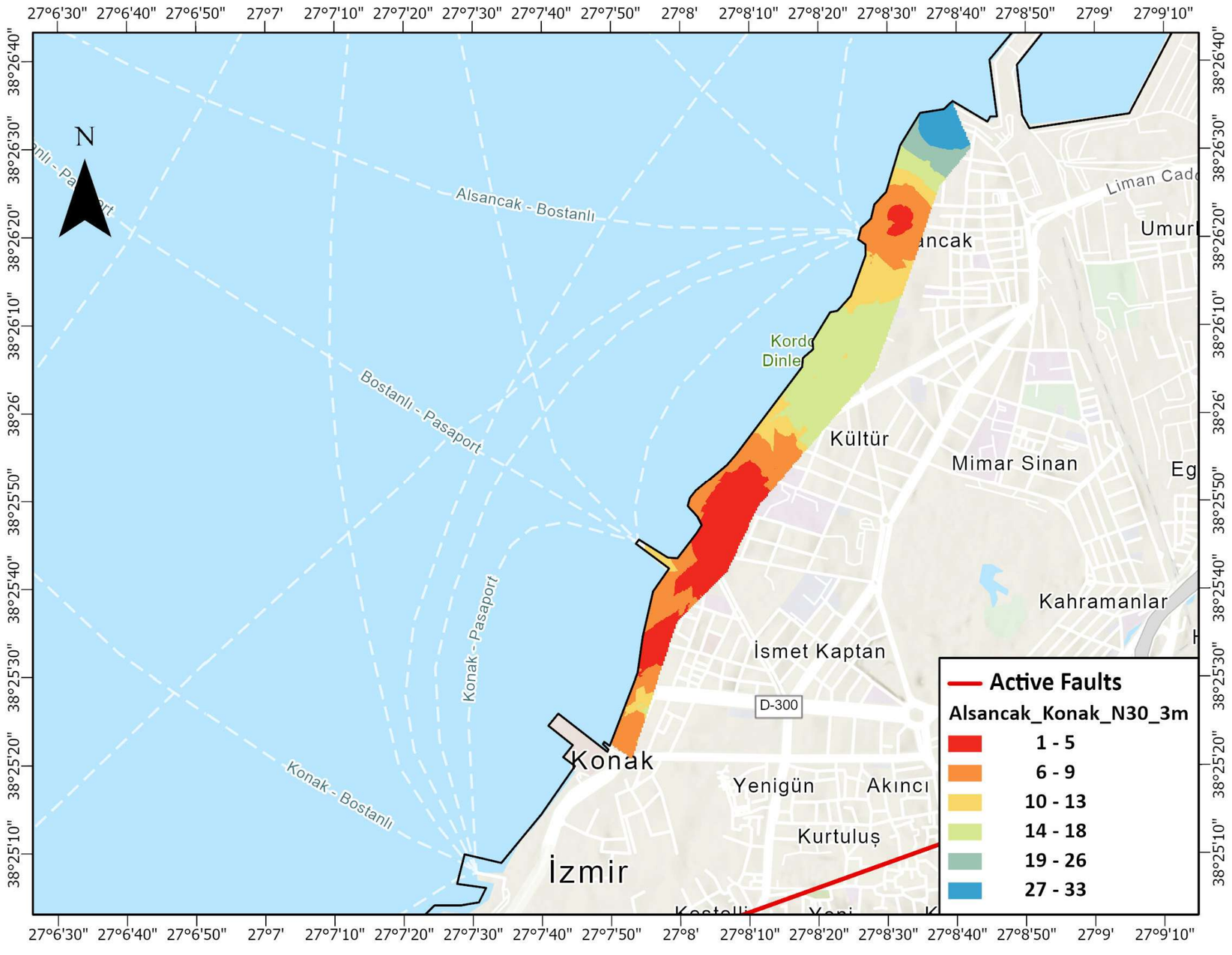

Figure A2.13 N_{30} distribution at 3 m depth in the Alsancak-Konak area

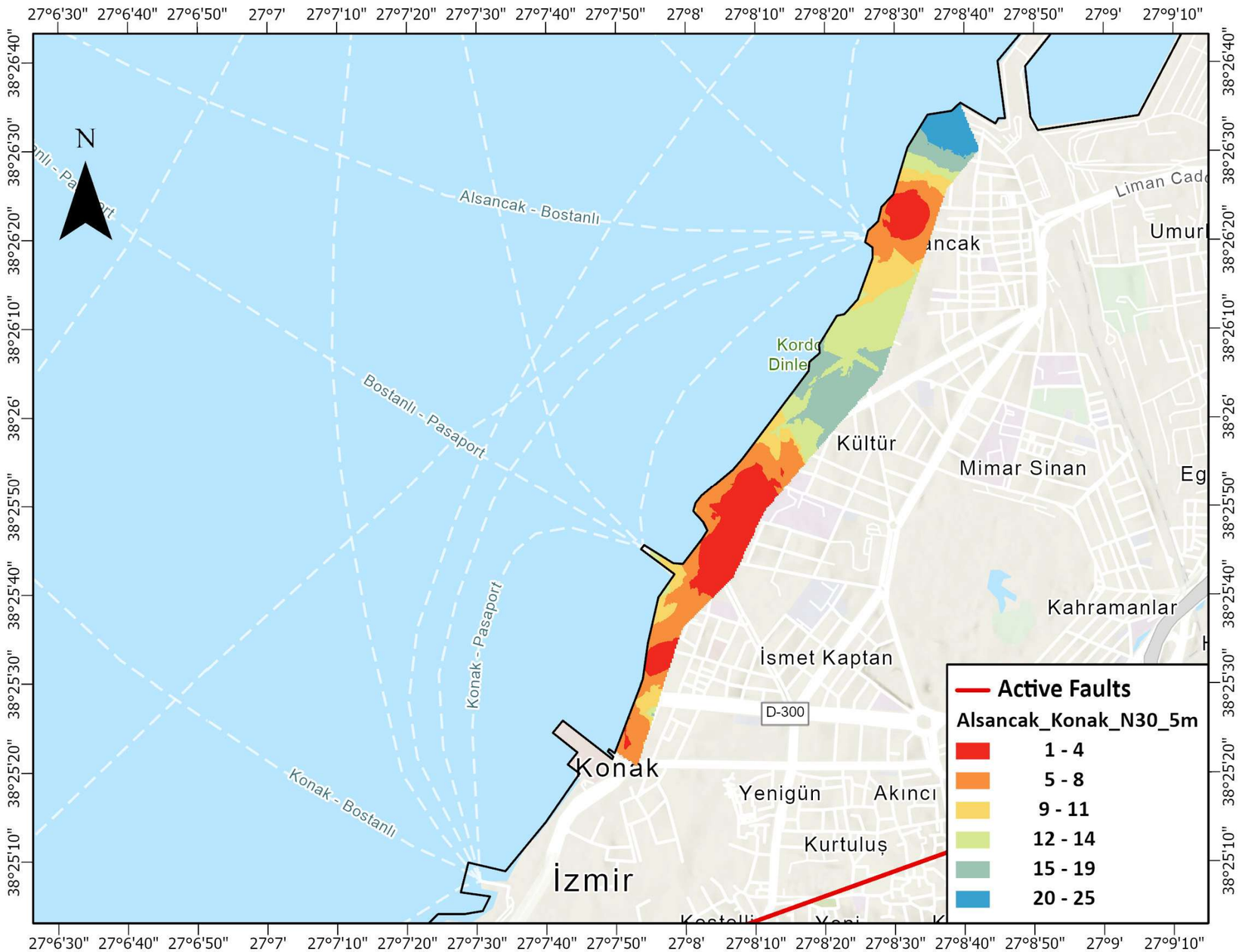

Figure A2.14 N_{30} distribution at 5 m depth in the Alsancak-Konak area

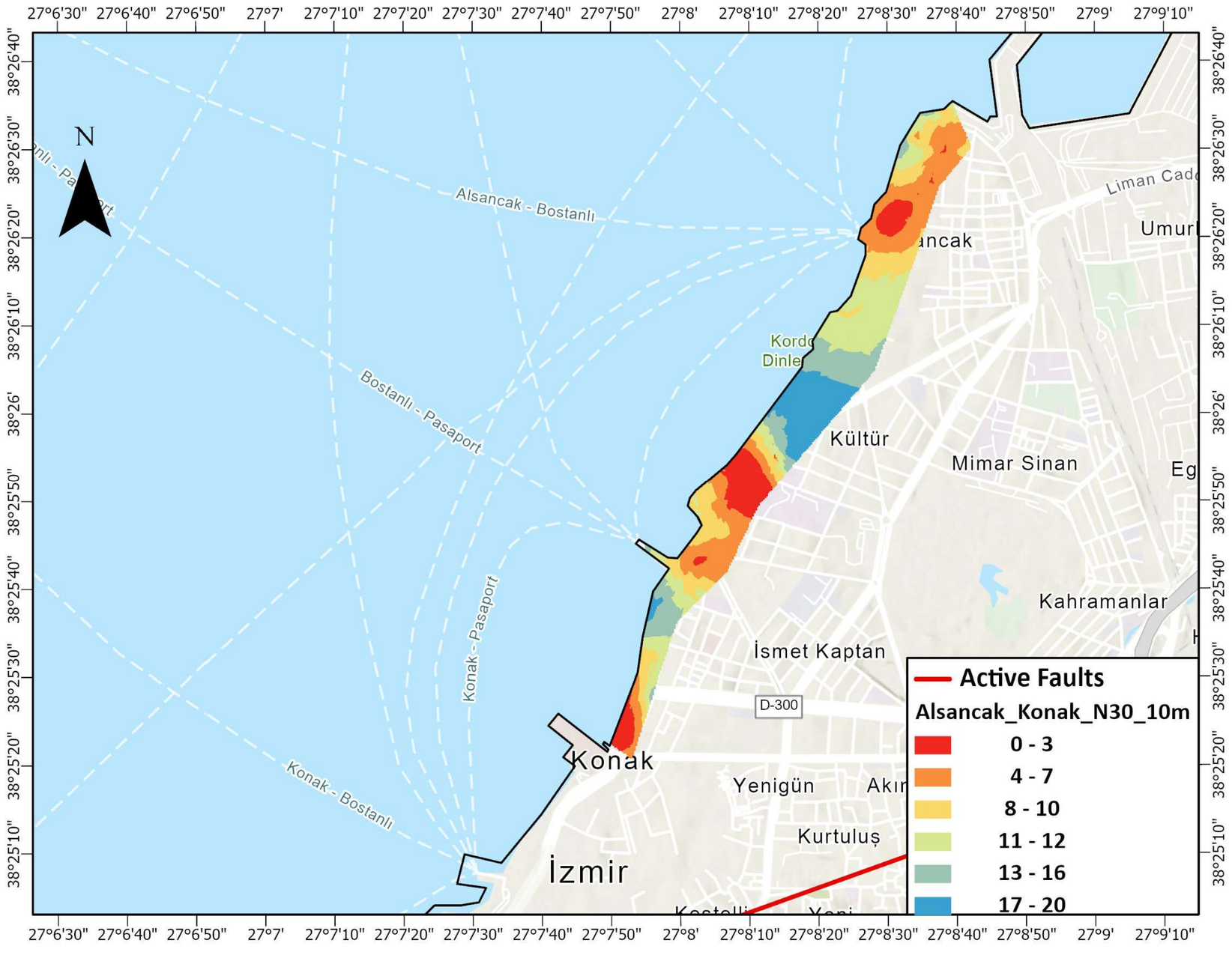

Figure A2.15 N_{30} distribution at 10 m depth in the Alsancak-Konak area

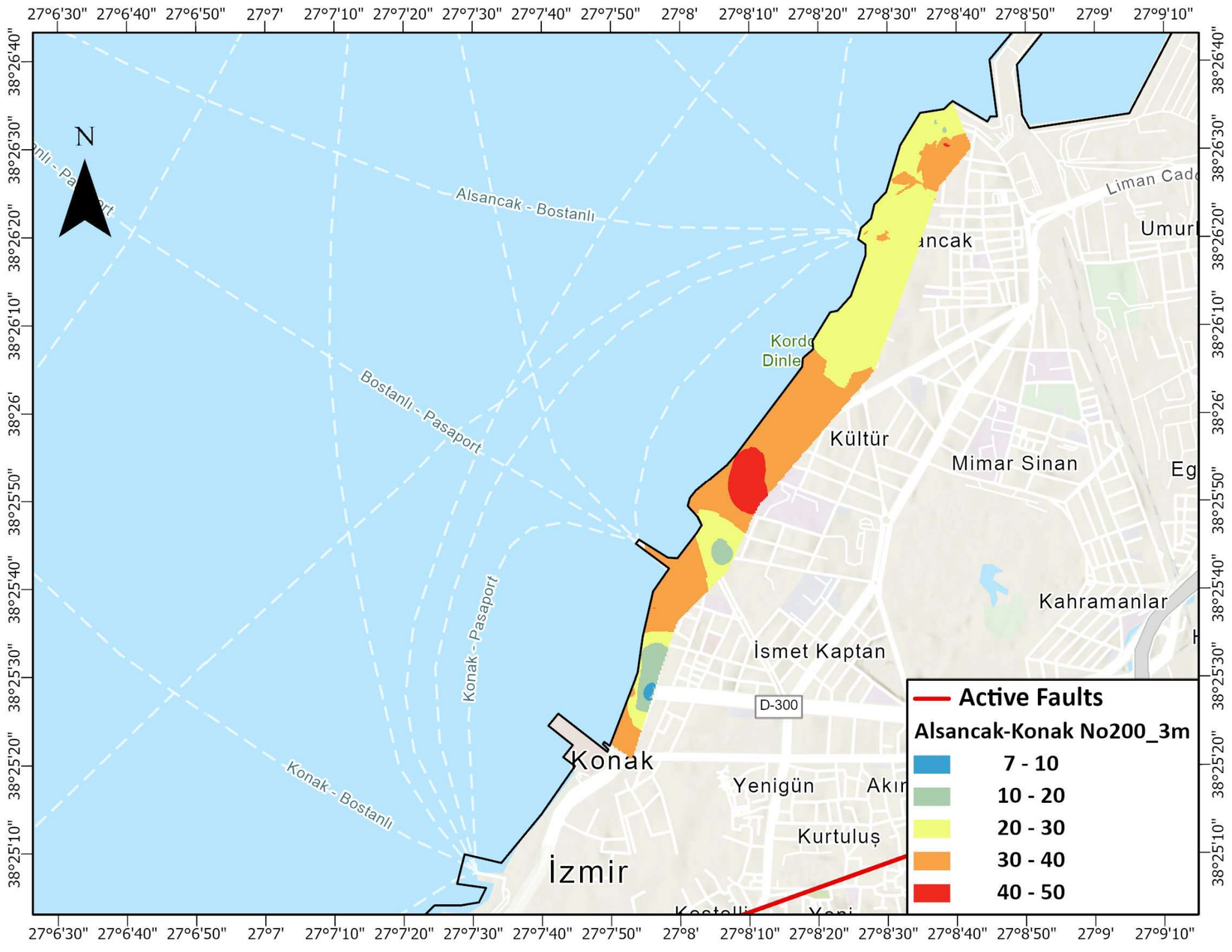

Figure A2.16 No200 distribution at 3 m depth in the Alsancak-Konak area

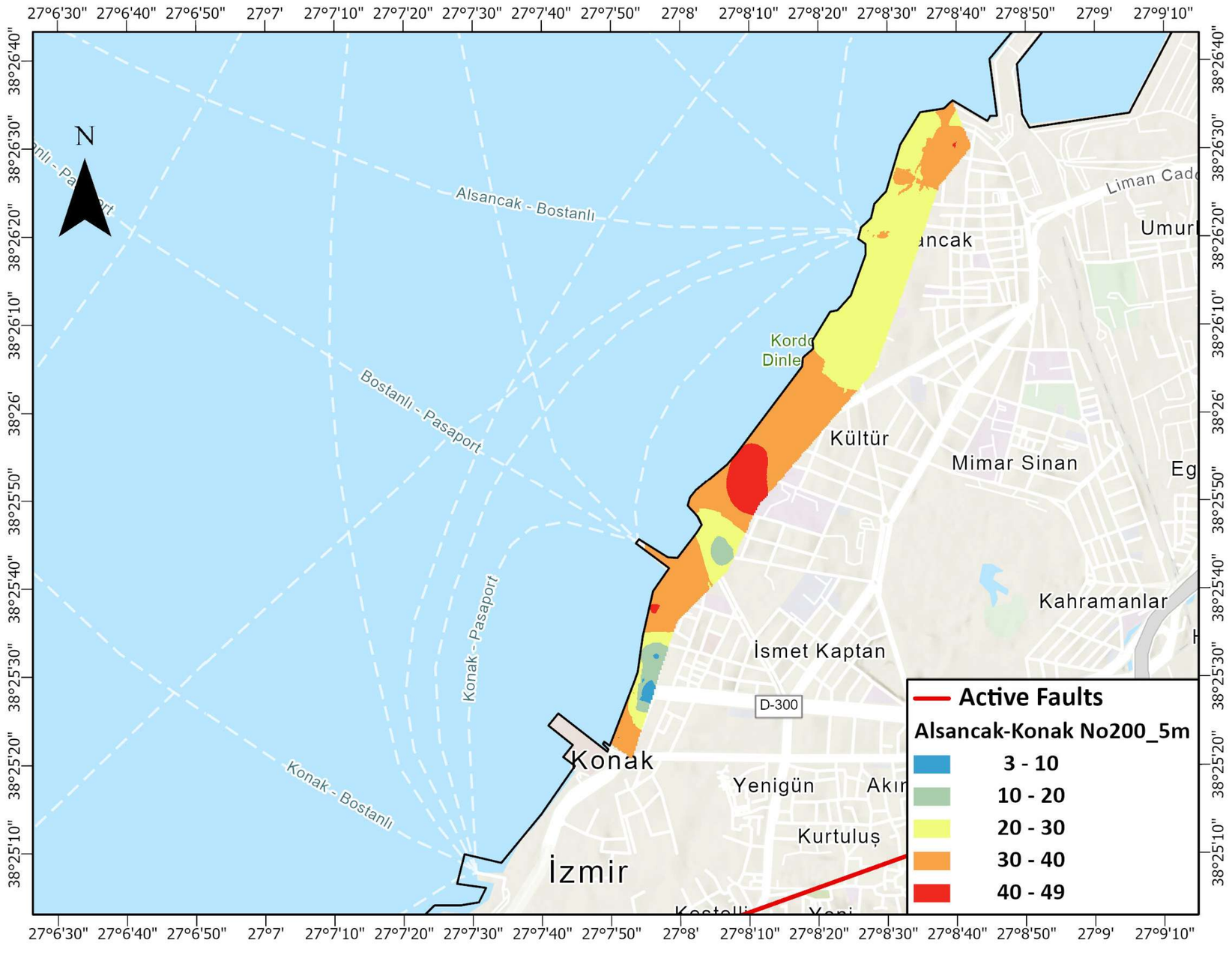

Figure A2.17 No200 distribution at 5 m depth in the Alsancak-Konak area

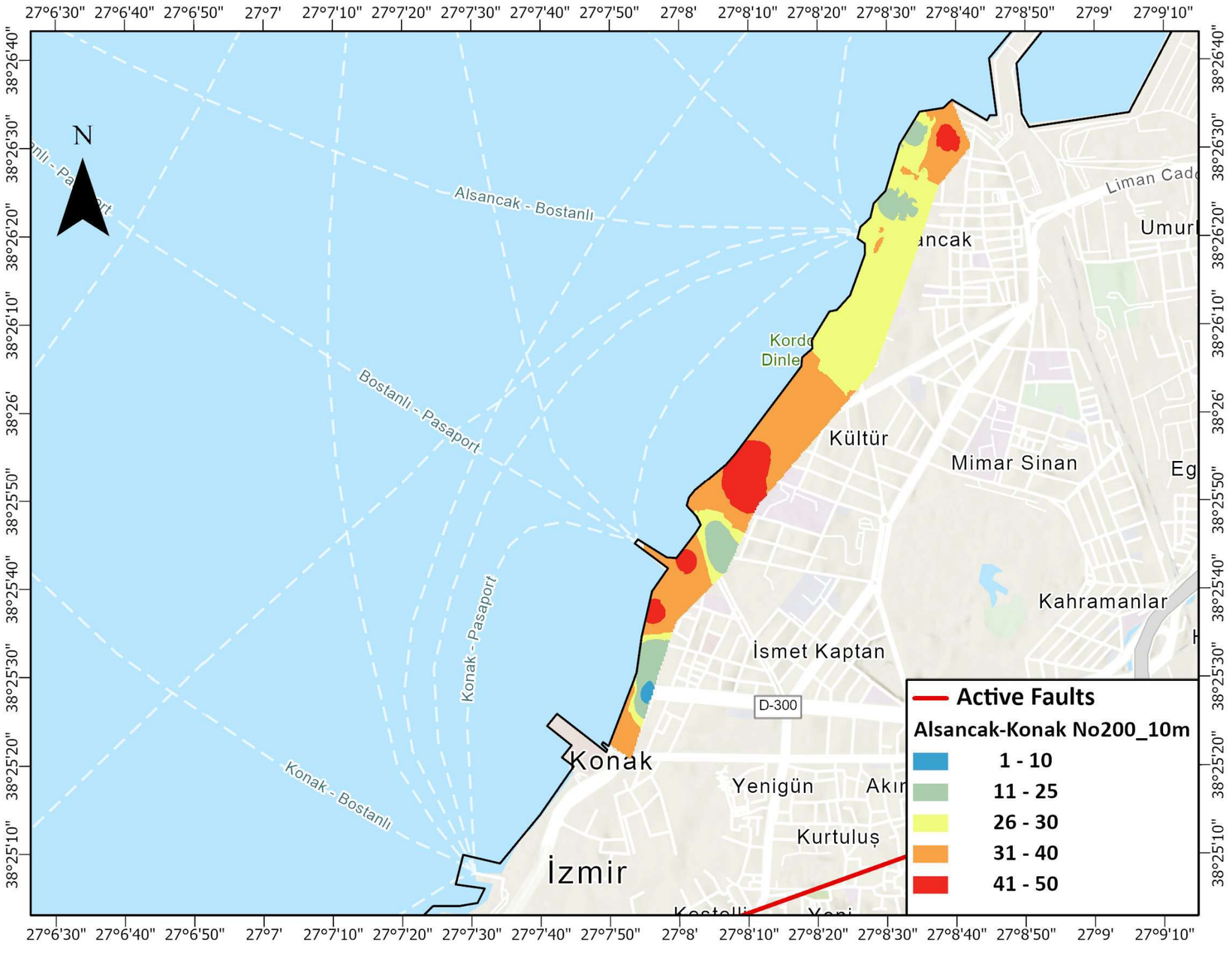

Figure A2.18 No200 distribution at 10 m depth in the Alsancak-Konak area

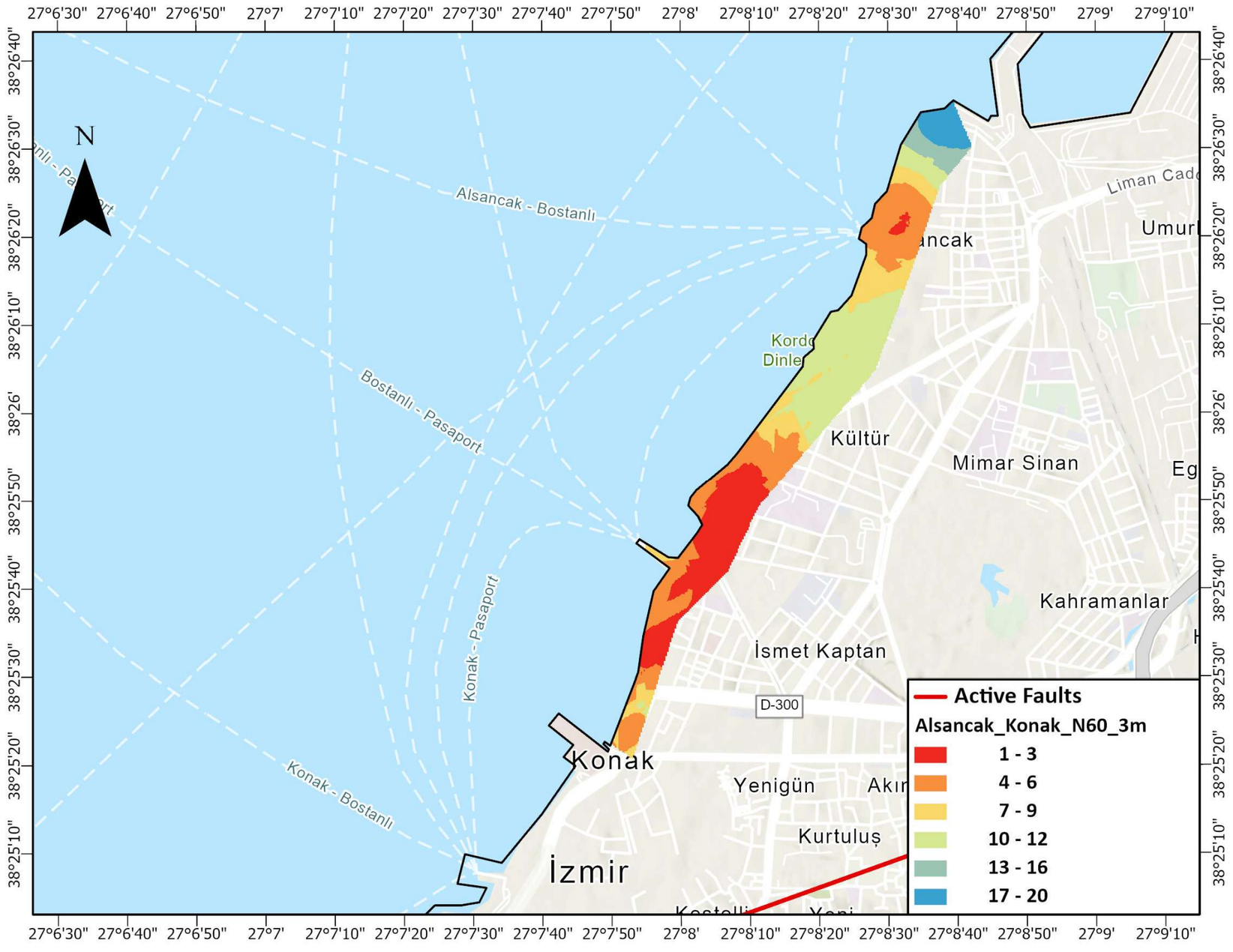

Figure A2.19 N_{60} distribution at 3 m depth in the Alsancak-Konak area

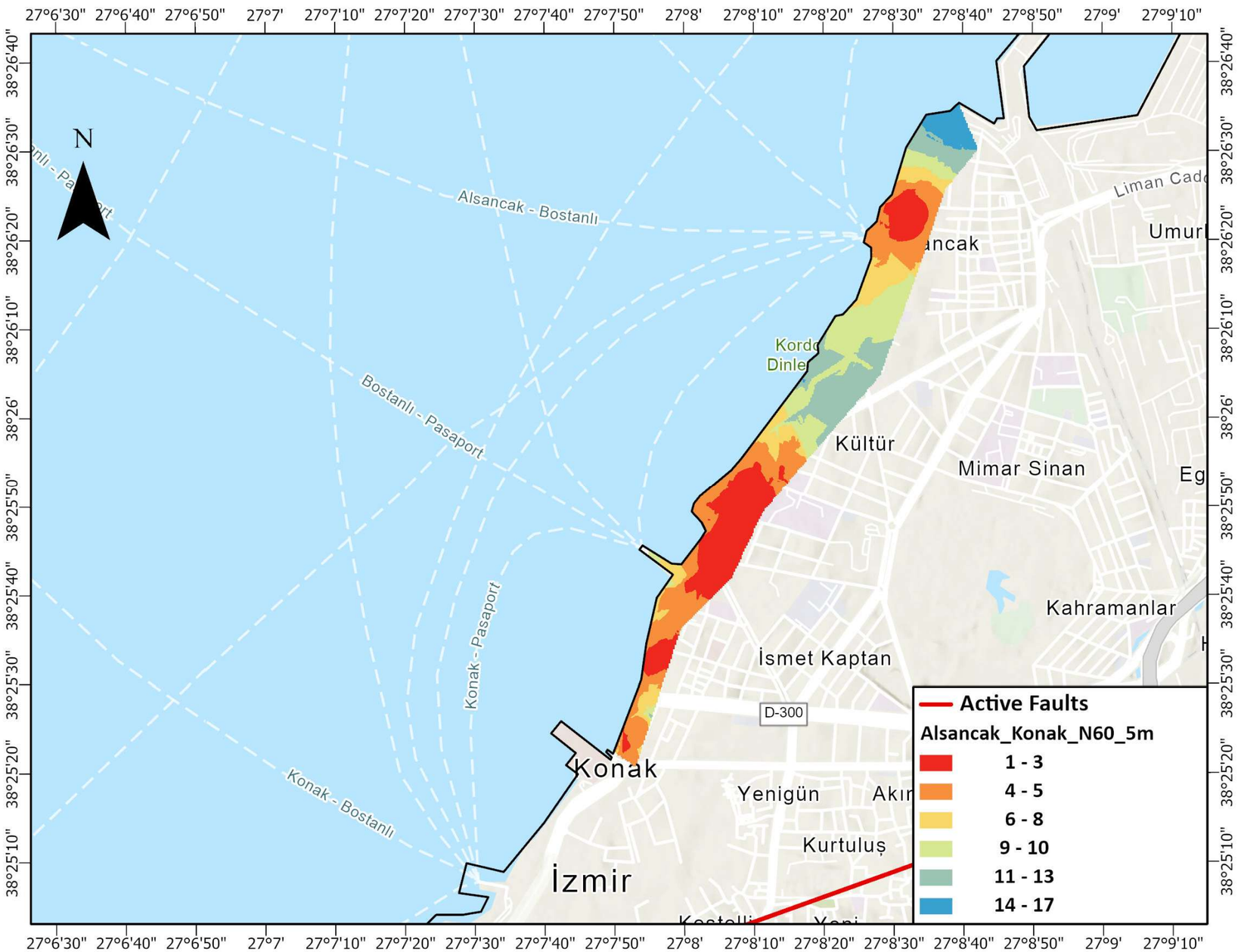

Figure A2.20 N_{60} distribution at 5 m depth in the Alsancak-Konak area

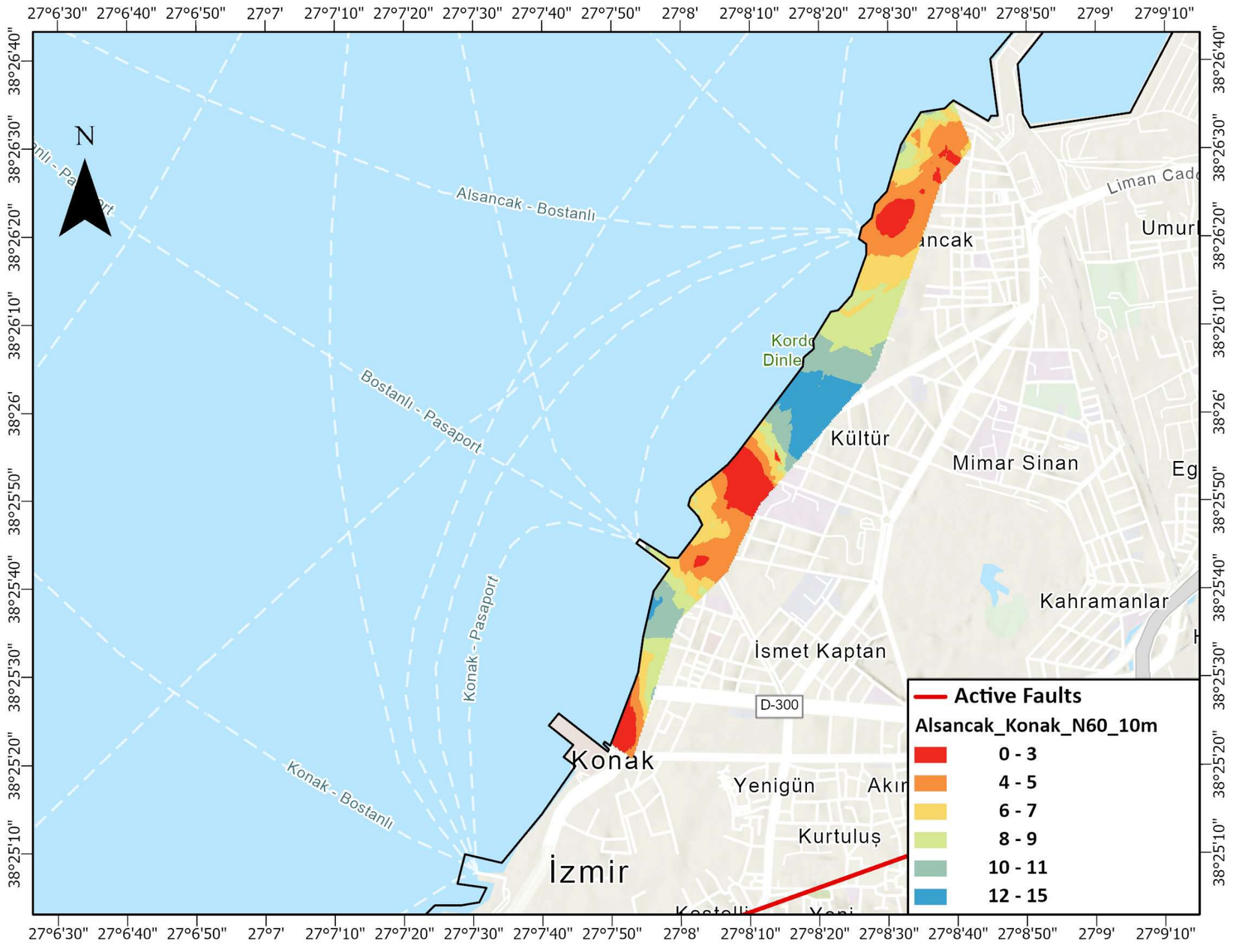

Figure A2.21 N_{60} distribution at 10 m depth in the Alsancak-Konak area

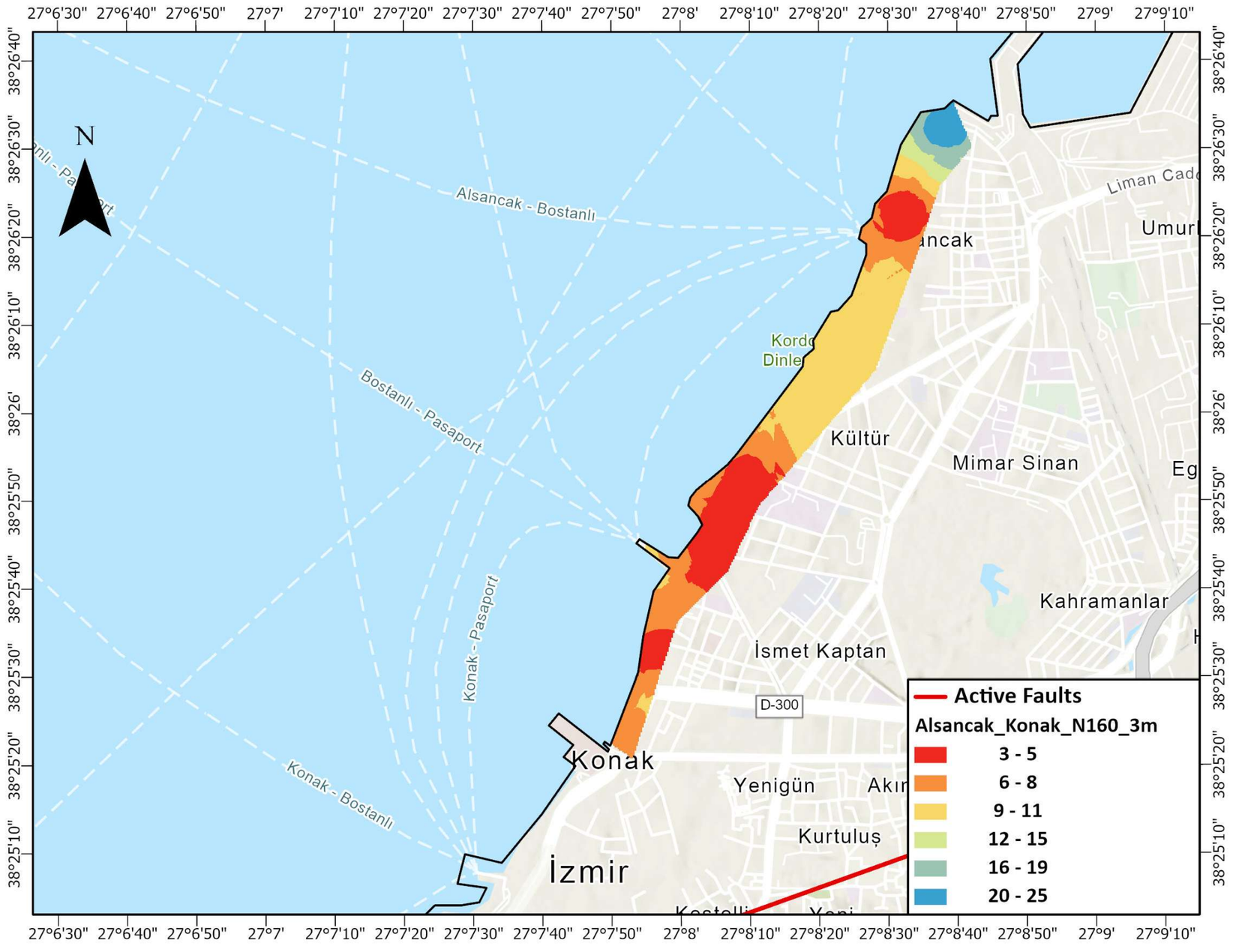

Figure A2.22 $(N_1)_{60}$ distribution at 3 m depth in the Alsancak-Konak area

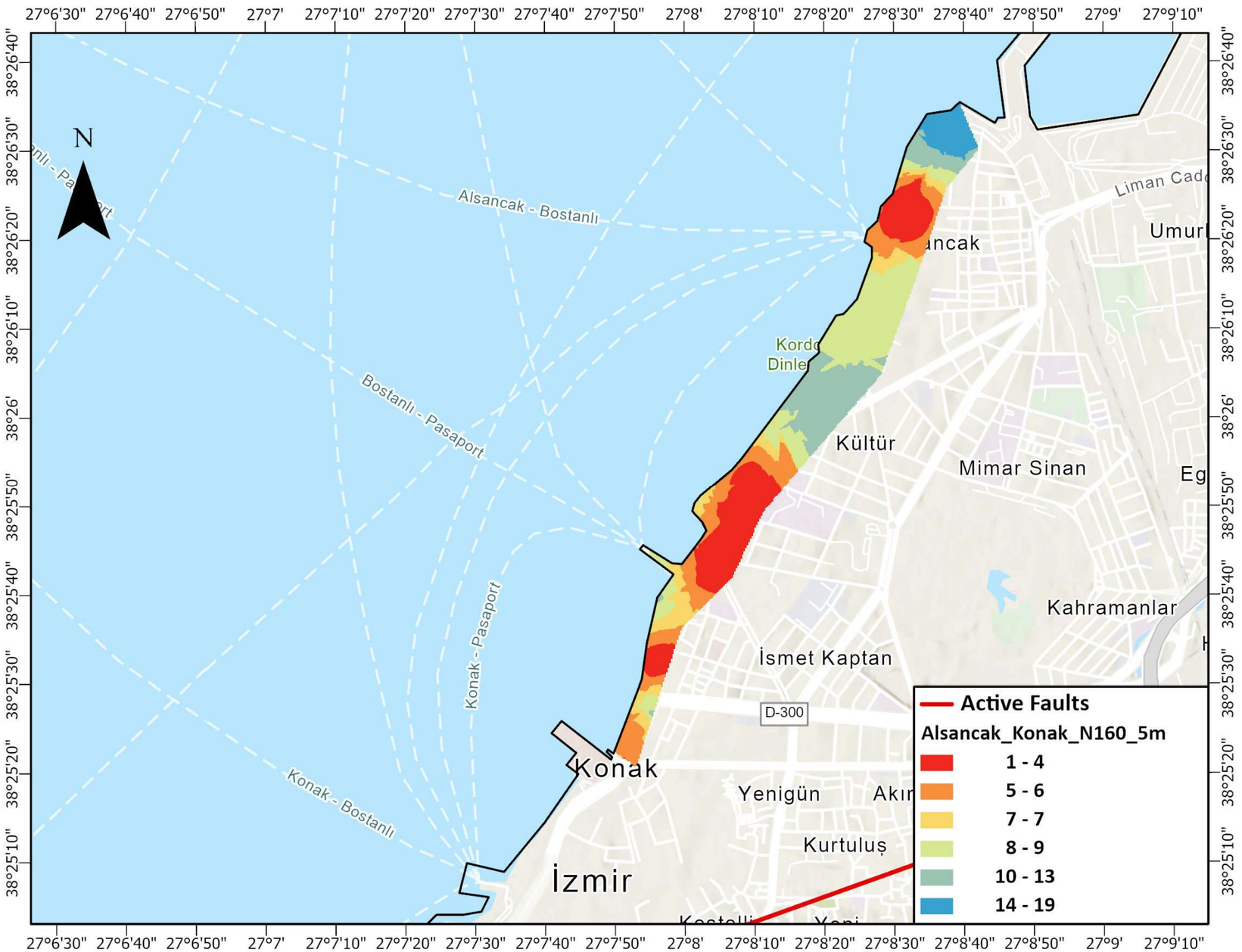

Figure A2.23 $(N_1)_{60}$ distribution at 5 m Depth in the Alsancak-Konak area

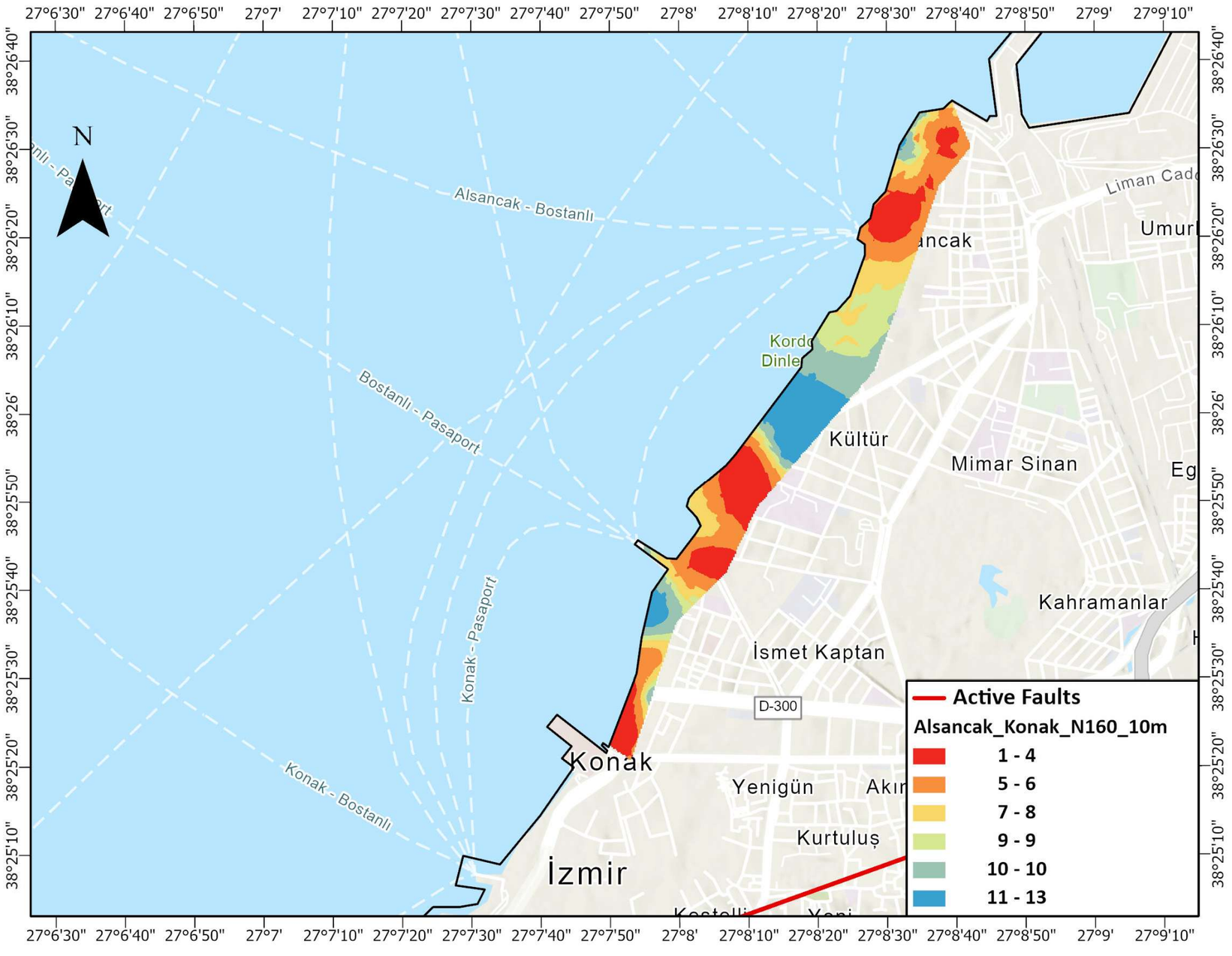

Figure A2.24 $(N_1)_{60}$ distribution at 10 m depth in the Alsancak-Konak area

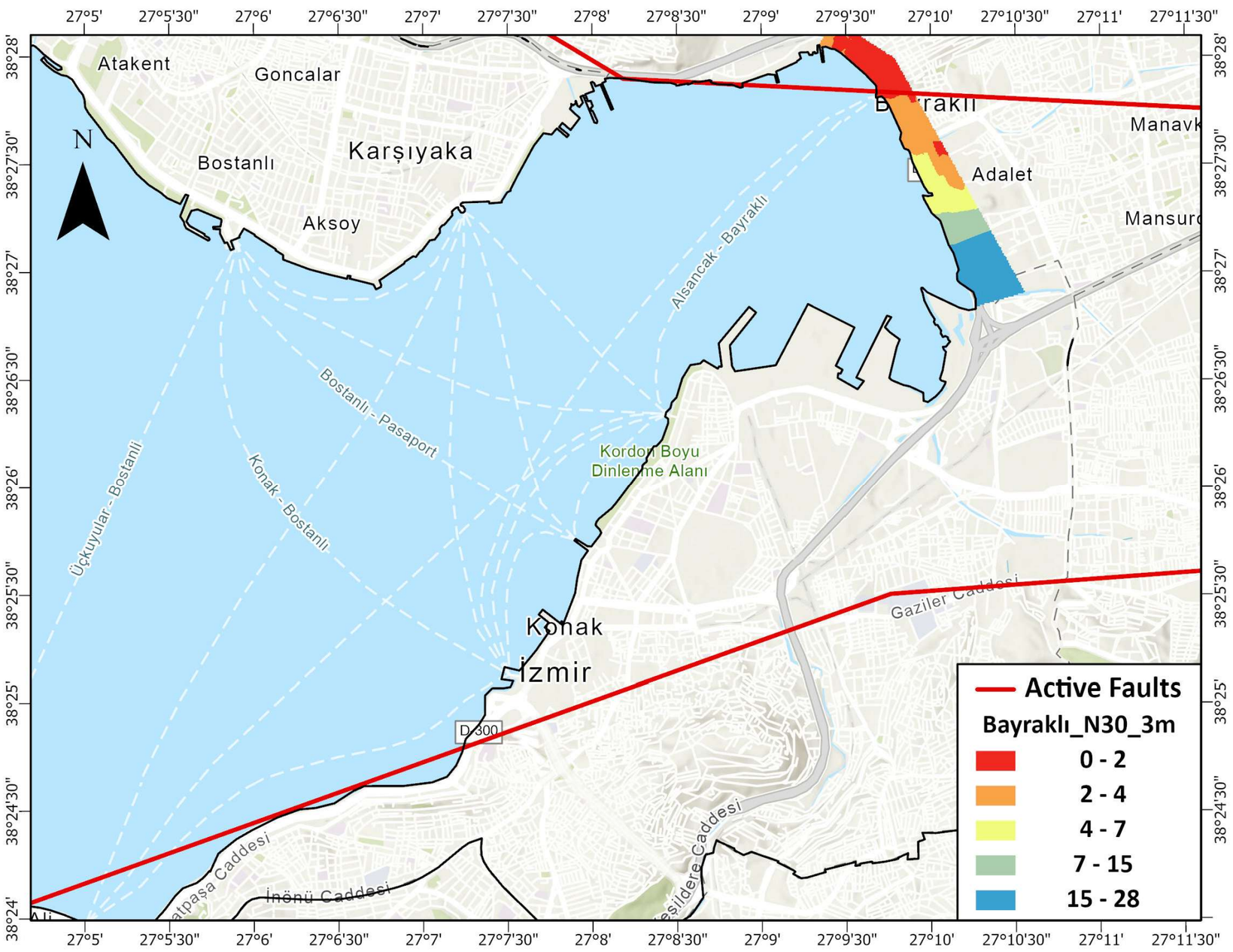

Figure A2.25 N_{30} distribution at 3 m depth in the Bayraklı area

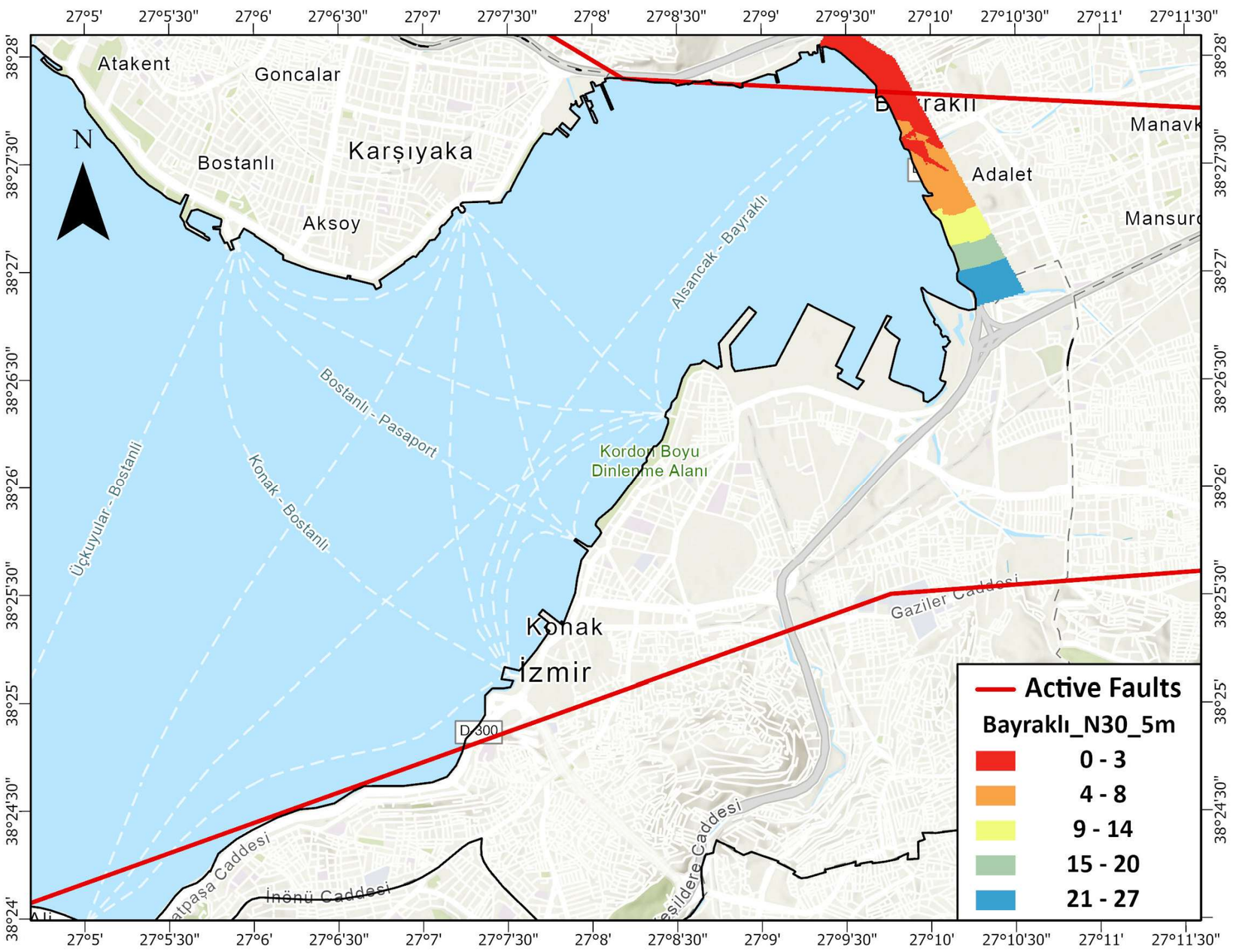

Figure A2.26 N_{30} distribution at 5 m depth in the Bayraklı area

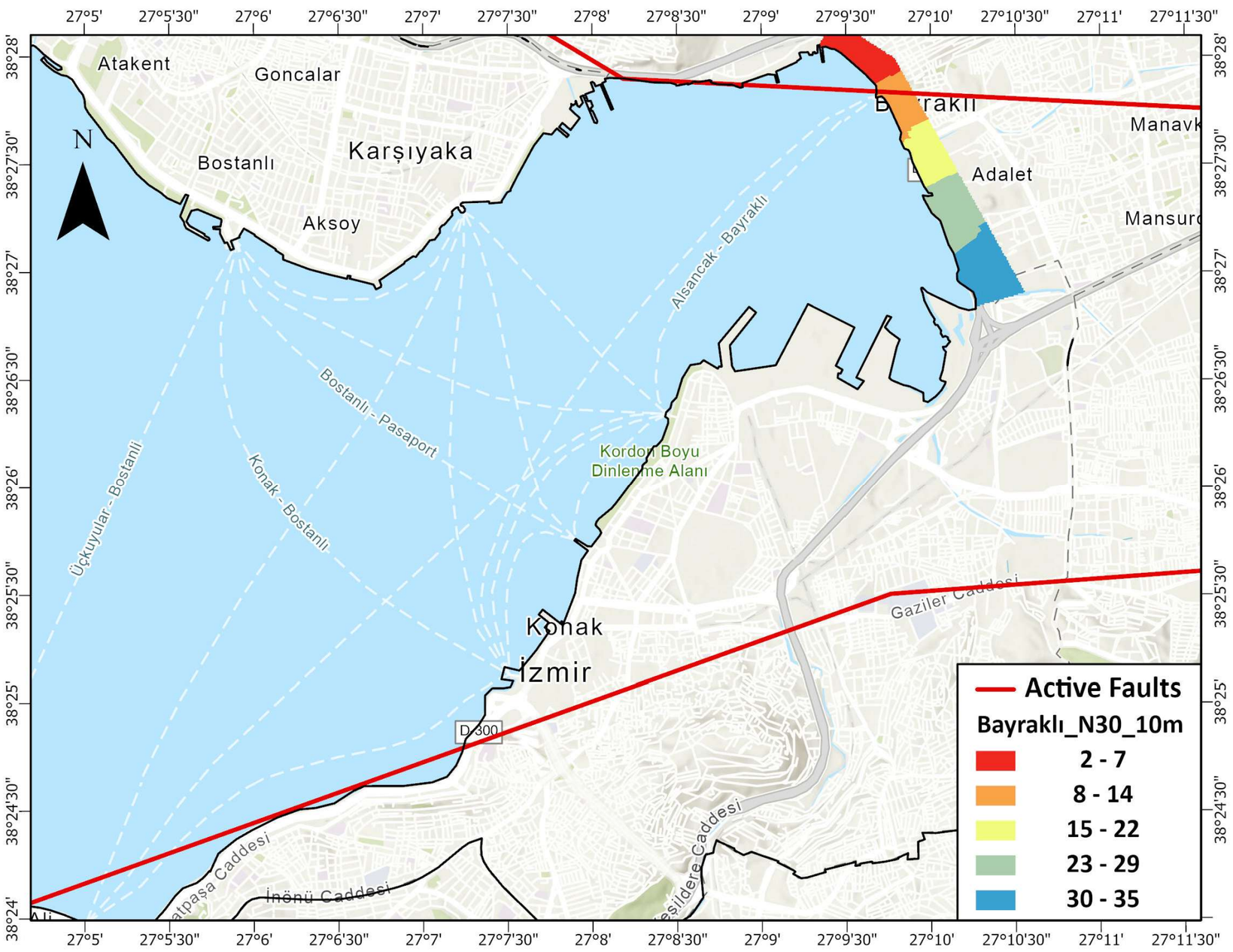

Figure A2.27 N_{30} distribution at 10 m depth in the Bayraklı area

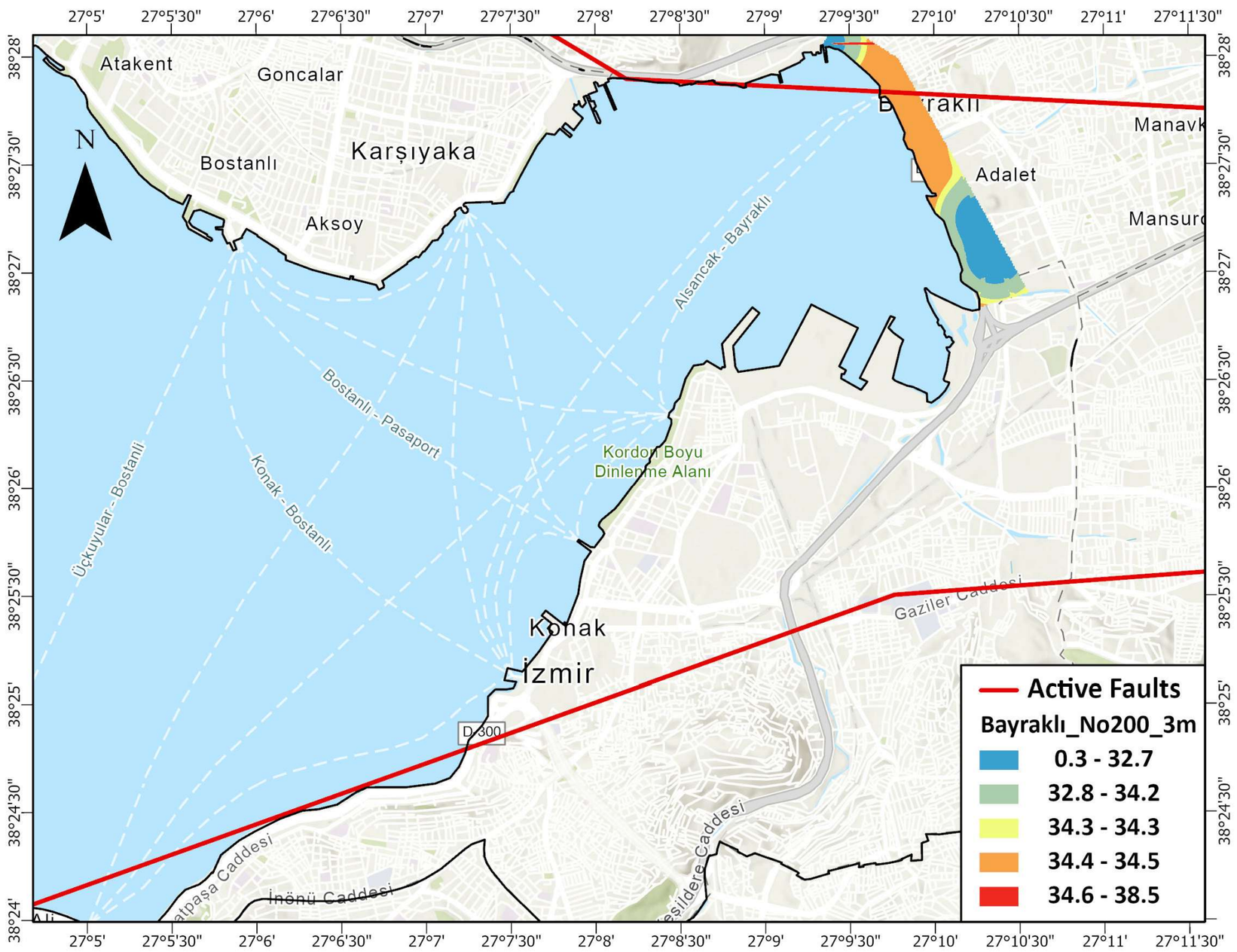

Figure A2.28 No200 distribution at 3 m depth in the Bayraklı area

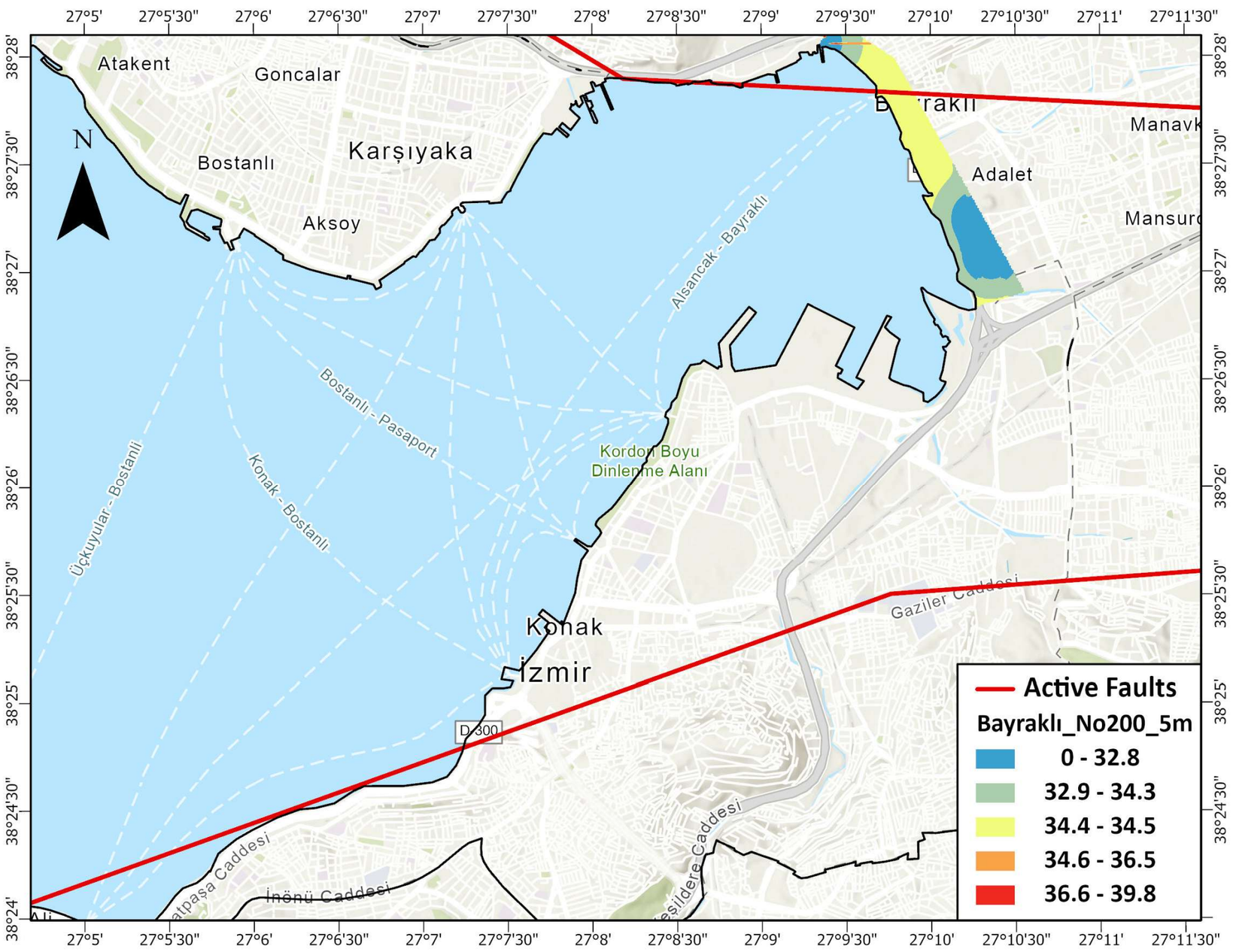

Figure A2.29 No200 distribution at 5 m depth in the Bayraklı area

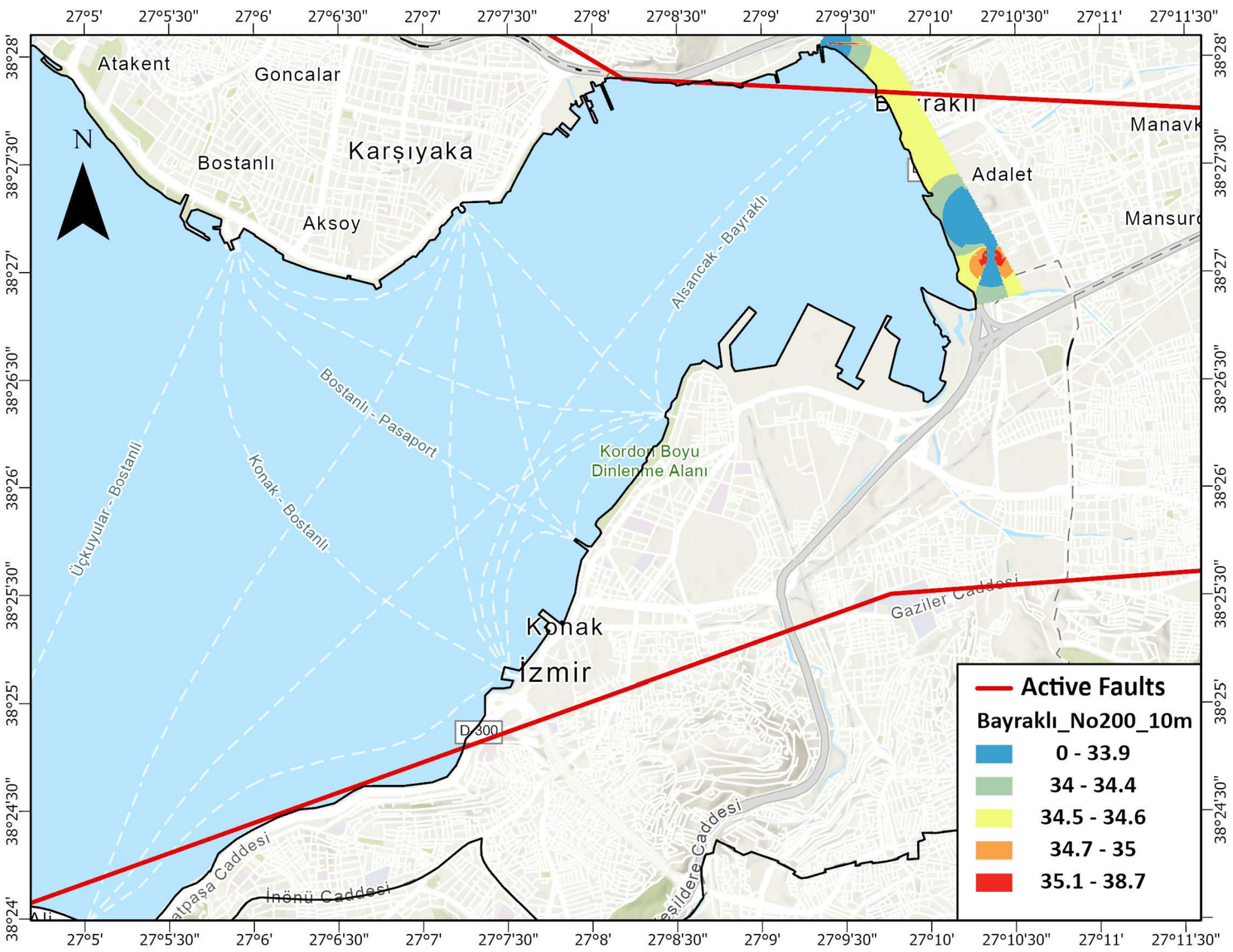

Figure A2.30 No200 distribution at 10 m depth in the Bayraklı area

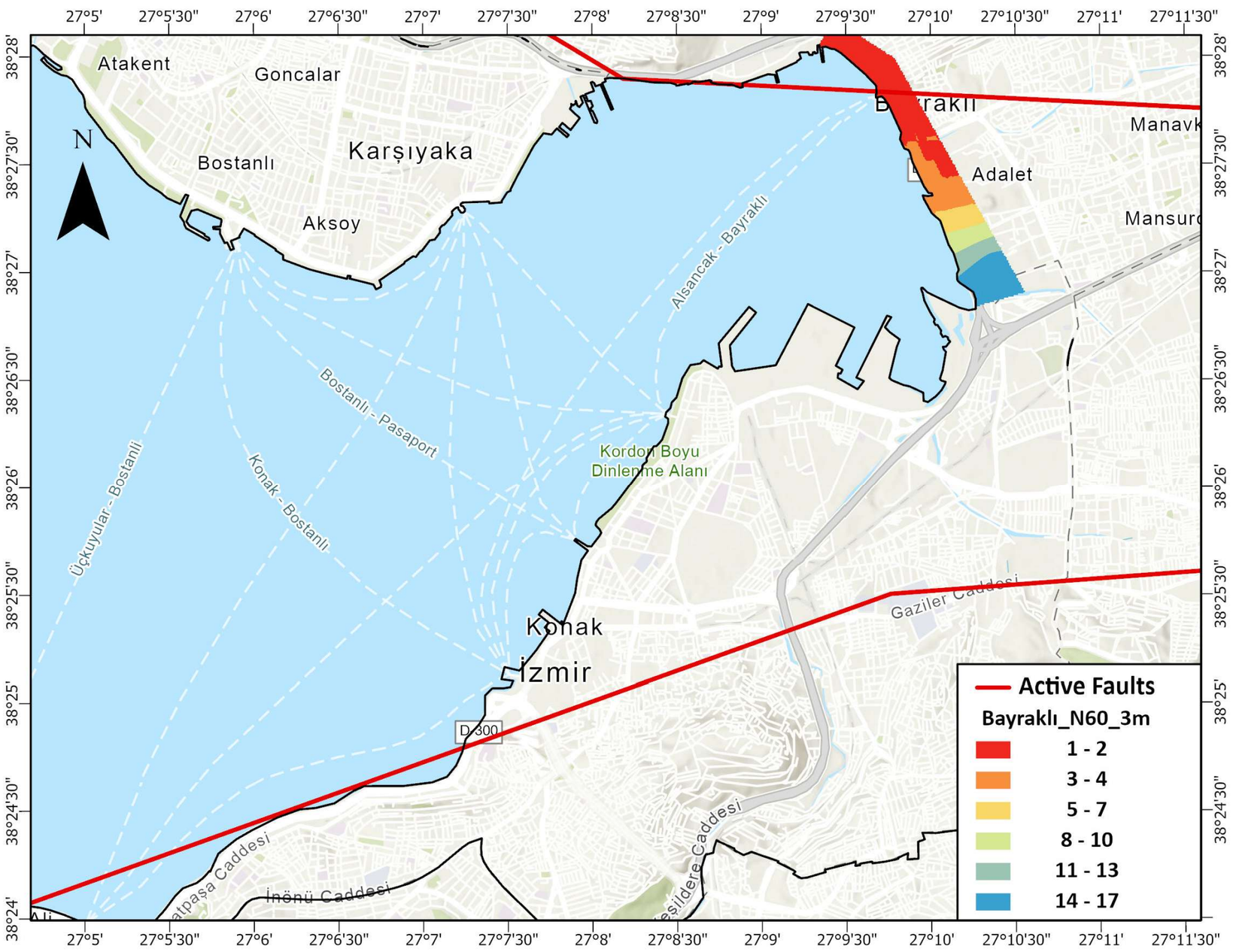

Figure A2.31 N_{60} distribution at 3 m depth in the Bayraklı area

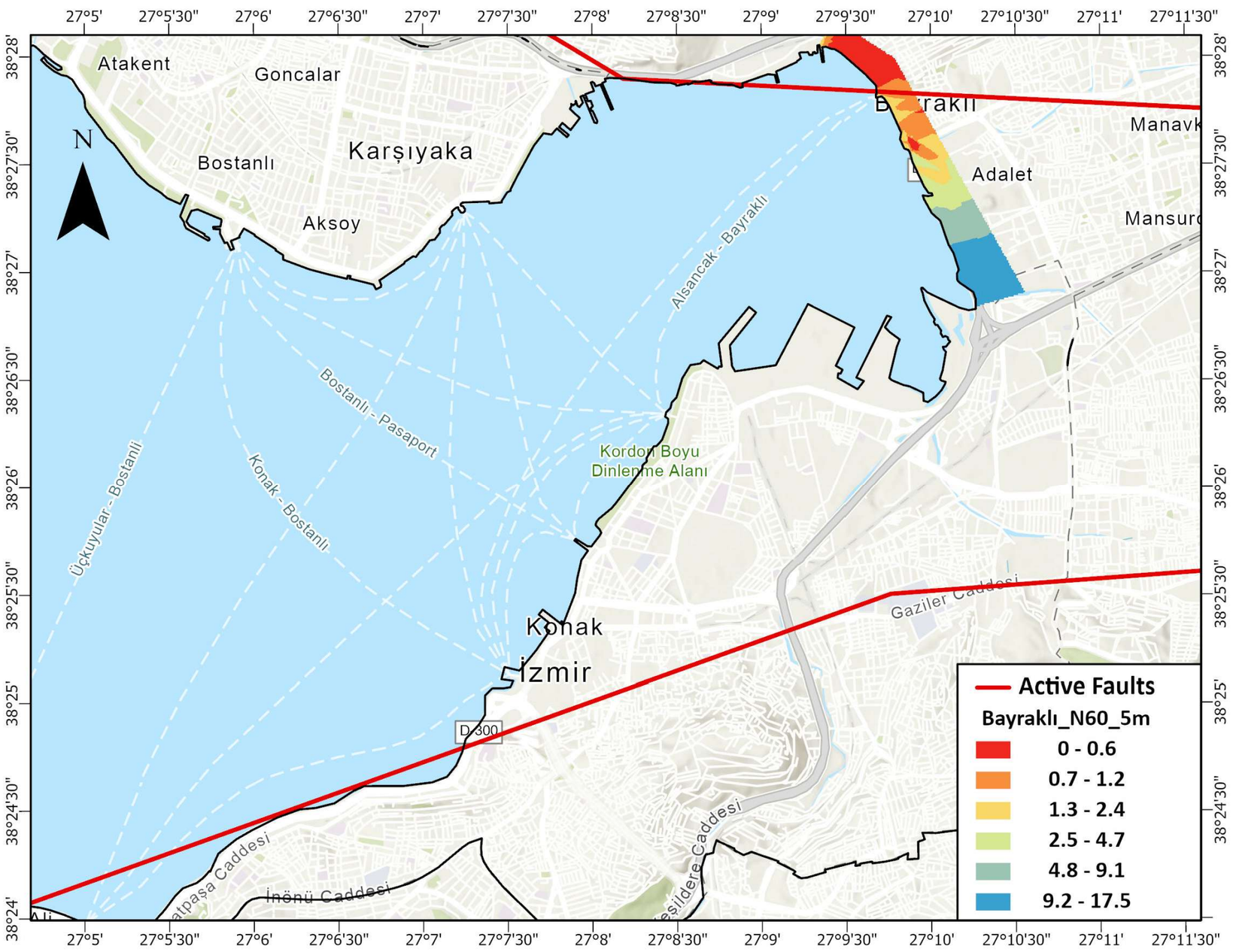

Figure A2.32 N_{60} distribution at 5 m depth in the Bayraklı area

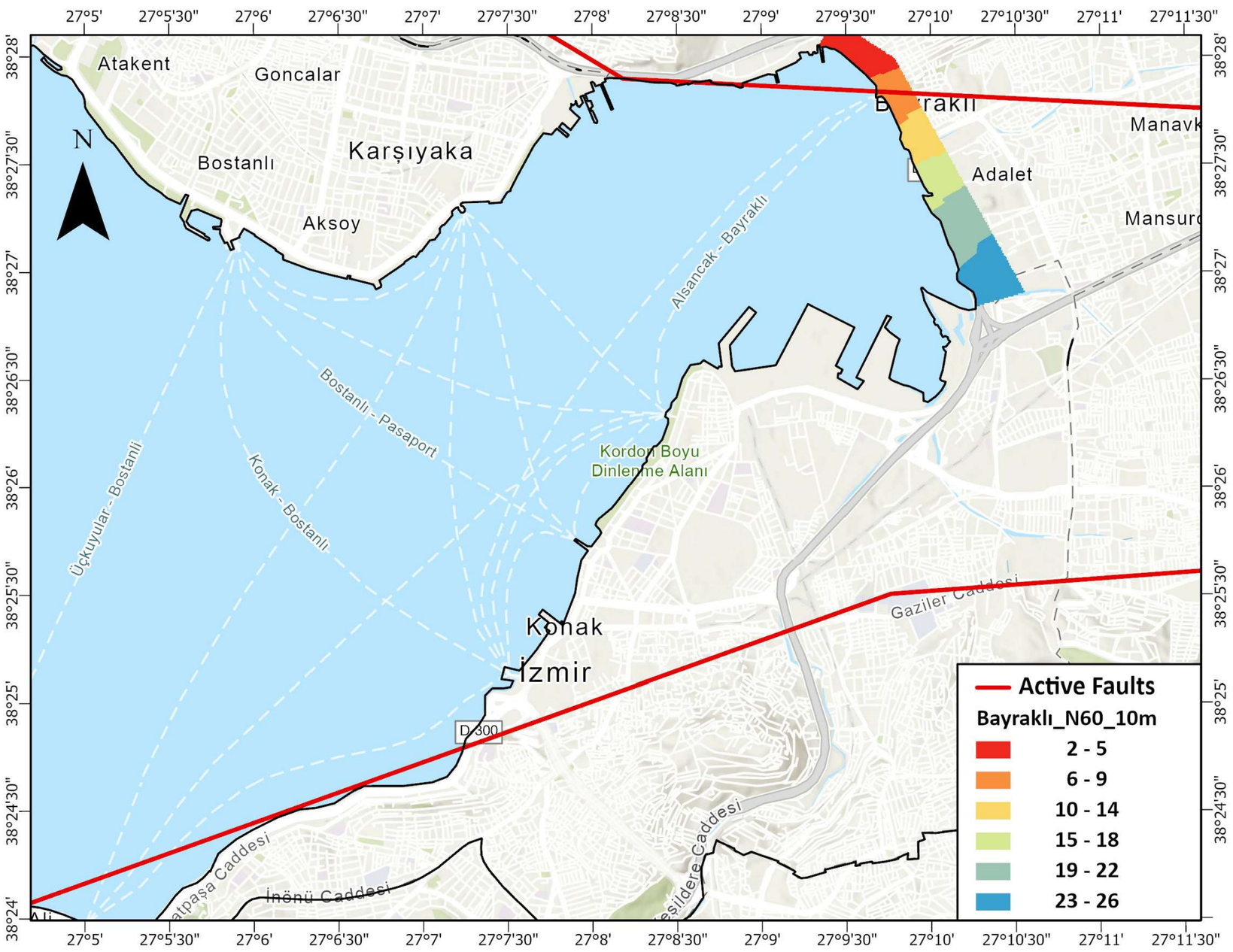

Figure A2.33 N_{60} distribution at 10 m depth in the Bayraklı area

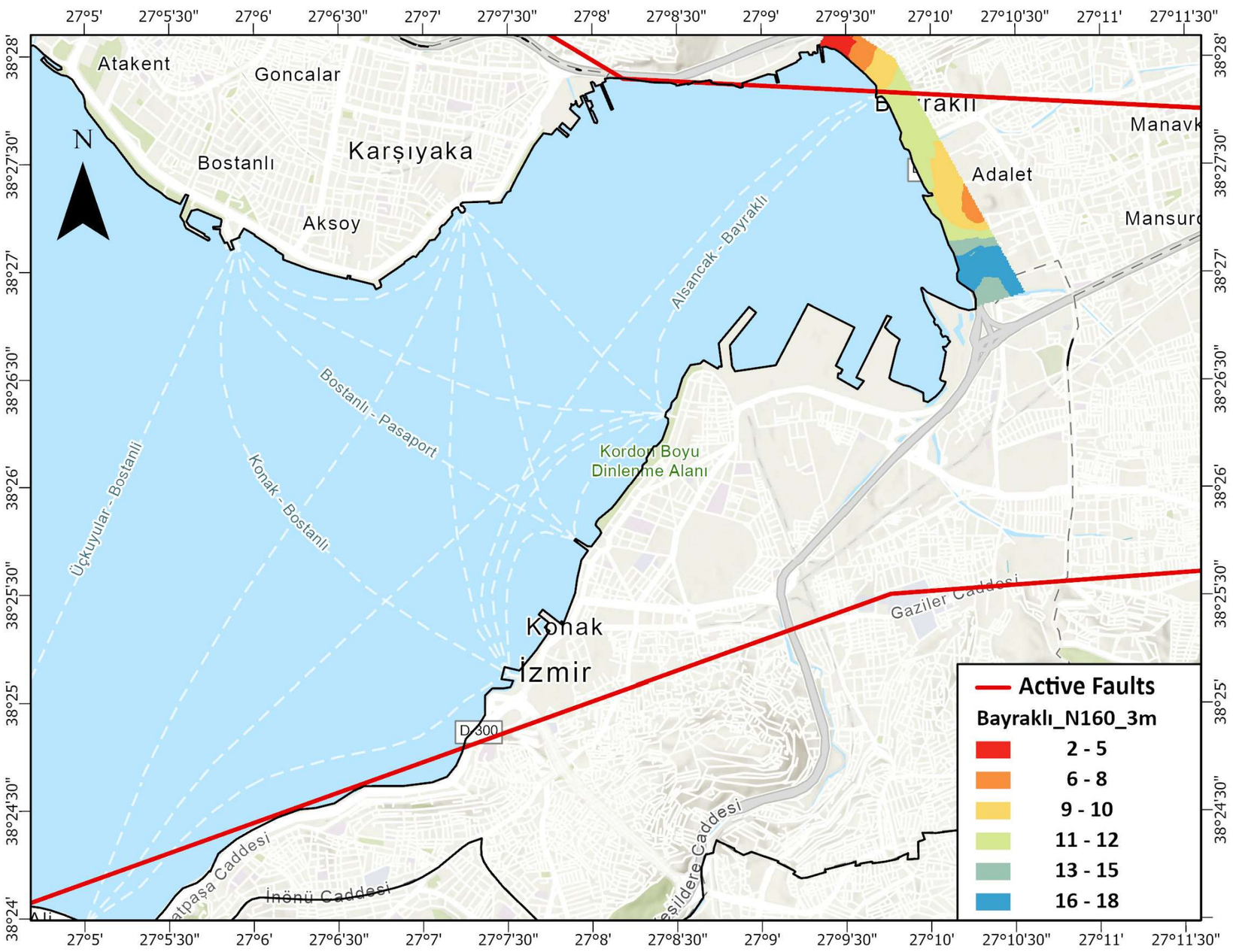

Figure A2.34 $(N1)_{60}$ distribution at 3 m depth in the Bayraklı area

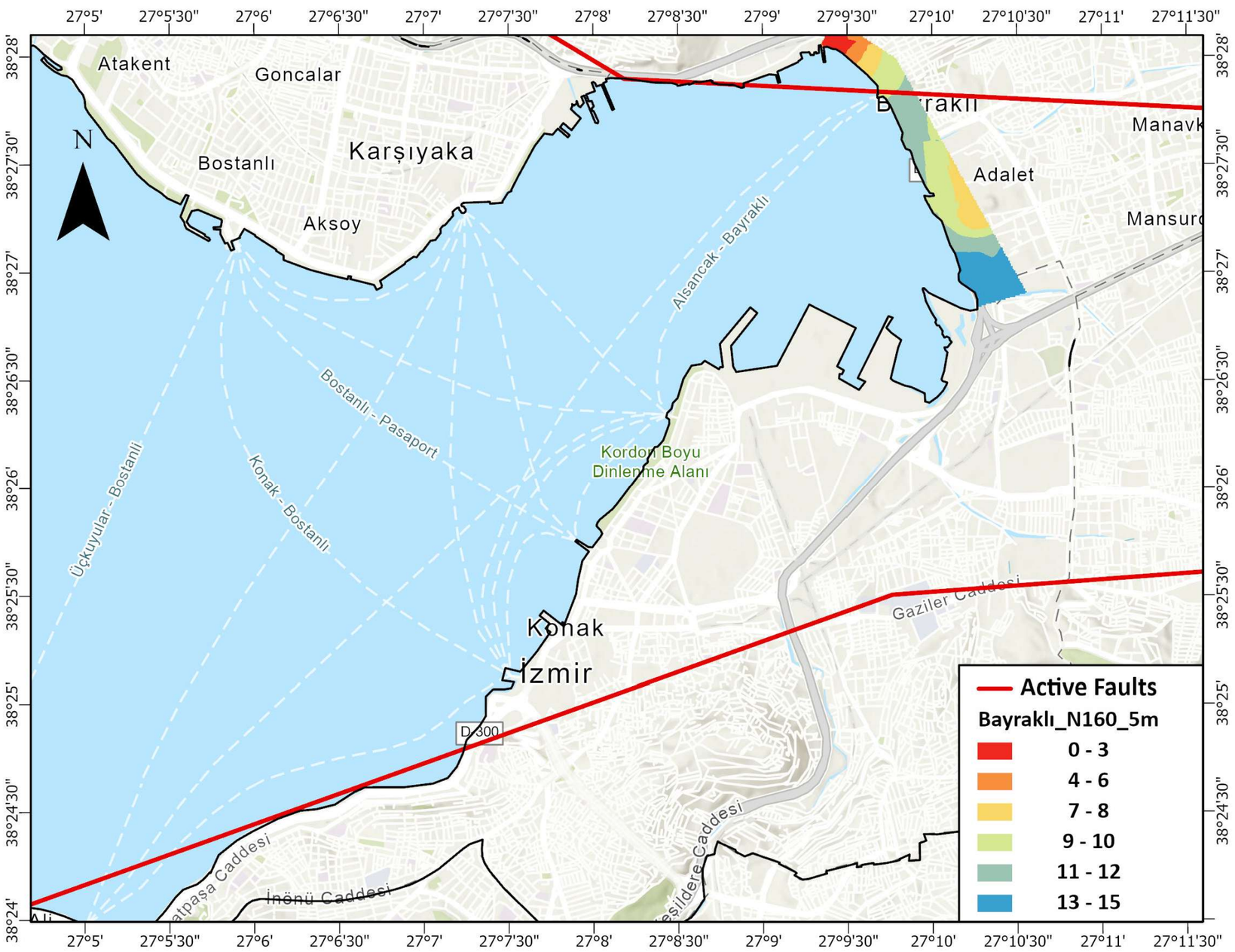

Figure A2.35 $(N1)_{60}$ distribution at 5 m depth in the Bayraklı area

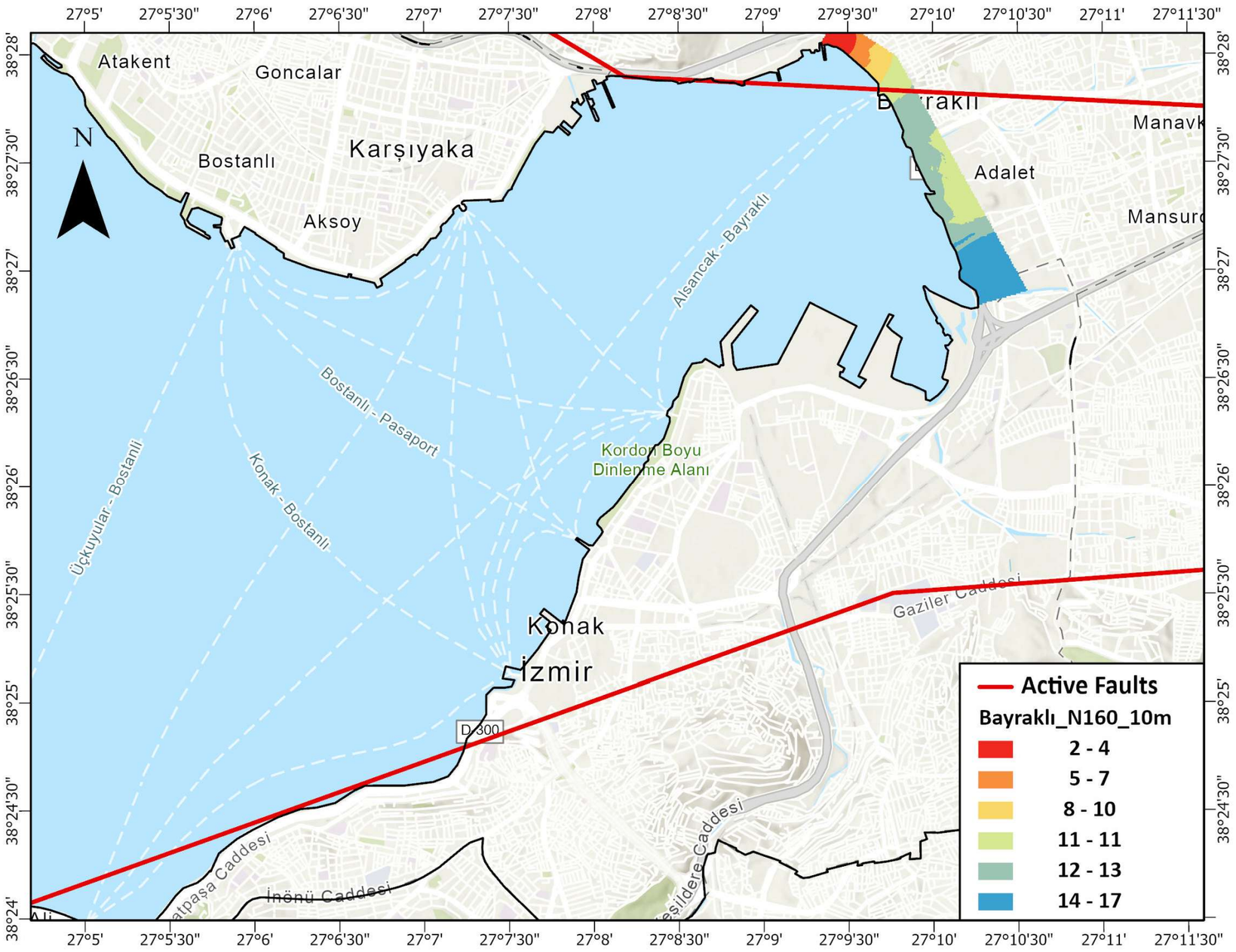

Figure A2.36 $(N1)_{60}$ distribution at 10 m depth in the Bayraklı area

Appendix-3: Liquefaction Analysis Results

Borehole #	Depth	$(N_1)_{60f}$	σ_{vo}	σ'_{vo}	rd	CSR_2	CSR_3	CRR	FS_2	FS_3
1_SK-1	8	29.85	148.1	95.8	0.93	0.431	0.164	0.457	1.53	6.16
1_SK-1	20.45	8.49	382.1	199.8	0.59	0.339	0.129	0.162	0.69	2.77
1_SK-1	22	8.32	400.1	207.8	0.58	0.331	0.126	0.160	0.70	2.80
1_SK-1	22.45	7.66	418.1	215.8	0.56	0.325	0.124	0.152	0.67	2.71
1_SK-1	24	7.52	436.1	223.8	0.55	0.320	0.122	0.150	0.68	2.73
1_SK-1	24.45	7.42	449.6	229.8	0.54	0.316	0.121	0.149	0.68	2.74
1_SK-1	25.5	7.33	463.1	235.8	0.53	0.313	0.119	0.148	0.68	2.75
1_SK-1	25.95	9.20	472.1	239.8	0.53	0.311	0.119	0.106	0.49	1.98
1_SK-1	26.5	9.13	481.1	243.8	0.53	0.309	0.118	0.105	0.49	1.98
1_SK-2	10.95	13.56	213.9	99.1	0.87	0.561	0.214	0.146	0.38	1.51
1_SK-2	12	13.08	228.9	106.6	0.85	0.544	0.208	0.141	0.37	1.50
1_SK-2	12.45	15.45	243.9	114.1	0.83	0.528	0.201	0.165	0.45	1.81
1_SK-2	13.5	14.96	258.9	121.6	0.80	0.510	0.195	0.160	0.45	1.82
1_SK-2	13.95	13.20	273.9	129.1	0.78	0.493	0.188	0.226	0.66	2.66
1_SK-2	15	12.83	288.9	136.6	0.75	0.475	0.181	0.220	0.67	2.69
1_SK-2	15.45	10.00	303.9	144.1	0.73	0.458	0.175	0.113	0.36	1.43
1_SK-2	16.5	9.75	318.9	151.6	0.70	0.442	0.169	0.111	0.36	1.45
1_SK-2	16.95	12.49	333.9	159.1	0.68	0.427	0.163	0.136	0.46	1.84
1_SK-2	18	12.20	348.9	166.6	0.66	0.413	0.157	0.133	0.46	1.87
1_SK-2	18.45	4.55	363.9	174.1	0.64	0.400	0.153	0.069	0.25	1.00
1_SK-2	19.5	4.45	378.9	181.6	0.62	0.388	0.148	0.068	0.25	1.02
1_SK-2	19.95	10.36	393.9	189.1	0.61	0.378	0.144	0.087	0.33	1.33
1_SK-2	21	10.17	408.4	196.2	0.59	0.369	0.141	0.085	0.33	1.34
1_SK-2	21.45	11.96	435.4	208.2	0.57	0.355	0.136	0.100	0.41	1.63
1_SK-2	24	11.63	462.4	220.2	0.55	0.345	0.131	0.097	0.41	1.64
1_SK-2	24.45	11.97	475.9	226.2	0.54	0.340	0.130	0.100	0.42	1.71
1_SK-2	25.5	11.81	489.4	232.2	0.53	0.336	0.128	0.099	0.42	1.71
1_SK-3	8.3	13.77	144.8	60.3	0.93	0.667	0.254	0.235	0.51	2.04
1_SK-3	8.6	13.38	152.1	63.8	0.93	0.658	0.251	0.229	0.50	2.02
1_SK-3	15	32.60	283.3	132.3	0.76	0.484	0.184	0.422	1.26	5.06
1_SK-3	15.2	31.30	307.1	143.6	0.72	0.457	0.174	0.367	1.16	4.66
1_SK-3	17.5	29.96	334.2	156.7	0.67	0.429	0.164	0.327	1.10	4.43
1_SK-3	18	29.52	343.1	161.4	0.66	0.420	0.160	0.316	1.09	4.37
1_SK-3	18.35	29.10	352.0	166.0	0.65	0.412	0.157	0.307	1.07	4.32
1_SK-3	18.85	28.70	361.0	170.7	0.64	0.404	0.154	0.298	1.06	4.28
1_SK-3	19.2	28.31	371.4	175.4	0.63	0.396	0.151	0.290	1.06	4.25
1_SK-3	20	27.98	381.6	179.6	0.61	0.389	0.148	0.284	1.05	4.24
1_SK-3	20.4	27.75	388.2	182.7	0.61	0.385	0.147	0.280	1.05	4.22
1_SK-4	7.85	12.50	154.4	73.1	0.94	0.589	0.225	0.165	0.40	1.63
1_SK-4	19.2	29.05	360.2	166.7	0.63	0.408	0.156	0.413	1.46	5.87

Borehole #	Depth	$(N_1)^*_{60}$	σ_{vo}	σ'_{vo}	rd	CSR_2	CSR_3	CRR	FS_2	FS_3
1_SK-4	19.5	28.73	367.7	170.4	0.62	0.402	0.153	0.398	1.43	5.75
1_SK-4	19.95	28.12	382.7	177.9	0.61	0.390	0.149	0.374	1.38	5.55
1_SK-4	21	27.54	397.7	185.4	0.59	0.380	0.145	0.354	1.34	5.41
1_SK-4	21.45	26.83	417.7	195.4	0.58	0.368	0.140	0.334	1.31	5.26
1_SK-6	0	28.69	42.8	20.3	0.98	0.620	0.236	0.396	0.92	3.70
1_SK-6	4.5	29.33	89.8	42.5	0.97	0.609	0.232	0.427	1.01	4.06
1_SK-6	4.95	26.34	104.0	49.3	0.96	0.606	0.231	0.321	0.76	3.07
1_SK-6	6	27.61	118.3	56.0	0.96	0.602	0.230	0.356	0.85	3.43
1_SK-6	6.45	12.59	132.5	62.8	0.95	0.598	0.228	0.137	0.33	1.33
1_SK-6	7.5	11.96	146.8	69.5	0.94	0.592	0.226	0.131	0.32	1.28
1_SK-6	7.95	22.68	175.3	83.0	0.92	0.579	0.221	0.252	0.63	2.52
1_SK-6	10.5	22.14	203.8	96.5	0.89	0.560	0.214	0.244	0.63	2.53
1_SK-6	10.95	23.62	218.0	103.3	0.87	0.548	0.209	0.267	0.70	2.82
1_SK-6	12	22.86	232.8	110.3	0.85	0.535	0.204	0.255	0.69	2.76
1_SK-6	12.5	27.04	247.0	117.0	0.83	0.521	0.199	0.340	0.94	3.78
1_SK-6	13.5	26.32	260.8	123.5	0.80	0.506	0.193	0.321	0.91	3.68
1_SK-6	13.95	13.96	299.5	139.7	0.73	0.466	0.178	0.150	0.46	1.86
1_SK-6	18	13.23	337.7	155.5	0.66	0.428	0.163	0.143	0.48	1.93
1_SK-6	18.45	12.23	363.2	166.0	0.62	0.407	0.155	0.167	0.59	2.37
1_SK-6	21	11.86	388.7	176.5	0.59	0.390	0.149	0.162	0.60	2.41
1_SK-6	21.45	11.68	401.5	181.7	0.58	0.383	0.146	0.160	0.60	2.43
1_SK-6	22.5	12.06	414.7	187.2	0.57	0.376	0.143	0.165	0.63	2.54
1_SK-6	23	11.99	420.2	189.4	0.56	0.374	0.142	0.164	0.63	2.55
1_SK-6	23.15	11.92	425.3	191.5	0.56	0.371	0.142	0.163	0.63	2.55
1_SK-6	23.6	11.19	441.0	198.0	0.55	0.365	0.139	0.155	0.61	2.46
1_SK-6	25	11.01	456.7	204.5	0.54	0.359	0.137	0.153	0.61	2.47
1_SK-6	25.45	12.98	466.1	208.8	0.53	0.356	0.136	0.096	0.39	1.56
1_SK-6	26	12.75	481.1	216.3	0.53	0.350	0.133	0.094	0.39	1.56
1_SK-6	26.95	13.54	496.1	223.8	0.52	0.344	0.131	0.101	0.42	1.69
1_SK-6	27.5	13.39	506.1	228.8	0.52	0.341	0.130	0.099	0.42	1.69
1_SK-7	11.8	9.01	218.5	99.7	0.86	0.562	0.214	0.126	0.32	1.30
1_SK-7	11.95	8.90	224.3	102.3	0.85	0.557	0.212	0.125	0.32	1.30
1_SK-7	13.55	6.27	253.5	116.0	0.80	0.523	0.199	0.099	0.27	1.10
1_SK-7	13.95	5.94	281.5	129.3	0.75	0.489	0.187	0.101	0.30	1.20
1_SK-7	16.5	5.64	311.5	143.5	0.70	0.455	0.173	0.098	0.31	1.25
1_SK-8	6	16.49	116.2	54.0	0.96	0.614	0.234	0.150	0.35	1.42
1_SK-8	6.45	5.39	132.7	63.0	0.95	0.597	0.228	0.057	0.14	0.56
1_SK-8	7.5	5.04	149.2	72.0	0.94	0.582	0.222	0.055	0.14	0.55
1_SK-16	1	2.87	32.6	15.1	0.99	0.635	0.243	0.058	0.13	0.52
1_SK-16	2.5	2.87	51.6	24.4	0.98	0.619	0.236	0.058	0.13	0.54
1_SK-16	2.95	3.06	66.3	31.5	0.98	0.611	0.233	0.059	0.14	0.56

Borehole #	Depth	$(N_1)^*_{60}$	σ_{vo}	σ'_{vo}	rd	CSR_2	CSR_3	CRR	FS_2	FS_3
1_SK-17	1	11.48	37.5	17.5	0.99	0.629	0.240	0.100	0.23	0.92
1_SK-17	3	12.24	61.4	29.1	0.98	0.613	0.234	0.107	0.25	1.01
1_SK-17	3.45	11.96	76.0	36.3	0.97	0.607	0.232	0.104	0.25	1.00
1_SK-18	1	10.52	33.6	15.6	0.99	0.634	0.242	0.118	0.27	1.08
1_SK-18	2.6	10.52	53.6	25.3	0.98	0.617	0.236	0.118	0.27	1.10
1_SK-18	3.05	11.22	72.1	34.4	0.97	0.609	0.233	0.124	0.29	1.18
1_SK-18	4.5	10.65	90.6	43.4	0.97	0.602	0.230	0.119	0.28	1.14
1_SK-18	4.95	4.77	118.0	55.7	0.96	0.602	0.230	0.085	0.20	0.82
1_SK-23	3	29.58	60.5	28.2	0.98	0.624	0.238	0.441	1.02	4.09
1_SK-25	3.5	23.51	80.1	35.6	0.97	0.649	0.248	0.271	0.60	2.42
1_SK-25	5.4	21.79	115.3	51.8	0.95	0.633	0.242	0.244	0.56	2.23
1_SK-25	7.3	19.75	139.0	63.0	0.94	0.619	0.236	0.221	0.52	2.07
1_SK-25	7.9	19.27	145.7	66.2	0.94	0.615	0.235	0.215	0.50	2.02
1_SK-25	8	18.98	149.9	68.2	0.93	0.612	0.234	0.211	0.50	2.00
1_SK-26	1.9	12.43	35.2	15.7	0.99	0.660	0.252	0.136	0.30	1.20
1_SK-26	2	12.43	40.4	18.1	0.99	0.653	0.250	0.136	0.30	1.21
1_SK-26	2.45	5.74	48.5	22.0	0.98	0.645	0.247	0.054	0.12	0.49
1_SK-31	3	6.12	58.3	26.0	0.98	0.650	0.249	0.081	0.18	0.72
1_SK-31	3.45	6.08	86.8	39.5	0.97	0.631	0.242	0.134	0.31	1.23
1_SK-32	3	14.28	63.0	28.0	0.98	0.652	0.250	0.153	0.34	1.36
1_SK-32	4	15.13	78.3	34.8	0.97	0.648	0.248	0.162	0.36	1.44
1_SK-32	4.7	14.22	88.7	39.4	0.97	0.646	0.247	0.153	0.34	1.36
1_SK-32	5.15	13.36	100.4	44.6	0.96	0.642	0.246	0.144	0.32	1.30
1_SK-33	0.5	0.96	16.2	7.2	1.00	0.665	0.255	0.049	0.11	0.43
1_SK-33	1.8	0.96	34.2	15.2	0.99	0.660	0.253	0.049	0.11	0.43
1_SK-33	2	0.96	46.8	20.8	0.98	0.657	0.251	0.049	0.11	0.43
1_SK-33	3.2	14.28	64.8	28.8	0.98	0.652	0.250	0.153	0.34	1.35
1_SK-33	4	15.17	73.8	32.8	0.97	0.650	0.249	0.162	0.36	1.44
1_SK-33	4.2	13.66	82.8	36.8	0.97	0.647	0.248	0.147	0.33	1.31
1_SK-34	0.5	0.96	13.1	5.8	1.00	0.666	0.255	0.060	0.13	0.52
1_SK-34	0.95	0.96	35.6	15.8	0.99	0.660	0.253	0.060	0.13	0.52
1_SK-34	3	1.02	63.0	28.0	0.98	0.652	0.250	0.058	0.13	0.52
1_SK-34	4	10.68	80.1	35.6	0.97	0.648	0.248	0.119	0.27	1.06
1_SK-34	4.9	9.72	96.8	43.0	0.96	0.643	0.246	0.111	0.25	0.99
1_SK-34	5.85	9.26	106.7	47.4	0.96	0.641	0.245	0.107	0.24	0.96
1_SK-34	6	10.23	109.0	48.5	0.96	0.639	0.245	0.115	0.26	1.04
1_SK-34	6.1	10.09	111.9	49.9	0.96	0.637	0.244	0.114	0.26	1.03
1_SK-35	2	0.96	40.1	17.8	0.99	0.658	0.252	0.060	0.13	0.52
1_SK-35	2.45	1.02	58.1	25.8	0.98	0.654	0.250	0.058	0.13	0.52
1_SK-35	4	1.08	76.4	34.1	0.97	0.645	0.247	0.057	0.13	0.51
1_SK-35	4.45	9.65	95.9	43.6	0.96	0.629	0.241	0.093	0.21	0.85

Borehole #	Depth	$(N_1)^*_{60}$	σ_{vo}	σ'_{vo}	rd	CSR_2	CSR_3	CRR	FS_2	FS_3
1_SK-35	6	9.77	115.4	53.1	0.96	0.617	0.236	0.094	0.22	0.88
1_SK-35	6.45	9.18	130.0	60.3	0.95	0.608	0.233	0.089	0.21	0.84
1_SK-35	7.5	19.03	145.4	67.9	0.94	0.598	0.229	0.252	0.61	2.43
1_SK-35	8	18.36	155.1	72.9	0.93	0.591	0.226	0.241	0.59	2.36
1_SK-35	8.45	16.90	180.7	86.0	0.91	0.571	0.219	0.219	0.55	2.22
1_SK-35	10.5	16.57	206.4	99.1	0.89	0.550	0.211	0.215	0.56	2.25
1_SK-36	3.5	3.06	67.1	29.8	0.97	0.651	0.249	0.073	0.16	0.64
1_SK-36	5.8	25.66	116.1	52.1	0.95	0.632	0.242	0.254	0.58	2.32
1_SK-36	7	23.93	132.2	59.9	0.95	0.620	0.237	0.229	0.53	2.13
1_SK-36	7.45	23.29	139.0	63.3	0.94	0.615	0.236	0.220	0.52	2.07
1_SK-36	7.7	4.27	151.7	69.7	0.93	0.604	0.231	0.076	0.18	0.73
1_SK-36	8.7	4.05	166.6	77.3	0.92	0.591	0.226	0.074	0.18	0.72
1_SK-36	9.15	3.98	171.7	79.9	0.92	0.587	0.225	0.074	0.18	0.72
1_SK-36	9.2	3.94	175.3	81.8	0.92	0.584	0.224	0.073	0.18	0.73
1_SK-36	9.5	3.87	180.9	84.7	0.91	0.579	0.222	0.073	0.18	0.73
1_SK-36	9.75	3.81	186.0	87.3	0.91	0.574	0.220	0.072	0.18	0.73
1_SK-36	10	3.93	193.2	91.0	0.90	0.568	0.218	0.073	0.19	0.74
1_SK-39	1.5	3.83	33.6	16.4	0.99	0.603	0.231	0.064	0.15	0.61
1_SK-39	1.95	23.91	48.3	23.5	0.98	0.599	0.230	0.272	0.65	2.62
1_SK-39	3	25.50	62.9	30.6	0.98	0.596	0.228	0.302	0.73	2.93
1_SK-39	3.45	22.10	106.8	52.0	0.96	0.587	0.225	0.231	0.57	2.27
1_SK-39	7.5	4.16	150.6	73.4	0.94	0.574	0.220	0.058	0.15	0.59
1_SK-39	7.95	3.97	165.3	80.5	0.93	0.568	0.217	0.057	0.15	0.58
1_SK-39	9	6.09	179.9	87.6	0.92	0.560	0.215	0.072	0.18	0.74
1_SK-39	9.45	5.86	194.5	94.8	0.91	0.552	0.211	0.070	0.18	0.73
1_SK-39	10.5	3.71	209.6	102.1	0.89	0.542	0.208	0.056	0.15	0.59
1_SK-39	11	3.63	218.9	106.6	0.88	0.535	0.205	0.055	0.15	0.60
1_SK-39	11.45	4.94	231.6	112.8	0.86	0.524	0.201	0.063	0.17	0.70
1_SK-39	12.3	4.81	244.2	119.0	0.84	0.513	0.196	0.063	0.18	0.70
1_SK-39	12.75	4.03	255.9	124.7	0.82	0.502	0.192	0.065	0.19	0.75
1_SK-39	13.5	3.94	267.6	130.4	0.80	0.490	0.188	0.064	0.19	0.76
1_SK-39	13.95	3.82	284.2	138.5	0.78	0.473	0.181	0.064	0.19	0.78
1_SK-39	15.2	3.73	298.8	145.6	0.75	0.457	0.175	0.063	0.20	0.80
1_SK-39	15.45	3.65	311.5	151.8	0.73	0.444	0.170	0.063	0.20	0.81
1_SK-39	16.5	29.75	326.1	158.9	0.70	0.430	0.164	0.451	1.51	6.06
1_SK-39	16.95	29.10	340.8	166.0	0.68	0.416	0.159	0.415	1.44	5.77
1_SK-39	18	28.50	355.4	173.1	0.66	0.403	0.154	0.388	1.39	5.57
1_SK-39	18.45	27.93	370.0	180.3	0.64	0.391	0.150	0.367	1.35	5.42
1_SK-39	19.5	27.39	384.6	187.4	0.62	0.380	0.146	0.350	1.33	5.31
2_SK-1	4.95	10.54	109.5	71.8	0.96	0.438	0.167	0.141	0.47	1.87
2_SK-1	6	11.22	124.3	79.0	0.96	0.448	0.171	0.149	0.48	1.92

Borehole #	Depth	$(N_1)^{*}_{60}$	σ_{vo}	σ'_{vo}	rd	CSR_2	CSR_3	CRR	FS_2	FS_3
2_SK-1	6.45	12.31	138.5	85.8	0.95	0.457	0.174	0.161	0.51	2.04
2_SK-1	7.5	11.85	152.8	92.5	0.94	0.463	0.177	0.156	0.48	1.95
2_SK-1	19.95	25.28	399.0	211.3	0.61	0.343	0.131	0.306	1.29	5.18
2_SK-1	21	24.91	412.9	217.6	0.59	0.336	0.128	0.298	1.28	5.14
2_SK-1	21.45	7.02	426.8	224.0	0.58	0.330	0.126	0.088	0.38	1.54
2_SK-1	22.5	6.92	440.6	230.4	0.57	0.325	0.124	0.087	0.39	1.55
3_SK-1	9.5	14.50	182.1	107.1	0.90	0.459	0.175	0.197	0.62	2.48
3_SK-1	10.5	14.12	195.2	112.9	0.89	0.459	0.175	0.192	0.60	2.42
3_SK-1	12.45	11.70	237.9	133.2	0.83	0.441	0.168	0.204	0.67	2.68
3_SK-1	13.5	11.41	252.2	139.9	0.80	0.432	0.165	0.200	0.67	2.68
3_SK-1	13.95	11.16	266.1	146.4	0.78	0.422	0.161	0.196	0.67	2.70
3_SK-1	15	10.91	280.5	153.0	0.75	0.412	0.157	0.193	0.68	2.72
3_SK-1	15.5	10.69	294.4	159.4	0.73	0.401	0.153	0.190	0.68	2.75
3_SK-1	18	24.20	334.9	177.6	0.66	0.372	0.142	0.462	1.79	7.20
3_SK-2	10.95	14.86	213.0	123.3	0.87	0.449	0.171	0.177	0.57	2.29
3_SK-2	12	14.47	227.3	130.0	0.85	0.443	0.169	0.173	0.56	2.26
3_SK-2	12.45	17.96	241.5	136.8	0.83	0.436	0.166	0.211	0.70	2.80
3_SK-2	13.5	17.53	255.8	143.5	0.80	0.427	0.163	0.205	0.69	2.79
3_SK-2	18.45	18.58	353.0	188.3	0.64	0.359	0.137	0.264	1.06	4.26
3_SK-2	19.5	18.28	366.9	194.6	0.62	0.351	0.134	0.258	1.06	4.26
3_SK-2	19.95	12.70	380.8	201.0	0.61	0.344	0.131	0.163	0.68	2.74
3_SK-2	21	12.49	395.1	207.6	0.59	0.337	0.128	0.160	0.69	2.76
3_SK-2	21.5	12.31	409.0	214.0	0.58	0.331	0.126	0.158	0.69	2.77
3_SK-2	22.5	12.13	422.4	220.1	0.57	0.326	0.124	0.156	0.69	2.78
3_SK-2	25.95	8.96	492.5	252.8	0.53	0.306	0.117	0.168	0.79	3.17
3_SK-2	27	8.83	507.5	260.3	0.52	0.303	0.116	0.166	0.79	3.18
3_SK-2	27.45	15.12	522.5	267.8	0.52	0.300	0.114	0.199	0.95	3.84
3_SK-2	28.5	14.92	537.5	275.3	0.51	0.297	0.113	0.196	0.95	3.83
3_SK-3	6.5	6.16	129.6	85.6	0.95	0.428	0.163	0.100	0.33	1.35
3_SK-3	7.5	5.92	144.1	92.9	0.94	0.436	0.166	0.097	0.32	1.29
3_SK-3	10.95	5.31	216.6	127.8	0.87	0.440	0.168	0.092	0.30	1.21
3_SK-3	12	5.17	231.1	134.9	0.85	0.435	0.166	0.091	0.30	1.21
3_SK-3	12.45	6.32	244.6	140.9	0.83	0.429	0.163	0.137	0.46	1.85
3_SK-3	13.5	6.19	258.1	146.9	0.80	0.421	0.161	0.135	0.46	1.86
3_SK-3	13.95	6.07	271.6	152.9	0.78	0.413	0.157	0.134	0.47	1.88
3_SK-3	15	7.73	285.6	159.1	0.75	0.403	0.154	0.153	0.55	2.20
3_SK-3	15.5	7.58	299.3	165.3	0.73	0.393	0.150	0.151	0.55	2.23
3_SK-3	16.5	7.45	312.7	171.5	0.70	0.383	0.146	0.150	0.56	2.26
3_SK-3	16.95	7.31	326.6	177.8	0.68	0.374	0.142	0.148	0.57	2.30
3_SK-3	18	7.18	340.9	184.4	0.66	0.364	0.139	0.146	0.58	2.33
3_SK-3	18.5	7.06	354.8	190.8	0.64	0.356	0.136	0.145	0.59	2.37

Borehole #	Depth	$(N_1)^{*}_{60}$	σ_{vo}	σ'_{vo}	rd	CSR_2	CSR_3	CRR	FS_2	FS_3
3_SK-4	1.5	22.95	29.8	29.8	0.99	0.295	0.112	0.253	1.24	4.98
3_SK-4	2	21.59	39.1	39.1	0.98	0.294	0.112	0.233	1.15	4.61
3_SK-4	2.6	19.90	48.0	46.0	0.98	0.305	0.116	0.211	1.00	4.01
3_SK-4	3	20.40	56.1	49.8	0.98	0.328	0.125	0.217	0.95	3.84
3_SK-4	3.45	19.14	70.3	56.6	0.97	0.361	0.138	0.202	0.81	3.25
3_SK-4	4.5	19.19	85.1	63.6	0.97	0.386	0.147	0.203	0.76	3.04
3_SK-4	5	24.42	98.8	69.8	0.96	0.406	0.155	0.372	1.32	5.31
3_SK-4	9.45	8.22	181.8	108.1	0.91	0.454	0.173	0.119	0.38	1.52
3_SK-4	10.5	8.41	195.9	114.6	0.89	0.453	0.173	0.121	0.39	1.55
3_SK-4	12.45	9.70	238.3	134.6	0.83	0.437	0.167	0.141	0.47	1.87
3_SK-4	13.5	9.45	252.9	141.6	0.80	0.428	0.163	0.138	0.47	1.88
3_SK-4	15	23.60	279.9	153.6	0.75	0.409	0.156	0.438	1.54	6.20
3_SK-5	12.5	5.15	238.8	135.8	0.83	0.434	0.165	0.124	0.41	1.65
3_SK-5	13.5	5.04	251.8	141.6	0.80	0.426	0.163	0.123	0.41	1.67
3_SK-5	13.95	23.46	265.3	147.6	0.78	0.418	0.159	0.333	1.15	4.63
3_SK-5	15	22.96	279.3	154.0	0.75	0.407	0.155	0.320	1.13	4.55
3_SK-6	6.5	7.05	126.8	82.8	0.95	0.433	0.165	0.110	0.37	1.47
3_SK-6	7.5	6.81	139.9	88.6	0.94	0.443	0.169	0.107	0.35	1.41
3_SK-6	21.5	18.87	410.4	216.4	0.58	0.329	0.125	0.216	0.95	3.81
3_SK-6	22.5	18.58	424.4	223.2	0.57	0.323	0.123	0.212	0.95	3.81
3_SK-6	24.5	14.97	465.4	241.4	0.54	0.311	0.119	0.189	0.87	3.52
3_SK-6	25.5	14.79	478.4	247.2	0.53	0.308	0.118	0.187	0.87	3.51
3_SK-6	25.95	6.60	491.9	253.2	0.53	0.306	0.117	0.106	0.50	2.02
3_SK-6	27	6.52	505.4	259.2	0.52	0.303	0.116	0.106	0.50	2.02
3_SK-6	27.45	18.42	518.9	265.2	0.52	0.301	0.115	0.257	1.23	4.95
3_SK-6	28.5	18.22	532.4	271.2	0.51	0.299	0.114	0.253	1.22	4.91
3_SK-6	28.95	18.02	545.9	277.2	0.50	0.297	0.113	0.328	1.60	6.42
3_SK-6	30	17.82	559.9	283.4	0.50	0.295	0.112	0.322	1.58	6.34
3_SK-7	7.5	2.25	141.4	90.1	0.94	0.440	0.168	0.066	0.22	0.87
3_SK-7	7.95	2.18	154.9	96.1	0.93	0.448	0.171	0.065	0.21	0.85
3_SK-7	9	2.12	168.4	102.1	0.92	0.452	0.172	0.065	0.21	0.83
3_SK-7	9.45	2.08	177.4	106.1	0.91	0.454	0.173	0.065	0.20	0.82
3_SK-7	16.5	10.96	310.3	169.1	0.70	0.386	0.147	0.194	0.72	2.91
3_SK-7	16.95	10.82	319.8	173.6	0.69	0.379	0.144	0.192	0.73	2.93
4_SK-1	7.95	9.24	108.0	85.7	0.93	0.348	0.133	0.106	0.44	1.77
4_SK-1	9.5	8.83	126.0	93.7	0.91	0.365	0.139	0.103	0.41	1.64
4_SK-1	18.95	22.42	302.4	170.2	0.62	0.331	0.126	0.302	1.32	5.29
4_SK-1	20.5	21.91	320.4	178.2	0.60	0.324	0.123	0.291	1.29	5.21
4_SK-2	10	2.26	117.0	99.5	0.90	0.316	0.120	0.066	0.30	1.22
4_SK-2	10.5	2.20	126.5	104.3	0.89	0.322	0.123	0.066	0.29	1.18
4_SK-3	6	0.91	63.8	61.6	0.96	0.296	0.113	0.049	0.24	0.95

Borehole #	Depth	$(N_1)^{\circ}_{60}$	σ_{vo}	σ'_{vo}	rd	CSR_2	CSR_3	CRR	FS_2	FS_3
4_SK-3	6.45	0.87	76.6	66.8	0.95	0.324	0.124	0.049	0.22	0.87
4_SK-5	5.8	0.00	84.6	63.1	0.95	0.381	0.145	0.049	0.18	0.74
4_SK-5	7.5	0.00	104.5	72.5	0.94	0.405	0.154	0.049	0.17	0.70
4_SK-6	12.95	11.76	182.3	117.5	0.81	0.375	0.143	0.151	0.58	2.34
4_SK-6	14	11.30	199.5	127.3	0.79	0.368	0.140	0.146	0.57	2.31
4_SK-6	19.95	21.56	313.9	184.1	0.62	0.315	0.120	0.333	1.53	6.15
4_SK-6	20	21.28	323.9	188.9	0.61	0.311	0.119	0.325	1.51	6.07
4_SK-6	21	20.93	337.6	195.4	0.59	0.306	0.117	0.315	1.48	5.97
4_SK-8	14.95	17.36	213.1	126.1	0.75	0.380	0.145	0.309	1.17	4.72
4_SK-8	15.45	16.67	234.1	136.9	0.72	0.368	0.140	0.292	1.14	4.61
4_SK-8	17	16.06	254.6	147.4	0.69	0.355	0.135	0.278	1.13	4.54
4_SK-8	39.45	17.38	695.4	360.7	0.46	0.262	0.100	0.310	1.70	6.85
4_SK-8	40.5	17.19	710.8	368.5	0.45	0.261	0.099	0.305	1.69	6.78
4_SK-10	13.45	6.92	179.8	95.1	0.80	0.449	0.171	0.107	0.34	1.39
4_SK-10	14.5	6.67	194.8	102.6	0.77	0.436	0.166	0.105	0.35	1.39
4_SK-10	14.95	17.16	209.8	110.1	0.74	0.424	0.162	0.227	0.77	3.11
4_SK-10	16	16.60	224.8	117.6	0.72	0.411	0.157	0.219	0.77	3.09
4_SK-10	34.95	26.12	616.6	316.8	0.47	0.275	0.105	0.313	1.64	6.60
4_SK-10	36	25.75	633.5	326.2	0.47	0.273	0.104	0.304	1.61	6.47
4_SK-11	5.7	0.00	89.7	48.7	0.95	0.525	0.198	0.051	0.14	0.57
4_SK-11	7.5	0.00	110.5	58.2	0.94	0.534	0.202	0.051	0.14	0.56
4_SK-11	7.95	0.00	124.3	64.6	0.93	0.536	0.203	0.050	0.13	0.54
4_SK-11	9	0.00	138.2	71.0	0.92	0.535	0.202	0.050	0.13	0.54
4_SK-11	12.95	7.34	214.1	104.4	0.81	0.498	0.188	0.109	0.32	1.28
4_SK-11	14	7.09	229.1	111.9	0.79	0.482	0.182	0.107	0.32	1.30
4_SK-11	40.95	12.50	758.4	368.7	0.45	0.277	0.105	0.215	1.12	4.55
4_SK-11	42	12.36	774.2	376.9	0.45	0.275	0.104	0.213	1.12	4.54
4_SK-11	42.45	10.70	789.9	385.2	0.45	0.273	0.103	0.190	1.00	4.07
4_SK-11	43.5	10.59	805.7	393.4	0.44	0.271	0.103	0.189	1.00	4.07
4_SK-11	43.95	11.23	821.4	401.7	0.44	0.269	0.102	0.197	1.06	4.28
4_SK-11	45	11.11	837.2	409.9	0.44	0.267	0.101	0.196	1.05	4.28
4_SK-12	15.95	3.13	262.9	143.1	0.71	0.391	0.148	0.069	0.25	1.02
4_SK-12	20.5	4.40	347.9	185.6	0.60	0.338	0.128	0.116	0.49	2.00
4_SK-12	20.95	15.65	362.9	193.1	0.59	0.331	0.125	0.270	1.17	4.76
4_SK-12	22	15.36	377.9	200.6	0.58	0.325	0.123	0.264	1.17	4.74
4_SK-12	22.45	15.10	392.4	207.6	0.57	0.320	0.121	0.259	1.17	4.73
4_SK-13	16.95	16.94	302.7	142.9	0.68	0.432	0.163	0.191	0.64	2.58
4_SK-13	18	16.47	318.4	151.2	0.66	0.416	0.157	0.186	0.64	2.61
4_SK-13	18.45	12.47	334.2	159.4	0.64	0.402	0.152	0.143	0.51	2.09
4_SK-13	19.5	12.16	349.9	167.7	0.62	0.389	0.147	0.140	0.52	2.11
4_SK-13	19.95	18.66	365.7	175.9	0.61	0.378	0.143	0.212	0.81	3.27

Borehole #	Depth	$(N_1)^*_{60}$	σ_{vo}	σ'_{vo}	rd	CSR_2	CSR_3	CRR	FS_2	FS_3
4_SK-13	21	18.24	381.4	184.2	0.59	0.368	0.139	0.206	0.81	3.28
4_SK-13	21.45	14.06	397.2	192.4	0.58	0.359	0.136	0.159	0.64	2.60
4_SK-13	22.5	13.77	412.9	200.7	0.57	0.350	0.133	0.156	0.64	2.61
4_SK-14	28.45	16.28	482.9	231.2	0.51	0.317	0.120	0.283	1.29	5.21
4_SK-14	29.5	16.10	495.7	236.4	0.50	0.315	0.119	0.279	1.28	5.17
4_SK-14	29.95	14.47	508.4	241.7	0.50	0.314	0.119	0.247	1.14	4.61
4_SK-54	13.45	15.40	171.3	136.5	0.80	0.298	0.113	0.265	1.28	5.16
4_SK-54	14.5	15.02	185.9	143.7	0.77	0.297	0.113	0.257	1.25	5.02
4_SK-54	24.45	11.24	380.3	235.6	0.54	0.261	0.099	0.143	0.79	3.19
4_SK-54	25.5	11.05	396.2	243.7	0.53	0.259	0.099	0.141	0.79	3.17
4_SK-54	26	10.94	405.9	248.7	0.53	0.258	0.098	0.140	0.78	3.15
4_SK-55	11	1.47	137.0	104.5	0.86	0.338	0.129	0.086	0.37	1.47
4_SK-55	12.5	1.43	152.6	110.4	0.84	0.345	0.131	0.085	0.36	1.44
4_SK-55	12.95	2.10	164.6	114.9	0.81	0.347	0.132	0.092	0.38	1.54
4_SK-55	14	2.06	176.6	119.4	0.79	0.347	0.132	0.092	0.38	1.53
4_SK-55	19.45	20.69	280.7	161.0	0.61	0.316	0.121	0.456	2.08	8.36
4_SK-55	21.5	19.93	305.7	173.5	0.59	0.308	0.117	0.406	1.90	7.66
4_SK-55	21.95	16.63	325.3	183.1	0.57	0.302	0.115	0.291	1.39	5.59
4_SK-55	23.5	16.21	344.8	192.6	0.56	0.297	0.113	0.282	1.37	5.50
4_SK-56	10.5	1.57	143.9	91.6	0.89	0.418	0.158	0.061	0.21	0.85
4_SK-56	10.95	3.04	157.0	97.3	0.87	0.420	0.159	0.073	0.25	1.01
4_SK-56	12	2.96	170.1	102.9	0.85	0.420	0.159	0.072	0.25	1.00
4_SK-56	12.45	3.60	183.3	108.5	0.83	0.418	0.158	0.077	0.27	1.08
4_SK-56	26	12.58	447.5	240.3	0.53	0.295	0.112	0.157	0.77	3.12
4_SK-56	26.45	13.82	462.6	247.8	0.52	0.292	0.110	0.171	0.84	3.42
4_SK-56	27.5	13.66	474.4	253.4	0.52	0.290	0.110	0.182	0.90	3.66
4_SK-56	27.7	13.61	478.7	255.5	0.52	0.289	0.109	0.181	0.90	3.66
4_SK-56	27.95	13.46	491.1	261.3	0.51	0.287	0.109	0.179	0.90	3.64
4_SK-66	13	4.71	161.8	124.3	0.82	0.318	0.121	0.119	0.54	2.17
4_SK-66	13.5	4.65	169.8	127.6	0.80	0.319	0.122	0.118	0.53	2.15
4_SK-66	13.95	6.55	178.3	131.1	0.79	0.319	0.122	0.139	0.63	2.53
4_SK-66	14.5	6.46	187.4	134.9	0.77	0.319	0.122	0.138	0.62	2.51
4_SK-66	15	6.37	195.7	138.4	0.75	0.318	0.121	0.137	0.62	2.51
4_SK-66	17.5	4.78	240.1	157.6	0.67	0.306	0.117	0.120	0.56	2.27
4_SK-66	18.95	4.57	272.0	172.3	0.63	0.297	0.113	0.117	0.57	2.30
4_SK-66	20	4.49	285.9	178.7	0.61	0.293	0.112	0.117	0.57	2.31
4_SK-66	24.95	14.65	395.6	235.9	0.54	0.269	0.102	0.192	1.03	4.16
4_SK-66	26	14.40	411.4	244.1	0.53	0.266	0.101	0.189	1.03	4.13
4_SK-67	6	0.00	88.5	73.5	0.94	0.339	0.129	0.072	0.31	1.23
4_SK-67	9	0.00	121.3	89.0	0.92	0.374	0.142	0.072	0.28	1.12
4_SK-67	27	21.86	483.7	271.2	0.52	0.277	0.106	0.338	1.76	7.07

Borehole #	Depth	$(N_1)_{60}^{\circ}$	σ_{vo}	σ'_{vo}	rd	CSR_2	CSR_3	CRR	FS_2	FS_3
4_SK-67	27.5	21.67	493.2	276.0	0.52	0.276	0.105	0.332	1.74	6.98
4_SK-67	27.95	17.90	503.2	281.0	0.51	0.274	0.105	0.247	1.30	5.23
4_SK-67	28.5	17.74	513.3	285.8	0.51	0.273	0.104	0.245	1.29	5.20
4_SK-67	29	17.62	522.1	289.9	0.51	0.272	0.104	0.243	1.29	5.17
4_SK-67	30.5	12.00	556.5	306.5	0.50	0.268	0.102	0.166	0.89	3.59
5_SK-1	4.95	16.11	104.6	75.8	0.96	0.397	0.150	0.279	1.01	4.11
5_SK-1	6	17.10	120.3	84.1	0.96	0.409	0.155	0.302	1.07	4.32
5_SK-1	6.45	2.98	135.3	91.5	0.95	0.419	0.159	0.101	0.35	1.41
5_SK-1	7.5	2.87	149.9	98.7	0.94	0.427	0.162	0.100	0.34	1.36
5_SK-1	18.45	12.98	372.3	208.6	0.64	0.342	0.130	0.162	0.68	2.76
5_SK-1	19.5	12.74	387.9	216.6	0.62	0.334	0.126	0.159	0.69	2.78
5_SK-2	9	2.12	163.9	101.6	0.92	0.443	0.168	0.092	0.30	1.22
5_SK-2	9.45	3.52	190.9	113.6	0.89	0.447	0.169	0.106	0.34	1.39
5_SK-2	12	3.35	217.9	125.6	0.85	0.441	0.167	0.105	0.34	1.39
5_SK-2	12.45	3.24	235.9	133.6	0.82	0.433	0.164	0.103	0.34	1.40
5_SK-2	14	3.15	253.9	141.6	0.79	0.422	0.160	0.103	0.35	1.42
5_SK-2	18.45	2.79	340.9	181.2	0.64	0.361	0.137	0.099	0.39	1.60
6_SK-1	1.5	1.91	41.3	26.3	0.98	0.455	0.174	0.063	0.20	0.80
6_SK-1	3	2.03	59.8	35.0	0.98	0.490	0.188	0.064	0.19	0.75
6_SK-1	3.45	2.88	78.8	44.0	0.97	0.510	0.195	0.071	0.20	0.80
6_SK-1	5	2.63	97.8	53.0	0.96	0.522	0.200	0.068	0.19	0.76
6_SK-1	5.45	2.67	121.5	64.3	0.95	0.530	0.203	0.069	0.19	0.75
6_SK-3	2	1.91	41.3	26.3	0.98	0.455	0.174	0.052	0.17	0.67
6_SK-3	2.5	1.91	50.3	30.5	0.98	0.475	0.182	0.052	0.16	0.64
6_SK-3	2.95	2.86	69.3	39.5	0.97	0.502	0.192	0.058	0.17	0.66
6_SK-3	4.5	2.75	88.3	48.5	0.97	0.517	0.198	0.057	0.16	0.64
6_SK-3	4.95	3.30	112.0	59.8	0.96	0.527	0.202	0.060	0.16	0.66
6_SK-4	6.5	2.60	126.6	67.6	0.95	0.523	0.200	0.056	0.15	0.62
6_SK-4	7	2.52	135.6	71.8	0.95	0.525	0.201	0.056	0.15	0.61
6_SK-5	0.75	1.91	32.2	22.0	0.99	0.426	0.163	0.052	0.18	0.71
6_SK-5	2.8	1.91	53.6	32.1	0.98	0.481	0.184	0.052	0.16	0.63
6_SK-5	3	2.03	59.8	35.0	0.98	0.490	0.188	0.053	0.16	0.62
6_SK-5	3.45	0.00	78.8	44.0	0.97	0.510	0.195	0.049	0.14	0.56
6_SK-5	5	0.00	97.8	53.0	0.96	0.522	0.200	0.049	0.14	0.54
6_SK-5	5.45	0.00	110.1	58.9	0.96	0.527	0.202	0.049	0.13	0.54
6_SK-6	4.6	0.00	99.5	52.5	0.96	0.536	0.205	0.051	0.14	0.55
6_SK-6	6	0.00	117.1	60.8	0.96	0.541	0.207	0.051	0.14	0.54
6_SK-6	6.45	0.00	139.9	71.6	0.94	0.542	0.207	0.051	0.14	0.54
6_SK-6	8.4	0.00	163.5	82.5	0.93	0.540	0.207	0.051	0.14	0.54
6_SK-7	2.5	1.96	65.0	37.5	0.98	0.497	0.190	0.063	0.18	0.73
6_SK-7	4.5	1.83	88.3	48.5	0.97	0.517	0.198	0.062	0.17	0.69

Borehole #	Depth	$(N_1)^{\circ}_{60}$	σ_{vo}	σ'_{vo}	rd	CSR_2	CSR_3	CRR	FS_2	FS_3
6_SK-7	4.95	1.69	106.3	57.1	0.96	0.526	0.201	0.061	0.17	0.67
7_SK-10	22	21.01	394.3	246.8	0.58	0.271	0.104	0.327	1.74	6.93
7_SK-10	22.5	20.85	402.8	250.6	0.57	0.270	0.104	0.322	1.72	6.87
7_SK-10	22.95	13.58	416.3	256.6	0.56	0.267	0.103	0.189	1.02	4.07
7_SK-10	24	13.42	429.8	262.6	0.55	0.265	0.102	0.187	1.02	4.06
7_SK-11	1.5	2.87	31.1	31.1	0.99	0.291	0.112	0.055	0.27	1.08
7_SK-11	1.95	2.53	44.6	44.6	0.98	0.290	0.111	0.053	0.26	1.05
7_SK-11	3	3.94	58.1	58.1	0.98	0.288	0.111	0.061	0.31	1.22
7_SK-11	3.45	3.62	68.9	68.9	0.97	0.287	0.110	0.059	0.30	1.18
7_SK-11	4.2	3.64	78.3	76.8	0.97	0.291	0.112	0.072	0.36	1.43
7_SK-11	4.5	2.85	85.1	79.8	0.97	0.304	0.117	0.066	0.32	1.26
7_SK-11	4.95	2.75	98.6	85.8	0.96	0.325	0.125	0.066	0.29	1.16
7_SK-11	6	2.23	112.1	91.8	0.96	0.344	0.132	0.062	0.26	1.04
7_SK-11	6.45	2.16	125.6	97.8	0.95	0.359	0.138	0.061	0.25	0.99
7_SK-11	7.5	9.79	139.1	103.8	0.94	0.371	0.143	0.128	0.50	1.98
7_SK-11	7.95	9.61	148.1	107.8	0.93	0.378	0.145	0.126	0.48	1.92
7_SK-11	8.5	12.12	157.5	112.0	0.93	0.384	0.147	0.210	0.79	3.15
7_SK-11	9	11.92	166.1	115.8	0.92	0.388	0.149	0.207	0.77	3.07
7_SK-12	1.5	10.52	32.8	32.8	0.99	0.291	0.112	0.129	0.64	2.55
7_SK-12	1.95	9.02	47.0	47.0	0.98	0.290	0.111	0.115	0.57	2.28
7_SK-12	3	6.13	61.3	61.3	0.98	0.288	0.111	0.089	0.45	1.78
7_SK-12	27.45	20.74	506.3	289.0	0.52	0.267	0.102	0.460	2.49	9.92
7_SK-12	28	20.59	515.7	293.2	0.51	0.266	0.102	0.448	2.43	9.71
7_SK-12	28.5	20.45	524.3	297.0	0.51	0.265	0.102	0.439	2.39	9.53
7_SK-14	16.5	8.02	295.2	171.2	0.70	0.353	0.136	0.156	0.64	2.55
7_SK-14	17.5	7.88	309.1	177.6	0.67	0.345	0.133	0.155	0.65	2.58
7_SK-14	18	7.79	317.9	181.6	0.66	0.341	0.131	0.154	0.65	2.60
7_SK-14	18.45	9.30	331.8	188.0	0.64	0.333	0.128	0.172	0.74	2.97
7_SK-14	19.5	9.14	345.6	194.4	0.62	0.327	0.125	0.170	0.75	3.00
7_SK-14	21.45	19.73	380.0	208.7	0.59	0.314	0.120	0.293	1.34	5.37
7_SK-14	22	19.56	388.9	212.4	0.58	0.311	0.119	0.289	1.34	5.34
7_SK-14	22.5	19.40	397.0	215.7	0.57	0.309	0.119	0.285	1.33	5.32
7_SK-14	22.95	21.69	409.7	221.0	0.56	0.305	0.117	0.349	1.65	6.58
7_SK-14	24	21.44	422.5	226.2	0.55	0.302	0.116	0.340	1.62	6.48
7_SK-15	1.5	18.17	31.9	31.9	0.99	0.291	0.112	0.187	0.93	3.70
7_SK-15	1.95	15.79	45.8	45.8	0.98	0.290	0.111	0.162	0.81	3.21
7_SK-15	3	18.64	59.7	59.7	0.98	0.288	0.111	0.192	0.96	3.85
7_SK-15	3.45	16.79	73.5	73.5	0.97	0.286	0.110	0.172	0.87	3.46
7_SK-15	4.5	12.27	87.4	87.4	0.97	0.285	0.109	0.127	0.64	2.57
7_SK-15	12	18.45	233.6	226.1	0.83	0.254	0.098	0.342	1.95	7.77
7_SK-15	13.5	18.09	252.6	235.4	0.80	0.254	0.098	0.330	1.88	7.49

Borehole #	Depth	$(N_1)^{*}_{60}$	σ_{vo}	σ'_{vo}	rd	CSR_2	CSR_3	CRR	FS_2	FS_3
7_SK-15	13.95	14.45	267.3	242.5	0.78	0.253	0.097	0.247	1.41	5.63
7_SK-15	15	14.24	281.9	249.6	0.75	0.250	0.096	0.243	1.40	5.59
7_SK-15	15.45	7.49	296.5	256.8	0.73	0.248	0.095	0.150	0.87	3.49
7_SK-15	16.5	7.39	311.1	263.9	0.70	0.245	0.094	0.149	0.88	3.50
7_SK-15	16.95	7.32	320.9	268.6	0.69	0.242	0.093	0.148	0.88	3.52
7_SK-15	36.45	22.92	688.2	438.5	0.47	0.216	0.083	0.403	2.69	10.73
7_SK-15	37.5	22.75	702.5	445.2	0.46	0.216	0.083	0.394	2.63	10.51
8_SK-1	2.85	12.96	59.4	48.2	0.98	0.357	0.137	0.173	0.70	2.79
8_SK-1	3.3	12.52	66.1	51.6	0.98	0.370	0.142	0.168	0.65	2.61
8_SK-1	5	4.49	106.5	72.5	0.96	0.418	0.161	0.078	0.27	1.07
8_SK-1	5.7	4.33	117.7	78.0	0.96	0.428	0.165	0.076	0.26	1.03
8_SK-1	6.15	4.73	125.5	81.8	0.95	0.433	0.167	0.080	0.27	1.06
8_SK-1	7.4	24.75	152.6	95.8	0.94	0.443	0.171	0.295	0.96	3.82
8_SK-1	23.8	22.14	508.9	286.9	0.55	0.289	0.111	0.353	1.76	7.02
8_SK-1	24.5	21.86	522.1	294.4	0.54	0.286	0.110	0.343	1.73	6.91
8_SK-1	24.95	21.50	539.4	304.1	0.54	0.281	0.108	0.317	1.63	6.48
8_SK-1	26	21.17	556.6	313.9	0.53	0.278	0.107	0.309	1.60	6.39
8_SK-1	26.45	20.85	573.9	323.6	0.52	0.274	0.105	0.301	1.58	6.30
8_SK-1	27.5	20.54	591.1	333.4	0.52	0.271	0.104	0.277	1.47	5.86
8_SK-1	27.95	20.24	608.4	343.1	0.51	0.268	0.103	0.271	1.46	5.81
8_SK-1	29	19.96	625.6	352.9	0.51	0.266	0.102	0.295	1.60	6.38
8_SK-1	29.45	19.78	637.1	359.4	0.50	0.264	0.101	0.290	1.59	6.33
8_SK-2	4	8.44	84.6	57.1	0.97	0.425	0.164	0.115	0.39	1.55
8_SK-2	4.5	8.17	92.4	60.9	0.97	0.434	0.167	0.112	0.37	1.48
8_SK-2	4.8	7.94	99.7	64.5	0.97	0.442	0.170	0.111	0.36	1.44
8_SK-2	5.25	6.85	111.4	70.2	0.96	0.451	0.174	0.101	0.32	1.28
8_SK-2	6	7.36	123.1	75.9	0.96	0.459	0.176	0.149	0.47	1.86
8_SK-2	6.45	3.13	137.7	83.0	0.95	0.466	0.179	0.102	0.32	1.26
8_SK-2	7.5	3.00	152.4	90.1	0.94	0.470	0.181	0.073	0.22	0.89
8_SK-2	7.95	11.56	167.0	97.2	0.93	0.473	0.182	0.162	0.49	1.97
8_SK-2	9	11.16	181.6	104.4	0.92	0.473	0.182	0.140	0.43	1.70
8_SK-2	9.45	10.91	191.4	109.1	0.91	0.472	0.182	0.137	0.42	1.67
8_SK-2	27.45	20.70	592.8	328.1	0.52	0.275	0.106	0.457	2.39	9.55
8_SK-2	28.5	20.40	610.1	337.8	0.51	0.272	0.105	0.435	2.30	9.19
8_SK-2	28.95	20.11	627.3	347.6	0.50	0.269	0.104	0.257	1.37	5.48
8_SK-2	30	19.84	644.6	357.3	0.50	0.267	0.103	0.252	1.36	5.44

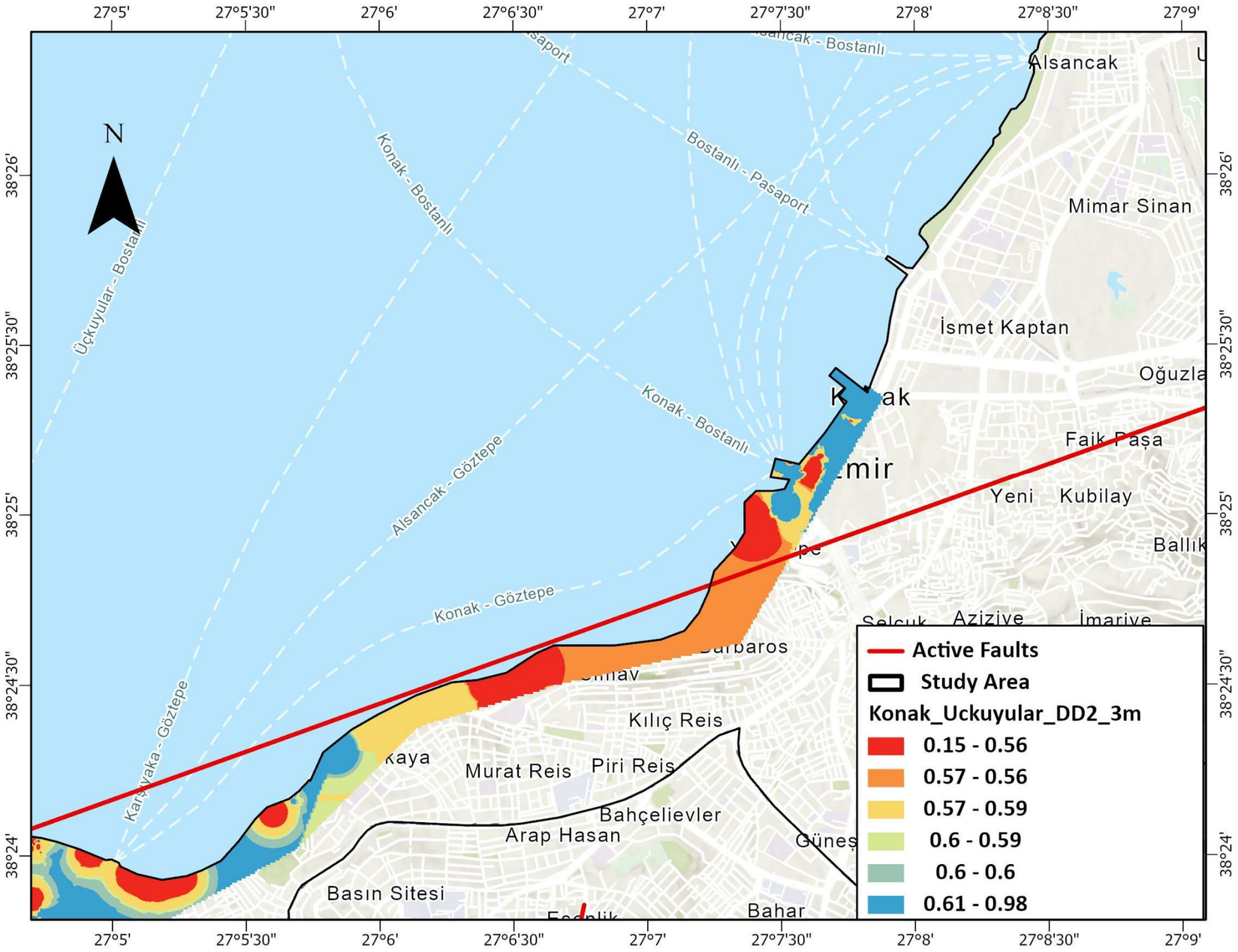

Figure A3.1 Factor of safety distribution for DD-2 (M_w=6.5) earthquake level at 3m depths in the Konak-Üçkuyular area

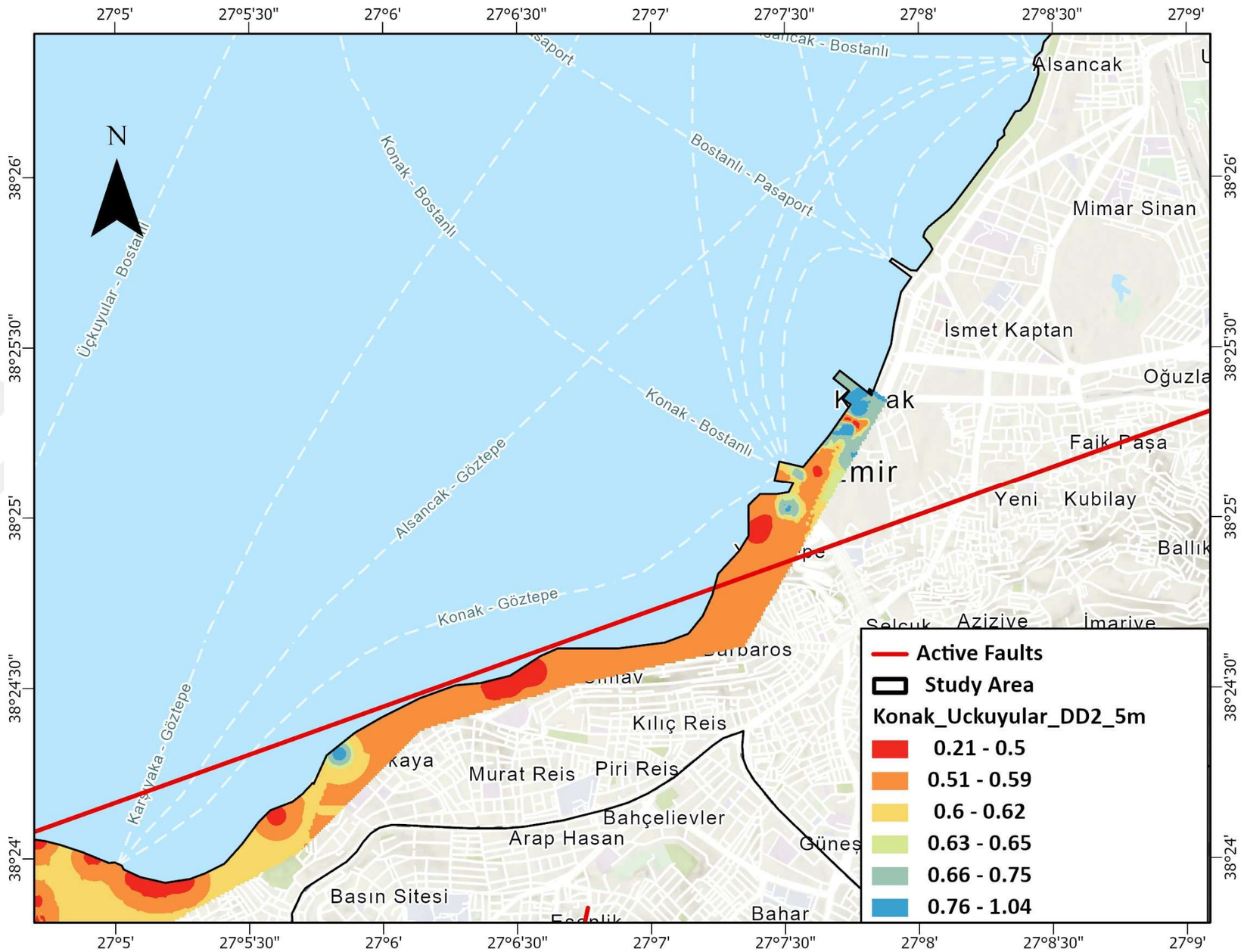

Figure A3.2 Factor of safety distribution for DD-2 (M_w=6.5) earthquake level at 5m depths in the Konak-Üçkuyular area

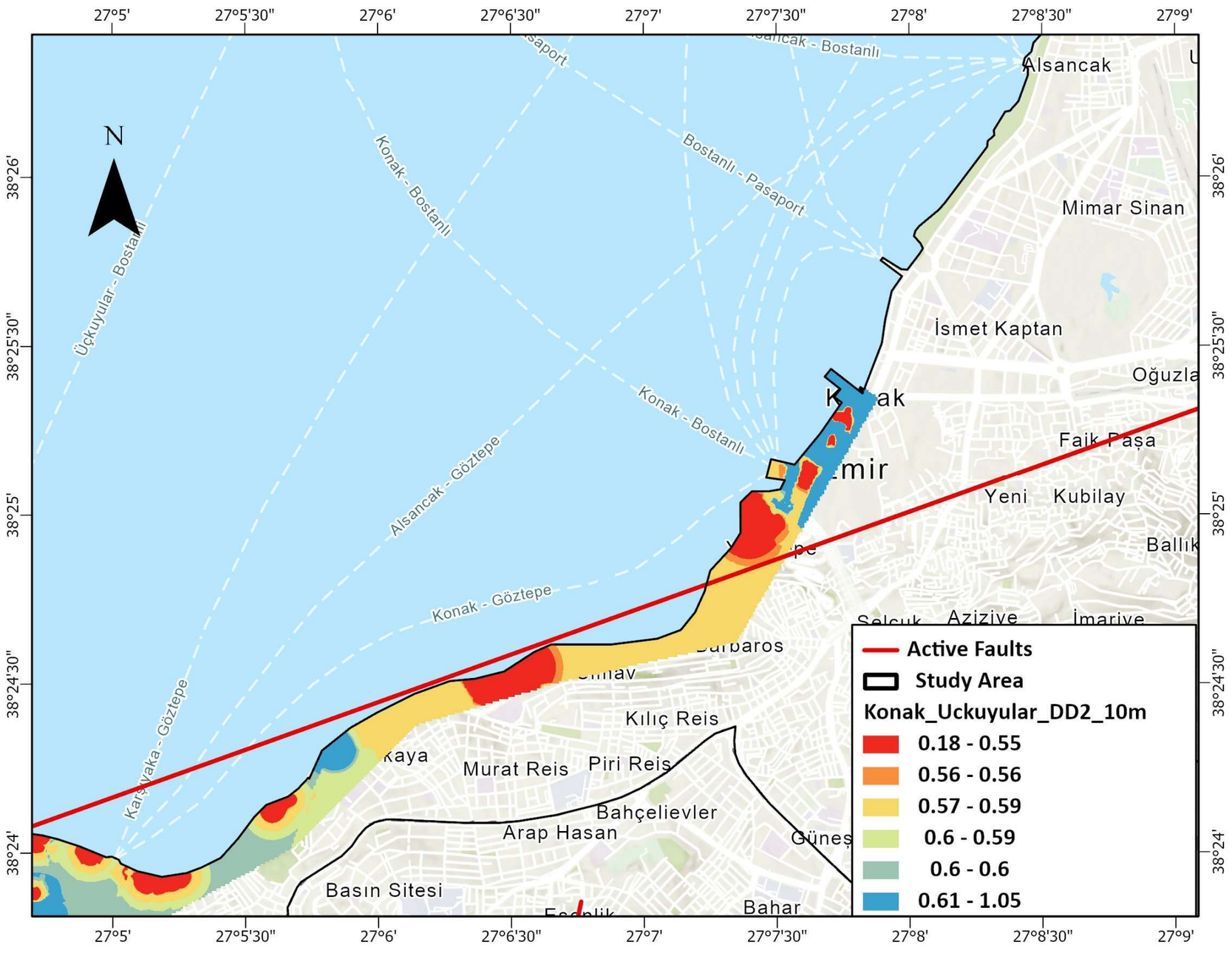

Figure A3.3 Factor of safety distribution for DD-2 (M_w=6.5) earthquake level at 10m depths in the Konak-Üçkuyular area

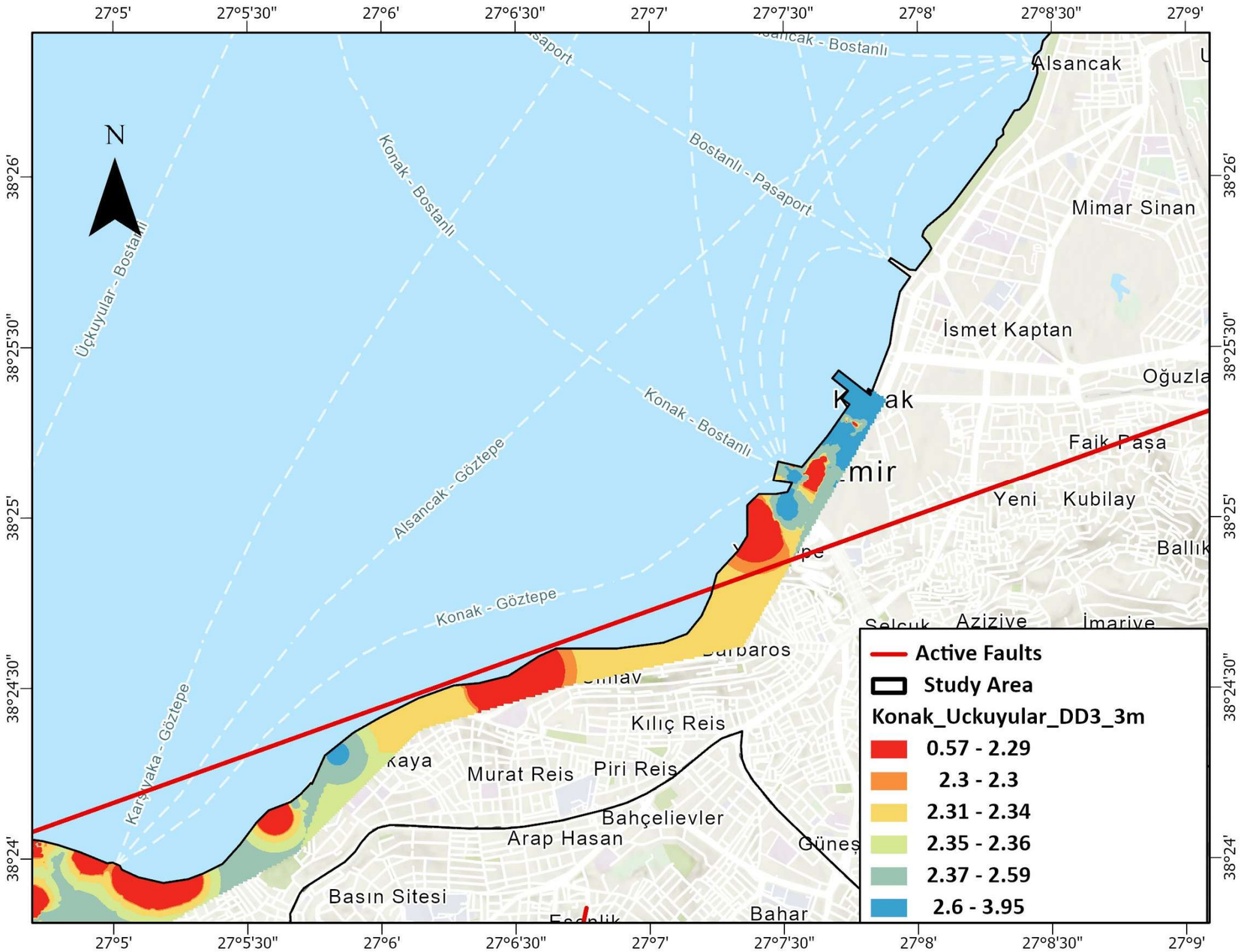

Figure A3.4 Factor of safety distribution for DD-3 (M_w=5.5) earthquake level at 3m depths in the Konak-Üçkuyular area

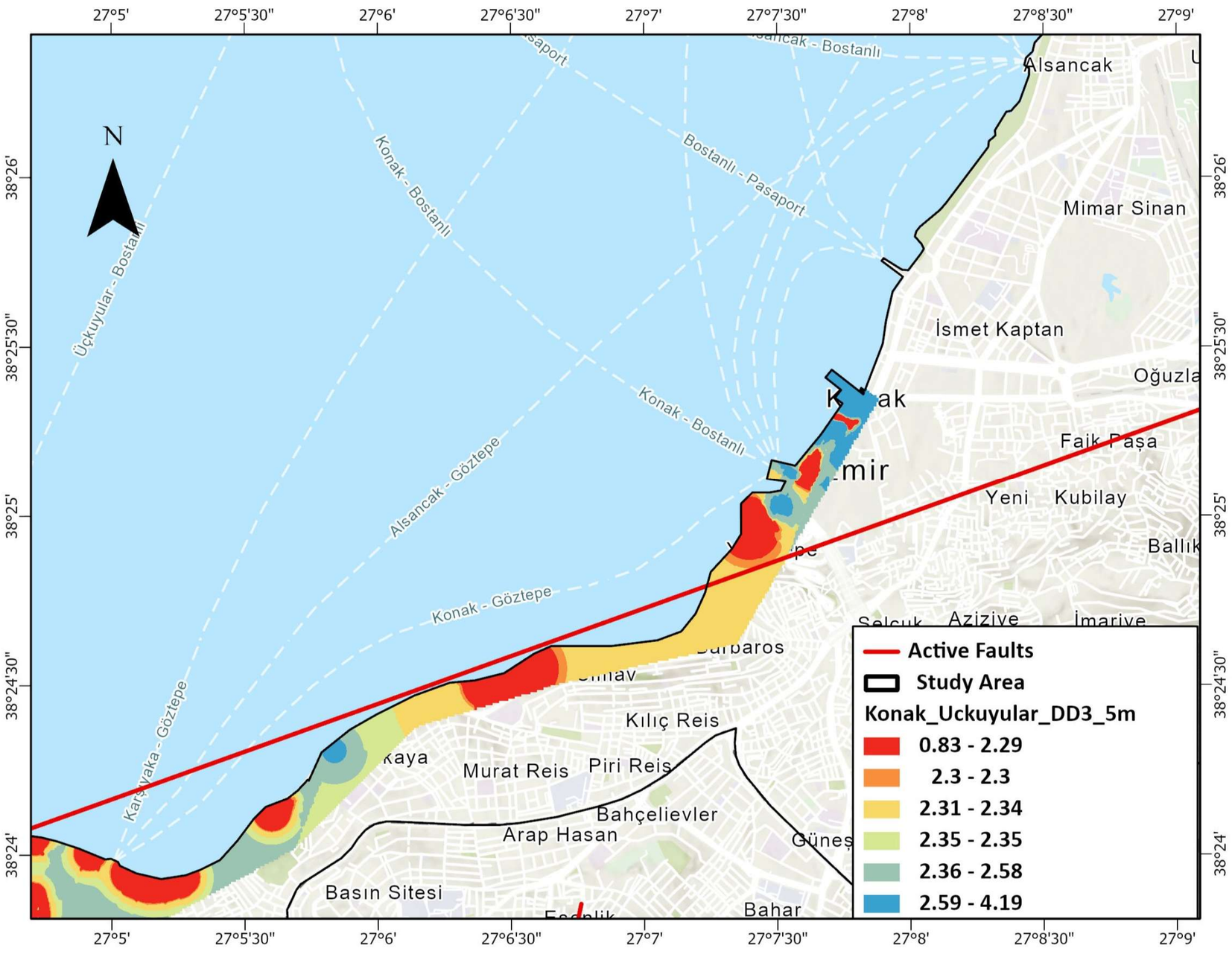

Figure A3.5 Factor of safety distribution for DD-3 (M_w=5.5) earthquake level at 5m depths in the Konak-Üçkuyular area

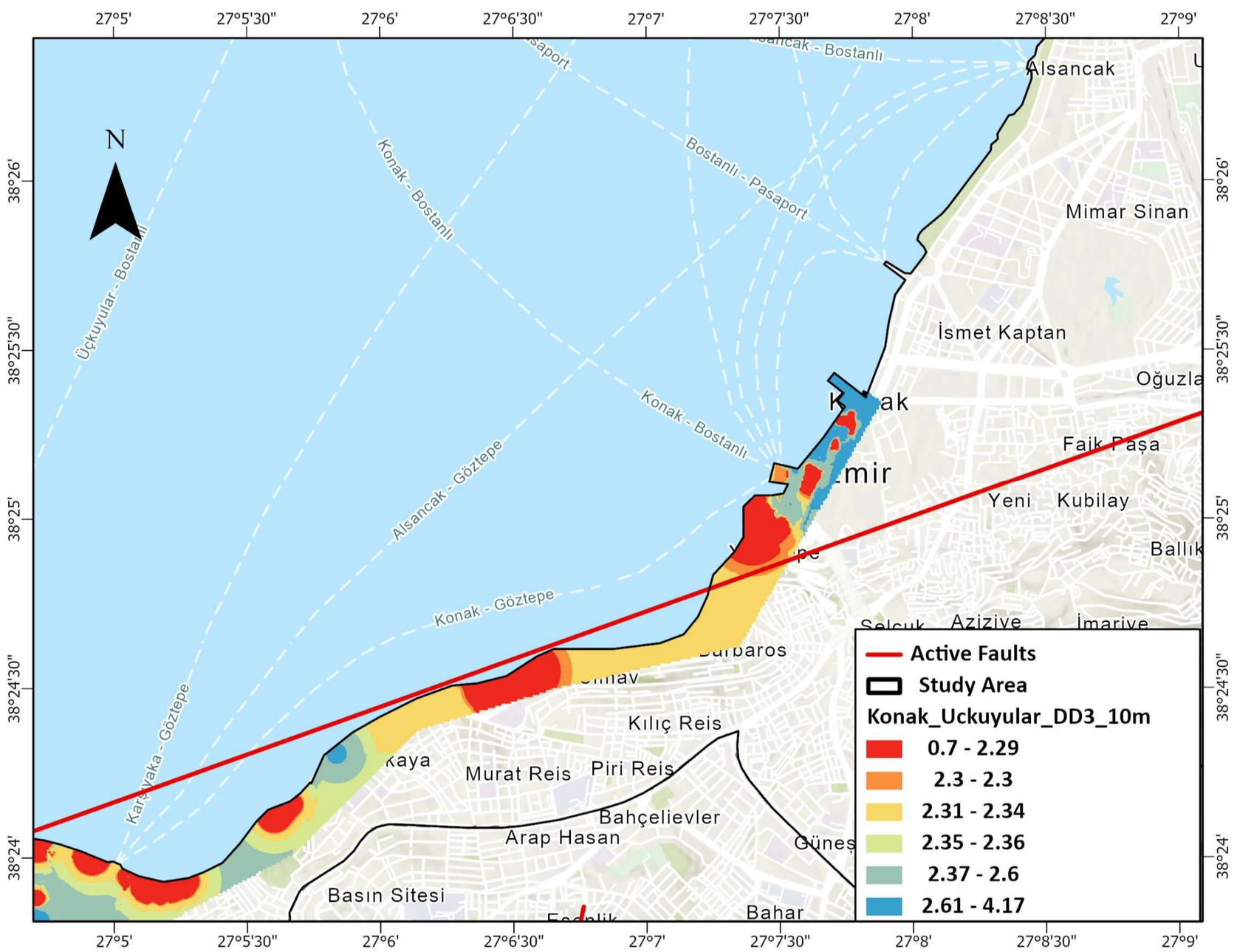

Figure A3.6 Factor of safety distribution for DD-3 (M_w=5.5) earthquake level at 10m depths in the Konak-Üçkuyular area

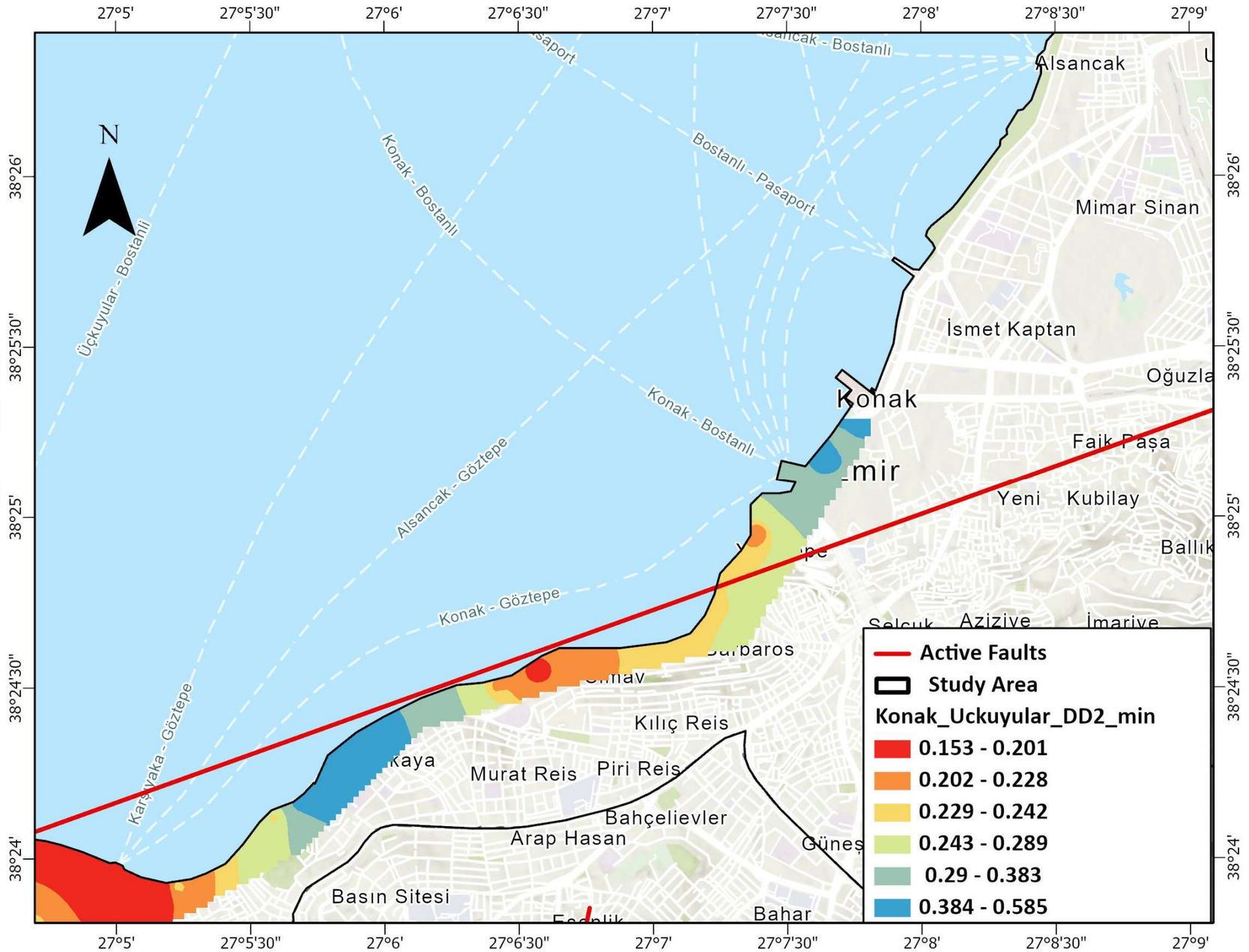

Figure A3.7 Factor of safety distribution for DD-2 (M_w=6.5) for minimum scenario in the Konak-Üçkuyular area

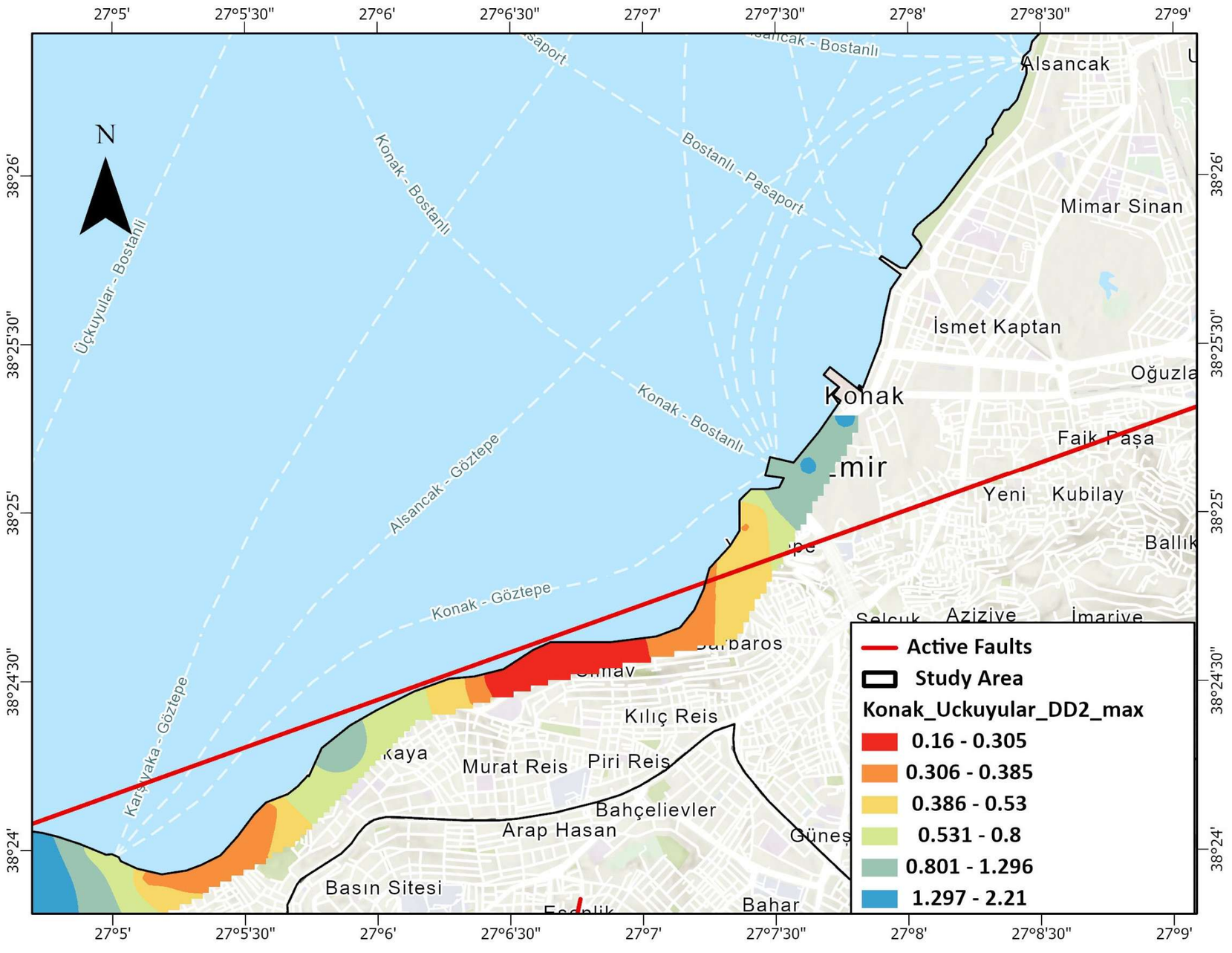

Figure A3.8 Factor of safety distribution for DD-2 (M_w=6.5) for maximum scenario in the Konak-Üçkuyular area

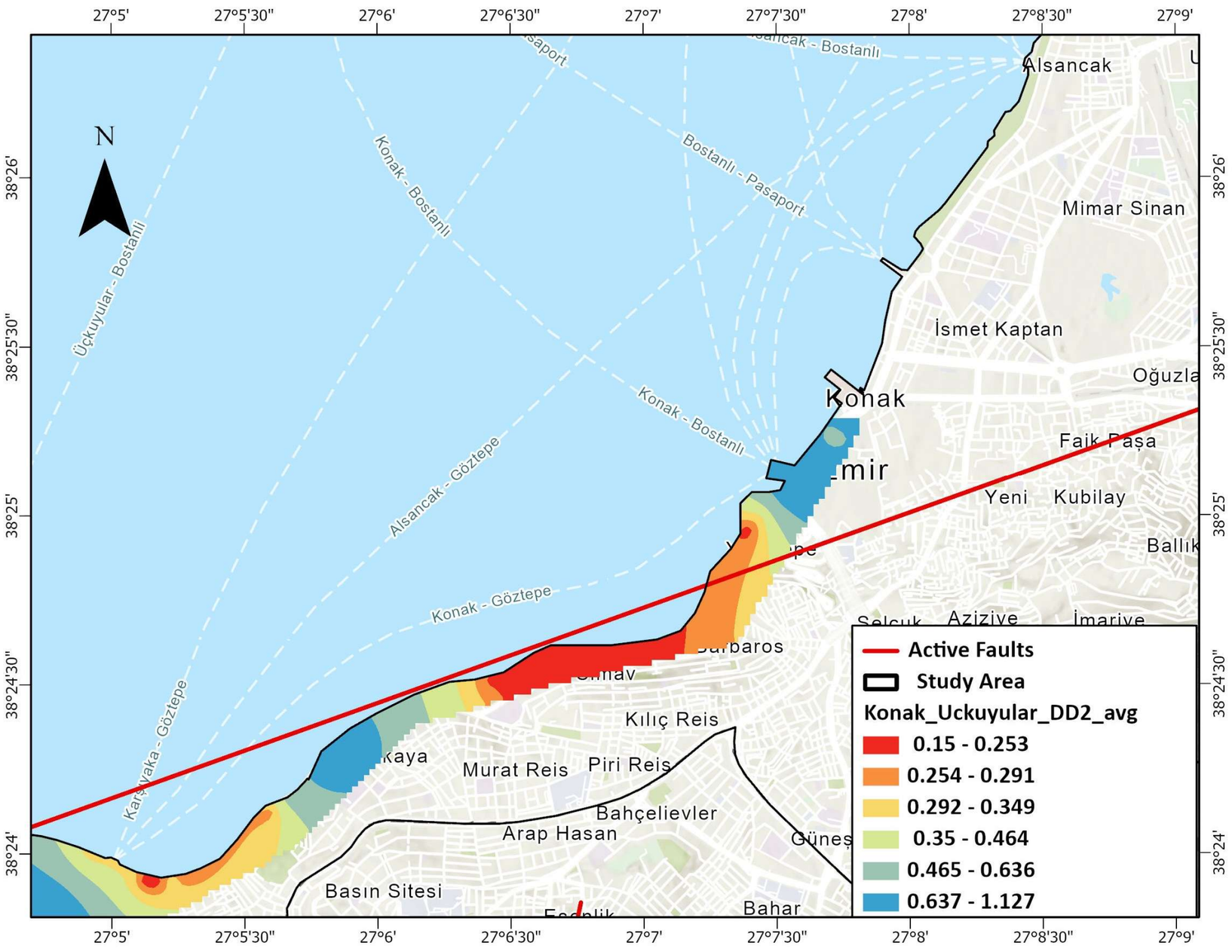

Figure A3.9 Factor of safety distribution for DD-2 (M_w=6.5) for avarage scenario in the Konak-Üçkuyular area

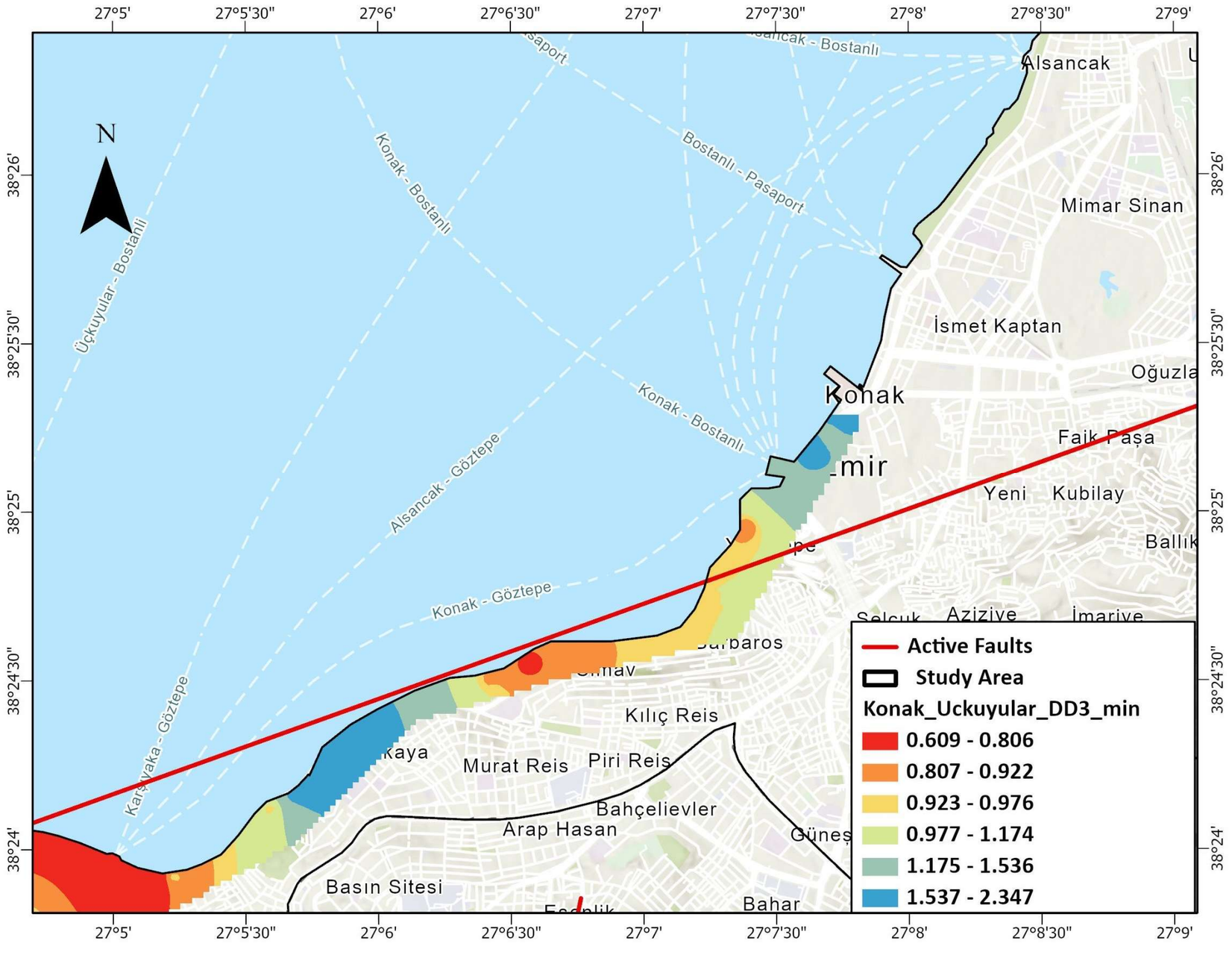

Figure A3.10 Factor of safety distribution for DD-3 (M_w=5.5) for minimum scenario in the Konak-Üçkuyular area

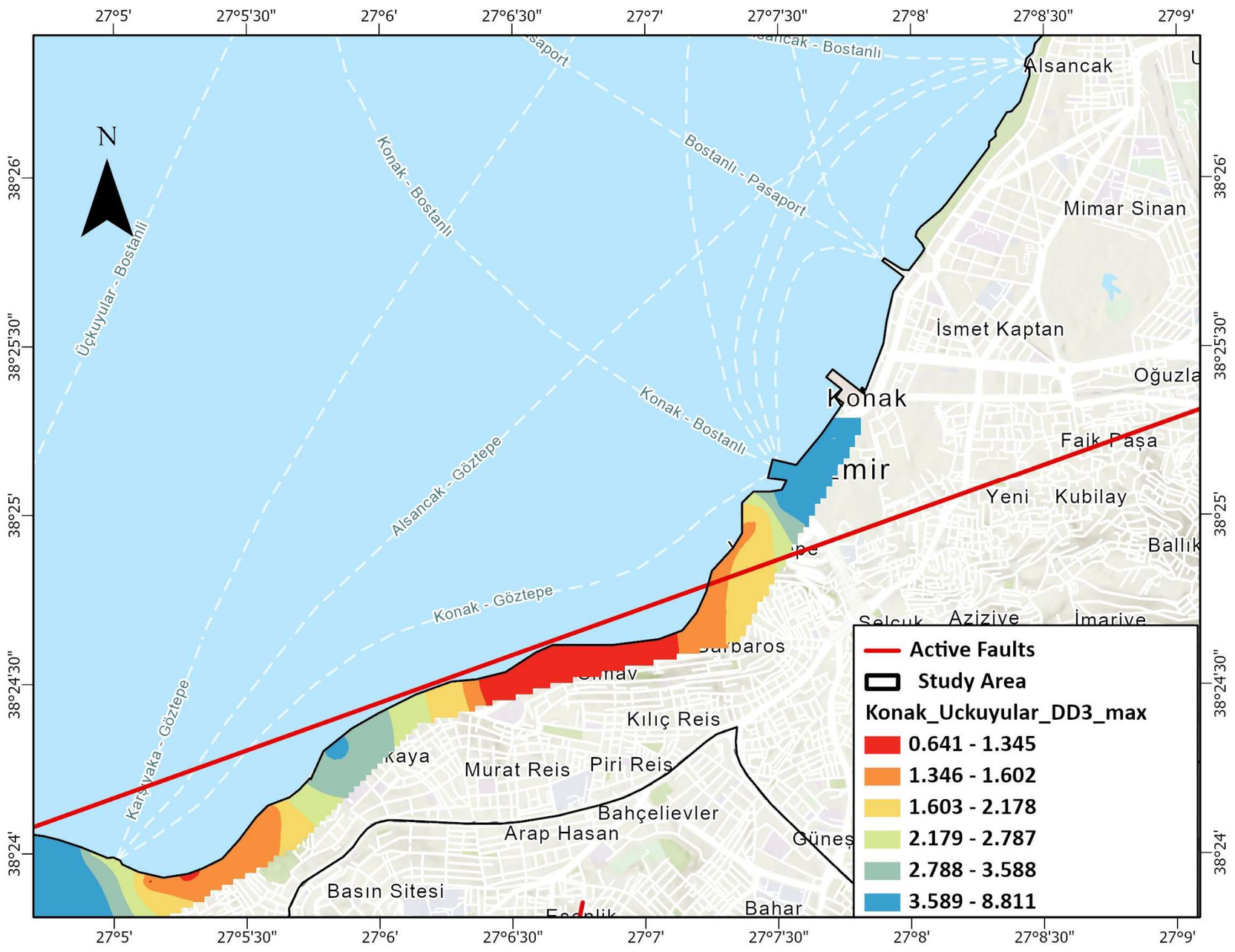

Figure A3.11 Factor of safety distribution for DD-3 (M_w=5.5) for maximum scenario in the Konak-Üçkuyular area

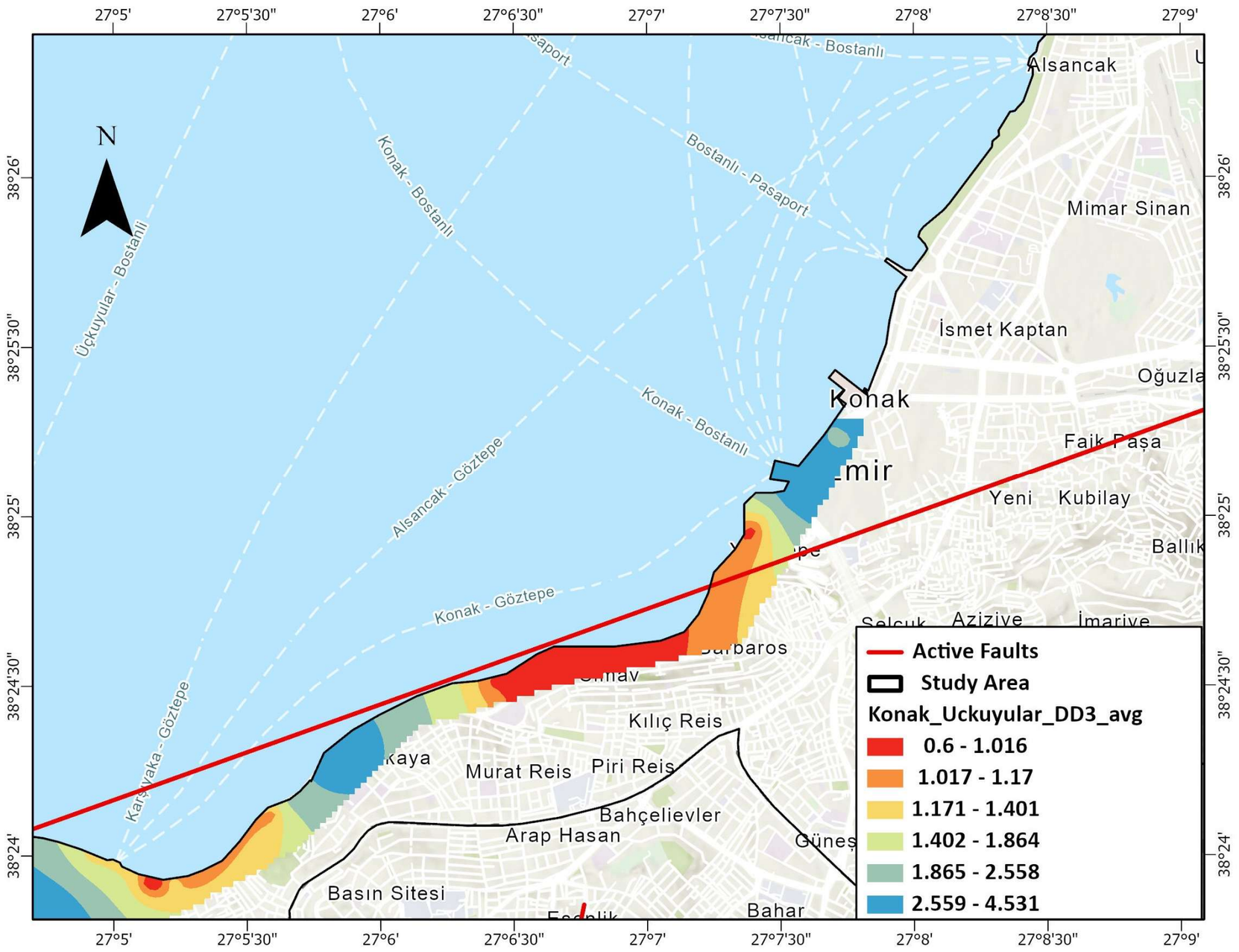

Figure A3.12 Factor of safety distribution for DD-3 (M_w=5.5) for avarage scenario in the Konak-Üçkuyular area

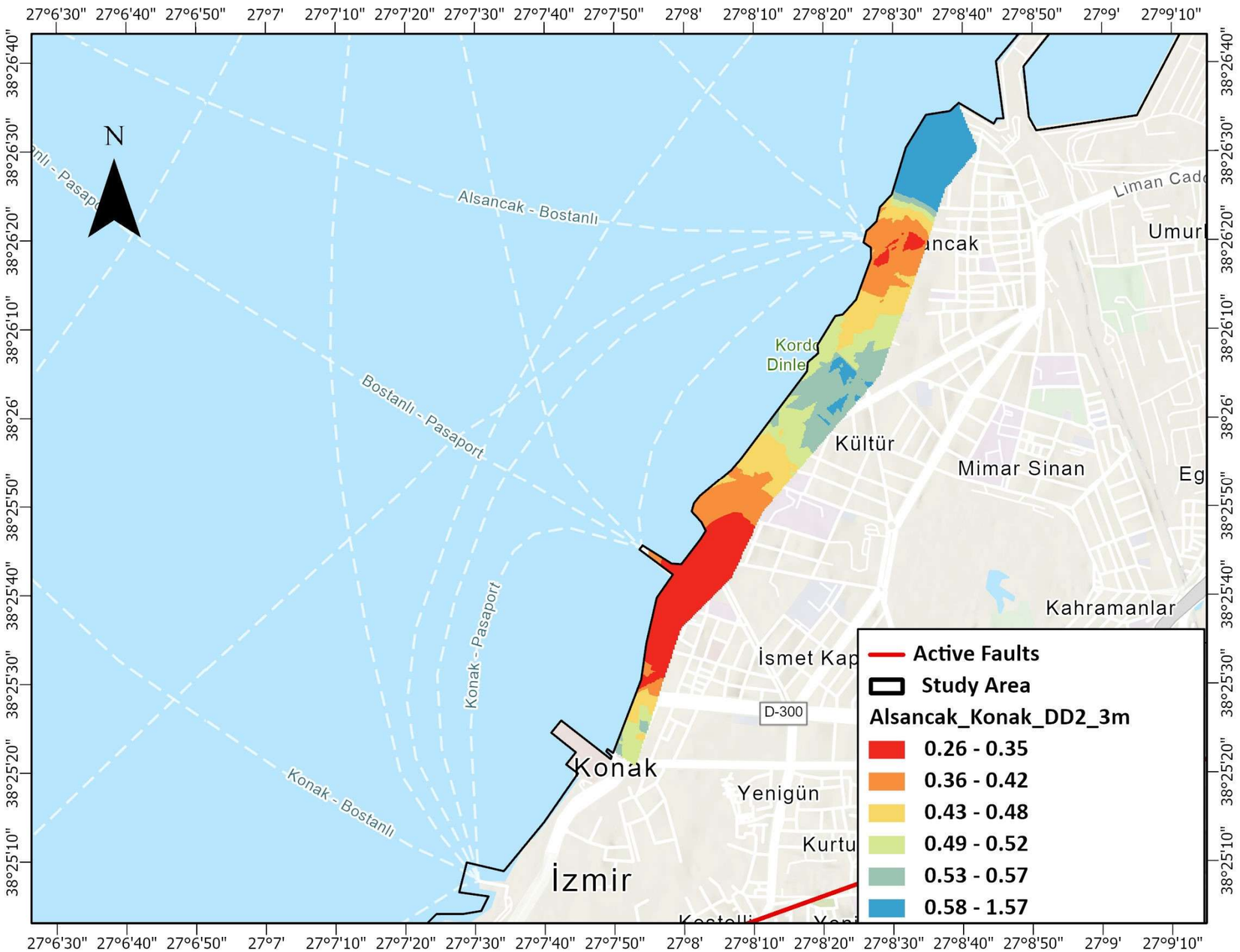

Figure A3.13 Factor of safety distribution for DD-2 (M_w=6.5) earthquake level at 3m depths in the Alsancak-Konak area

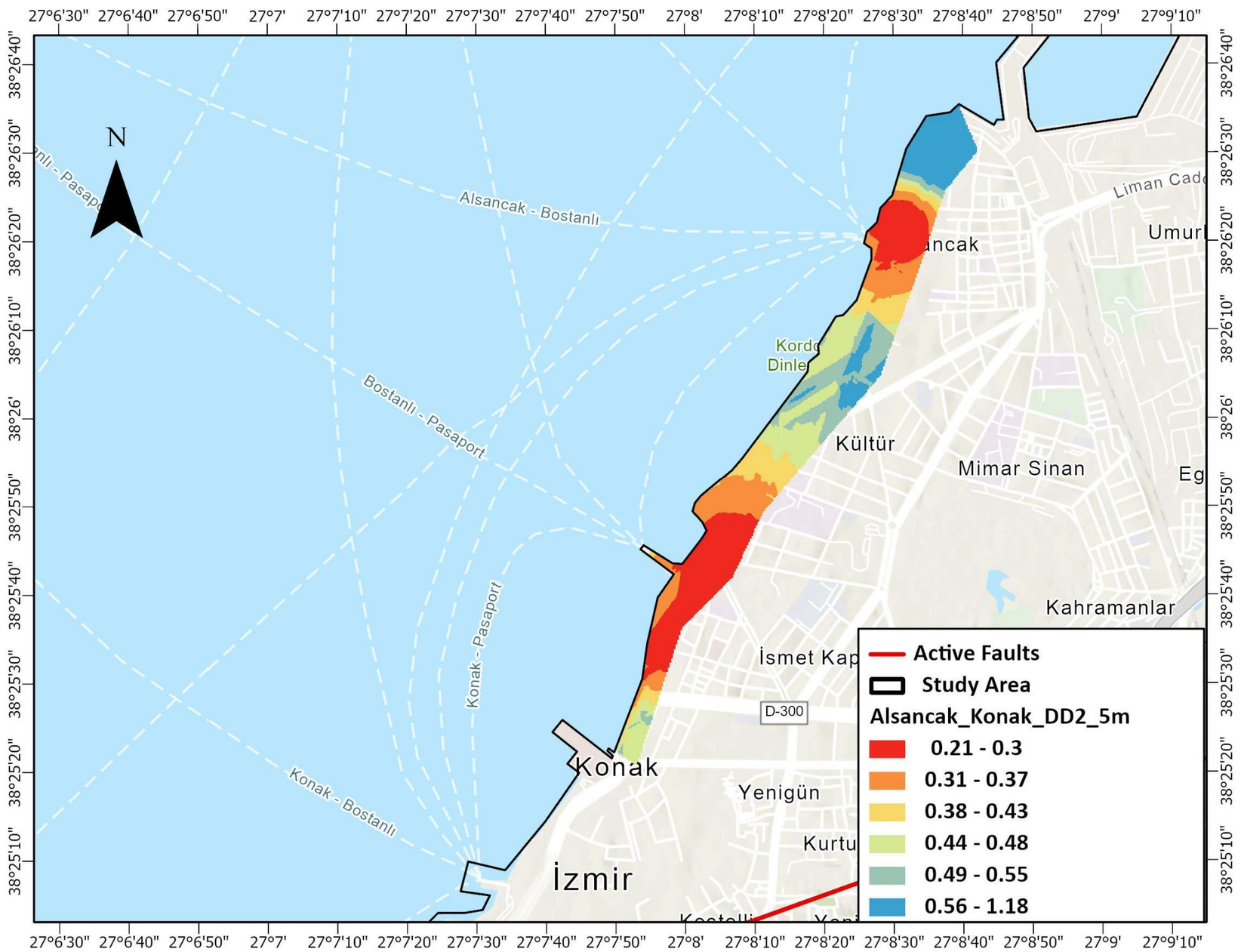

Figure A3.14 Factor of safety distribution for DD-2 (M_w=6.5) earthquake level at 5m depths in the Alsancak-Konak area

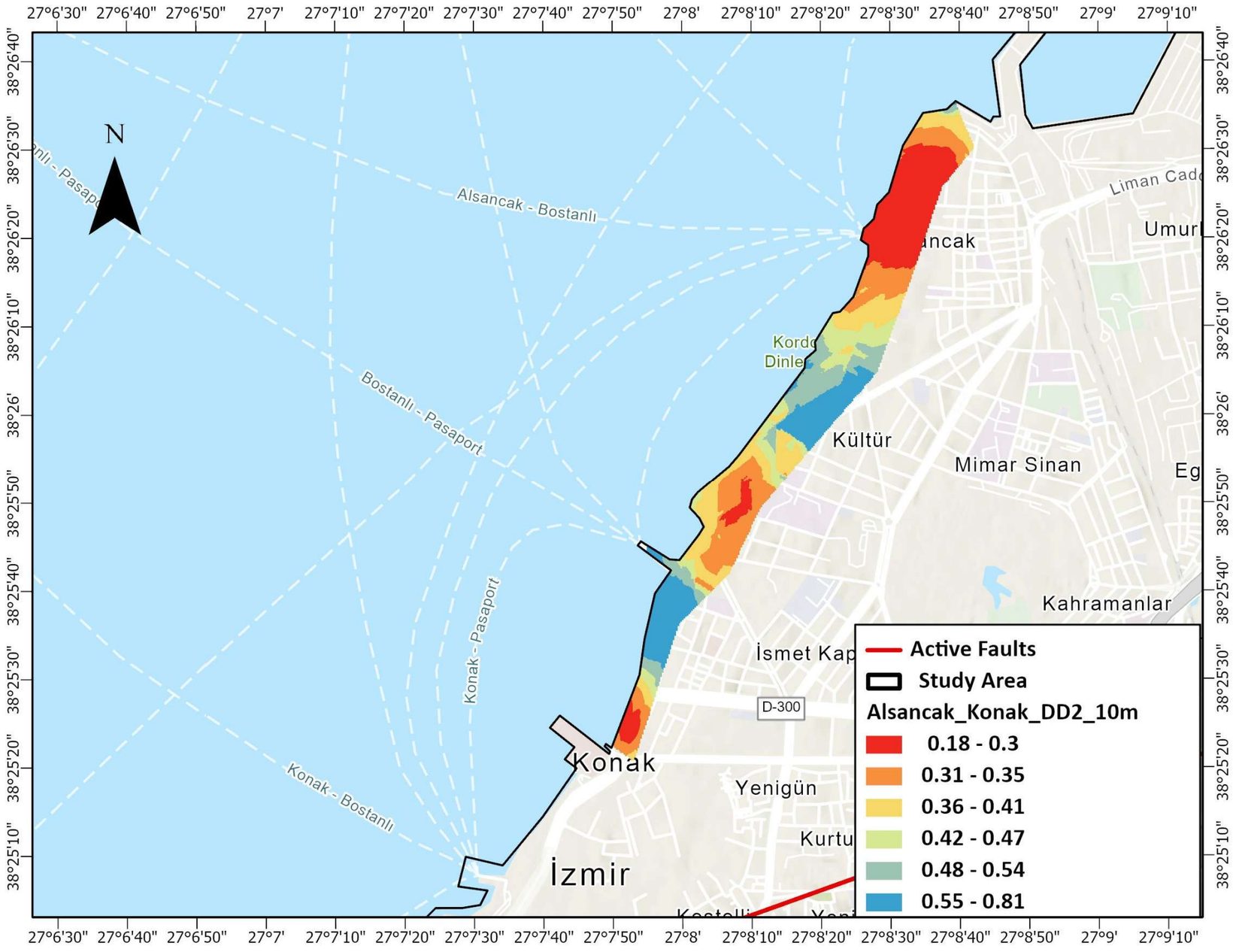

Figure A3.15 Factor of safety distribution for DD-2 (M_w=6.5) earthquake level at 10m depths in the Alsancak-Konak area

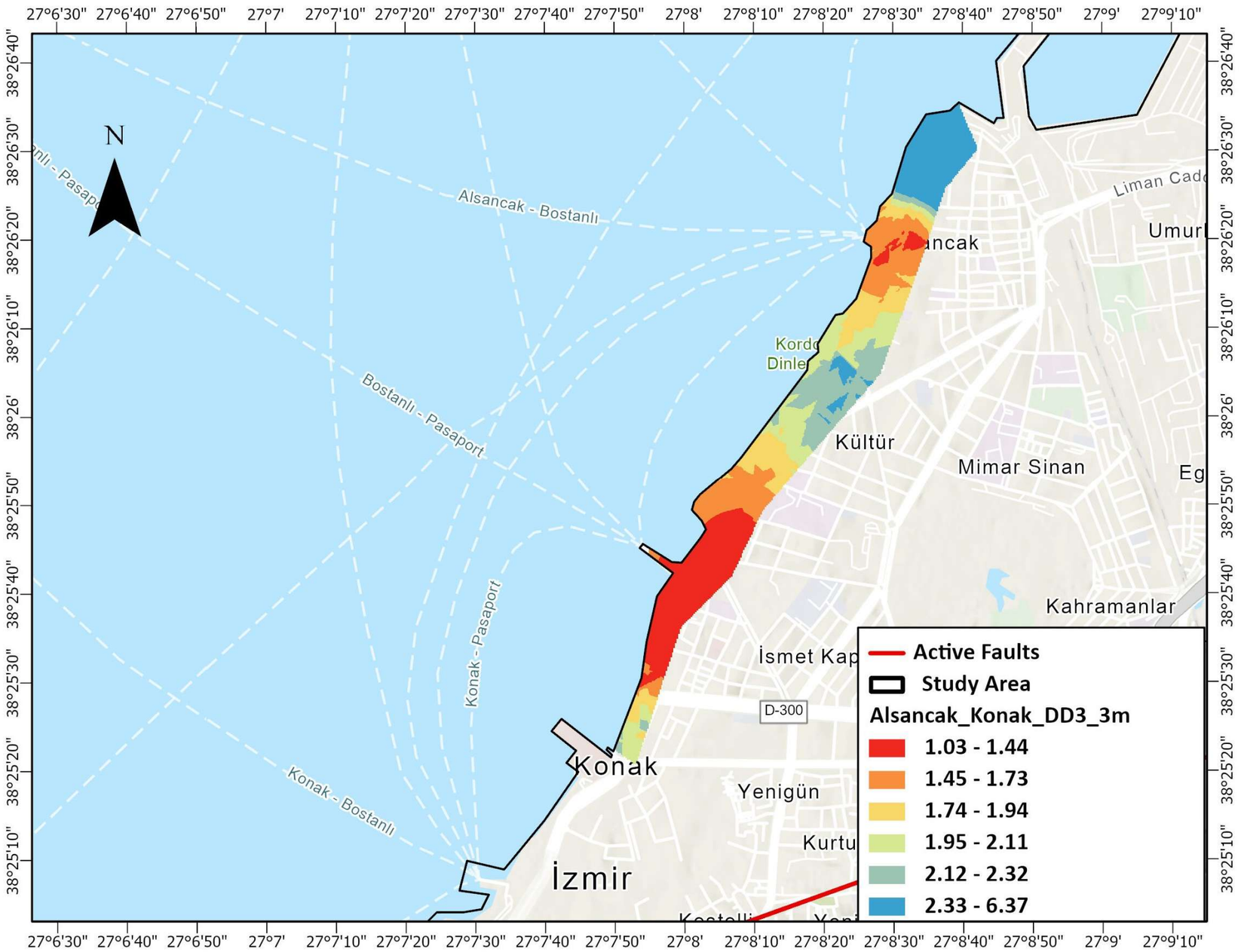

Figure A3.16 Factor of safety distribution for DD-3 (M_w=5.5) earthquake level at 3m depths in the Alsancak-Konak area

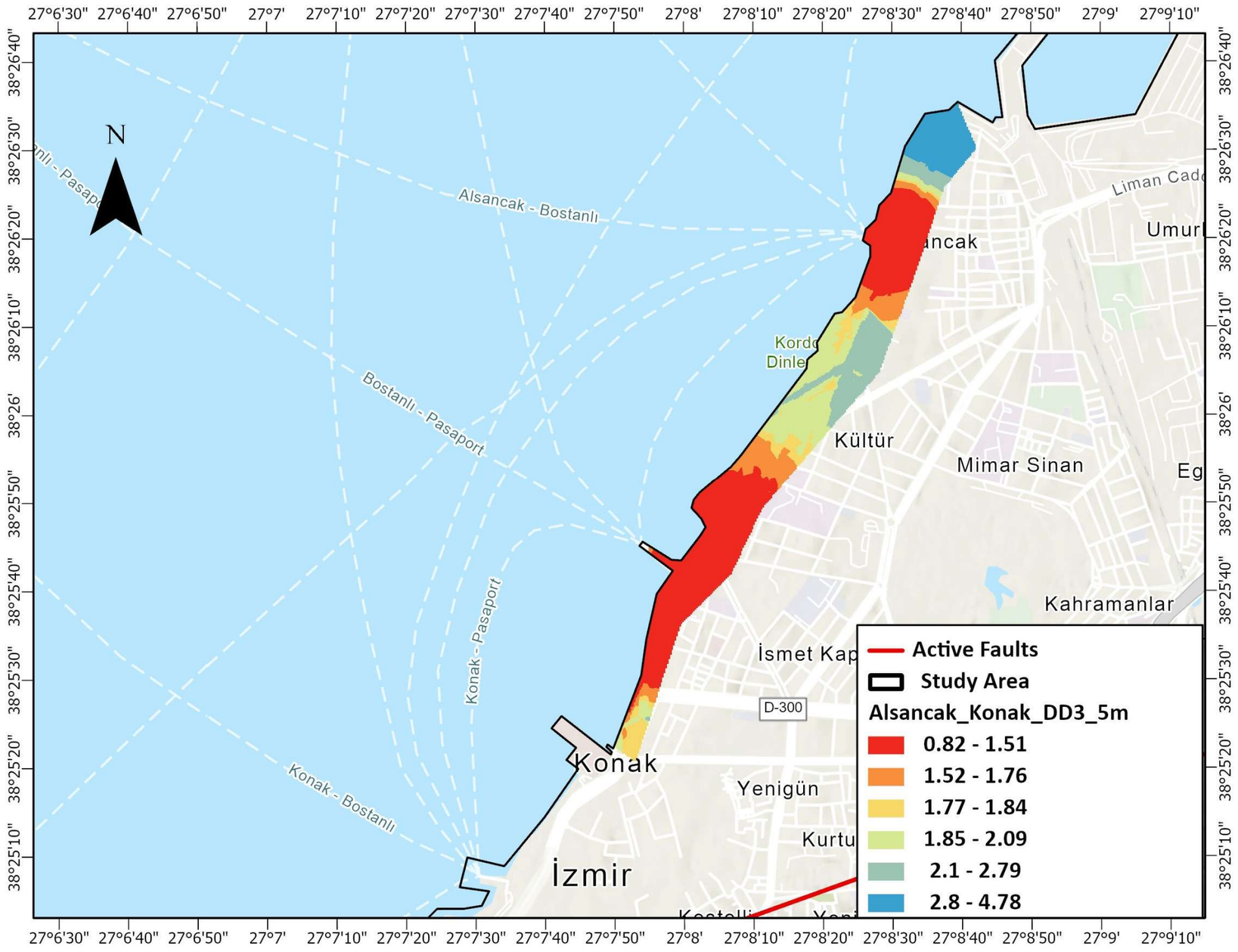

Figure A3.17 Factor of safety distribution for DD-3 (M_w=5.5) earthquake level at 5m depths in the Alsancak-Konak area

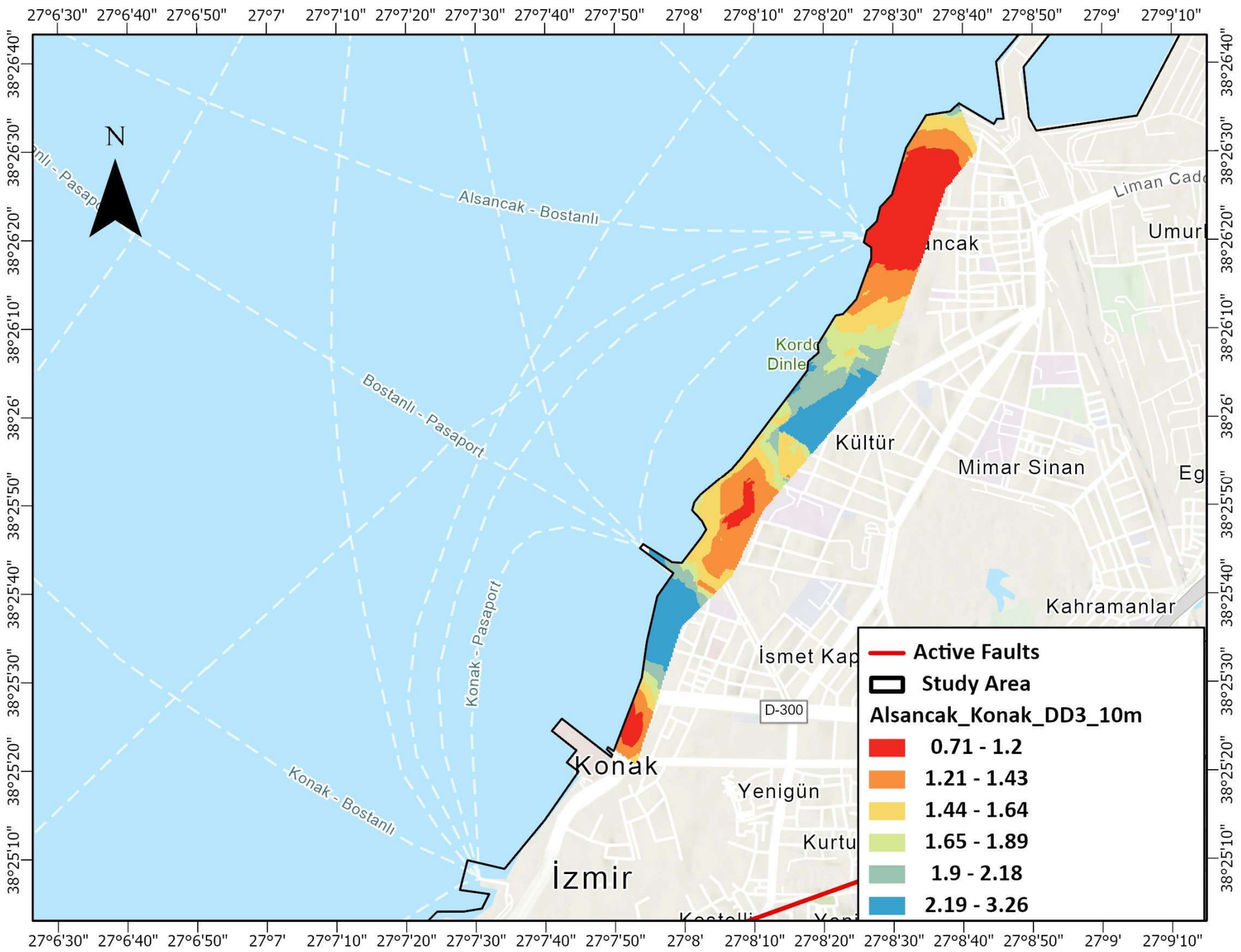

Figure A3.18 Factor of safety distribution for DD-3 (M_w=5.5) earthquake level at 10m depths in the Alsancak-Konak area

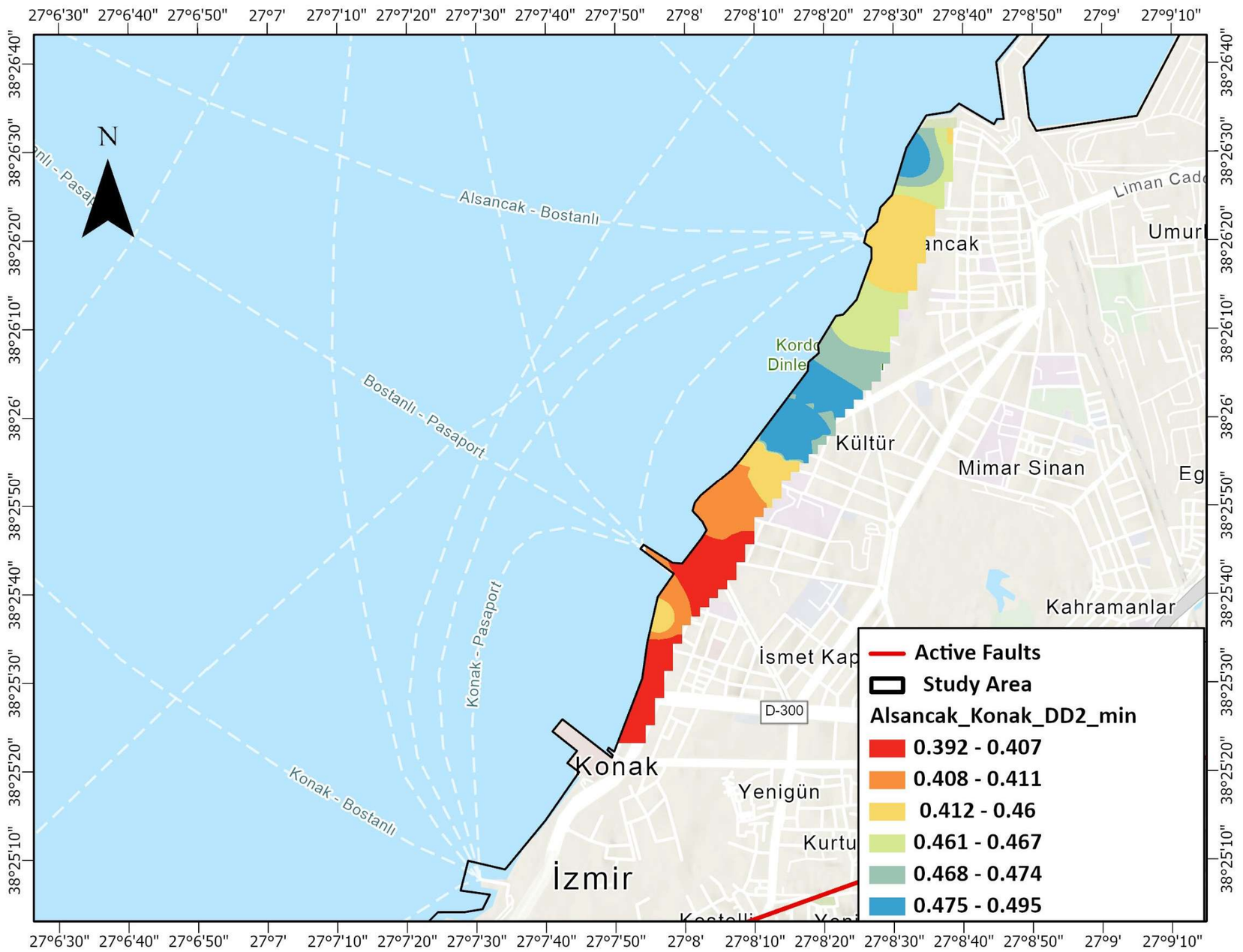

Figure A3.19 Factor of safety distribution for DD-2 (M_w=6.5) for minimum scenario in the Alsancak-Konak area

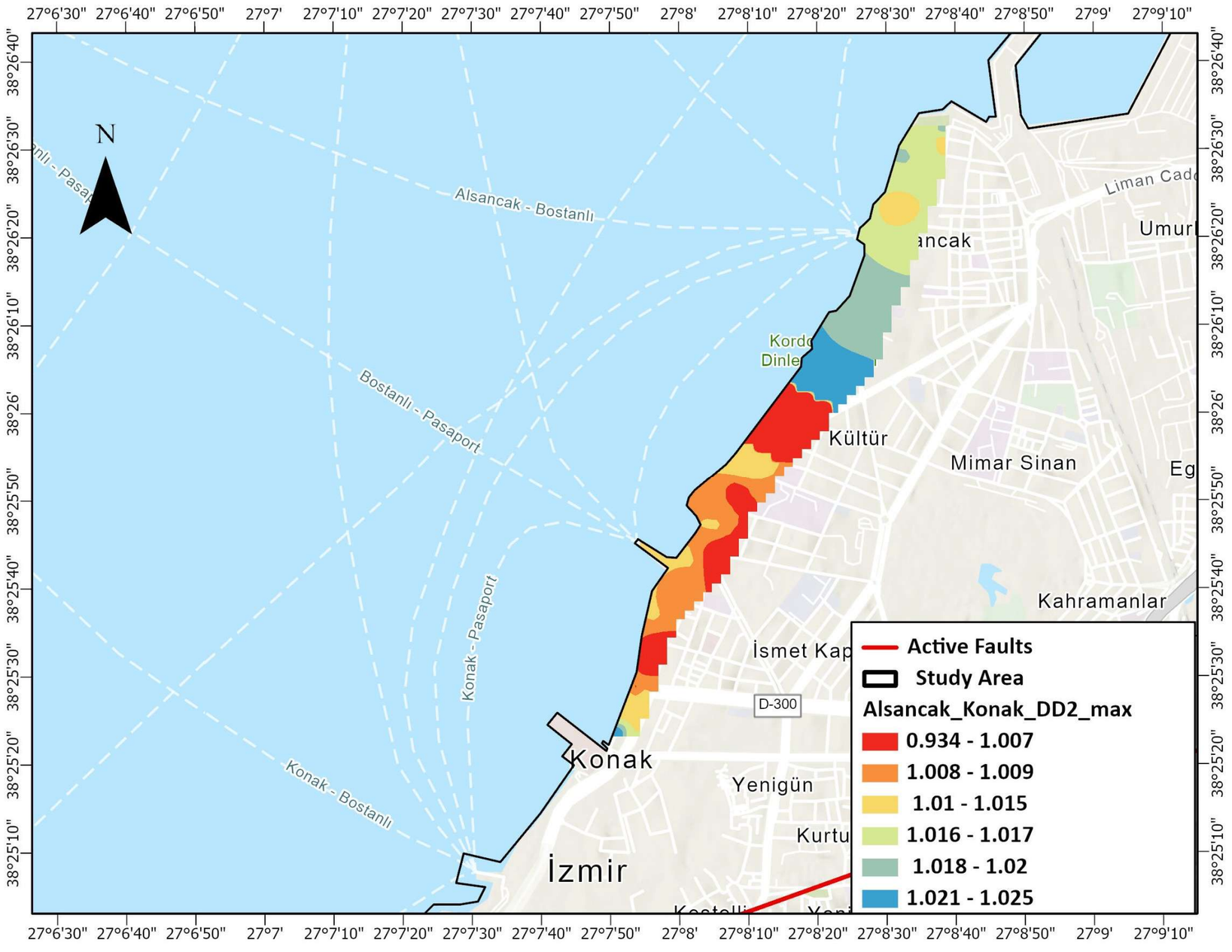

Figure A3.20 Factor of safety distribution for DD-2 (M_w=6.5) for maximum scenario in the Alsancak-Konak area

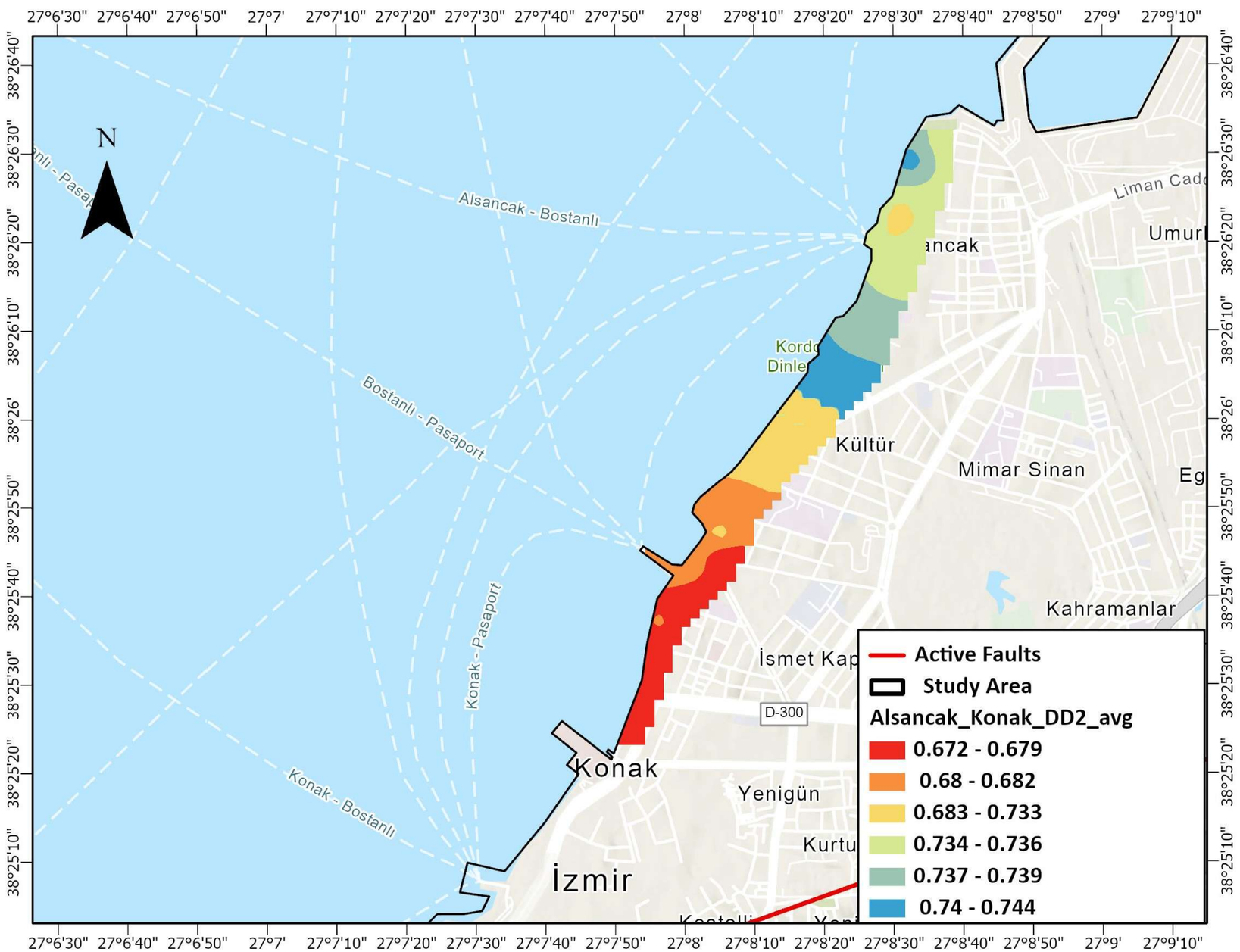

Figure A3.21 Factor of safety distribution for DD-2 (M_w=6.5) for avarage scenario in the Alsancak-Konak area

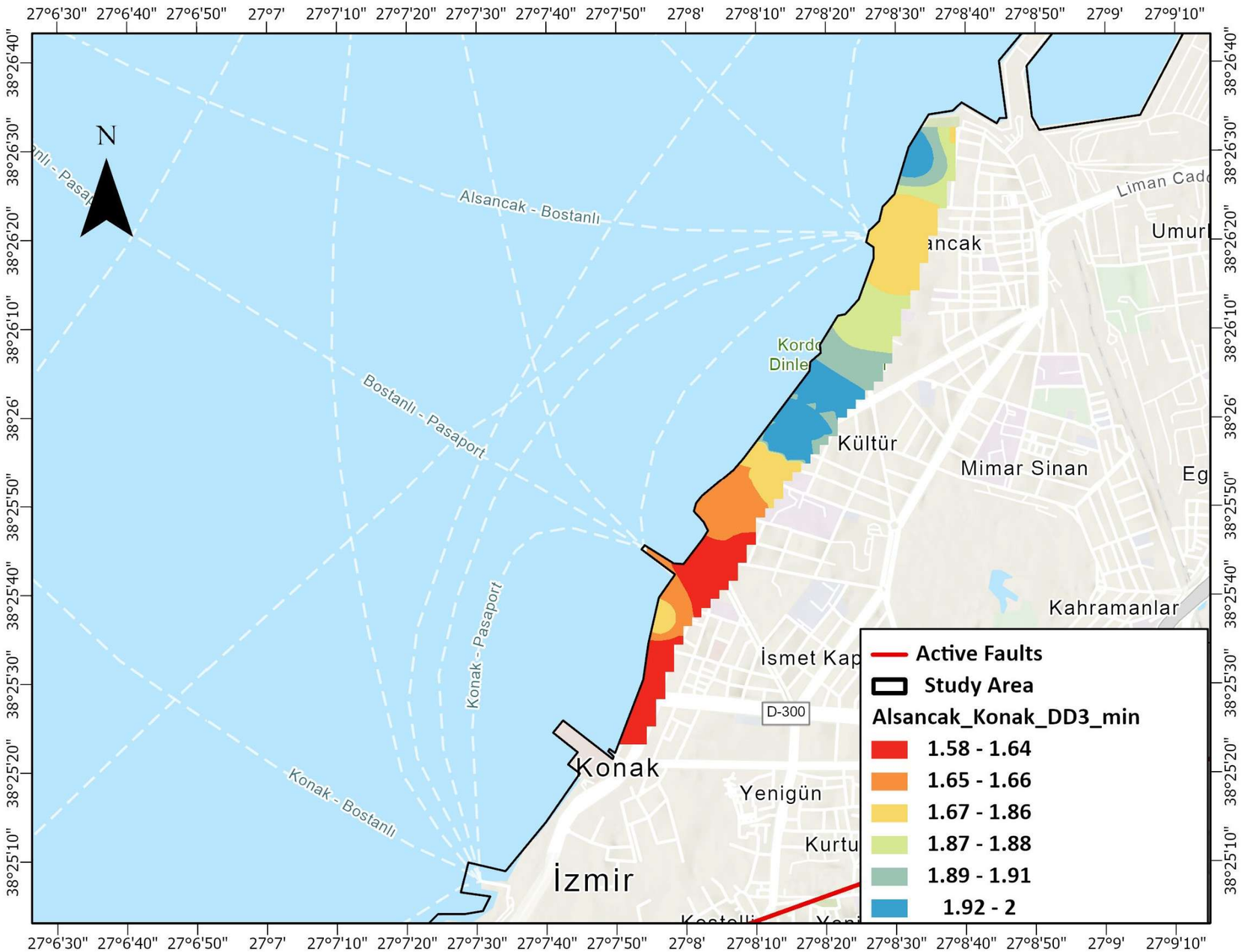

Figure A3.22 Factor of safety distribution for DD-3 (M_w=5.5) for minimum scenario in the Alsancak-Konak area

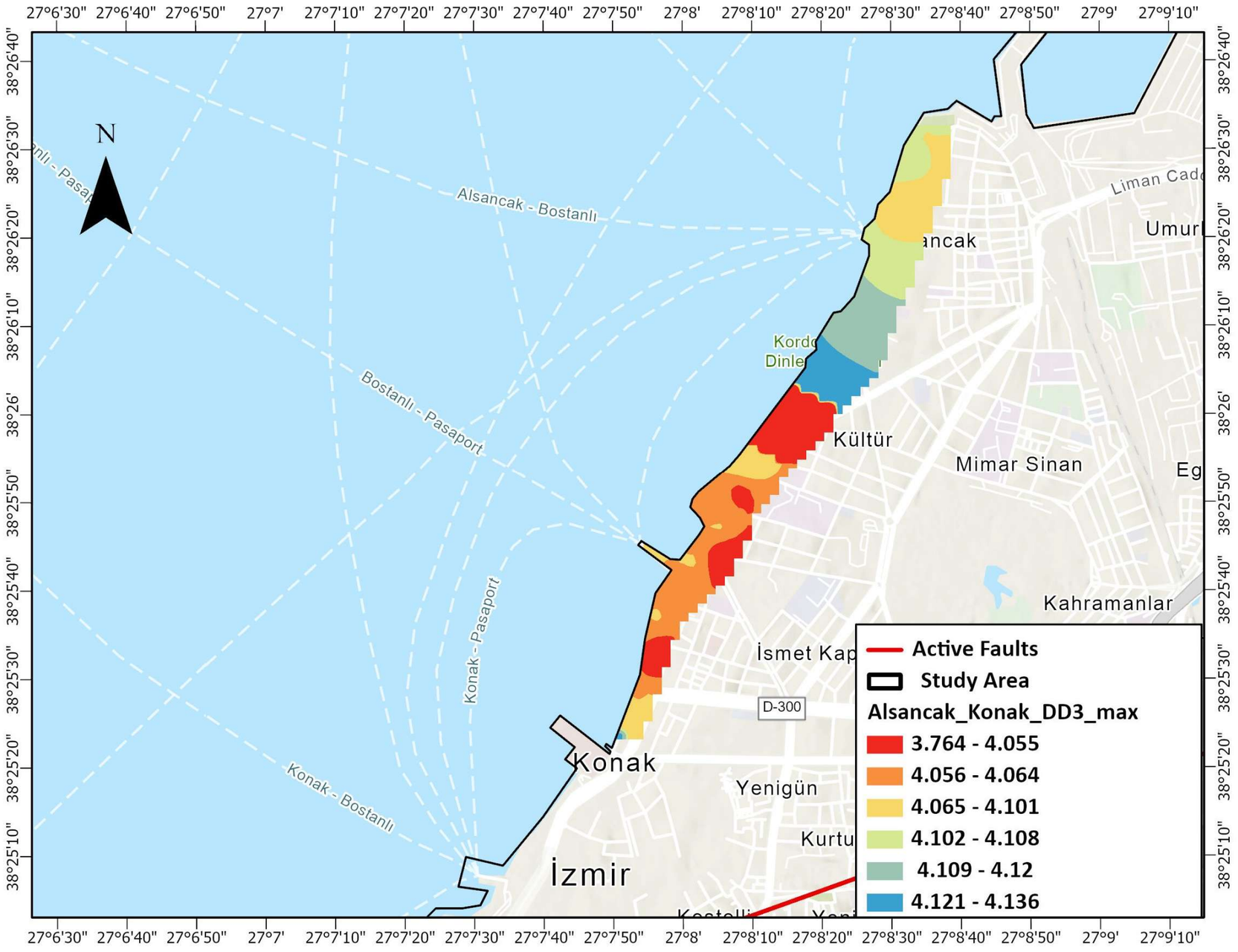

Figure A3.23 Factor of safety distribution for DD-3 (M_w=5.5) for maximum scenario in the Alsancak-Konak area

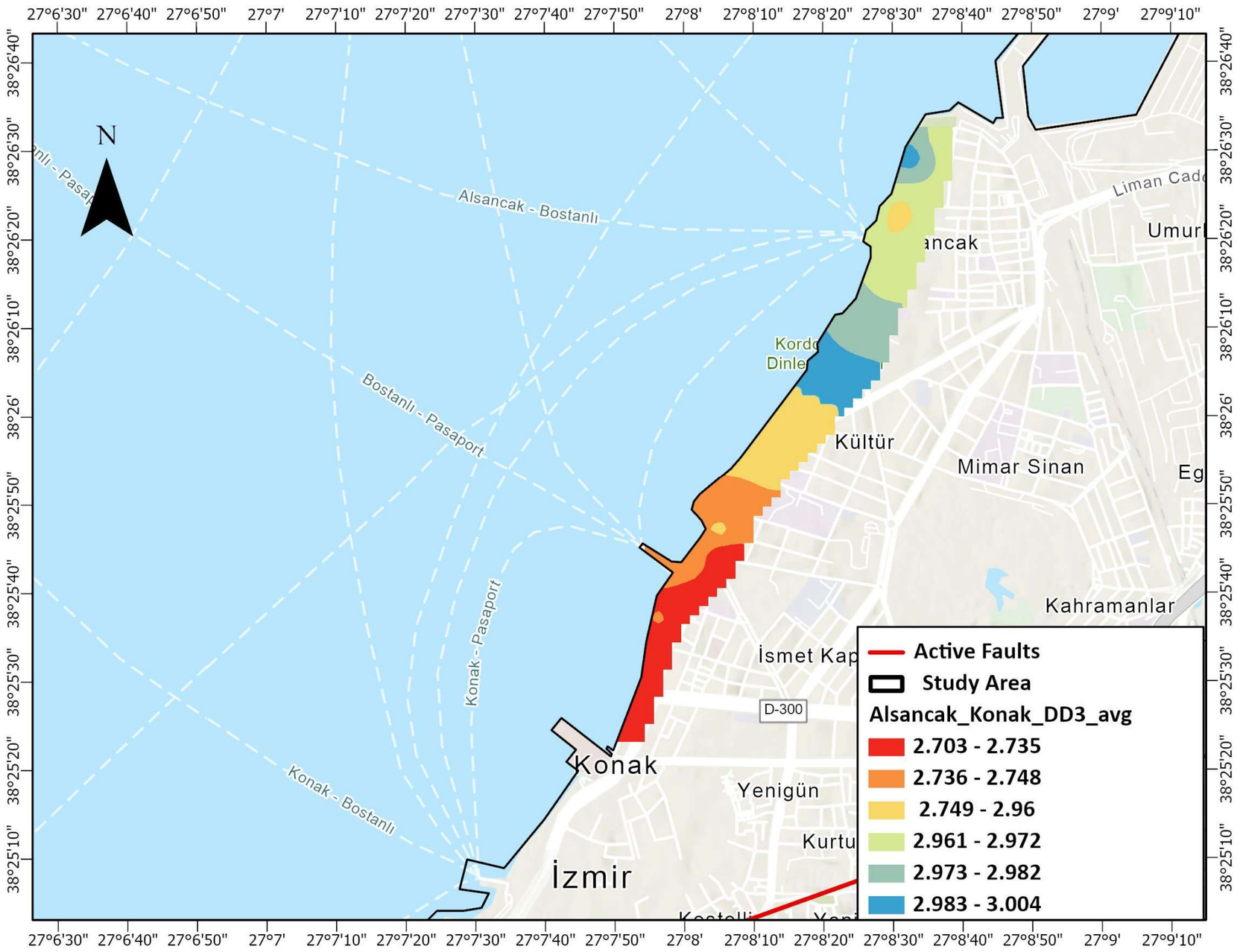

Figure A3.24 Factor of safety distribution for DD-3 (M_w=5.5) for average scenario in the Alsancak-Konak area

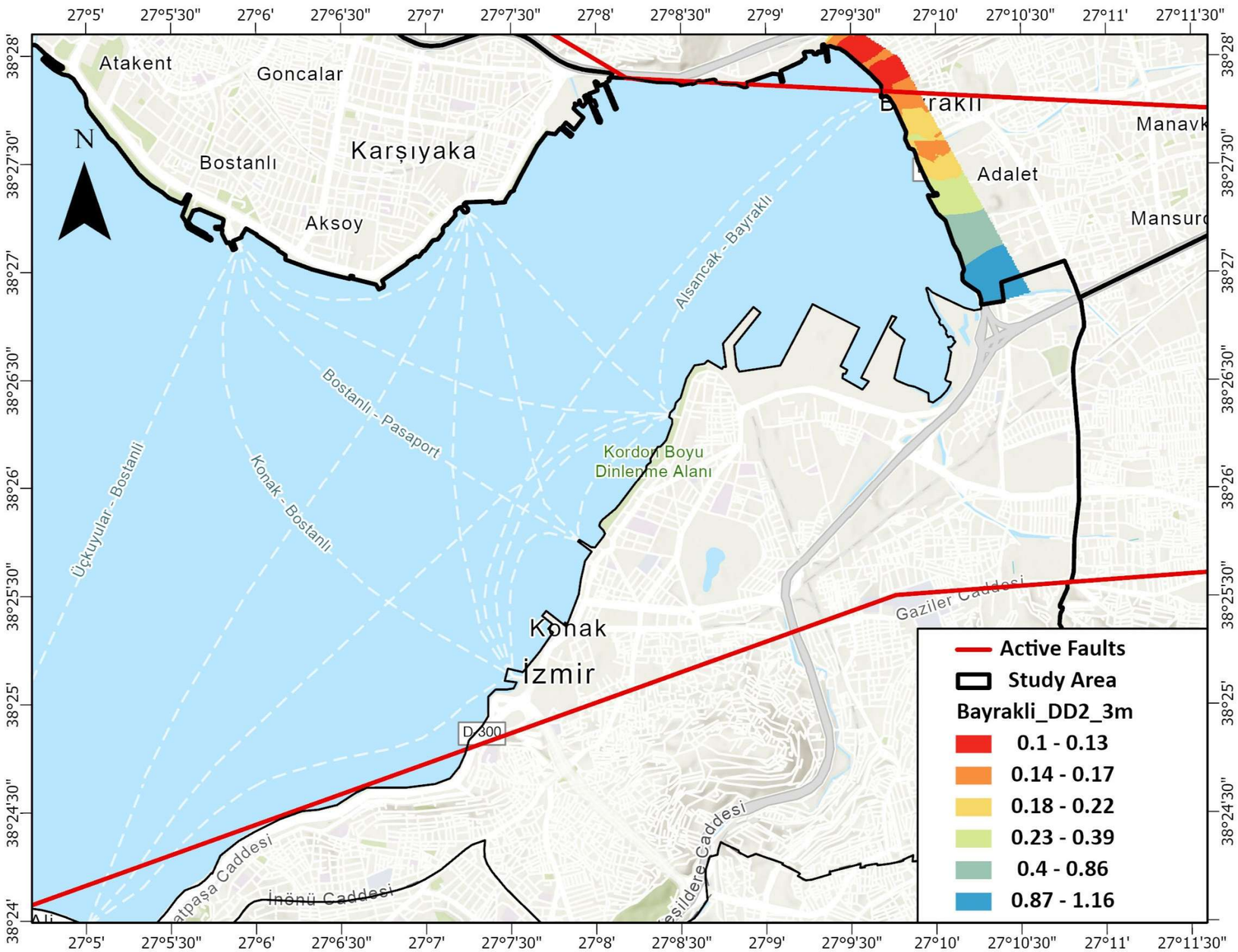

Figure A3.25 Factor of safety distribution for DD-2 (M_w=6.5) earthquake level at 3m depths in the Bayraklı area

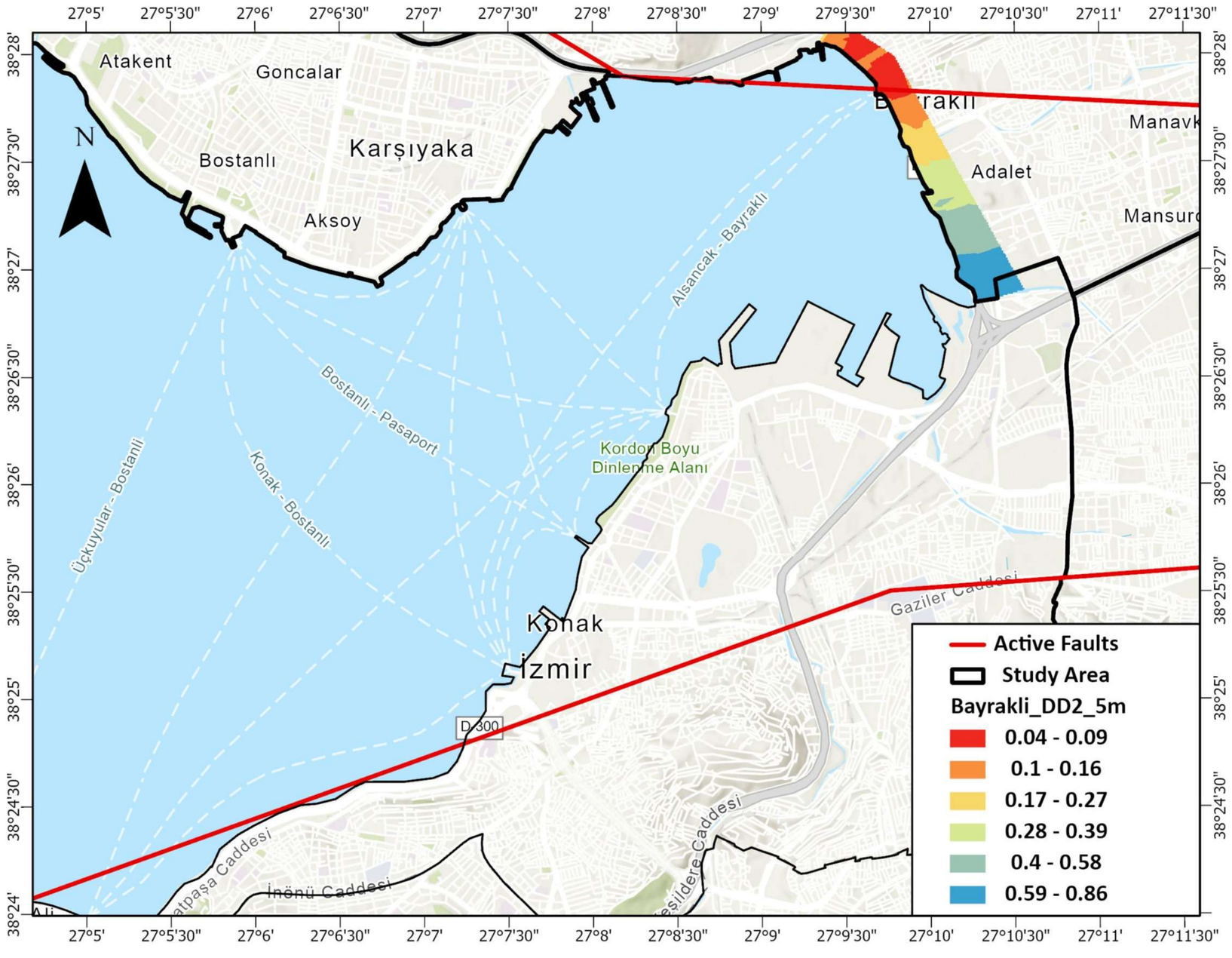

Figure A3.26 Factor of safety distribution for DD-2 (M_w=6.5) earthquake level at 5m depths in the Bayraklı area

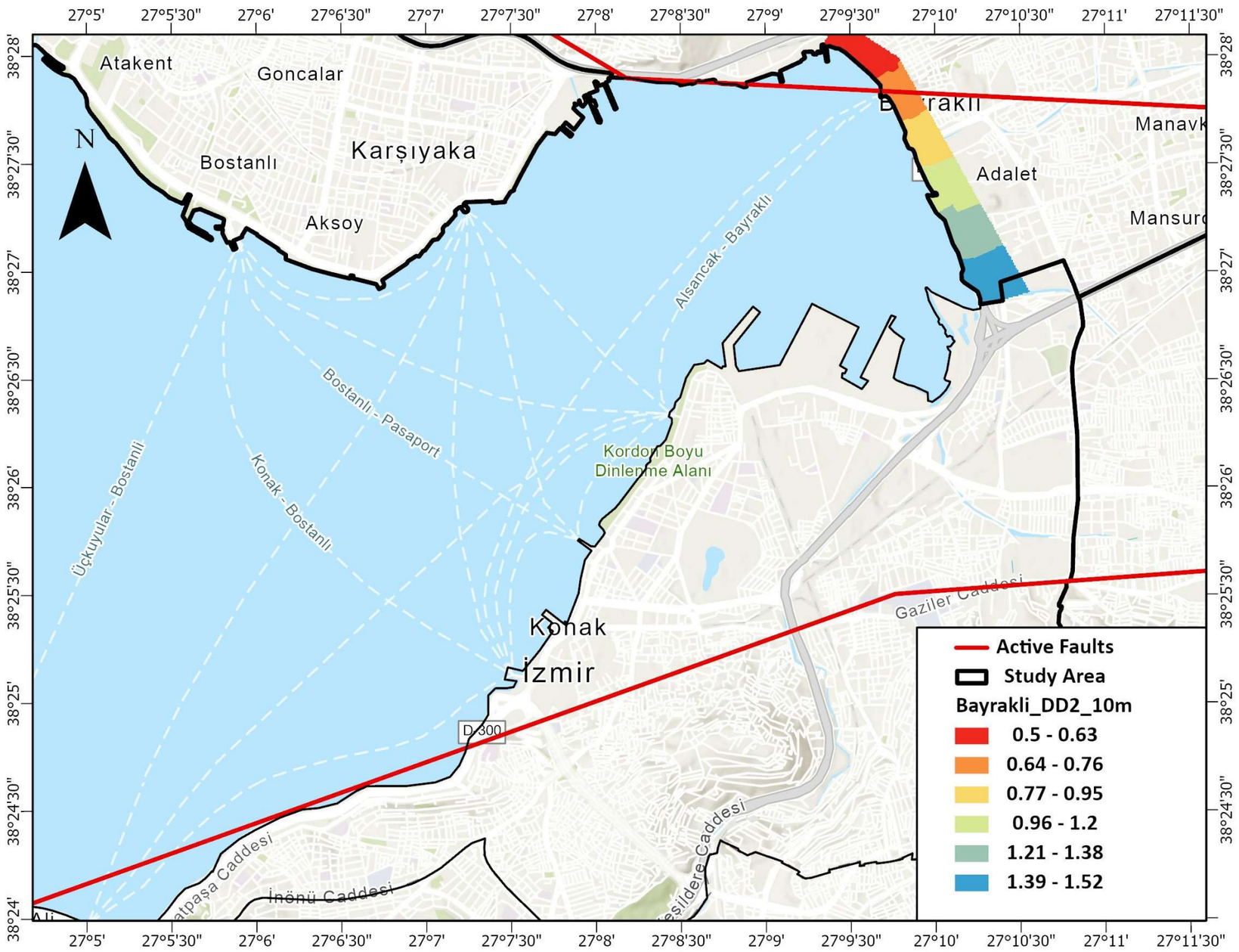

Figure A3.27 Factor of safety distribution for DD-2 (M_w=6.5) earthquake level at 10m depths in the Bayraklı area

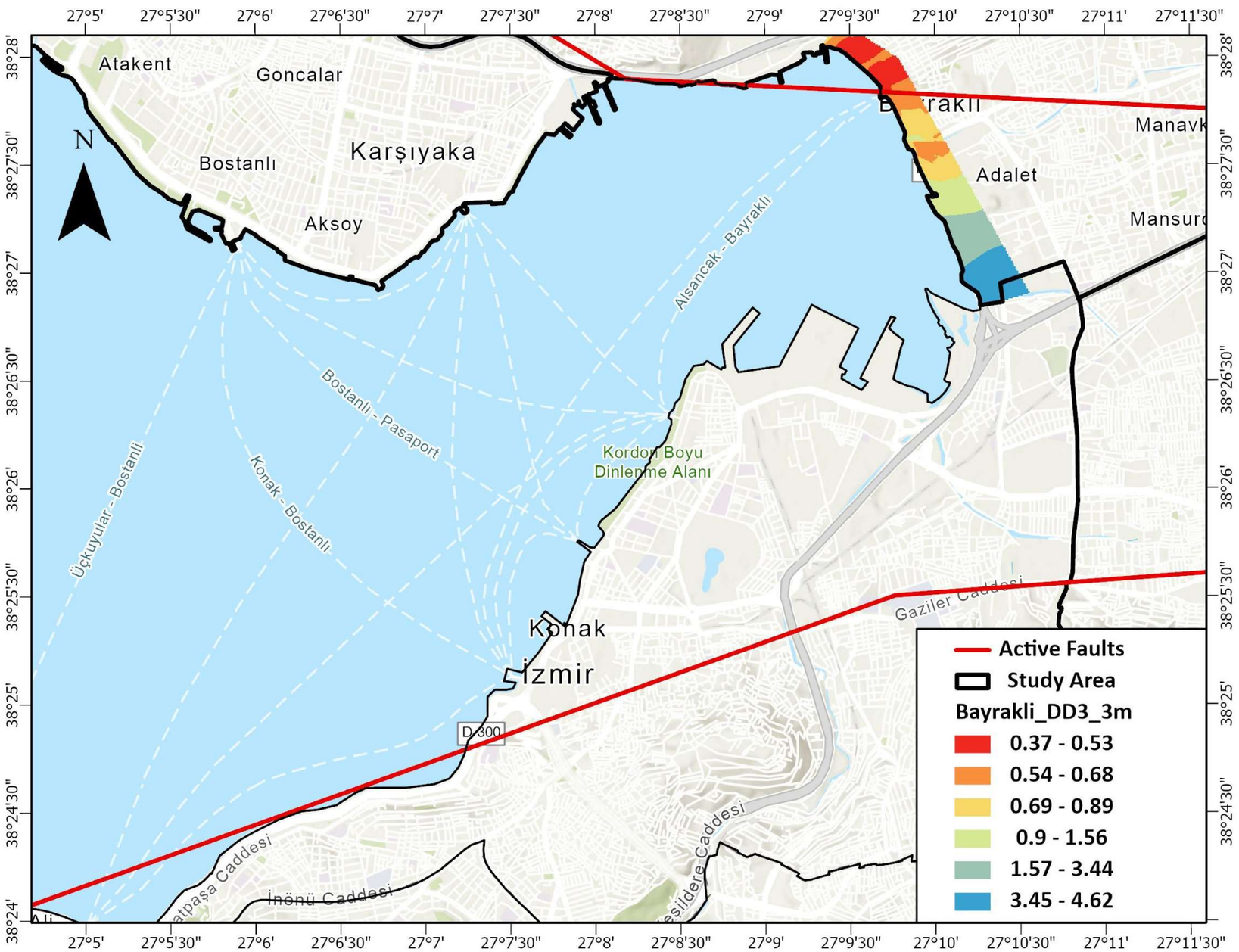

Figure A3.28 Factor of safety distribution for DD-3 (M_w=5.5) earthquake level at 3m depths in the Bayraklı area

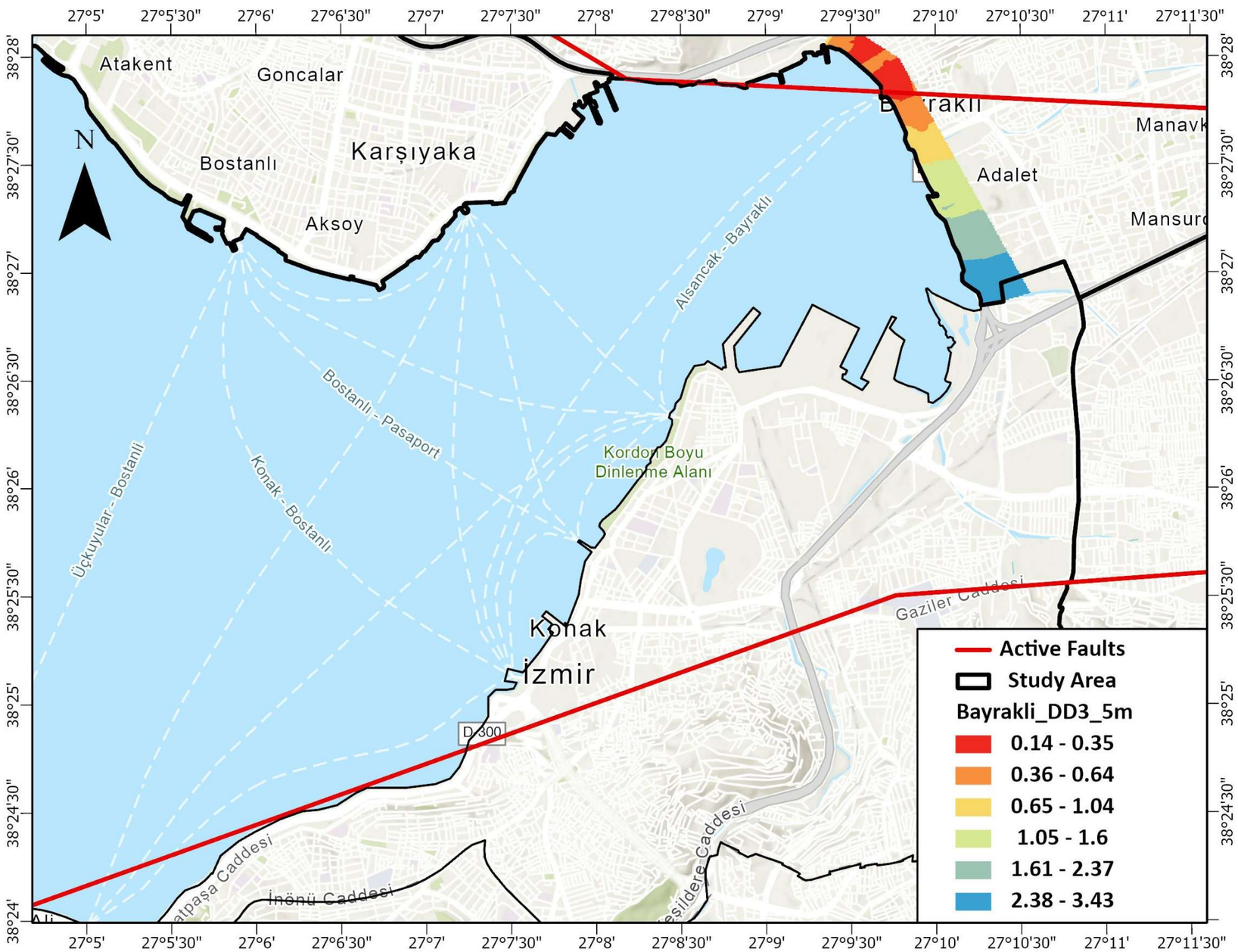

Figure A3.29 Factor of safety distribution for DD-3 (M_w=5.5) earthquake level at 5m depths in the Bayraklı area

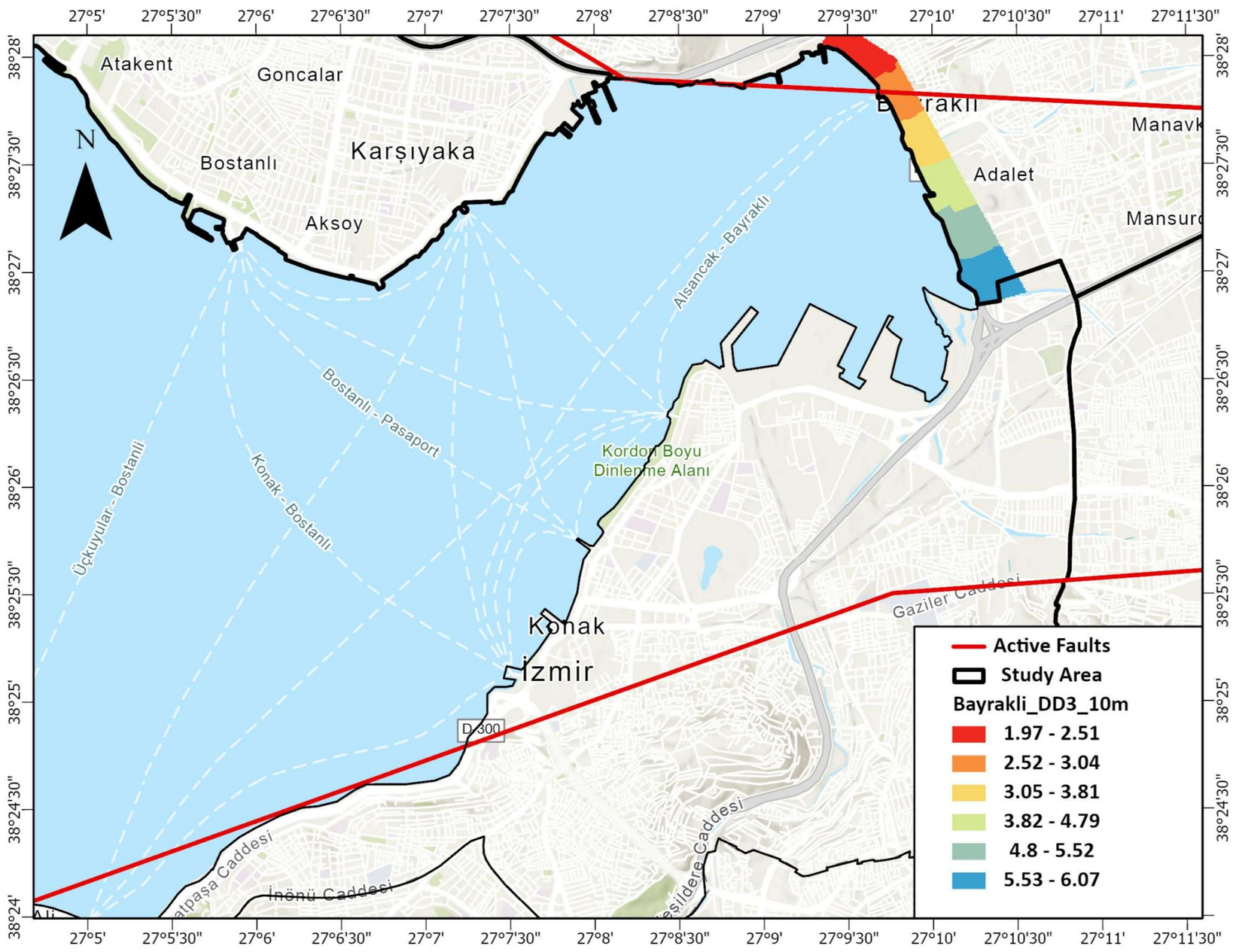

Figure A3.30 Factor of safety distribution for DD-3 (M_w=5.5) earthquake level at 10m depths in the Bayraklı area

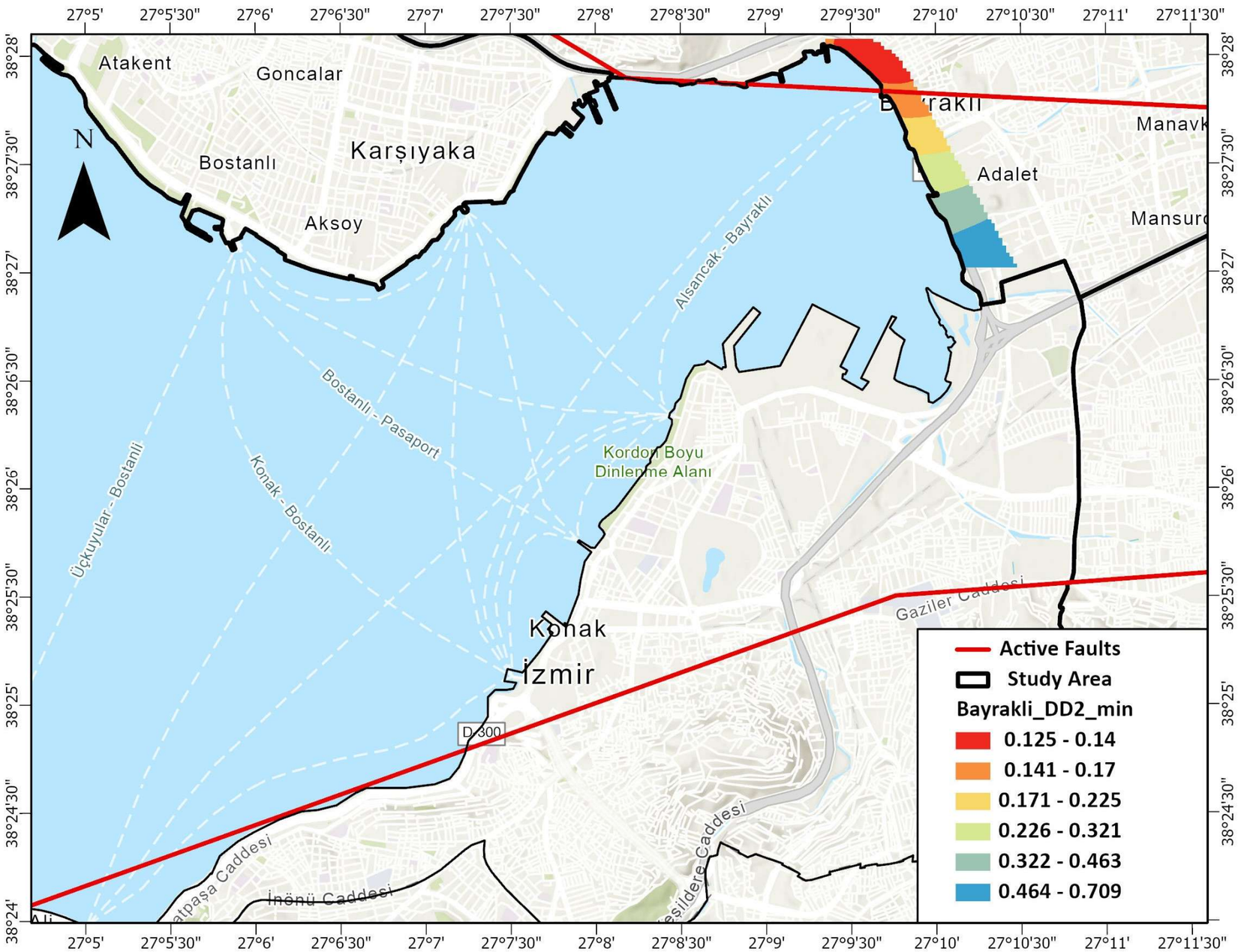

Figure A3.31 Factor of safety distribution for DD-2 (M_w=6.5) for minimum scenario in the Bayraklı area

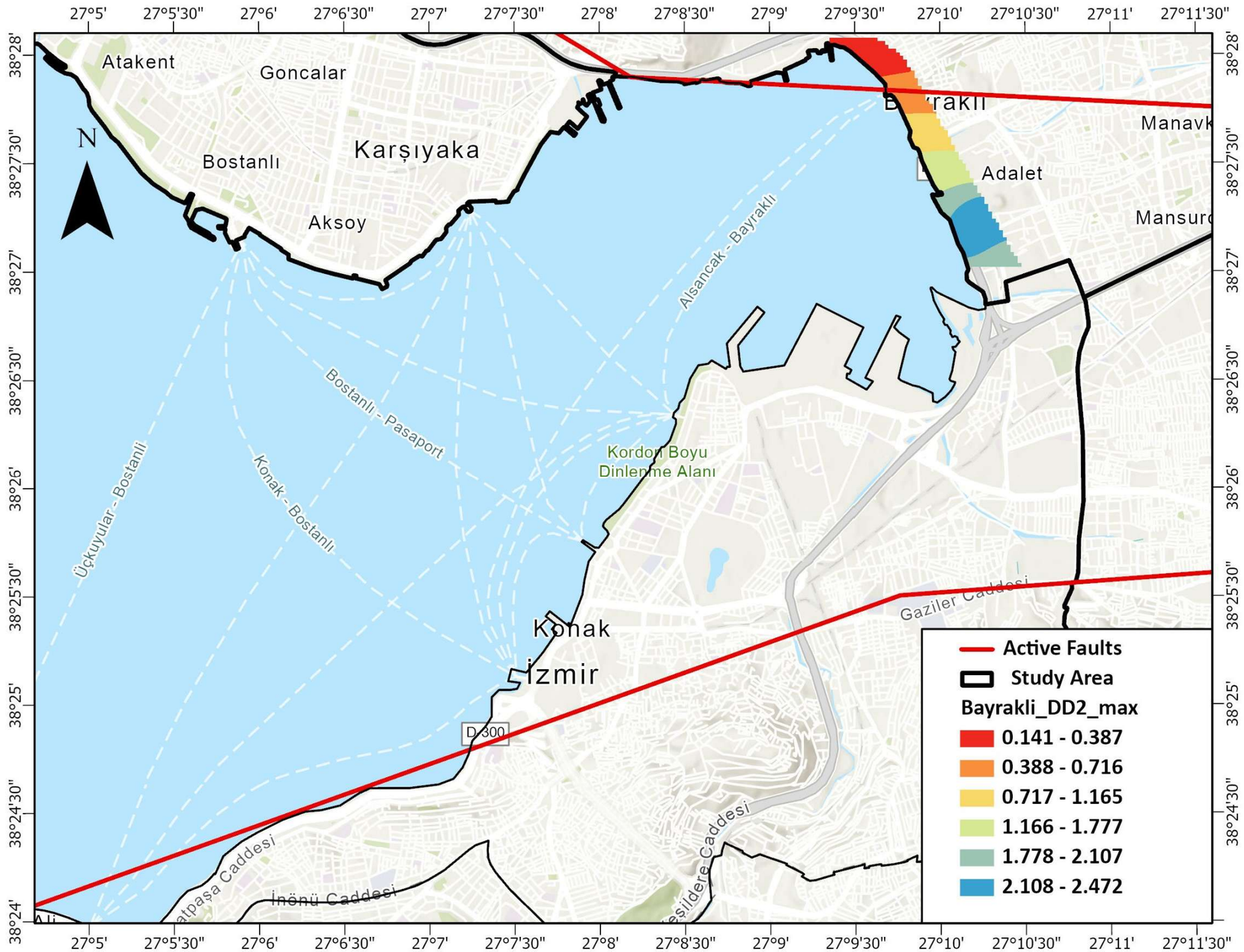

Figure A3.32 Factor of safety distribution for DD-2 (M_w=6.5) for maximum scenario in the Bayraklı area

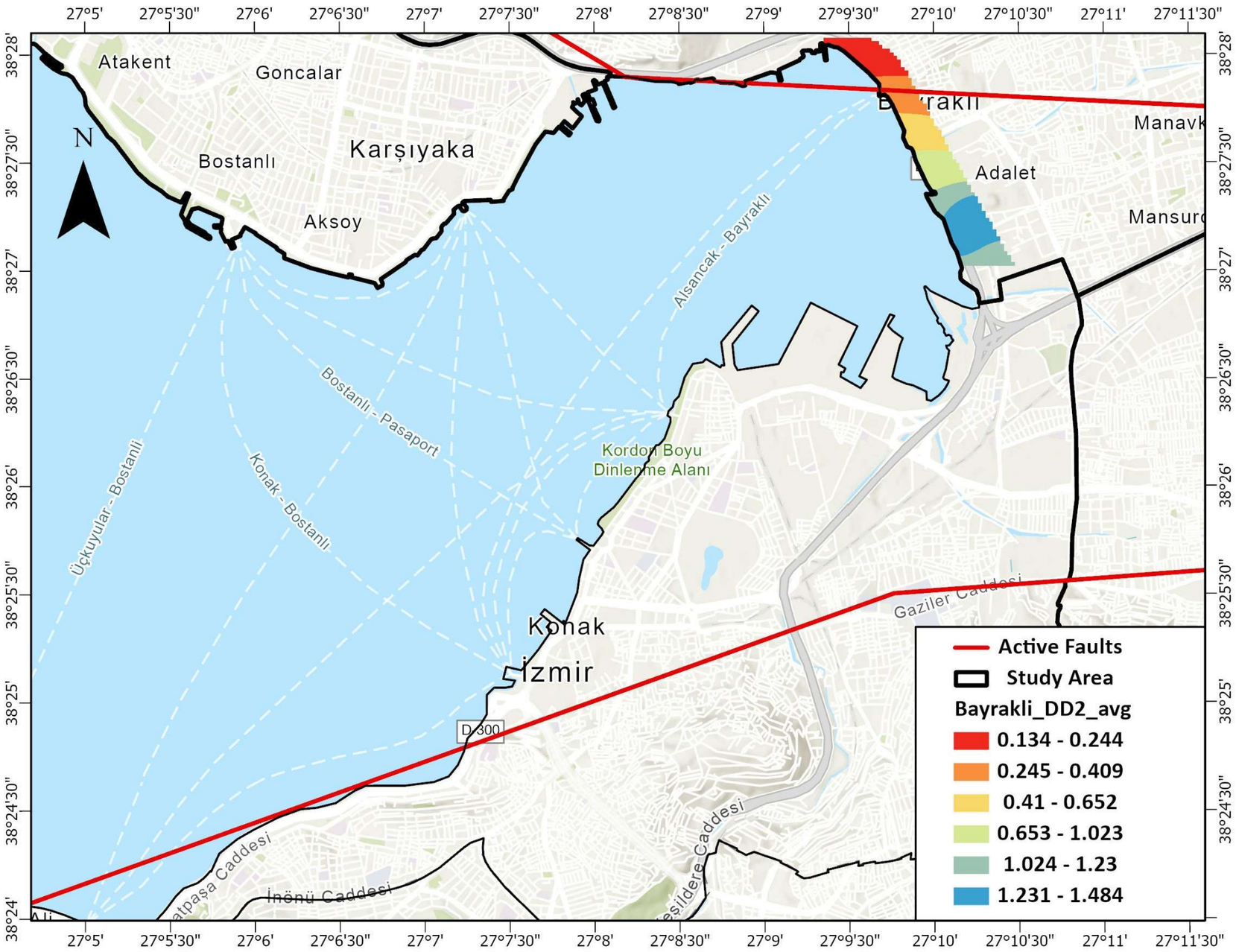

Figure A3.33 Factor of safety distribution for DD-2 (M_w=6.5) for avarage scenario in the Bayraklı area

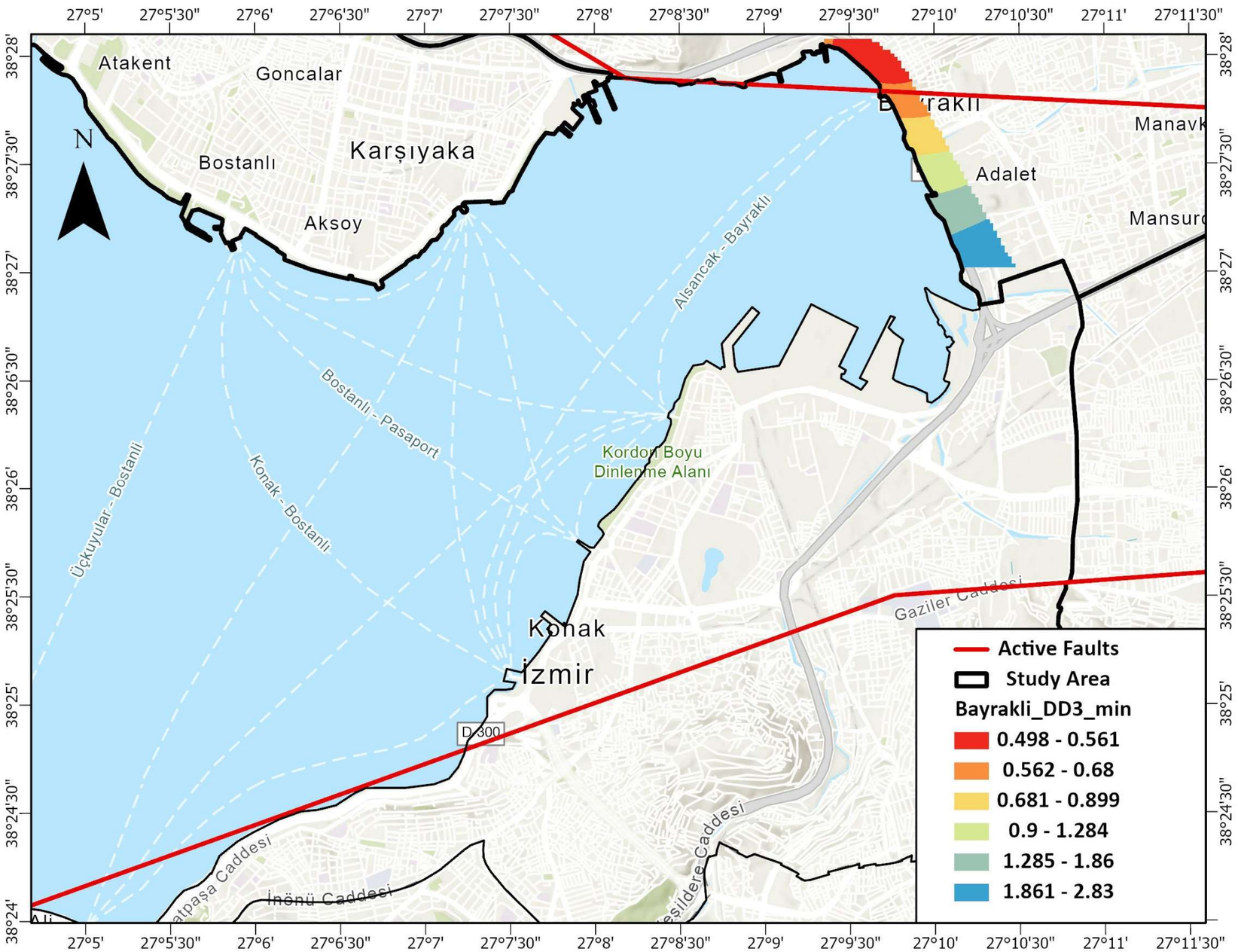

Figure A3.34 Factor of safety distribution for DD-3 (M_w=5.5) for minimum scenario in the Bayraklı area

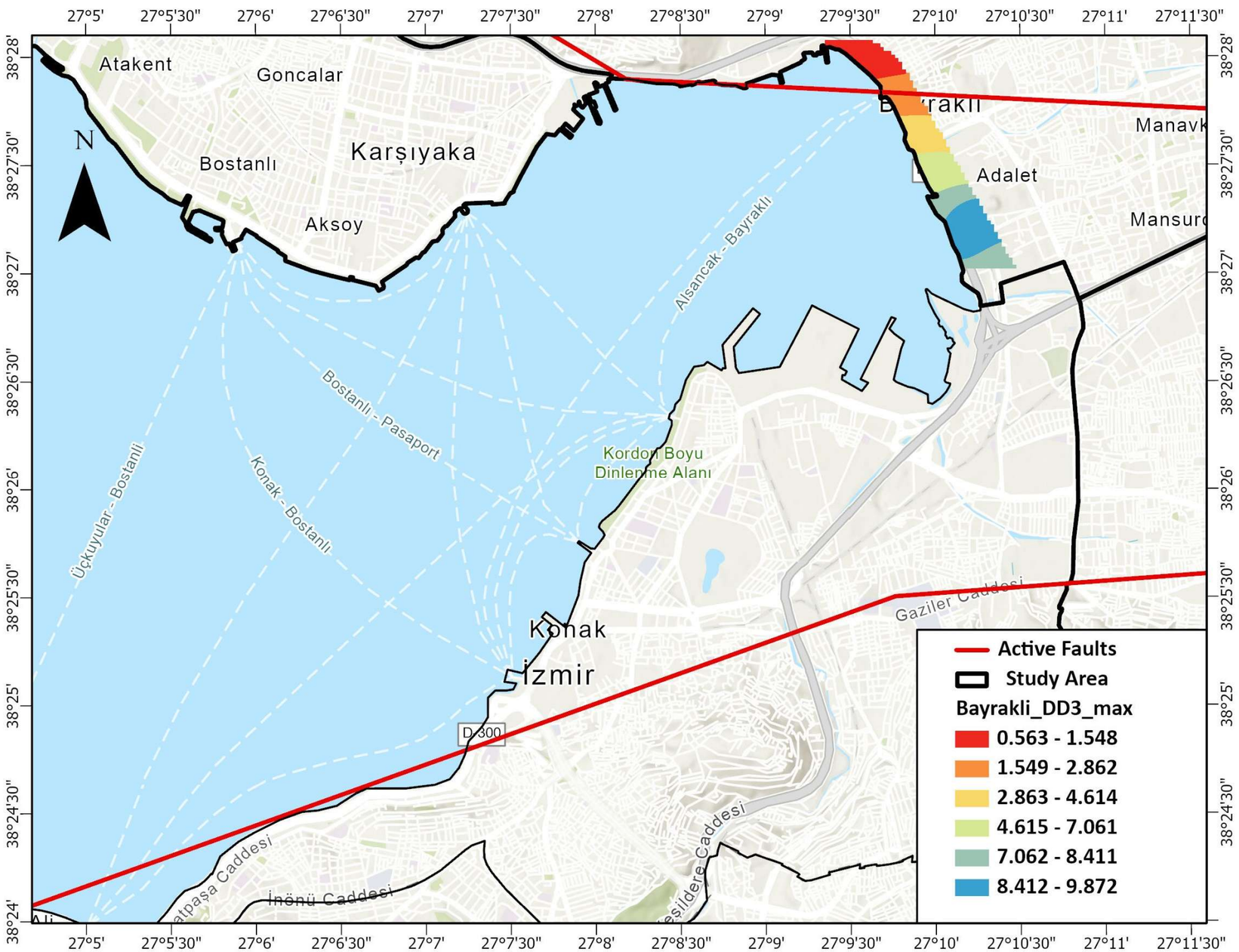

Figure A3.35 Factor of safety distribution for DD-3 (M_w=5.5) for maximum scenario in the Bayraklı area

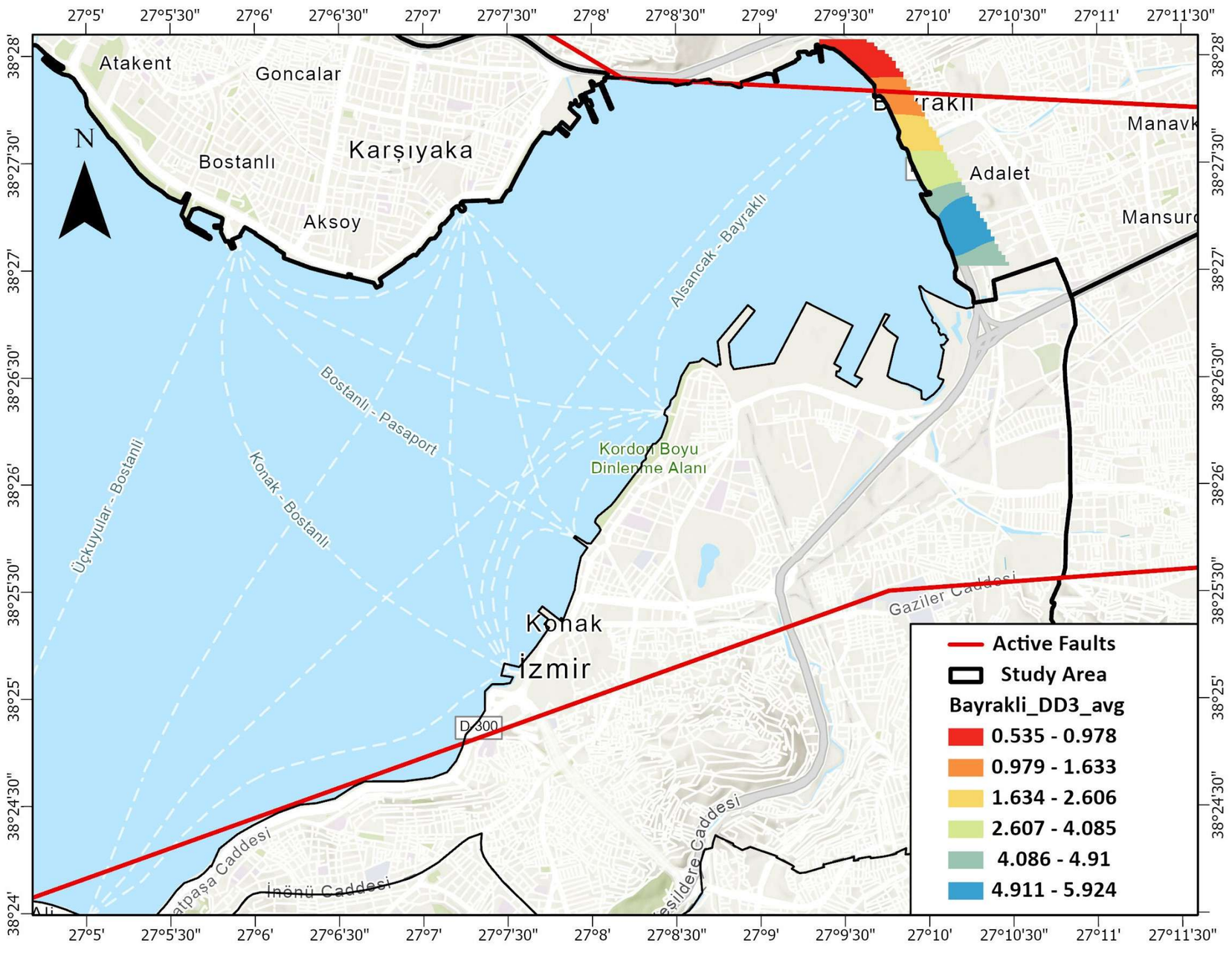

Figure A3.36 Factor of safety distribution for DD-2 (M_w=6.5) for avarage scenario in the Bayraklı area

Appendix-4: Post-Earthquake Settlement Analysis Results

Borehole #	St(2)cm	St(3)cm	Borehole #	St(2)cm	St(3)cm
1_SK-1	0.4		**4_SK-1**	10.0	5.6
1_SK-2	13.4	9.4	**4_SK-2**	6.4	4.3
1_SK-3	4.9		**4_SK-3**		13.1
1_SK-4	4.4		**4_SK-6**	5.6	3.0
1_SK-6	48.9	27.2	**4_SK-8**	4.8	1.5
1_SK-7	19.0	13.7	**4_SK-10**	10.1	5.8
1_SK-8	11.0	8.1	**4_SK-11**	6.5	4.5
1_SK-16	27.0	21.5	**4_SK-12**	7.4	5.3
1_SK-17	12.8	8.6	**4_SK-13**	10.2	5.6
1_SK-18	62.1	47.4	**4_SK-54**	3.0	0.8
1_SK-23	2.8	0.9	**4_SK-55**	26.4	21.8
1_SK-25	10.0	5.4	**4_SK-56**	19.3	13.8
1_SK-26	4.3	3.4	**4_SK-66**	19.5	12.7
1_SK-31	14.2	11.2	**4_SK-68**	4.5	3.0
1_SK-32	9.2	7.3	**4_SK-181**	4.8	3.1
1_SK-33		36.5	**5_SK-1**	18.4	10.7
1_SK-34		45.4	**5_SK-2**	39.5	28.1
1_SK-35	46.5	39.0	**6_SK-1**	43.6	33.4
1_SK-36	24.3	17.7	**6_SK-3**	43.7	36.7
1_SK-39	81.3	59.1	**6_SK-4**	8.6	6.7
2_SK-1	10.5	6.5	**6_SK-5**	27.0	26.1
3_SK-1	16.0	10.2	**6_SK-7**	31.9	24.1
3_SK-2	12.8	6.2	**7_SK-11**	48.1	33.2
3_SK-3	42.8	29.5	**7_SK-12**	7.1	4.6
3_SK-4	33.9	20.3	**7_SK-14**	11.4	8.0
3_SK-5	9.4	5.1	**7_SK-15**	19.2	7.6
3_SK-6	6.4	4.4	**8_SK-1**	12.9	7.6
3_SK-7	21.3	16.0	**8_SK-2**	26.5	18.5

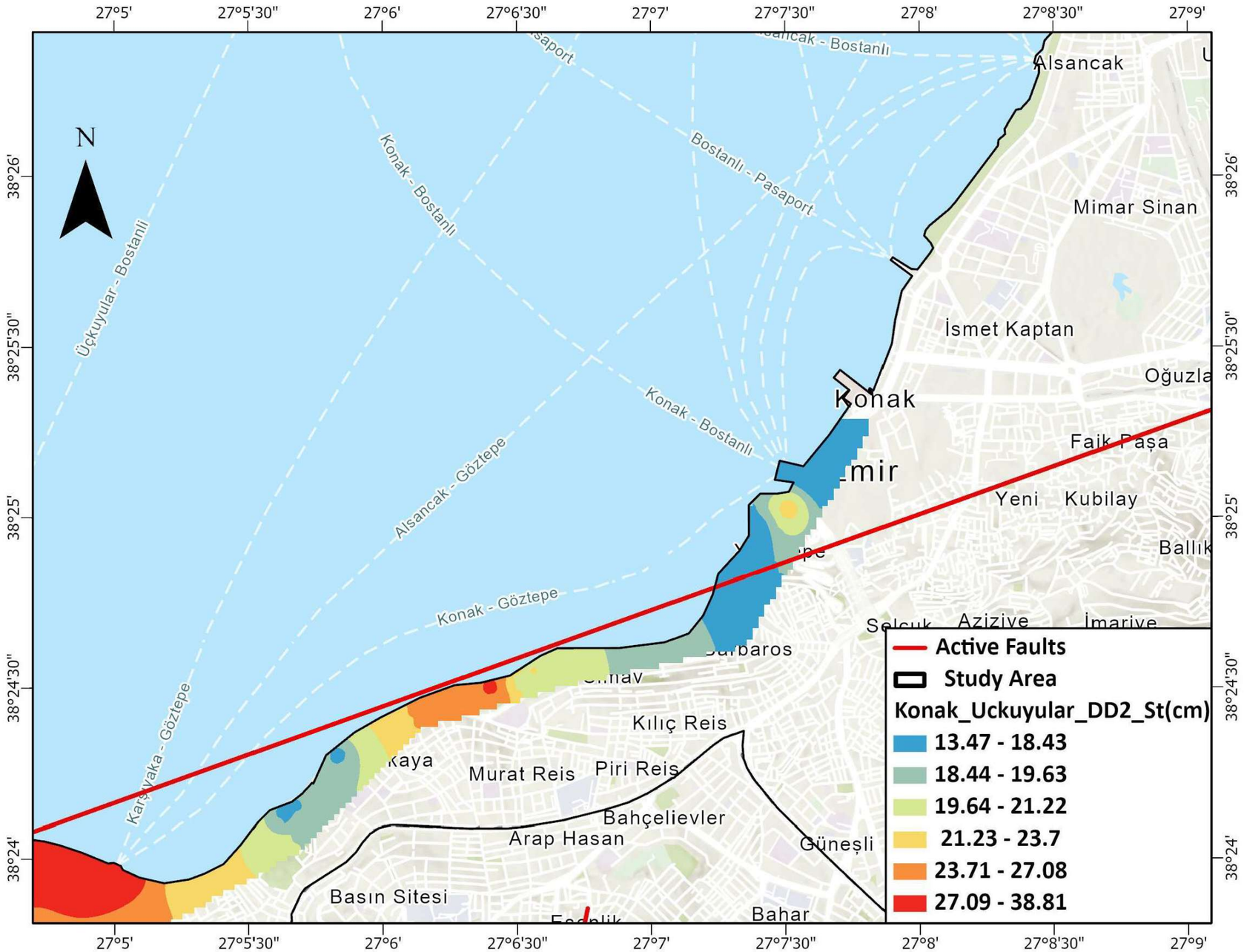

Figure A4.1 Post-earthquake settlement distribution for DD-2 (M_w=6.5) earthquake level in the Konak-Üçkuyular area

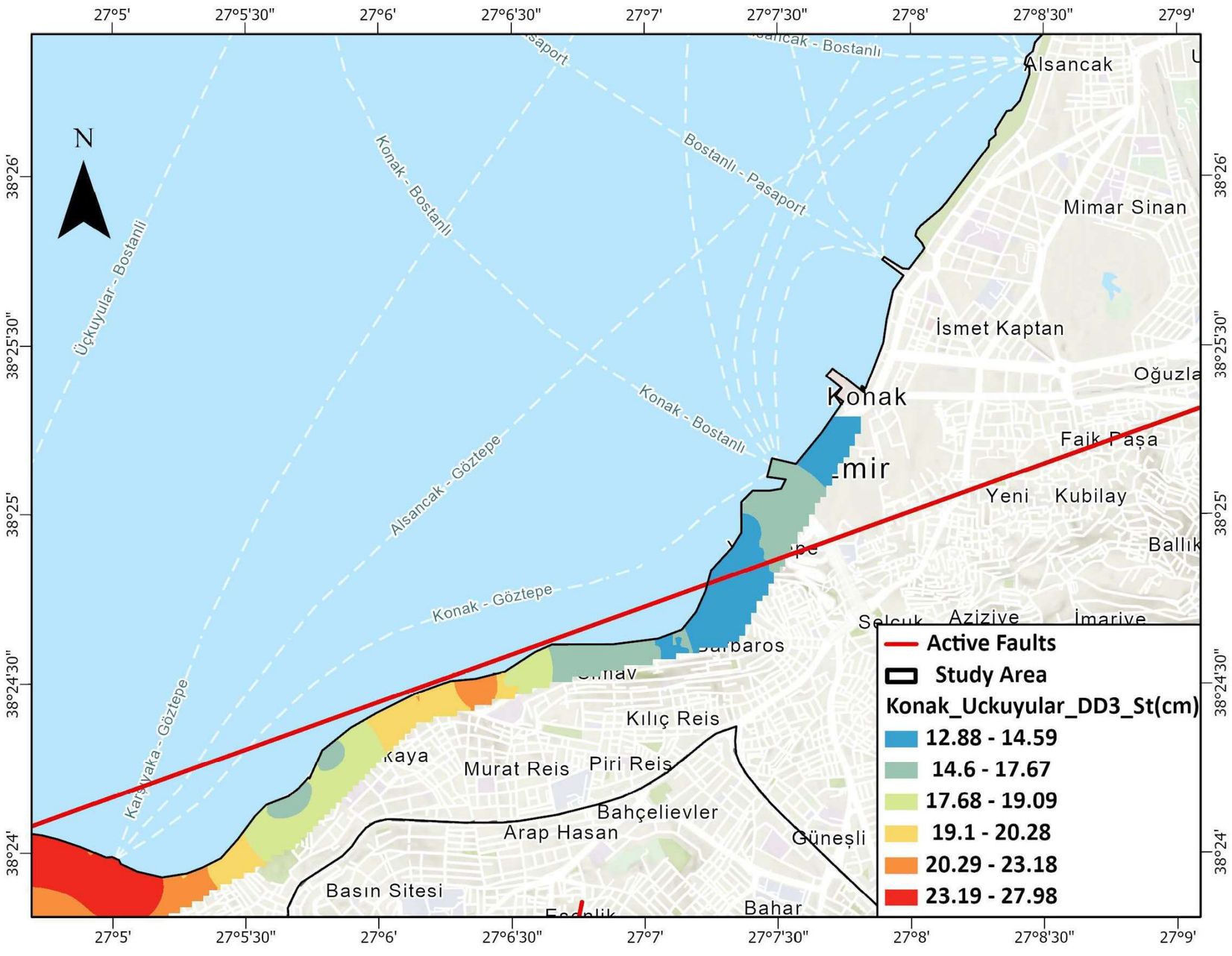

Figure A4.2 Post-earthquake settlement distribution for DD-3 (M_w=5.5) earthquake level in the Konak-Üçkuyular area

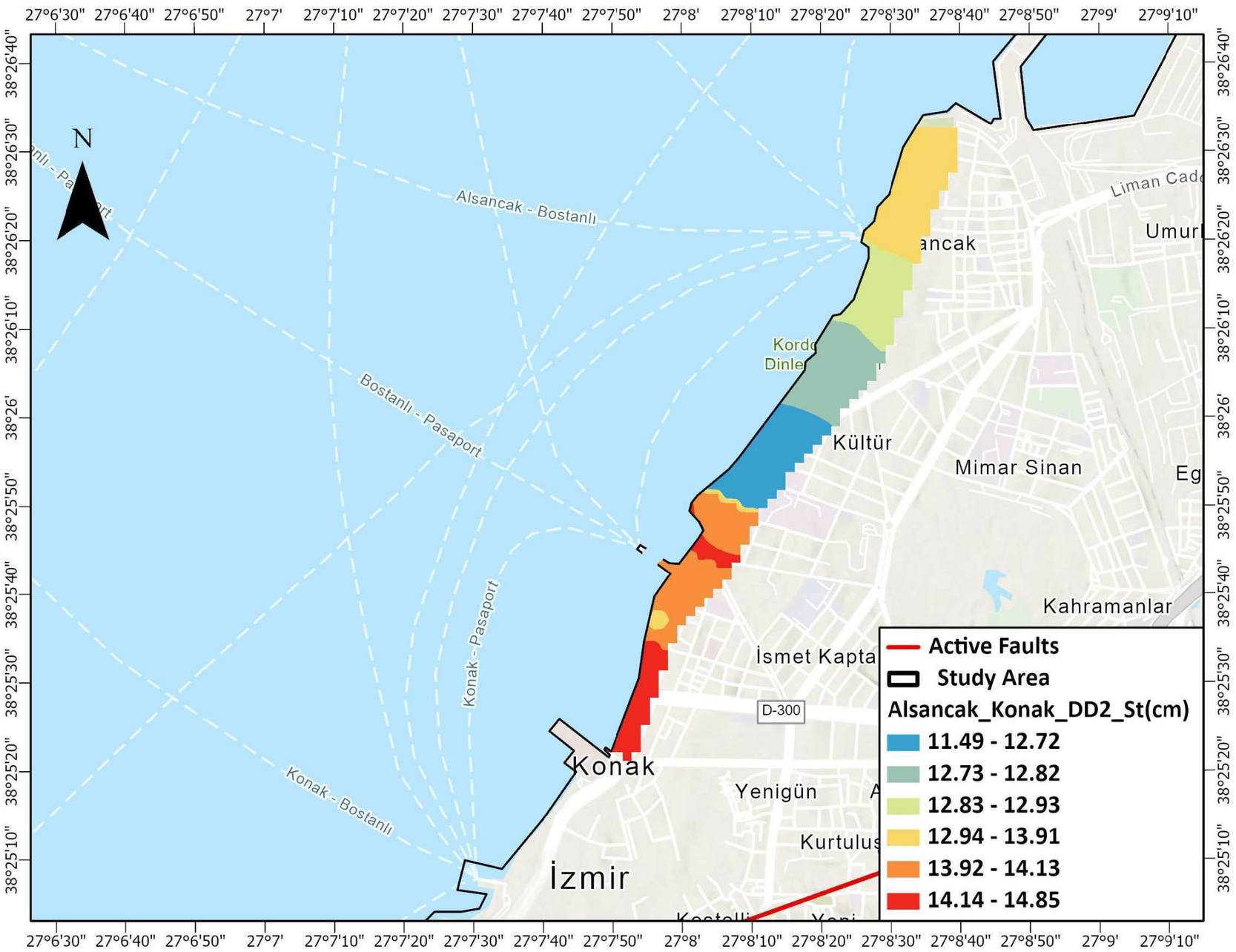

Figure A4.3 Post-earthquake settlement distribution for DD-2 (M_w=6.5) earthquake level in the Alsancak-Konak area

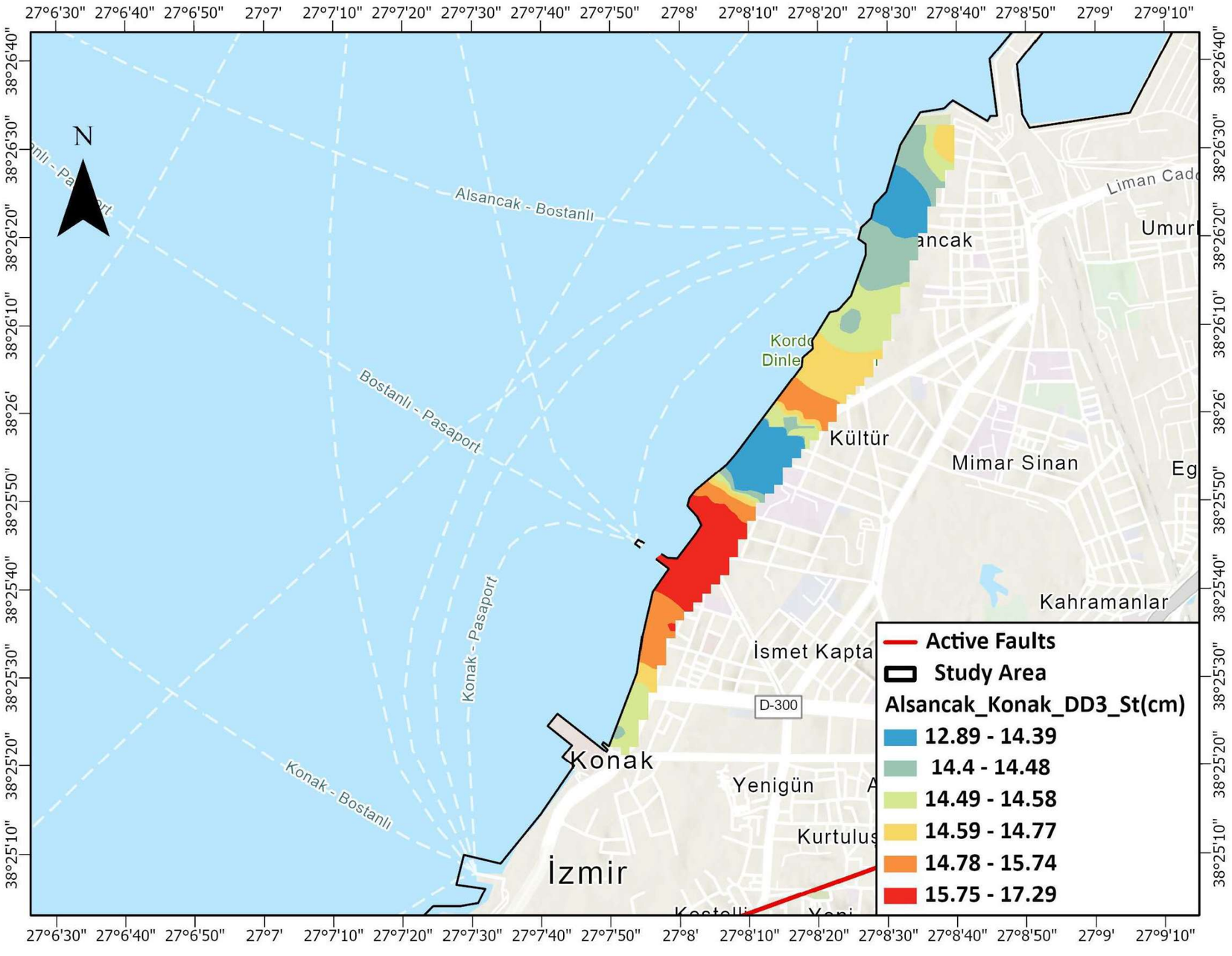

Figure A4.4 Post-earthquake settlement distribution for DD-3 (M_w=5.5) earthquake level in the Alsancak-Konak area

Appendix-5: ArcGIS Database

Appendix-6: Python Codes

```
import arcpy
import math

# Specify the path to your table
table_path = r"C:\Users\atspi\OneDrive\Masaüstü\ARCGIS-TEZ\Pinar_Tez\Pinar_Tez.gdb\T_1_SK_1__ExportTable3"  # Update accordingly

# Define the field names for EDG and CN
edg_field = "EDG"
cn_field = "CN"

# Process each record using an UpdateCursor
with arcpy.da.UpdateCursor(table_path, [edg_field, cn_field]) as cursor:
    for row in cursor:
        edg_value = row[0]  # Get the value from the EDG field
        print(f"EDG Value: {edg_value}")  # Print the EDG value
        if edg_value is not None and edg_value > 0:  # Perform calculation if EDG is greater than 0
            cn_value = math.sqrt(100 / edg_value)
            cn_value = cn_value if cn_value < 1.7 else 1.7
            print(f"Calculated CN Value: {cn_value}")  # Print the calculated CN value
            row[1] = cn_value  # Assign the calculated value to the CN field
        else:
            print("EDG Value is None or 0")  # Print a message if EDG is invalid
            row[1] = None  # Set CN field to None
        cursor.updateRow(row)

print("Calculation completed, and the CN field has been updated.")
```

Figure A6.1 Overburden Pressure Correction

```
import arcpy
import math

# Specify the path to your table
table_path = r"C:\Users\atspi\OneDrive\Masaüstü\ARCGIS-TEZ\Pinar_Tez\Pinar_Tez.gdb\T_1_SK_1__ExportTable3"  # Update accordingly

# Define field names
start_field = "Top"
end_field = "Bottom"
cr_field = "CR"

# Process each record using an UpdateCursor
with arcpy.da.UpdateCursor(table_path, [start_field, end_field, cr_field]) as cursor:
    for row in cursor:
        start_value = row[0]  # Get the value from the Start field
        end_value = row[1]    # Get the value from the End field

        if start_value is not None and end_value is not None:
            average = (start_value + end_value) / 2  # Calculate the average
            # Perform calculations
            if average < 3:
                cr_value = 0.75
            elif average < 4:
                cr_value = 0.8
            elif average < 6:
                cr_value = 0.85
            elif average < 10:
                cr_value = 0.95
            else:
                cr_value = 1
            row[2] = cr_value  # Assign the calculated value to the CR field
        else:
            row[2] = None  # Set CR to None if either value is missing

        cursor.updateRow(row)

print("Calculation completed, and the CR field has been updated.")
```

Figure A6.2 Rod Length Correction

```
import arcpy

# Specify the path to your table
table_path = r"C:\Users\atspi\OneDrive\Desktop\ARCGIS-TEZ\Pinar_Tez\Pinar_Tez.gdb\T_1_SK_2__ExportTable"

# Check the field names
fields = arcpy.ListFields(table_path)
field_names = [field.name for field in fields]

# Fields that should have the data type `DOUBLE` (only select existing fields)
fields_to_convert = [
    "N30", "CN", "CR", "N60", "rd", "MSF",
    "F_N1_60", "G", "LL", "PL", "PI", "c__kPa_", "CRR7_5", "CRR7_5_",
    "CSR__1_", "CSR__2_", "CSR__3_", "Fs__1_", "Fs__2_", "Fs__3_",
    "Fs___1_", "Fs___2_", "Fs___3_", "F_N1_60_i", "MSF_1_", "MSF_2_",
    "MSF_3_", "Tav", "Du", "EDGs", "Ev", "Si"
]

# Filter out the existing fields
fields_to_convert = [field for field in fields_to_convert if field in field_names]

# Add new fields and copy the values to temporary fields
for field in fields_to_convert:
    temp_field = f"{field}_temp"
    arcpy.management.AddField(table_path, temp_field, "DOUBLE")
    arcpy.management.CalculateField(table_path, temp_field, f"!{field}!", "PYTHON3")
    arcpy.management.DeleteField(table_path, field)
    arcpy.management.AlterField(table_path, temp_field, field)

print("Field data types have been changed to DOUBLE.")
```

Figure A6.3 Code to convert columns to numeric

```
import arcpy

# Specify the path to your table
table_path = r"C:\Users\atspi\OneDrive\Desktop\ARCGIS-TEZ\Pinar_Tez\Pinar_Tez.gdb\T_1_SK_1__ExportTable4"  # Update as needed

# Specify the field names
n30_field = "N30"
cn_field = "CN"
ov_field = "OV"
cr_field = "CR"
n60_field = "N60"

# Use UpdateCursor to process each record in the table
with arcpy.da.UpdateCursor(table_path, [n30_field, cn_field, ov_field, cr_field, n60_field]) as cursor:
    for row in cursor:
        n30_value = row[0]  # Get the value from the N30 field

        if n30_value == "R":
            n60_value = "R"  # If N30 value is "R", set N60 value to "R"
        elif n30_value is None:
            n60_value = None  # If N30 value is None, set N60 value to None
        else:
            # Get the values from the OV and CR fields
            ov_value = row[2]
            cr_value = row[3]

            # Check if the values are numeric
            if all(isinstance(value, (int, float)) for value in [n30_value, ov_value, cr_value]):
                n60_value = n30_value * ov_value * cr_value
            else:
                n60_value = None  # If not numeric, set N60 value to None

        row[4] = n60_value  # Write the calculated value to the N60 field
        cursor.updateRow(row)

print("Calculation is complete and the N60 field has been updated.")
```

Figure A6.4 Corrected SPT Calculation N_{60}

```
import arcpy

# Specify the path to your table
table_path = r"C:\Users\atspi\OneDrive\Desktop\ARCGIS-TEZ\Pinar_Tez\Pinar_Tez.gdb\T_1_SK_1__ExportTable4"  # Update as needed

# Specify the field names
n30_field = "N30"
cn_field = "CN"
ov_field = "OV"
cr_field = "CR"
n160_field = "F_N1_60"

# Use UpdateCursor to process each record in the table
with arcpy.da.UpdateCursor(table_path, [n30_field, cn_field, ov_field, cr_field, n160_field]) as cursor:
    for row in cursor:
        n30_value = row[0]  # Get the value from the N30 field

        if n30_value == "R":
            n160_value = "R"  # If N30 value is "R", set F_N1_60 value to "R"
        elif n30_value == "":
            n160_value = ""  # If N30 value is empty, set F_N1_60 value to an empty string
        else:
            # Get the values from the CN, OV, and CR fields
            cn_value = row[1]
            ov_value = row[2]
            cr_value = row[3]

            # Check if the values are numeric
            if all(isinstance(value, (int, float)) for value in [n30_value, cn_value, ov_value, cr_value]):
                n160_value = n30_value * cn_value * ov_value * cr_value
            else:
                n160_value = None  # If not numeric, set F_N1_60 value to None

        row[4] = n160_value  # Write the calculated value to the F_N1_60 field
        cursor.updateRow(row)

print("Calculation is complete and the F_N1_60 field has been updated.")
```

Figure A6.5 Corrected SPT Calculation $(N_1)_{60}$

```
import arcpy
import math

# Specify the path to your table
table_path = r"C:\Users\atspi\OneDrive\Desktop\ARCGIS-TEZ\Pinar_Tez\Pinar_Tez.gdb\T_1_SK_2__ExportTable"  # Update as needed

# Specify the field names
f_n1_60_field = "F_N1_60"
f_no200_field = "F_No200"
f_n1_60_i_field = "F_N1_60_i"

# Use UpdateCursor to process each record in the table
with arcpy.da.UpdateCursor(table_path, [f_n1_60_field, f_no200_field, f_n1_60_i_field]) as cursor:
    for row in cursor:
        f_n1_60_value = row[0]  # Get the value from the F_N1_60 field
        f_no200_value = row[1]  # Get the value from the F_No200 field

        try:
            # Check if the values are numeric
            if isinstance(f_n1_60_value, (int, float)) and isinstance(f_no200_value, (int, float)):
                if f_n1_60_value == "R":
                    f_n1_60_i_value = ""  # If F_N1_60 value is "R", set F_N1_60_i value to an empty string
                elif f_n1_60_value in (None, "") or f_no200_value in (None, 0):
                    f_n1_60_i_value = ""  # If F_N1_60 value is empty or None, or if F_No200 value is None or 0, set F_N1_60_i value to an empty string
                elif f_no200_value <= 5:
                    f_n1_60_i_value = f_n1_60_value  # If F_No200 value is less than or equal to 5, set F_N1_60_i value equal to F_N1_60 value
                elif f_no200_value < 35:
                    f_n1_60_i_value = (1.76 - (190 / (f_no200_value * f_no200_value))) + (0.99 + (math.pow(f_no200_value, 1.5) / 1000)) * f_n1_60_value
                else:
                    f_n1_60_i_value = 5 + 1.2 * f_n1_60_value  # For other cases
            else:
                f_n1_60_i_value = ""  # Leave non-numeric values as empty

            row[2] = f_n1_60_i_value  # Write the calculated value to the F_N1_60_i field
            cursor.updateRow(row)

        except Exception as e:
            print(f"An error occurred: {e}")

print("Calculation is complete and the F_N1_60_i field has been updated.")
```

Figure A6.6 Fine Content Correction to SPT $(N_1)_{60}^{*}$

```
import arcpy
import math

# Specify the path to your table
table_path = r"C:\Users\atspi\OneDrive\Desktop\ARCGIS-TEZ\Pinar_Tez\Pinar_Tez.gdb\T_1_SK_1__ExportTable1"  # Update as needed

# Specify the field names
top_field = "Top"
bottom_field = "Bottom"
rd_field = "rd"

# Use UpdateCursor to process each record in the table
with arcpy.da.UpdateCursor(table_path, [top_field, bottom_field, rd_field]) as cursor:
    for row in cursor:
        top_value = row[0]  # Get the value from the Top field
        bottom_value = row[1]  # Get the value from the Bottom field

        if top_value is not None and bottom_value is not None:
            average_value = (top_value + bottom_value) / 2
            numerator = 1 - 0.4113 * (average_value ** 0.5) + 0.04052 * average_value + 0.001753 * (average_value ** 1.5)
            denominator = 1 - 0.4177 * (average_value ** 0.5) + 0.05729 * average_value - 0.006205 * (average_value ** 1.5) + 0.00121 * (average_value ** 2)

            if denominator != 0:  # Add a check to prevent division by zero
                rd_value = numerator / denominator
            else:
                rd_value = None  # If division by zero, set rd value to None
        else:
            rd_value = None  # If either Top or Bottom value is None, set rd value to None

        row[2] = rd_value  # Write the calculated value to the rd field
        cursor.updateRow(row)

print("Calculation is complete and the rd field has been updated.")
```

Figure A6.7 Stress Reduction Coefficient

```
import arcpy

# Specify the path to your table
table_path = r"C:\Users\atspi\OneDrive\Desktop\ARCGIS-TEZ\Pinar_Tez\Pinar_Tez.gdb\T_1_SK_1__ExportTable1"  # Update as needed

# Specify the MSF_2_ field
msf_2_field = "MSF_2_"

# Calculate the formula
msf_value = (10 ** 2.24) / (6.5 ** 2.56)

# Use UpdateCursor to process each record in the table
with arcpy.da.UpdateCursor(table_path, [msf_2_field]) as cursor:
    for row in cursor:
        row[0] = msf_value  # Write the calculated value to the MSF_2_ field
        cursor.updateRow(row)

print("Calculation is complete and the MSF_2_ field has been updated.")


import arcpy

# Specify the path to your table
table_path = r"C:\Users\atspi\OneDrive\Desktop\ARCGIS-TEZ\Pinar_Tez\Pinar_Tez.gdb\T_1_SK_1__ExportTable1"  # Update as needed

# Specify the MSF_3_ field
msf_3_field = "MSF_3_"

# Calculate the formula
msf_value = (10 ** 2.24) / (5.5 ** 2.56)

# Use UpdateCursor to process each record in the table
with arcpy.da.UpdateCursor(table_path, [msf_3_field]) as cursor:
    for row in cursor:
        row[0] = msf_value  # Write the calculated value to the MSF_3_ field
        cursor.updateRow(row)

print("Calculation is complete and the MSF_3_ field has been updated.")
```

Figure A6.8 Magnitude Scaling Factors

```
import arcpy

# Specify the path to your table
table_path = r"C:\Users\atspi\OneDrive\Desktop\ARCGIS-TEZ\Pinar_Tez\Pinar_Tez.gdb\T_1_SK_1__ExportTable1"  # Update as needed

# Specify field names
f_n1_60_i_field = "F_N1_60_i"
f_no200_field = "F_No200"
crr7_5_field = "CRR7_5_"

# Use UpdateCursor to process each record in the table
with arcpy.da.UpdateCursor(table_path, [f_n1_60_i_field, f_no200_field, crr7_5_field]) as cursor:
    for row in cursor:
        f_n1_60_i_value = row[0]  # Get the value from the F_N1_60_i field
        f_no200_value = row[1]  # Get the value from the F_No200 field

        # If F_N1_60_i is empty, set CRR7_5_ to None
        if f_n1_60_i_value in (None, ""):
            crr7_5_value = None

        # If F_N1_60_i < 30 and F_No200 <= 50, perform the calculation
        elif f_n1_60_i_value < 30 and f_no200_value <= 50:
            # Apply the formula
            crr7_5_value = (1 / (34 - f_n1_60_i_value)) + (f_n1_60_i_value / 135) + (50 / ((f_n1_60_i_value * 10 + 45) ** 2)) - (1 / 200)

        else:
            crr7_5_value = None  # If conditions are not met, set CRR7_5_ to None

        row[2] = crr7_5_value  # Write the calculated value to the CRR7_5_ field
        cursor.updateRow(row)

print("Calculation is complete and the CRR7_5_ field has been updated.")
```

Figure A6.9 Cyclic Resistance Ratio, $CRR_{7.5}$*

```
import arcpy

# Specify the path to your table
table_path = r"C:\Users\atspi\OneDrive\Desktop\ARCGIS-THESIS\Borehole_Idealized\Borehole_Idealized.gdb\BoreholePointsRev"  # Update as needed

# Define field names
a_2_field = "a_2_"  # Initial value
f_n1_60_i_field = "F_N1_60_i"  # F_N1_60_i
no200_field = "F_No200"  # No200 field
edg_field = "EDG"  # EDG
dg_field = "DG"  # DG
rd_field = "rd"  # rd
csr_2_field = "CSR__2_"  # Field to be calculated

# Process each record in the table using UpdateCursor
with arcpy.da.UpdateCursor(table_path, [a_2_field, f_n1_60_i_field, no200_field, edg_field, dg_field, rd_field, csr_2_field]) as cursor:
    for row in cursor:
        a_2_value = row[0]  # a_2_field
        f_n1_60_i_value = row[1]  # F_N1_60_i
        no200_value = row[2]  # No200
        edg_value = row[3]  # EDG
        dg_value = row[4]  # DG
        rd_value = row[5]  # rd

        # Check conditions
        if f_n1_60_i_value in (None, ""):
            csr_2_value = None  # If F_N1_60_i is empty, set CSR__2_ to empty
        elif f_n1_60_i_value > 30:
            csr_2_value = None  # If F_N1_60_i is greater than 30, set CSR__2_ to empty
        elif f_n1_60_i_value < 30 and no200_value < 50:
            # Check if values are numeric
            if all(isinstance(value, (int, float)) for value in [a_2_value, f_n1_60_i_value, no200_value, edg_value, dg_value, rd_value]):
                csr_2_value = 0.65 * a_2_value * (dg_value / edg_value) * rd_value
            else:
                csr_2_value = None  # If not numeric, set CSR__2_ to None
        else:
            csr_2_value = None  # If conditions are not met, set CSR__2_ to None

        row[6] = csr_2_value  # Write the calculated value to CSR__2_
        cursor.updateRow(row)

print("Calculation completed, and CSR__2_ field has been updated.")
```

Figure A6.10 Cyclic Stress Ratio, CSR (for DD2 Level)

```
import arcpy

# Specify the path to your table
table_path = r"C:\Users\atspi\OneDrive\Masaüstü\ARCGIS-TEZ\Sondaj_Idealize\Sondaj_Idealize.gdb\BoreholePointsRev"  # Update as needed

# Specify field names
crr_75i_field = "CRR7_5_"  # CRR7_5_ field
csr_2_field = "CSR__2_"    # CSR__2_ field
msf_2_field = "MSF_2_"     # MSF_2_ field
fs_2i_field = "Fs___2_"    # Fs___2_ field

# Process each record using UpdateCursor
with arcpy.da.UpdateCursor(table_path, [crr_75i_field, csr_2_field, msf_2_field, fs_2i_field]) as cursor:
    for row in cursor:
        crr_75i_value = row[0]
        csr_2_value = row[1]
        msf_2_value = row[2]

        # Check conditions
        if csr_2_value in (None, "") or crr_75i_value in (None, ""):
            fs_2i_value = None  # If CSR__2_ or CRR7_5_ is empty, set Fs___2_ to None
        else:
            # Ensure values are numeric
            if all(isinstance(value, (int, float)) for value in [crr_75i_value, csr_2_value, msf_2_value]) and csr_2_value != 0:
                fs_2i_value = (crr_75i_value / csr_2_value) * msf_2_value
            else:
                fs_2i_value = None  # If not numeric or CSR__2_ is zero, set Fs___2_ to None

        row[3] = fs_2i_value  # Write the calculated value to the Fs___2_ field
        cursor.updateRow(row)

print("Calculation completed, and the Fs___2_ field has been updated.")
```

Figure A6.11 Factor of Safety, FS (for DD2 Level)